

---

# Computational study of thermotechnical two-phase flow configurations with scale-resolving turbulence models

---

Zur Erlangung des akademischen Grades Doktor-Ingenieur (Dr.-Ing.)  
Vorgelegte Dissertation von Ivan Joksimović aus Belgrad, Serbien  
Tag der Einreichung: 01. November 2022, Tag der Prüfung: 20. Dezember 2022

1. Review: apl. Prof. Dr.-Ing. habil. Suad Jakirlić
2. Review: Prof. Dr.-Ing. Jeanette Hussong
3. Review: Prof. Dr.-Ing. habil. Rodion Groll  
Darmstadt



TECHNISCHE  
UNIVERSITÄT  
DARMSTADT

Mechanical Engineering  
Department



Computational study of thermotechnical two-phase flow configurations with scale-resolving turbulence models

Submitted doctoral thesis by Ivan Joksimović

1. Review: apl. Prof. Dr.-Ing. habil. Suad Jakirlić
2. Review: Prof. Dr.-Ing. Jeanette Hussong
3. Review: Prof. Dr.-Ing. habil. Rodion Groll

Date of submission: 01. November 2022

Date of thesis defense: 20. Dezember 2022

Darmstadt

Bitte zitieren Sie dieses Dokument als:

URN: urn:nbn:de:tuda-tuprints-urn:nbn:de:tuda-tuprints-237663

URL: <http://tuprints.ulb.tu-darmstadt.de/>

Dieses Dokument wird bereitgestellt von tuprints,

E-Publishing-Service der TU Darmstadt

<http://tuprints.ulb.tu-darmstadt.de>

[tuprints@ulb.tu-darmstadt.de](mailto:tuprints@ulb.tu-darmstadt.de)

CC BY-SA 4.0 International

Dedicated to my wife Marija, to my family and to my  
friends



---

## Erklärungen laut Promotionsordnung

### **§8 Abs. 1 lit. c PromO**

Ich versichere hiermit, dass die elektronische Version meiner Dissertation mit der schriftlichen Version übereinstimmt.

### **§8 Abs. 1 lit. d PromO**

Ich versichere hiermit, dass zu einem vorherigen Zeitpunkt noch keine Promotion versucht wurde. In diesem Fall sind nähere Angaben über Zeitpunkt, Hochschule, Dissertationsthema und Ergebnis dieses Versuchs mitzuteilen.

### **§9 Abs. 1 PromO**

Ich versichere hiermit, dass die vorliegende Dissertation selbstständig und nur unter Verwendung der angegebenen Quellen verfasst wurde.

### **§9 Abs. 2 PromO**

Die Arbeit hat bisher noch nicht zu Prüfungszwecken gedient.

Darmstadt, 01. November 2022

---

I. Joksimović



# Abstract

---

The present work deals with the further development of a novel scale-resolving model of turbulence, in terms of its computational validation and in-depth analysis of its predictive performance under the conditions of complex interacting flow and thermal fields, as encountered in the thermotechnical two-phase flow systems. Computational capturing of the phenomena being presently of interest that commonly characterize industrial flow configurations and require coupled modeling of multiple flow fields include: high turbulence intensity and large-scale instabilities, heat transfer and interphase interaction accounting also for free surface-induced effects. Their correct capturing is either beyond the capabilities of classical RANS (Reynolds-Averaged Navier-Stokes) models with respect to their inherent time-averaged theoretical foundation or is too costly for correspondingly well-resolved LES and DNS approaches. By resolving the spectrum to a reasonable extent in a grid-spacing free manner, it is expected that the most important flow features will be captured directly, while the non-resolved residual turbulence will be modeled with highest possible accuracy. Particularly suitable for the latter are the models relying on the second-moment closure concept, as presented in Jakirlić and Maduta (2015). The key question behind the outlined research is whether the accuracy of the model and competitive resources for its performance (reflected in the relatively modest grid size, as compared with LES methods) can be extended far beyond the parameter space used for its calibration and development. This dissertation addresses this question by examining some specifically configured thermotechnical flow configurations using a higher-order, scale-resolving turbulence model, termed as Improved Instability-Sensitive Reynolds-Stress Model (IIS-RSM), and associated numerical algorithms in the context of the Sensitized RANS framework.

In total, six complex flow configurations, involving a variety of all the above-mentioned phenomena, are covered by the modeling paradigm adopted. Systematical testing of the scale-resolving capability of the model scheme is initially performed over a range of canonical, but relevant pipe configurations. Afterwards, the IIS-RSM is systematically validated in simulating thermal mixing in three differently configured T-junction configurations that exhibit a complex flow topology resulting from structural variations in inflow properties and strong temperature gradients causing high-level turbulence instabilities. Moreover, the flow cases were chosen that cover the widest possible range of Reynolds numbers consistent with practically relevant operational conditions. The eddy-resolving Reynolds-stress model was further coupled with the Euler-Lagrangian methodological framework to evaluate its suitability

---

for predicting two-phase flow systems. Accordingly, three gas-liquid two-phase flow configurations were selected, representing differently arranged bubbly columns and a bubble stream generated by an emerged water jet exiting into a pool. The latter flow configuration occurring at a high Reynolds number is characterized by a jet-induced secondary motion. Additionally, model formulations describing the Bubble-Induced-Turbulence (BIT), including the model recently proposed by Ma et al. (2020), are tested for the first time as part of the complete computational model operating in a scale-resolving mode.

In addition to the common results interpretation showing the evolution of global properties and individual profiles of various variables characterizing the underlying flow and thermal fields as well as those of turbulence quantities, Proper-Orthogonal-Decomposition (POD) is used throughout the work to analyze and extract coherent flow features as a means of identifying prevalent flow mechanisms.

All simulation results show a high degree of accuracy with respect to the available experimental or otherwise numerically determined reference data. Both the statistical properties of the flow and its dynamic behavior are correctly captured qualitatively and quantitatively by the model, with remarkable reductions in the necessary spatial and temporal resolution. In the calculations of the two-phase bubbly columns, the quality of the previous studies is maintained, while the robustness and stability of the calculations have been significantly improved. Certain weak points of the IIS-RSM have been identified, and indications for future improvements are proposed and presented in the conclusion. In this way, a reliable computational tool is obtained that is capable of accurately predicting a variety of computationally challenging flow phenomena.



# Zusammenfassung

---

Die vorliegende Arbeit befasst sich mit der Weiterentwicklung eines neuartigen skalenauflösenden Turbulenzmodells im Hinblick auf dessen numerische Validierung und die eingehende Analyse seiner prädiktiven Leistungsfähigkeiten unter den Bedingungen komplex interagierender Strömungs- und Wärmefelder, wie sie in thermotechnischen Zweiphasenströmungssystemen anzutreffen sind. Zur numerischen Erfassung der behandelten Phänomene, die eine Reihe an industriellen Strömungskonfigurationen charakterisieren und eine gekoppelte Modellierung mehrerer Strömungsfelder erfordern, gehören: hohe Turbulenzintensität und großräumige Instabilitäten, Wärmeübertragungsvorgänge und Interphasenwechselwirkung unter Berücksichtigung von Effekten, die durch freie Oberflächen verursacht werden. Ihre korrekte Erfassung übersteigt entweder die Möglichkeiten klassischer RANS-Modelle (Reynolds-Averaged Navier-Stokes) im Hinblick auf ihre inhärente zeitgemittelte theoretische Grundlage oder ist zu kostspielig für entsprechend gut aufgelöste LES- und DNS-Ansätze. Durch die gitterfreie Auflösung des Spektrums in einem entsprechenden Umfang wird erwartet, dass die wichtigsten Strömungsmerkmale direkt erfasst werden, während die nicht aufgelöste Turbulenz mit höchstmöglicher Genauigkeit modelliert wird. Für Letzteres eignen sich besonders die Modelle, die auf dem Konzept der Dynamik der Momente zweiter Ordnung der Geschwindigkeitsfluktuationen beruhen, wie in Jakirlić and Maduta, 2015 vorgestellt. Die zentrale Frage, die sich hinter den dargestellten Forschungsaktivitäten verbirgt, ist, ob die Genauigkeit und die wettbewerbsfähigen Ressourcen für die Modelleleistung weit über den für die Kalibrierung und Entwicklung des Modells verwendeten Parameterraum hinaus erweitert werden können. Diese Dissertation befasst sich mit dieser Frage, indem sie einige spezifisch konfigurierte thermo-technische Strömungskonfigurationen unter Verwendung eines skalenauflösenden Turbulenzmodells höherer Ordnung (Improved Instability-Sensitive Reynolds-Stress Model, IIS-RSM) und zugehöriger numerischer Algorithmen im Kontext der 'Sensitized-RANS' Methode untersucht.

Insgesamt werden sechs komplexe Strömungskonfigurationen, die durch eine Vielzahl der oben genannten Phänomene charakterisiert sind, durch das eingesetzte Modellierungskonzept abgedeckt. Die wirbelauflösende Fähigkeit des Modells wird zunächst systematisch für eine Reihe kanonischer, aber relevanter Rohrkonfigurationen getestet. Anschließend wird das IIS-RSM systematisch bei der Simulation der thermischen Vermischung in drei unterschiedlich konfigurierten T-Verbindungsstück-Konfigurationen validiert, die eine komplexe Strömungstopologie aufweisen, die sich

---

aus strukturellen Variationen der Einströmeigenschaften und starken Temperaturgradienten ergibt, die verstärkte Turbulenzinstabilitäten verursachen. Darüber hinaus wurden die Strömungsfälle so gewählt, dass sie den größtmöglichen Bereich von Reynoldszahlen abdecken, die mit praktisch relevanten Betriebsbedingungen kompatibel sind. Das wirbelaflösende Reynolds-Spannungsmodell wurde mit dem Euler-Lagrange'schen methodologischen Verfahren gekoppelt, um dessen Eignung für die Vorhersage von Zweiphasen-Strömungssystemen zu bewerten. Dementsprechend wurden drei Gas-Flüssigkeits-Zweiphasen-Strömungskonfigurationen ausgewählt, die unterschiedlich angeordnete Blasenäulen und einen Blasenstrom darstellen, der durch einen austretenden Wasserstrahl erzeugt wird, der in eine Wasservorlage mündet. Die letztgenannte Strömungskonfiguration, die bei einer hohen Reynoldszahl auftritt, ist durch eine strahlinduzierte Sekundärbewegung gekennzeichnet. Darüber hinaus werden Modellformulierungen zur Beschreibung der blaseninduzierten Turbulenz (Bubble-Induced-Turbulence, BIT), einschließlich des kürzlich von Ma et al., 2020 vorgeschlagenen Modells, zum ersten Mal als Teil des vollständigen Berechnungsmodells getestet, das in einem skalenaflösenden Modus arbeitet.

Zusätzlich zu der allgemeinen Ergebnisinterpretation, die die Entwicklung globaler Eigenschaften und individueller Profile verschiedener Variablen zeigt, die die zugrunde liegenden Strömungs- und Wärmefelder sowie die Turbulenzgrößen charakterisieren, wird in der gesamten Arbeit die Proper-Orthogonal-Decomposition (POD) verwendet, um kohärente Strömungsmerkmale zu analysieren und zu extrahieren, um die dominierenden Strömungsmechanismen zu identifizieren.

Alle Simulationsergebnisse zeigen ein hohes Maß an Genauigkeit im Vergleich mit den verfügbaren experimentellen- oder anderweitig ermittelten numerischen Referenzdaten. Sowohl die statistischen Eigenschaften der Strömung als auch ihr dynamisches Verhalten werden durch das Modell qualitativ und quantitativ korrekt erfasst, wobei die erforderliche räumliche und zeitliche Auflösung deutlich reduziert wird. Bei den Berechnungen der zweiphasigen Blasenäulen wird die Qualität der in früheren Studien gewonnenen Ergebnisse wiedergegeben, aber die Robustheit und Stabilität der Berechnungen wurden deutlich verbessert. Bestimmte Schwachstellen des Modells wurden identifiziert, und es wurden Hinweise für künftige Verbesserungen vorgeschlagen und in der Schlussfolgerung vorgestellt. Auf diese Weise erhält man ein zuverlässiges Berechnungsmodell, das in der Lage ist, eine Vielzahl von numerisch anspruchsvollen Strömungsphänomenen genau vorherzusagen.

# Acknowledgements

---

The present work was carried out during my activity as a research assistant at the Institute of Fluid Mechanics and Aerodynamics (Fachgebiet Strömungslehre und Aerodynamik – FG SLA) of the Technical University of Darmstadt, in the period October 2019 to September 2022. I would like to express my sincere gratitude to Prof. Cameron Tropea and Prof. Jeanette Hussong, the former and current directors of the FG SLA, for the opportunity to conduct the dissertation at their institute. I would also like to thank Prof. Hussong for her critical review of the thesis as well as for the numerous discussions that have had a decisive impact on the current form of the written version. My special thanks go to my immediate supervisor Prof. Suad Jakirlić, who initiated the topic of the thesis and who actively supported me in all its phases. His profound knowledge in the field of turbulence modeling and related numerical algorithms contributed greatly to the success of the work. Additionally, I would like to thank Prof. Rodion Groll for accepting the review of this thesis.

This doctoral research was fully funded within the framework of the DAAD (Deutscher Akademischer Austauschdienst) initiative "Research Scholarships - Doctoral Studies in Germany". I express my deepest gratitude to DAAD for the given opportunity, funding and support. All the calculations outlined in this thesis were performed on high-performance computer Lichtenberg at the NHR Centers NHR4CES at TU Darmstadt. I gratefully acknowledge the computing resources and support. Reference LES results, presented in Chapter 7 were made available by Dr. Ryan Tunstall and Dr. Alex Skillen from the University of Manchester, to whom I remain indebted.

To my current and former colleagues from SLA numerics team: Dr. -Ing. Robert Maduta, Dr.-Ing. Sebastian Wegt, Maximilian Bopp and Dr. -Ing. Lukas Kutej, as well as to my former students: M.Sc. Louis Krüger and M.Sc. Tarik Čorbo, I thank for the productive and motivating working environment, as well as for many useful discussions and comments in the field of numerics. By no means least, I would like to thank all other colleagues and friends from the SLA team for the positive and friendly atmosphere both in and outside of the office!

Back home in Belgrade, I would like to thank a dear friend, Dr. Nikola Mirkov, for introducing me to the "magic" and for encouraging and nurturing my knowledge in the field of CFD. Because of that, I consider him to be my other mentor. To my high-school mathematics professor Biljana Ignjić, I would like to thank for teaching me pedantry and precision in solving of mathematical problems. Order in the head equals the order on paper!

---

Last but not least, I would like to thank my family and friends for standing by my side: to my wife Marija, for her love, support and courage to step in to the unknown with me. To both of our families, and our dear friends, both in Serbia and in Germany, I remain grateful for their care and wisdom which was readily given during the most challenging of times. I dedicate this thesis first and foremost to them.

# Contents

---

<b>Abstract</b>	<b>viii</b>
<b>Zusammenfassung</b>	<b>x</b>
<b>Acknowledgements</b>	<b>xii</b>
<b>1. Introduction and motivation</b>	<b>1</b>
1.1. Objectives and outline of this thesis . . . . .	3
<b>2. Theoretical foundations</b>	<b>7</b>
2.1. Basic equations of fluid dynamics . . . . .	7
2.1.1. Continuity equation . . . . .	9
2.1.2. Momentum equation . . . . .	9
2.1.3. Energy equation . . . . .	11
2.2. Basic considerations of the finite volume theory . . . . .	13
2.2.1. Reconstruction of spatial derivatives . . . . .	15
2.2.2. Reconstruction of temporal derivatives . . . . .	19
2.2.3. Solution of the coupled linear system of equations . . . . .	20
2.3. Modeling of two-phase dispersed flows . . . . .	23
<b>3. Turbulence modeling in single- and two-phase flows</b>	<b>31</b>
3.1. Introduction . . . . .	31
3.2. Review of the current modeling practices for turbulent flows . . . . .	35
3.2.1. Full closure strategy for Reynolds stress tensor . . . . .	40
3.2.2. Boussinesq hypothesis - eddy viscosity models . . . . .	45
3.2.3. Near-wall turbulence modeling . . . . .	46
3.3. Towards the spectral resolution - eddy sensitized variants of RANS models . . . . .	47
3.4. Modeling of turbulent scalar transport . . . . .	54
3.5. Bubble-induced turbulence . . . . .	55
<b>4. Post-processing techniques</b>	<b>59</b>
4.1. Proper-Orthogonal-Decomposition: finding the coherent structures in the turbulent flow field . . . . .	59
4.1.1. Initial examples - strengths and weaknesses . . . . .	63

4.2. Visualization of Anisotropy - componentality contours based on barycentric coordinates . . . . .	70
<b>5. Flow configuration I: Generation of inlet turbulence</b>	<b>73</b>
5.1. Discussion of results . . . . .	76
5.2. Conclusions . . . . .	83
<b>6. Flow configuration II: Turbulent thermal mixing in a T-Junction</b>	<b>85</b>
6.1. Wall jet case . . . . .	92
6.2. Impinging jet case . . . . .	104
6.3. Conclusions . . . . .	107
<b>7. Flow Configuration III: Temporal dynamics of secondary flows in a T-Junction with an upstream elbow</b>	<b>109</b>
7.1. Results . . . . .	112
7.2. Conclusions . . . . .	128
<b>8. Flow configuration IV: Two phase flows in buoyancy driven bubble columns</b>	<b>129</b>
8.1. Gas-liquid flows in wall bounded domains: bubble column case . .	131
8.2. Bubble plume in quiescent water . . . . .	145
8.3. Conclusions . . . . .	151
<b>9. Flow Configuration V: Bubble plume in open-channel cross-flow</b>	<b>153</b>
9.1. Free-surface modeling considerations . . . . .	156
9.2. Open-channel developed turbulence . . . . .	159
9.3. Main case . . . . .	166
9.4. Conclusions . . . . .	180
<b>10. Conclusions and outlook</b>	<b>181</b>
10.1. Outlook . . . . .	185
<b>Bibliography</b>	<b>186</b>
<b>A. Appendix - Improved-Instability-Sensitive Reynolds-Stress-Model</b>	<b>213</b>
<b>B. Appendix - Nomenclature</b>	<b>215</b>
<b>C. Curriculum Vitae</b>	<b>229</b>

# 1. Introduction and motivation

---

Methods of Computational Fluid Dynamics (CFD), representing a tool for calculating the numerical solution to the system of governing fluid flow equations, have been used for more than 70 years as an aid in the engineering and design of flow systems, according to Richardson and Lynch (2007). Despite the enormous experience, the accurate reproduction of flow processes as encountered in industrial plants remains an open area of research and optimization. Apart from the availability of computing power and the maturity of the numerical method used, the broad spectrum of flow phenomena represents the greatest challenge in the application of CFD. These are notably: high level of turbulence, complex flow topologies (secondary flows, anisotropy-related mechanisms, recirculation zones etc.), presence of one or more phases in the flow domain, non-isothermal conditions (heat transfer or/and phase change), and chemical reactions to name just a few. Over the years, a variety of modeling approaches have been developed to simulate either the single phenomenon or the chosen combination of the previously mentioned phenomena, with each approach having its advantages and disadvantages.

Accordingly, the prime motivation for this work is to numerically integrate and validate the predictive performance of different modeling strategies for fluid flow simulation and analysis relevant to the field of thermotechnical systems. These strategies could eventually be combined into a single computational framework to provide a modular tool that can be used flexibly to solve a wide range of flow problems. In order to achieve the most possible universality and flexibility mentioned above, several key issues for the application of CFD in the field of industrial flows need to be addressed.

The first open problem is related to the usage of the appropriate turbulence model, which should be capable to accurately predict large variety of the complex turbulent flow phenomena. As outlined in Chapter 3, the model adopted for this work represents the novel, eddy-resolving (ER) RANS model by Maduta (2013), which is capable to resolve the turbulent spectrum to an appropriate extent, while modeling the residual turbulence with the adequately sensitized full second-moment closure (SMC). Further discussion on the advantages of SMC in combination with spatial resolution in terms of implicitly incorporated mesh-related parameters will follow in Chapter 3. So far, Maduta's model has been successfully used over the variety of flow configurations occurring at moderate Reynolds numbers  $Re$  (e.g. Jakirlić and Maduta (2015) or Maduta and Jakirlić (2016)), while keeping the necessary computational resources below those, which are required by correspondingly well-

resolved LES methodology. Based on this initial success, the question discussed in this thesis is whether the demonstrated accuracy can be successfully (and at what costs) extrapolated to the flows with industrially relevant, high  $Re$  number characteristics and complex flow conditions. Additionally, interaction of the model equations, formulated in a grid spacing-free manner, with the grid resolution applied could not be adequately understood so far, due to its implicit influence on the flow topology. Although the problem of the model's inherent spectral resolution was analyzed in certain detail in Köhler et al. (2018), no definite answer to the precise model's correlation with the mesh resolution limit could be found. This thesis aims at adequately closing this knowledge gap. As from the point of other flow fields like temperature, concentration etc., the treatment of their unresolved fluxes and their influence on the final result still remains the topic of open discussion.

Second open problem, discussed in this thesis, is related to the integration of the turbulence model with the strategies for simulating multiphase flow regimes, commonly encountered in industrial flow systems. Rationale behind the modeling framework in multiphase flows depends mainly on the assumptions made by the model of turbulence. This is dominantly reflected in the choice of smallest scale (detail of the interfacial surface, bubble/droplet size etc.) that could be resolved by the model. On the account of that, specific classes of flows need to be sort for the model validation, with highly turbulent, dispersed bubbly flows being selected for this work. Previously, Ullrich (2017) aimed at integrating the above-mentioned Maduta's ER-SMC model with the Two-fluid modeling (TFM) framework for several cases of pipe flows. One of the main obstacles was the predominantly unstable computational methods, which often made it impossible to obtain results in complex geometries. Additionally, the conflicting assumptions underlying the turbulence model and the TFM resulted in multiple scattering artifacts in the solution. In-depth discussion on the topic will follow in Chapter 2. This motivates the integration of an alternative, Euler-Lagrange (EL) two-phase flow model with the presently used model of turbulence, in quest for obtaining and testing a more stable conjuncture of two modeling strategies. State of the art in modeling of turbulent dispersed bubbly flows is reviewed in high detail in Chapters 2 and 8. Related to their multiphase nature, thermotechnical flow systems may often be characterized by the presence of the free-surface (domain-scale separation between the phases), in which the structures created by the anisotropy of the flow often fall beyond the closure capabilities of conventional RANS models, requiring an LES-like approach, which is often too expensive for the industrial use. Behavior of the eddy-sensitized turbulence models remains poorly tested under such conditions as well, motivating the analysis in this thesis. Lastly, partial resolution of turbulence spectrum in two phase flows opens the problems of energy transfer between the dispersed phase and the carrier phase, at the sub-grid (modeled) scale of the flow. This will be referred to as to the Bubble-Induced-Turbulence (BIT), which still remains the area of systematic research, and its assumptions need to be further addressed in combination with eddy-resolving models, as per Dhotre et al. (2013).



## 1.1. Objectives and outline of this thesis

As discussed in the previous section, this thesis aims at integrating the computationally optimized simulation framework for handling the industrially relevant flow problems in thermal engineering installations. Here, to describe the dynamics of the residual unresolved turbulence, an eddy-sensitized RANS model, based on the full second-moment closure (introduced under the acronym IIS-RSM throughout the work) is tested on a set of experimentally studied flow configurations that closely reflect some of the relevant components of the thermotechnical piping systems. In addition to extending the application of the model to flow configurations with boundary conditions beyond the range of those used for its original calibration and development, this work will also highlight its advantages and weaknesses. For the purpose of modeling the heat-transfer in terms of sub-grid fluxes, two commonly used approaches, *Simplified-Gradient-Hypothesis* (SGDH) and *Generalized-Gradient-Hypothesis* (GGDH) will be outlined in Chapter 2 and tested in Chapter 6.

In addition, the presently adopted eddy-resolving, second-moment closure model is for the first time (to the authors knowledge) integrated into the Euler-Lagrange (EL) simulation framework for modeling dispersed bubbly flow regimes. The intention is to increase the robustness of the model in the flow cases where the bubble-size corresponds closely to the meso-scale, i.e. in the case where the mesh size and the bubble size are comparable. At the same time, problems related to the stability of the second-moment closure integrated into Euler-Euler methodology are adequately addressed. Furthermore, the performance of two models for Bubble-Induced-Turbulence (BIT) is assessed within the EL-IIS-RSM eddy-resolving framework. As a third objective, the coupling of the IIS-RSM in conjunction with the free-surface modeling considerations is introduced. The aim behind it is testing whether the reduced meshing resolution required by the IIS-RSM may adequately predict the complex secondary flow events, which stem from the turbulence anisotropy. In-depth discussion about the state of the art in hybridisation of eddy-resolving strategies and modeling assumptions for multiphase flow follows in Chapter 2.

For performing the simulations, an open-source C++ library OpenFOAM®, (version v2112) offering a set of finite-volume (FV) solvers that operate on arbitrary shaped unstructured meshes, is used throughout this work. Programmatic implementation of all the models outlined in this thesis was performed within the framework of the present thesis. Numerical rationale behind the finite-volume-method (FVM), as well as theoretical considerations behind the algorithms for the solution of pressure-velocity coupled problems is outlined in more detail in Chapter 2. For the extraction of coherent flow patterns, Proper-Orthogonal-Decomposition (POD) is tested as an integral part of the analysis framework for thermotechnical piping systems. Over the recent years, POD technique has gained substantial popularity as a state of the art tool for isolating most energetic physical mechanisms (Lu et al.

(2019)), thus giving a valuable insight into the flow dynamics. The implementation of the POD procedure in the open source Python code also represents the activity carried out in the context of the present work.

Based on the above introduced objectives, the thesis is organized as follows:

In **Chapter 2** the modeling background necessary for describing the numerical solution of single, but also dispersed two-phase flows is presented. Next to the derivation of evolution equations for individual flow variables, the state of the art in different modeling strategies for two-phase flows is discussed along with advantages and disadvantages of various approaches. At the end, modeling rationale for their usage in this thesis is discussed.

In **Chapter 3**, the problems of turbulence modeling in single and two-phase flows is discussed. Derivation, evolution and mathematical analysis of the IIS-RSM is presented in detail, with initial strengths and weaknesses outlined. Additionally, two models handling the bubble-induced-turbulence are outlined; the models are to be used for in Chapters 8 and 9.

In **Chapter 4**, post-processing techniques for the analysis of eddy-resolving turbulence models are discussed. Next to the visualisation of turbulence anisotropy using the barycentric contour maps, identification of dynamic coherent structures in the flow field by the means of Proper-Orthogonal-Decomposition (POD) is outlined, with core advantages and disadvantages discussed and demonstrated. In this way, a greater insight is given into the evolution of coherent flow structures, which are usually obscured by the random turbulent pulsations.

In **Chapter 5**, the performance of IIS-RSM is systematically tested over a wide range of Reynolds numbers, by means of computing the fully-developed pipe flow. Accuracy in predicting the first- and second-order statistics, as well as the behaviour of the model in terms of the spectral resolution is assessed. This study provides a thorough analysis on the optimal mesh metrics and the creation of the precursor data-base for use in Chapters 6 and 7.

In **Chapter 6**, the performance of IIS-RSM is tested in two cases involving complex thermal mixing of two fluid streams in a T-Junction configuration characterized by different flow topologies originating from different flow rate ratios. Here, both the statistical properties of the flow, as well as its dynamical response play an important role in the T-Junction design. The model is tested at the level of maximal Reynolds number, with aims of showing that the accuracy in solution can be achieved with the substantially reduced grid cell number and diminished mesh-topology dependence, in comparison with concurring eddy-resolving strategies. Identification of correlated flow structures in the wake of the mixing zone will be investigated in the post-processing phase using POD.

In **Chapter 7**, another industrially relevant case, involving a T-Junction with an upstream elbow will be reproduced by applying the IIS-RSM. Correct capture of switching dynamics, involving a pair of curvature-induced secondary vortices is

assessed, along with its influence on the mixing properties in the outlet region of the T-Junction. Possible parasitic influences of precursor simulations are analyzed using the POD method.

In **Chapter 8**, the IIS-RSM is tested in conjunction with Euler-Lagrange (EL) framework for simulating the buoyancy driven, dispersed gas-liquid flows in bubble columns. Additionally, two bubble-induced-turbulence (BIT) models are tested. It is demonstrated how different modeling frameworks interact in terms of predicting the statistical two-phase flow quantities and the turbulence-resolving properties of the model. Certain limitations of IIS-RSM in terms of reproducing the fluctuating flow field are addressed based on the calculation of free bubble jets.

In **Chapter 9**, the predictive performance of IIS-RSM is tested by computing a free-surface flow in an open channel with a submerged bubble jet in the crossflow, where the computationally determined flow topology is largely influenced by the correct prediction of turbulence anisotropy. The exact boundary conditions that apply to the modeled turbulence at the free surface are derived. Finally, in this Chapter most of the modeling work described in this thesis is performed, where the effect of almost all flow phenomena presented in the previous chapters are to be simulated in parallel.

The thesis concludes with **Chapter 10**, which outlines the conclusions drawn from the research conducted and provides directions for improvement and future research efforts.



## 2. Theoretical foundations

---

In this Chapter, some base postulates and equations from the field of computational fluid dynamics (CFD) will be introduced. Next to the governing laws for the single-phase flow problems, strategies for simulating the dispersed, two-phase bubbly flows will be addressed as well. Lastly, certain aspects related to the numerical solution of the system of governing equations will be introduced, within the framework of Finite-Volume-Method (FVM) theory.

### 2.1. Basic equations of fluid dynamics

#### 2.1.0.1. Material derivative and Reynolds transport theorem

When tackling with flow problems, large number of individual fluid parcels represent a challenging task when formulating basic equations involving their motion. Although the Lagrangian approach (in which the observer is fixated on the individual parcel) will be used in this Chapter for simulating two-phase flow problematic, governing equations of fluid dynamics are usually derived in the Eulerian frame of reference, where the observer is fixed to a coordinate system. Let  $\phi$  be any conserved property of the flow. Then its dependence of spatial and temporal coordinates is expressed as:

$$\phi = \phi(x_k, t) \quad (2.1)$$

with  $k = 1, 2, 3$  for each of Cartesian coordinates. Therefore, any evolution in  $\phi$  can be expanded around the point  $(x_k, t)$  using the Taylor series as:

$$\begin{aligned} \phi(x_k + \Delta x_k, t + \Delta t) &= \phi(x_k, t) + \\ &+ \frac{\partial \phi}{\partial t} \Delta t + \frac{1}{2} \frac{\partial^2 \phi}{\partial t^2} \Delta t^2 + \dots \\ &+ \frac{\partial \phi}{\partial x_k} \Delta x_k + \frac{1}{2} \frac{\partial^2 \phi}{\partial x_k^2} \Delta x_k^2 + \dots \end{aligned} \quad (2.2)$$

Taking the net change in  $\phi$ , and dividing by  $\Delta t$ , one gets in the limit case:

$$\lim_{\Delta x_k, \Delta t \rightarrow 0} \frac{\phi(x_k + \Delta x_k, t + \Delta t) - \phi(x_k, t)}{\Delta t} = \frac{D\phi}{Dt} = \frac{\partial \phi}{\partial t} + \frac{\partial \phi}{\partial x_k} U_k \quad (2.3)$$

Here, in the limit case, finite differences were transformed in to differentials. Additionally, higher order terms in the Taylor expansion 2.2 have been neglected. Relation 2.3 is also known as a *material derivative*, and denotes the net change of  $\phi$  in the Eulerian reference frame. Taking the change is spatial shift  $\Delta x_k$  with respect to time, velocity vector  $U_k$  is obtained in the limit case. Here, a so-called non-conservative form of the material derivative is given:

$$\frac{D\phi}{Dt} = \frac{\partial\phi}{\partial t} + \vec{U} \cdot \nabla(\phi) \quad (2.4)$$

Let  $f$  be the density of  $\phi$ , defined as:

$$\phi = \int_V f dV \quad (2.5)$$

where  $V$  is an arbitrary shaped material volume. Therefore, material derivative of  $\phi$  can be extended into:

$$\frac{D\phi}{Dt} = \frac{D}{Dt} \int_V f dV \quad (2.6)$$

After substituting the order of integration and derivation, and by applying the derivation on  $f dV$ , we get:

$$\frac{D\phi}{Dt} = \int_V \left[ \frac{Df}{Dt} + f \frac{D(dV)}{Dt} \frac{1}{dV} \right] dV \quad (2.7)$$

Following a detailed theoretical discussion of Gauss-Ostrogradski Theorem (see Crnojević (2014)), one can prove that for material volume:

$$\frac{D(dV)}{Dt} \frac{1}{dV} = \nabla \cdot \vec{U} \quad (2.8)$$

Substitution of previous equation into the 2.7 yields:

$$\frac{D\phi}{Dt} = \int_V \left[ \frac{Df}{Dt} + f \nabla \cdot \vec{U} \right] dV \quad (2.9)$$

With the respect to the definition of material derivative 2.4 and by compressing the terms, we get:

$$\frac{D\phi}{Dt} = \int_V \left[ \frac{\partial f}{\partial t} + \nabla \cdot (\vec{U} f) \right] dV \quad (2.10)$$

Equation 2.10 enables us to express a material derivative in a so-called conservative, which will be of immense importance in following sections.

### 2.1.1. Continuity equation

Let us observe an arbitrary shaped material volume  $V$ , in which total mass  $m$  is contained. By using the definition of density  $\rho$ , one can write:

$$m = \int_V \rho dV \quad (2.11)$$

Mass-conservation postulate states that the net-change of  $m$  in the material volume can only come from the presence of internal mass sources  $S$ . In all other cases, mass is constant. In the integral form, this reads:

$$\frac{Dm}{Dt} = \int_V S dV \quad (2.12)$$

By using the conservative form of material derivative 2.10, one obtains:

$$\frac{Dm}{Dt} = \int_V \left[ \frac{\partial \rho}{\partial t} + \nabla \cdot (\rho \vec{U}) \right] dV = \int_V S dV \quad (2.13)$$

or in the local form, previous equation reads:

$$\frac{\partial \rho}{\partial t} + \nabla \cdot (\rho \vec{U}) = S \quad (2.14)$$

Relation 2.14 represents a general form of the continuity equation. Very often, mass sources don't exist, so the equation 2.14 takes the form:

$$\frac{\partial \rho}{\partial t} + \nabla \cdot (\rho \vec{U}) = 0 \quad (2.15)$$

Finally, if the changes of density can be neglected, i.e.  $\rho = \text{const.}$  (incompressible flow), equation 2.14 takes a so called divergence-free (solenoidal) form:

$$\nabla \cdot \vec{U} = 0 \quad (2.16)$$

or in the indexed notation:

$$\frac{\partial U_i}{\partial x_i} = 0 \quad (2.17)$$

### 2.1.2. Momentum equation

Total momentum contained within the material volume can be expressed as:

$$\vec{M} = \int_V \rho \vec{U} dV \quad (2.18)$$

where  $\rho \vec{U}$  can be understood as a momentum density. Newton's second law states that the net change of momentum inside the material volume is equal to the sum of all forces (surface and volumetric forces) acting upon it:

$$\frac{D\vec{M}}{Dt} = \vec{F}_A + \vec{F}_V \quad (2.19)$$

Forces acting on the surface of material volume can be expressed as:

$$\vec{F}_A = \int_A \bar{\sigma} \cdot \vec{n} dA \quad (2.20)$$

where  $\bar{\sigma}$  is the (second-order) tensor of surface forces, and  $A$  is the surface of the material volume, with the surface normal unit-vector  $\vec{n}$ . Volumetric (body) forces may be expressed using their specific acceleration  $\vec{f}$ :

$$\vec{F}_V = \int_V \rho \vec{f} dV \quad (2.21)$$

By using the Gaussian rule for surface integrals and combining the conservative form of material derivative for  $\vec{M}$  (2.10) with (2.20 - 2.21), one gets in the local form:

$$\frac{\partial}{\partial t} (\rho \vec{U}) + \nabla \cdot (\rho \vec{U} \vec{U}) = \rho \vec{f} + \nabla \cdot \bar{\sigma} \quad (2.22)$$

In general, effect of surface forces can be decomposed in the part affecting the volume of the fluid parcel (compression/expansion) and part affecting its shape (deformation). Effects of compression/expansion will originate from the changes in static pressure  $p$ , defined as:

$$p = -\frac{1}{3} \text{tr}(\bar{\sigma}) \quad (2.23)$$

Change of shape of the material volume is sublimed in the shear-stress tensor  $\bar{\tau}$ , defined as:

$$\bar{\sigma} = -p \cdot I + \bar{\tau} \quad (2.24)$$

where  $I$  is the unit tensor. By combining equations 2.22 to 2.24, we arrive at the so-called *Navier* form of the momentum equation:

$$\frac{\partial}{\partial t} \rho \vec{U} + \nabla \cdot (\rho \vec{U} \vec{U}) = \rho \vec{f} - \nabla p + \nabla \cdot \bar{\tau} \quad (2.25)$$

If the fluid exhibits the linear relation between the stress and strain (as will all the fluids used in this work), a so-called *Stokes*-closure is provided for the shear-stress term in the form:

$$\bar{\tau} = 2\mu \left[ \frac{1}{2} (\nabla \vec{U} + \nabla \vec{U}^T) - \frac{1}{3} \nabla \cdot \vec{U} \right] \quad (2.26)$$

where  $\mu$  is the dynamic viscosity coefficient, which may either be a scalar, or a tensor (in case of anisotropic fluids, which are not considered in this work). Finally, general conservative form of the momentum equation is obtained as:



$$\frac{\partial}{\partial t} \rho \vec{U} + \nabla \cdot (\rho \vec{U} \vec{U}) = \rho \vec{f} - \nabla p + \nabla \cdot \left( 2\mu \left[ \frac{1}{2} (\nabla \vec{U} + \nabla \vec{U}^T) - \frac{1}{3} \nabla \cdot \vec{U} \right] \right) \quad (2.27)$$

In the index notation, previous equation reads:

$$\frac{\rho \partial U_i}{\partial t} + \frac{\partial}{\partial x_k} (\rho U_i U_k) = \rho f_i - \frac{\partial p}{\partial x_i} + 2\mu S_{ij}^d \quad (2.28)$$

where  $S_{ij}^d$  is the deviatoric part of the strain tensor:

$$S_{ij}^d = \frac{1}{2} \left( \frac{\partial U_i}{\partial x_j} + \frac{\partial U_j}{\partial x_i} \right) - \frac{1}{3} \frac{\partial U_k}{\partial x_k} \quad (2.29)$$

If the flow is incompressible, insertion of 2.16 into 2.27 yields:

$$\frac{\partial \vec{U}}{\partial t} + \nabla \cdot (\vec{U} \vec{U}) = \vec{f} - \frac{1}{\rho} \nabla p + \nu \nabla^2 \vec{U} \quad (2.30)$$

or in the indexed notation:

$$\frac{\partial U_i}{\partial t} + \frac{\partial}{\partial x_k} (U_i U_k) = f_i + \frac{1}{\rho} \frac{\partial p}{\partial x_i} + \frac{\partial}{\partial x_k} \left( \nu \frac{\partial U_i}{\partial x_k} \right) \quad (2.31)$$

which is a general form of the momentum equation applied in this thesis. Due to the incompressible nature of the flow, used numerical solver divides the pressure variable in advance with the density  $p/\rho$ , hence creating a co-called *kinematic-pressure*, which will be of importance while interpreting results in Chapters 5 to 9. Analogously,  $\nu$  denotes the value of *kinematic viscosity*. System of equations completely describing the dynamics of incompressible flows with constant fluid properties, involves the continuity equation 2.16 and the momentum equation 2.31, and is named *Navier-Stokes* (NS) equations.

### 2.1.3. Energy equation

According to the first law of thermodynamics, one can state that the change of total energy  $E$  within the material volume is due to the rate of work (performed by the volumetric and surface forces), as well as due to the thermal energy, created/destroyed, or transported along the boundaries of the material volume:

$$\frac{DE}{Dt} = \dot{Q}_V + \dot{Q}_A + \dot{W}_V + \dot{W}_A \quad (2.32)$$

The individual terms are modeled as:

$$E = \int_V e dV = \int_V \left( i + \frac{1}{2} \vec{U} \cdot \vec{U} \right) dV \quad (2.33)$$

where  $e$  is the sum of the internal energy  $i$ , and the kinetic energy  $K$ . Work of the body forces is obtained as

$$\dot{W}_V = \int_V \vec{f} \cdot \vec{U} dV \quad (2.34)$$

and the work of surface forces as:

$$\dot{W}_A = \int_A \left( -p\vec{I} + \vec{\tau} \right) \cdot \vec{U} dA = \int_V \left( -\nabla \cdot (p\vec{U}) + \nabla \cdot (\vec{\tau} \cdot \vec{U}) \right) dV \quad (2.35)$$

Finally, heat-transfer through the boundary of the material volume is calculated as:

$$\dot{Q}_s = \int_A \vec{q}_A \vec{n} dA = \int_V \nabla \cdot \vec{q}_A dV \quad (2.36)$$

where  $\vec{q}_A$  is the specific heat flux. By combining all the terms, one arrives at the transport equation for the total energy in the index notation:

$$\frac{\partial e}{\partial t} + \frac{\partial}{\partial x_i} (U_i e) = U_i f_i - \frac{\partial}{\partial x_i} (U_i p) + \frac{\partial}{\partial x_i} (\tau_{ij} U_j) + \frac{\partial q_i}{\partial x_i} \quad (2.37)$$

When operating with non-isothermal flows, as will be presented in Chapters 6 and 7, all flow-related thermal effects are governed by the equation 2.37. Choice of variable  $e$  is not optimal since it combines the influences of internal energy, as well as the kinetic energy. Kinetic energy is therefore first eliminated from the system. First, transport equation for  $K$  is derived by multiplying the momentum-transport equation 2.28 with  $U_i$ , and dividing the result by 2, thus obtaining:

$$\frac{\partial K}{\partial t} + \frac{\partial}{\partial x_k} (U_i K) = U_i U_k \frac{\partial U_i}{\partial x_k} + f_i U_i + \frac{\partial p}{\partial x_i} U_i + \frac{\partial}{\partial x_k} \left( \nu \frac{\partial K}{\partial x_k} \right) - \underbrace{\nu \frac{\partial U_i}{\partial x_k} \frac{\partial U_i}{\partial x_k}}_{\varepsilon} \quad (2.38)$$

Note that the last term in the equation 2.38 represents a sink-term, denoting the transfer of mechanical energy into the thermal energy by the action of viscous effects. It is further denoted as the viscous dissipation -  $\varepsilon$ .

Ultimately, equation 2.38 is subtracted from 2.37, obtaining the transport equation for the internal energy  $i$ . However, internal energy is for this case also a non-favorable variable and needs to be transformed directly into the temperature, which can be measured. This is done firstly by transforming the internal energy into the enthalpy variable  $h = i + p/\rho$ , and then expressing the temperature as the function of enthalpy. After a lengthy derivation which will not be repeated here (for details, see Crnojević (2014), or Darwish and Moukalled (2021)), one obtains the temperature transport equation in the form:

$$\frac{\partial T}{\partial t} + \frac{\partial}{\partial x_k} (U_k T) = \frac{\partial}{\partial x_k} \left( \alpha \frac{\partial T}{\partial x_k} \right) \quad (2.39)$$

with  $\alpha$  being the temperature diffusivity, expressed as:

$$\alpha = \frac{k}{\rho c_p} \quad (2.40)$$

where  $k$  is the thermal conductivity of the fluid,  $\rho$  is its density, and  $c_p$  is the constant-pressure heat capacity.

## 2.2. Basic considerations of the finite volume theory

System of Navier-Stokes equations (2.16, 2.31), along with the temperature transport equation (2.39) represents a system of non-linear partial differential equations, whose analytical solutions exist only in small set of highly simplified cases. In all other cases, relevant to the engineering practice, analytical solutions are excluded, and hence, appropriate numerical procedures must be used for the solution obtainment. Choice of the numerical method for the solution is governed by multitude of parameters, such as: experience of the author, availability of software and simplicity of procedure implementation, governing models of turbulence and many more.

In this thesis, finite-volume-method (FVM) will be applied. As a main advantage, FVM is inherently conservative with respect to the governing equations, and may operate with arbitrary shaped mesh cells (tetrahedral, hexahedral, polyhedral, etc.), which is of highest benefit when dealing with complex geometries in the industrial practice. Additionally, treatment and implementation of differential operators and various numerical models is straightforward (in physical space, without the transformation of coordinates etc.), which substantially eases the programming of the scientific software. FVM hence remains the method of choice for the majority of available CFD codes and frameworks. One of the key deficiencies of finite volume method is its relatively low order of accuracy (usually second-order accurate) in the operator reconstruction. This dictates that for the detailed resolution of smallest flow scales, appropriately large number of cells need to be used, which hinders the application for scale-resolving simulations on large  $Re$ . However, FVM is by far the most matured method in the computational fluid dynamics arsenal, and is widely used in a number of commercially and openly available codes. In this section, some of the principal strategies of finite volume method, as described in any number of reference textbooks (e.g. Ferziger et al. (2012), Versteeg and Malalasekera (2007)) will be introduced, with special attention to those specific integration and reconstruction procedures, used in this thesis. For all simulation cases outlined further on, an open-source, C++ library OpenFOAM® (*OpenFOAM: User Guide v2112* (2022)) will be used. For an interested reader, in-depth numerical analysis of FVM, accompanied by the specifics of programming implementation of FVM into the code is published in high detail in Darwish and Moukalled (2021).

Similarly to the finite-difference-method (FDM), values of any flow variable are stored at discrete points in space and time. Principal strategy behind the FVM is the division of the computational domain into the finite number of non-overlapping cells of as shown in Figure 2.1, so that the total volume of the domain is expressed as:

$$V = \sum_{i=1}^{N_{cells}} V_i \quad (2.41)$$

where  $V_i$  is the volume of the individual cell. For each cell, its center is found at point  $P$ . Values of the discretized, generic flow variable  $\phi_i$  are stored at cell-centres, associated with the spatial coordinate  $\vec{x}_P$ . Additionally, each cell is defined by the chosen number of polygonal faces  $N_{faces}$  that made up its outer area  $A_i$ :

$$A_i = \sum_{i=j}^{N_{faces}} A_f \quad (2.42)$$

where  $A_f$  is the area of the selected face. For each of the cell faces, unit vector normal  $\vec{n}_f$  is defined. Each face is associated with two adjacent points: the owner- $P$  and the neighbour point  $N$ .

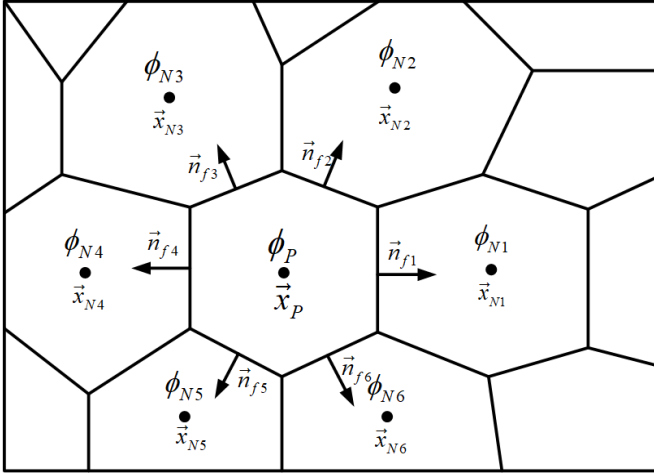


Figure 2.1.: Two dimensional representation of the generic, arbitrary shaped FVM mesh, with characteristic geometrical parameters of the cell.

Transport equations governing the evolution of flow variables presented in this, and the following Chapter can all be reduced to the generic equation:

$$\frac{\partial \phi}{\partial t} = -\nabla \cdot (\vec{U}\phi) + \nabla \cdot (\Gamma \nabla \phi) + S(\phi) \quad (2.43)$$

where  $\phi$  is the transported variable,  $\Gamma$  its diffusivity, and  $S$  its source/sink within the cell. Previous equation can also be represented in a form:

$$\frac{\partial \phi}{\partial t} = NS(\phi) \quad (2.44)$$

where  $NS$  is the non-linear Navier-Stokes operator, encompassing the right-hand-side of the equation 2.43. Integration of equation 2.43 hence yields:

$$\frac{\partial}{\partial t} \int_{V_i} \phi dV - \int_{V_i} NS(\phi) dV = 0 \quad (2.45)$$

Since the information of  $\phi$  is not continuously available, adequate approximations of integral and differential operators need to be addressed. Discretisation of the right-hand side will follow in short, and for now, following simplification will be engaged:

$$\int_{V_i} NS(\phi) dV = INS(\phi) \quad (2.46)$$

where  $INS$  is the value of cell-integrated  $NS$  operator. As already said, instead of the continuous representation which will follow in the analytical solution, FVM discretisation is based on finding the values of  $\phi$  in discrete time and space points. Hence, the complete problematic of FVM is based on finding the appropriate approximations for the temporal and spatial derivatives.

### 2.2.1. Reconstruction of spatial derivatives

Spatial operator  $INS(\phi)$  sublimates the cell-integrated influences of convection, diffusion and the presence of source terms.

$$INS = - \underbrace{\int_V \nabla \cdot (\vec{U}\phi) dV}_{Convection} + \underbrace{\int_V \nabla \cdot (\Gamma \nabla \phi) dV}_{Diffusion} + \underbrace{\int_V S dV}_{Source} \quad (2.47)$$

Accuracy of reconstruction for each of the mentioned terms will directly influence the physical mechanisms associated with the respective term. Since the flow phenomena encountered in this work tackle the problematic of turbulence, which is the class of flows especially influenced by the convection mechanisms, strategies for the reconstruction of convection term will be treated in more detail, whereas the diffusion- and source-term influence will be discussed in a general manner.

**Source term approximation** is usually performed using the midpoint rule:

$$\int_V S(\phi) dV \approx S_i(\phi_i) V_i \quad (2.48)$$

Usually, source-term linearisation is used, which decomposes it into:

$$S_i = S_{p,i} \phi_i + S_{u,i} \quad (2.49)$$

where  $S_{p,i}$  and  $S_{u,i}$  are the implicit and explicit portions of the source term.

**Laplacian-term approximation** which governs the diffusion mechanism is first cell-integrated using the Gaussian rule like:

$$\int_V \nabla \cdot (\Gamma \nabla \phi) dV = \int_A \Gamma \nabla \phi \cdot \vec{n} dA = \sum_{j=1}^{N_{faces}} \int_{A_f} \Gamma \nabla \phi \cdot \vec{n}_f dA \quad (2.50)$$

Hence, in order to calculate the Laplacian term, integration of the gradient of  $\phi$  needs to be performed on every cell face. Again, by using the midpoint rule for the approximation of integrals, previous equation reads:

$$\sum_{j=1}^{N_{faces}} \int_{A_f} \Gamma \nabla \phi \cdot \vec{n}_f dA \approx \sum_{j=1}^{N_{faces}} (\Gamma \nabla \phi \cdot \vec{n})_f A_f \quad (2.51)$$

where index  $f$  denotes that the value of diffusive fluxes needs to be calculated at the geometric center of each face. As a next step, gradient at the face center needs to be calculated. Since the value of  $\phi$  at the face-centres is not readily available, appropriate interpolation is performed, whereas the stencil is made around the cells, sharing the face (owner + neighbour). The exact procedure will not be highlighted here since the interpolation stencil may pose to be highly complex in case of the non-orthogonal, skewed meshes which are usually found in the engineering practice. Concerning the up-to-date description of interpolation stencils for this case, interested reader is referred to Mirkov et al. (2015). Suffice to say that for the orthogonal grid, face gradient value may be calculated using the second-order accurate finite difference stencil as:

$$\nabla \phi \approx \frac{\phi_P - \phi_N}{\vec{x}_P - \vec{x}_N} \quad (2.52)$$

where  $\vec{x}_P$  and  $\vec{x}_N$  are the position vectors of the points  $P$  and  $N$ , as seen in Figure 2.2.

**Gradient term approximation** is done similarly to the Laplacian term, by taking the sum of surface integrals as:

$$\int_{V_i} \nabla \phi dV = \int_{A_i} \phi \vec{n} dA = \sum_{j=1}^{N_{faces}} (\phi \vec{n}_f) dA \approx \sum_{j=1}^{N_{faces}} (\phi \vec{n}_f)_f A_f \quad (2.53)$$

where the value of  $\phi$  at the face center needs to be appropriately interpolated.

### 2.2.1.1. Interpolation schemes for the convective term

Due to the tight interconnection between the convective term in the momentum equation, and the quality of turbulence resolution, schemes for the reconstruction of the convective part will be discussed in greater detail. Repeating the integration step in the previous subsection, convective term is without further redo reduced to:

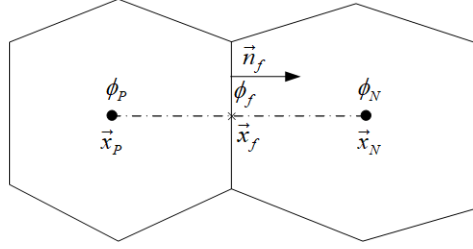


Figure 2.2.: Reconstruction of face-center values, based on the owner-neighbour stencil. Mesh is non-skewed.

$$\int_{V_i} \nabla \cdot (\vec{U}\phi) dV = \int_{A_i} \phi(\vec{U} \cdot \vec{n}) dA \approx \sum_{j=1}^{N_{faces}} \phi_f F_f \quad (2.54)$$

Here, the variable  $F_f$  denotes the volumetric flux at the face centre, made through subliming  $F_f = \vec{U}_f \cdot \vec{n}_f A_f$ . Hence, in order to reconstruct the convective term, one needs to approximate the value of the face fluxes, as well as the value of  $\phi$  at face centres. This is done through the usage of the adequately chosen interpolation scheme.

**Upwind differencing scheme (UDS)** approximates the value of  $\phi$  in dependence of of the upstream neighbour point, as:

$$\phi_f = \begin{cases} \phi_P & \text{if } F_f > 0 \\ \phi_N & \text{if } F_f < 0 \end{cases} \quad (2.55)$$

Hence, if the net volumetric flux is negative, it is assumed that the flow property carried by  $\phi$  is directly taken over from the neighbour cell. In contrast, if the flow is advected from the cell, it takes the value from the owner node. An important asset of the UDS scheme is its unconditional boundness, which doesn't yield non-physical, oscillatory solutions (Ferziger et al. (2012)). This scheme will therefore be used for discretizing the divergence term in the temperature transport equation throughout this thesis. However, on the account of its boundness, UDS is associated with large diffusive error, and the low (first) order of accuracy, which is non-adequate for the scale-resolving flows that will be presented in this thesis. However, since the application of UDS scheme leads to the highly stable computation, it is usually employed in ill-conditioned problems (exemplary for discretizing transport equation for Reynolds stress tensor, outlined in the next Chapter).

**Central-differencing-scheme** (CDS) is formally <sup>1</sup> second-order accurate scheme where the face value of  $\phi$  is calculated using the linear interpolation stencil of the neighbour nodes as:

$$\phi_f = \phi_P \lambda_f + \phi_N (1 - \lambda_f) \quad (2.56)$$

where  $\lambda_f$  is the face interpolation factor calculated as:

$$\frac{\vec{x}_f - \vec{x}_P}{\vec{x}_N - \vec{x}_P} \quad (2.57)$$

Next to its higher order of accuracy, dispersive nature of CDS scheme makes it applicable for the usage in scale-resolving simulations. However, due to its dispersivity, solution is not guaranteed to fulfill the boundness criterion, and non-physical oscillations may appear, provided that the whole numerical system is not sufficiently diffusive.

In order to couple the boundness provided by the low-order (LO) UDS scheme, as well as the accuracy of higher-order (HO) CDS scheme in an optimal way, a so-called  $\gamma$ -blending is provided as:

$$\phi_f = \gamma \phi_f^{HO} + (1 - \gamma) \phi_f^{LO} \quad (2.58)$$

where  $\gamma$  is the appropriately selected limiter. List of the possible limiter combinations is non-exhaustive and beyond the scope of this work. Interested reader is referred to: Sweby (1984), Peric (1985) or Jasak (1996) for a more in-depth discussion of blended schemes. Relevant for this thesis and to the fields of scale-resolving simulations is:

**filteredLinear3 scheme**, which is an OpenFOAM® native scheme, developed purposefully for use with scale-resolving flows (*OpenFOAM: User Guide v2112* (2022)). It aims at limiting the CDS scheme, i.e. locally applying the portion of UDS scheme to the flow in order to eliminate the high-wave number oscillations, created as a result of CDS dispersivity. For that purpose *filteredLinear3* will always (unless stated otherwise) be used for discretizing the divergence term in the momentum equation. Limiter is calculated based on the nodal values of  $\phi$  and  $\nabla\phi$  at the face-neighbouring nodes as:

---

<sup>1</sup>Second order accuracy is achieved only in case of orthogonal, non-skewed meshes. In other cases, order of accuracy may be reduced due to the additional interpolation needed.



$$\gamma = \max(\min(1 - C_{lim} \frac{[2\vec{d} \cdot (\nabla\phi)_N - (\phi_N - \phi_P)][2\vec{d} \cdot (\nabla\phi)_P - (\phi_N - \phi_P)]}{[2\vec{d} \cdot (\nabla\phi)_N + 2\vec{d} \cdot (\nabla\phi)_P]^2}, 1), 0) \quad (2.59)$$

where  $C_{lim}$  is the user-specified constant, and  $\vec{d}$  is the vector connecting the nodes  $P$  and  $N$ . Use of formulation 2.59 effectively compares the two sided gradients at the face, in order to detect the checker-boarding (staggering) artefacts in the solution, artificially decreasing  $\gamma$ , and hence providing a more UDS influence in order to eliminate it. Value of  $C_{lim}$  is non-unique and needs to be determined in dependence of the case specifics. If not said otherwise, a value of  $C_{lim} = 0.1$  is applied throughout this thesis.

## 2.2.2. Reconstruction of temporal derivatives

By applying the discretisation schemes presented in previous subsection, continuous nonlinear spatial operator  $INS(\phi)$  is approximated with its discrete form  $\overline{INS}(\phi)$ , subliming the divergence-, laplacian-, gradient-, and source term as  $INS(\phi) \approx \overline{INS}(\phi_i)$ . Since  $\phi$  is discretely defined not only in space, but in time as well, problematic of the temporal propagation is based on finding  $\phi_i^t$ , based on the initial value:  $\phi_i^{t-\Delta t}$ <sup>2</sup>, where  $\Delta t$  is the time step size. First, a left-hand side volume integral 2.45 is approximated again using the midpoint rule as:

$$\frac{\partial}{\partial t} \int_{V_i} \phi dV \approx \frac{\partial \phi_i}{\partial t} V_i \quad (2.60)$$

By using the Taylor expansion around the temporal point  $t$ , one may derive different stencils. Here, some of the most popular, second-order accurate schemes available in OpenFOAM® for the simulation of scale resolving flows are presented:

**Crank-Nicolson time scheme** (CN) derived in Crank and Nicolson (1947) is a second-order accurate, implicit time scheme, which when used with a constant time step leads to:

$$\frac{\partial \phi_i^t}{\partial t} \approx \frac{\phi_i^t - \phi_i^{t-2\Delta t}}{2\Delta t} \quad (2.61)$$

Hence, equation 2.45 is approximated by using the CN scheme in OpenFOAM® as:

$$\frac{\phi_i^t - \phi_i^{t-2\Delta t}}{2\Delta t} = \overline{INS}(\phi_i^t) \quad (2.62)$$

<sup>2</sup>Or any number of time-steps into the past.

CN scheme possesses a dominant dispersive error, which in turn may lead to the spurious oscillations present in the solution. Therefore, it is used only when the diffusivity of the system causes vanishing of resolved turbulence (exemplary at low  $Re$ ). If not stated otherwise, CN will not be used further on.

**Backward differencing scheme** (BDF) is another very popular scheme available in OpenFOAM®, for the purposes of this work more adequate due to the lower dispersivity with respect to time in comparison with the CN scheme. Time derivative is approximated as

$$\frac{\partial \phi_i^t}{\partial t} \approx \frac{3\phi_i^t - 4\phi_i^{t-\Delta t} + \phi_i^{t-2\Delta t}}{2\Delta t} \quad (2.63)$$

and equation 2.45, approximated by using the BDF scheme, reads:

$$\frac{3\phi_i^t - 4\phi_i^{t-\Delta t} + \phi_i^{t-2\Delta t}}{2\Delta t} = \overline{INS}(\phi_i^t) \quad (2.64)$$

BDF will be a standard scheme for temporal discretisation, used throughout this thesis. Since both schemes are implicit, no limitation of the time-step size is needed, as in the explicit schemes (exemplary Runge-Kutta of any order). Nonetheless, limitation in time step size is introduced in order to match the spatial and temporal resolution of the model, based on the value of Courant number. For each cell, value of Courant number is calculated in dependence of time step  $\Delta t$  as, using the relation:

$$Co = \frac{\Delta t}{2V_i} \sum_{j=1}^{N_{faces}} |F_j| \quad (2.65)$$

where  $F_j$  is the value of volumetric flux at face centers, as introduced in the previous sub-section. Time step is limited using the criterion  $max(Co) < 1$ . Usually, value of  $max(Co) = 0.6$  is set throughout this work.

### 2.2.3. Solution of the coupled linear system of equations

By using the discretisation schemes for both space- and time derivatives, as presented in previous subsections, initially nonlinear partial differential transport equation for the flow variable  $\phi$  is transformed (linearized) into the system of algebraic equations with the form:

$$\mathbf{A} \cdot \Phi = \mathbf{b} \quad (2.66)$$

where  $\Phi$  is the column vector which stores the information of  $\phi$  at every cell center,  $\mathbf{A}$  is the square (and often sparse) system matrix, and  $\mathbf{b}$  is the free vector, encompassing any explicit correction of the discretized transport equation for  $\phi$ . Within the class of incompressible flows, which will be discussed in this work, two main questions concerning the solution of discretized system of NS equations will be addressed. First, what algorithm should be used to solve the individual linear equation, of type

2.66. Second, what procedure should be used to solve the system of discretized NS equations (including other equations, e.g. energy equation), taking into the account that that the obtained solution must not only satisfy the momentum equation, but the continuity equation as well. For the solution of the individual equation of the form 2.66, OpenFOAM® is supplied with a wide variety of linear equation solvers, including the Smooth Solvers (SS), Conjugate-Gradients-Solvers (CG), as well as the Geometric-Algebraic-Multigrid solvers (GAMG), details of which will not be repeated here. Interested reader is referred to the *OpenFOAM: User Guide v2112* (2022) or Versteeg and Malalasekera (2007) for an in depth analysis.

As for the solution of the coupled system of discretized Navier-Stokes equation, Pressure-Implicit algorithm with Splitting of Operators (PISO) by Issa (1986) will be used. PISO represents an algorithm for simulating incompressible, transient flows. For reasons explained further on, usage of PISO loop enforces the limitation of the time-step  $\Delta t$  as to ensure that  $\max(Co) < 1$ . For the class of RANS turbulence models (as introduced in the next Chapter), this is usually a computationally too expensive limitation, since the number of individual time steps is substantially higher than by using alternative pressure-velocity coupling algorithms (exemplary (transient) SIMPLE algorithm, Patankar (1981)). Transient features of such flows can be captured accurately by using much larger time-steps. However, for the flow cases considered in this thesis, scale-resolving nature of the turbulence models is already in need of matching spatial and temporal resolution, hence  $\max(Co) < 1$  is already satisfied. That makes the usage of PISO loop adequate for this work. As a first step in PISO loop, discretized momentum equation is expressed in a form:

$$\mathbf{M} \cdot \mathbf{U} = -\nabla \mathbf{p} + \mathbf{S} \quad (2.67)$$

where  $\mathbf{S}$  can be any explicit velocity correction (like the particle interaction term, presented in the next section). As a solution of equation 2.67, velocity field satisfying the momentum equation (but not the continuity equation) is calculated. Therefore, 2.67 is referred to as *momentum predictor*. In order to make a velocity field solenoidal as well, correction is needed, which is done through the pressure-variable (note that for incompressible flow, pressure only plays a continuity enforcing role). First, left-hand side of 2.67 is decomposed as:

$$\mathbf{M} \cdot \mathbf{U} - \mathbf{S} = \mathbf{A} \cdot \mathbf{U} - \mathbf{H} \quad (2.68)$$

where  $\mathbf{A} = \text{diag}(\mathbf{M})$  is the matrix containing the diagonal entries of  $\mathbf{M}$ .  $\mathbf{H}$  matrix takes into account the influence of all neighbour cells onto the momentum, as well as the influence of sources. By inserting the previous equation into 2.67,  $\mathbf{U}$  can be directly expressed as:

$$\mathbf{U} = -\mathbf{A}^{-1} \cdot \nabla \mathbf{p} + \mathbf{A}^{-1} \cdot \mathbf{H} \quad (2.69)$$

which should lead to the correct solution (that satisfies continuity and momentum), provided that the  $\mathbf{H}$  and  $\mathbf{p}$  are calculated correctly. Therefore, equation 2.69 is referred to as *momentum corrector*. At this point, continuity is brought up to the system. By taking the divergence of 2.69, and equating it with zero (as to ensure continuity), one gets the Laplacian equation for pressure:

$$\nabla \cdot (\mathbf{A}^{-1} \cdot \nabla \mathbf{p}) = \nabla \cdot (\mathbf{A}^{-1} \cdot \mathbf{H}) \quad (2.70)$$

By solving the equation 2.70, one obtains the corrected value of pressure, which leads to the fulfillment of continuity equation. Equation 2.70 carries the name: *pressure corrector*. By far, derived systems of equation form an identical set, used in other pressure-velocity coupling algorithms. What differentiates them from PISO are the individual steps taken. Note that for the velocity-correction step (2.69), correct values of velocity are obtained if both values for  $\mathbf{H}$  and  $\nabla \mathbf{p}$  are correctly captured.

The principal idea behind the PISO loop is that, assuming that for the small time steps (hence the limitation,  $max(Co) < 1$ ), pressure-velocity coupling mirrored through  $\nabla \mathbf{p}$  carries more importance (Jasak (1996)) than the momentum correction. Note that additionally, for small time steps, matrix  $\mathbf{M}$  gets a more pronounced diagonal dominance, providing a faster and more stable convergence, without any under-relaxation. Therefore, momentum prediction is made only once, whereas the multiple corrections of pressure and velocity are performed in a single time-step. Algorithmic description of PISO loop is given in 1.

---

**Algorithm 1** Description of PISO algorithm.

---

- 1: Time-step start, initial values for  $\mathbf{U}$  and  $\mathbf{p}$  taken from previous time-step.
  - 2: Solve the momentum predictor 2.67, obtain intermediate solution for  $\mathbf{U}$ .
  - 3: Calculate matrices  $\mathbf{A}$  and  $\mathbf{H}$ .
  - 4: Solve the pressure-correction equation 2.70, obtain the new value of  $\mathbf{p}$ .
  - 5: Solve the momentum-correction equation 2.69, obtain the new value of  $\mathbf{U}$ .
  - 6: Perform an inner loop over the steps 3 to 5, until convergence.
  - 7: Solve discretized transport equation for other variables, e.g. temperature.
  - 8: Update boundary conditions and proceed to the next time-step.
-

## 2.3. Modeling of two-phase dispersed flows

Flow configurations encountered in the engineering practise are often characterised by the presence of multiple phases, including the combinations of gaseous-, fluid- and solid- phase. Presence of more than a single phase often makes the numerical modeling of turbulent flows extremely challenging, since not only the adequate tackling with turbulence modeling needs to be addressed (as presented in the next Chapter), but also the physics of phase-interaction mechanisms (including the mass-, momentum-, and energy transfer), which occur at their own set of length-scales needs to be adequately captured.

Related to this work, gas-liquid two-phase systems will be discussed. Depending on the characteristic scale of the flow, several regimes can be identified in the gas liquid flows: **Separated** (segregated) flow regime, where the scale of the interface-boundary is comparable with the dimension of the observed (computational) domain, **Dispersed** flow regime, where the interface-boundary is characterised by the scale much smaller than the characteristic dimension of the domain, and finally, any intermediate regime combining the two. As the most complex combination, the so-called **Transient** regime can be obtained. Here, the initially single-phase liquid changes into the two-phase flow regime, featuring the number of intermediary regimes, and then again to single phase flow, but of the gaseous phase (exemplary in the evaporating systems). Based on the above, it is clear that by taking the adequate strategy for numerical modeling, several modeling-, as well as computational obstacles need to be overcome. For an in-depth overview of the hierarchy of the currently employed methods, interested reader is referred to Sommerfeld (2017).

### 2.3.0.1. Interface capturing methods

As far as the modeling goes, among the simplest, and most universal methods for simulationg the two-phase flows are the interface capturing methods, which featured continuous improvement and evolution across the last half a century. These are exemplary: **Marker and Cell** (Harlow and Welch (1965)), **Volume of the Fluid - VoF** (Noh and Woodward (1976), Hirt and Nichols (1981)), **Level-set** (Sussman et al. (1994)), as well as **Front-tracking** (Tryggvason et al. (2001)) methods. As the main advantage, interface- capturing techniques are able to reconstruct an arbitrary shaped boundary between two fluids, using the minimalist modeling approach (exemplary, in the **VoF** approach, a single term capturing the surface-tension influence is added to the momentum equation), which substantially increases the robustness and general applicability of the model. For tracking the front, advection equation for the phase indicator function  $\chi$  is solved:

$$\frac{\partial \chi}{\partial t} + \nabla \cdot (\vec{U} \chi) = 0 \quad (2.71)$$

where  $\chi$  takes the value of 1 in the dispersed phase, and 0 for the carrier phase (or the other way around). Although the certain challenges of the interface-reconstruction may be posed by the numerics (e.g., problematic of interface compression, Okagaki et al. (2021)), they can be dealt with by applying adequate numerical procedures, and higher-order interpolation schemes. The simplicity of the model and robustness of its use are regrettably paid for on the side of the computing resources, since usually, (due to the low order of accuracy of FVM), a large number of cells is needed to accurately resolve the interface. This means that for most of the industrially relevant, dispersed flows, sole application of interface-capturing is beyond the computational capability. Nonetheless, these methods are readily combined with the turbulence models already requiring the very fine mesh resolution (DNS/LES), exemplary in the cases involving the breakup- and atomisation, e.g. Desjardins et al. (2013), Abbas et al. (2021). Very often, hybridisation with other strategies, exemplary with Lagrangian-Particle-Tracking (LPT) is used to cover a large number of scales (Heinrich and Schwarze (2020)). For this thesis however, application of interface capturing is not of interest since the exact nature of scale-resolving turbulence model, presented in the following Chapter, enables the use of coarser meshes which hinders the interface reconstruction. That will make the mesh used in Chapters 8 and 9 at least an order of magnitude to coarse to track the front of small dispersed bubbles.

### 2.3.0.2. Two-fluid (Euler-Euler) method

Very often, exact resolution involving the position and velocity, as well as the front-tracking of every particle/droplet/bubble is of little consequence for the flow research. Rather, an averaged description of phase evolution suffices for the study of multiphase flows. Under the assumption that both the carrier, and the dispersed phase exhibit the macroscopic behaviour of the continuum, evolution equations for both phases can be derived within the Eulerian reference frame, hence giving the method the name Euler-Euler (EE). Here, all the properties of the dispersed phase (velocity, temperature etc.) are *phase-averaged* in order to obtain statistical properties of the bubble swarm, inside of the cell. Exact interpretation of the averaging procedure (temporal-, ensemble-, or volume averaging) is not too important, since the resulting equations take the identical form. In the case of volume averaging, it is assumed that the control volume (mesh cell) is larger than the particle size, but again much smaller than the characteristic scale of the flow system, as to make the averaging meaningful (Elghobashi and Abou-Arab (1983)). Volume-fraction of the individual phase within the cell can be obtained as:

$$\alpha = \bar{\chi} \tag{2.72}$$

where the over-bar operator indicates the averaging procedure. Physical interpretation of  $\alpha$  is straightforward, and represents either the fraction of the cell, occupied by the bubbles, or the probability of bubble occurrence in the cell. In total, phase-

averaged conservation equations need to be solved separately for each of the phases in the flow, whereas on the account of averaging, information about the interfacial phenomena is lost, and needs to be phenomenologically modeled through various source terms in the respective equations. Adding to the stiffness of the system, modeling of multiphase turbulence represents yet another matter since next to the phase-averaging, each of the instantaneous equations needs to be additionally subjected either to the filtering-, or RANS-based averaging (as will be shown in the next Chapter). This produces additional unclosed terms with their own modeling approximations. When tackling the turbulence problematic, either the turbulence equations are solved for each phase separately (adding to the system stiffness, especially with highly complex turbulence models used), or the appropriate mixture assumptions are used (Behzadi et al. (2004)).

If the solution of EE method is sought within the scale-resolving framework, additional limitation is posed on the cell size, where the minimal cell-related scale is proposed by Milelli et al. (2001). It was determined that for the optimal results, minimal cell size  $\Delta$  must be at least 20% higher than the maximum bubble diameter  $d_b$  (In contrast to the interface-capturing methods, where the upper bound on the cell size is set). As for the momentum-based interaction, closure laws in the identical form as with Euler-Lagrange framework are used, and will be introduced in the following section.

The ultimate benefit of EE framework in conjuncture with scale-resolving computations is the greater universality in simulating different flow regimes (in comparison with Euler-Lagrange approach), as well as the modest computation resources (especially in the case of dense dispersed flows), that are dictated more dominantly by the model of turbulence. Although some numerical issues exist in the context of numerical diffusion (Fraga et al. (2016)), they can be solved by using the higher-order computational schemes.

Concerning the model of turbulence used in this thesis (IIS-RSM, introduced in the next Chapter), scale-resolving simulations using the EE strategy have already been performed in Ullrich et al. (2014) and Ullrich (2017), on flow configurations involving the: two-phase developed flows in pipe systems, buoyancy driven flow in bubble column, as well as the two-phase flow in a sudden expansion configuration. Although the general high-accuracy and superiority of the model of turbulence was demonstrated, several key issues were reported, which motivated the usage of Euler-Lagrange framework further on. First, the overall stability of the model could not be guaranteed due to the non-stable implementation of the EE model in OpenFOAM®, as well as due to the inherently unstable nature of the turbulence model. In order to achieve robust computations, various numerical remedies such as an increase in scheme-diffusivity and smaller time-stepping were needed. Additionally, model of turbulence showed extreme sensitivity to phase averaging, and turbulence properties of the carrier phase needed to be mapped directly to the dispersed phase. Lastly, due to the violation of Milelli criterion, scale-resolving nature of turbulence model persistently tried to represent the averaged-out interfacial scales on the mesh, which

posed the question of hybridisation of EE method with an appropriate interface tracking strategy, like in Cerne et al. (2001). Concluding, usage of EE methodology with the current scale-resolving turbulence model could not be proven robust for the meso-scale bubbly flows, hence it was deemed unfit for usage in this thesis.

### 2.3.0.3. Euler-Lagrange methods

Euler-Lagrange (EL) frameworks employs the spatio-temporal evolution of the continuous (carrier) phase equations in the Eulerian frame of reference, using the equations of motion already derived in this Chapter for the single phase flow. As for the secondary phase, it is assumed to take the dispersed form, which makes it optimal to track within the Lagrangian frame of reference. Here, it is also assumed that the dispersed phase accounts for the parcels smaller than the size of computational cell, which again leads to the necessity for the cell-size limitation according to Milelli et al. (2001). Since the bubble-scale interaction with the carrier fluid is not captured, it will be reflected through the modulation of unresolved turbulence scales. Problematic and modeling of this so-called *bubble induced turbulence BIT* is addressed in the next Chapter. Hence, a spatio-temporal evolution of finite number of computational parcels, taken as point-masses, are used to represent the secondary phase. Here, a parcel is defined as a cluster of particles<sup>3</sup>, sharing the same properties.

EL framework is optimally matched with the resolution needs of the dispersed gaseous flow cases outlined in this work. According to Dhotre et al. (2013) evolution of each bubble can be calculated directly, without introducing the numerical problematic associated with EE approach. Usage of the highly complex turbulence models will prove to be substantially more robust for the EL approach, in comparison with EE strategy, without the need for mapping assumptions, or numerical stabilisation of the solution procedure. On the negative side, solution of EL problems may lead to exhaustion of computational resources in cases involving large number of particles, since the motion of each individual particle needs to be included. However, for the flow cases outlined in this thesis, final number of bubbles is smaller, or comparable with the mesh size, hence no additional computational burden is added to the system.

Any property variations within the bubble (such as temperature, internal flow dynamics etc.) are neglected, and a so-called 0-D model with constant and uniform properties of gaseous phase is used. Additionally, no mass transfer between the phases is considered, hence no mass (and momentum) sinks and sources will be modeled. With that in mind, instantaneous position- $\vec{x}_b$  and velocity of the individual parcel -  $\vec{U}_b$  can be determined by solving the following system of ordinary differential equations (ODE)s:

$$\frac{d\vec{x}_b}{dt} = \vec{U}_b \quad (2.73)$$

---

<sup>3</sup>In this context of this work, *particle* refers to any point-mass, not strictly to solid particle.



$$m_b \frac{d\vec{U}_b}{dt} = \vec{F}_d + \vec{F}_l + \vec{F}_{vm} + \vec{F}_s + \vec{F}_g + \vec{F}_b \quad (2.74)$$

Here,  $m_b$  represents the mass of the computational parcel. Since the resources available for this thesis allowed tracking of each individual bubble, terms *parcels* and *bubbles* will be used interchangeably since each parcel will contain only one bubble. On the right-hand-side, surface- and volumetric forces acting on the bubble are noted. Their modeling still represents an open question for engineers due the lack of modeling universality, as well as the uncertainty in the application, leading to the large number of closures (Rusche (2003)). Since the scope of this thesis dominantly focuses on turbulence-related effects and not on improving the closure laws, modeling of bubble forces is performed in accordance with common best practices, e.g: Delnoij et al. (1997), Mitrou et al. (2018). Rotation, as well as the collision phenomena between the Lagrangian parcels are not taken into account. Namely, although the volume fraction of bubbly flow cases presented in the upcoming Chapters will exceed the four-way-coupling limit, as proposed by Elghobashi (1994) (hence making it a dense suspension), collision, coalescence and breakup of bubbles are intentionally left out. As will be seen in the reference experimental cases presented in Chapters 8 and 9, a single class of bubble sizes is used to describe the dynamics of the dispersed phase, without the need for additional modeling. Lastly, no effect of turbulence dispersion is taken into account. This has been justified with the fact that the dominant part of turbulent pulsations can already be resolved with the eddy-resolving Reynolds-stress model (as will be presented in the following Chapter), leaving a very small portion unresolved (as also reported in Ullrich (2017)). With that in mind forces on the RHS of equation can be interpreted as: drag-, lift-, virtual mass-, surface-, gravitational- and buoyancy force.

**Drag force** acts collinearly with direction of the relative motion, and reacts to changes in relative velocity between the carrier phase and the bubbles. It represents one of the most important forces governing the interaction of phases as per Ishii and Hibiki (2010). It is expressed as:

$$F_d = \frac{1}{2} \frac{d_b^2 \pi}{4} \rho C_d |\vec{U} - \vec{U}_b| (\vec{U} - \vec{U}_b) \quad (2.75)$$

where the  $\vec{U}$  and  $\rho$  denote the velocity- and density of the continuous phase, respectively. The value of the drag coefficient  $C_d$  is determined according to the model proposed by Schiller (1933):

$$C_d = \max \left[ \min \left( \frac{16}{Re_b} (1 + Re_b^{0.687}), \frac{48}{Re_b} \right), \frac{8}{3} \frac{Eo}{Eo + 4} \right] \quad (2.76)$$

where  $Re_b$  and  $Eo$  are Reynolds and Eötvös number of the bubble respectively, calculated as:

$$Re_b = \frac{d_b |\vec{U} - \vec{U}_b|}{\nu}, \quad Eo = \frac{g(\rho - \rho_b)d_b^2}{\sigma} \quad (2.77)$$

where  $\sigma$  is the surface tension on the interface between the continuous phase and the dispersed phase, and  $d_b$  is the diameter of the bubble. Relation 2.76 is used primarily due to the robustness in numerical implementation and use, as well as due to the proven performance over a wide range of computational cases. Note that in 2.76, effects related to acceleration are neglected (steady-state drag force). They will be covered later on.

**Lift force** (Saffman force) acts perpendicularly towards the direction of the relative motion (i.e. perpendicularly to the direction of the drag force), whenever the bubble encounters the zone of continuous-phase vorticity, exemplary in the boundary layer, or in the free jet. It is usually modeled as proposed by Auton (1987):

$$\vec{F}_l = m_g \frac{\rho}{\rho_b} C_l (\vec{U} - \vec{U}_b) \times \nabla \times \vec{U} \quad (2.78)$$

In case of the upwardly oriented, unidirectional continuous flow which will be presented in Chapters 8 and 9, (and provided that the lift coefficient  $C_l$  is positive), bubble velocity will be greater than the continuous phase velocity. Hence, lift force will tend to push the dispersed phase in the direction opposite of the carrier velocity gradient, i.e. away from the plume center/closer to the walls. Value of the lift coefficient  $C_l$  has been the object of long debate, without any definitive answer. Usually, value for  $C_l$  is optimized, as to obtain the congruence with the experimental data, whereas the ranges  $C_l = 0.1 \div 0.5$  are usually encountered (Auton (1987), Lopez de Bertodano et al. (1990), Hill (1998)). In this work, similarly to the modeling of the drag force, lift coefficient  $C_l$  can be calculated as per Tomiyama et al. (2002):

$$C_l = \begin{cases} \min(0.288 \tanh(0.121 Re), f) & \text{if } Eo_H < 4 \\ 0.27 & \text{if } Eo_H > 10 \\ f & \text{otherwise} \end{cases} \quad (2.79)$$

$$f = 0.00105 Eo_H^3 - 0.0159 Eo_H^2 - 0.204 Eo_H + 0.474$$

$$Eo_H = \frac{g(\rho_l - \rho_g)d_H^2}{\sigma}, \quad d_H = d_b^3 \sqrt{1 + 0.163 Eo^{0.757}}$$

**Virtual (added) mass force** accounts for the transients effects, stemming from the need to additionally deflect the volume of the carrier phase, as the dispersed phase is moving through it. It is modeled like:

$$F_{vm} = \rho V_b C_{vm} \left( \frac{D\vec{U}}{Dt} \right) - \frac{d\vec{U}_b}{dt} \quad (2.80)$$

where almost by the rule, constant value of the coefficient  $C_{vm} = 0.5$  is taken.

**Surface-, gravitational-, - and buoyancy forces** do not require any modeling, and their combined influence is calculated as:

$$\vec{F}_s + \vec{F}_g + \vec{F}_b = V_b \left( \nabla p + \nabla \cdot \vec{\tau} \right) + m_b \vec{g} \left( 1 - \frac{\rho}{\rho_b} \right) \quad (2.81)$$

Numerical considerations of EL algorithms are beyond the scope of this work. Implementation of EL algorithm in OpenFOAM®, as well as the problematic of temporal integration and tracking of parcels on the unstructured grids are addressed in more detail in *OpenFOAM: User Guide v2112* (2022), as well as in the works of Iudiciani (2009) and Macpherson et al. (2009). Suffice to say that the single-phase PISO loop, presented in Algorithm 1 is modified in the following way:

First, after the beginning of the new time step, bubble-momentum, and bubble-position equations (2.73,2.74) are time-integrated for each parcel, during the whole Eulerian time step  $\Delta t$ . Positions, velocities as well as the history of cell-occupancy are calculated. Afterwards, the following momentum source term is added to the *momentum-predictor* equation 2.67:

$$\vec{S}_i = \frac{1}{\Delta t V_i} \sum_{j=1}^{N_b} m_{b,j} \left( \vec{U}_{b,j,0} - \vec{U}_{b,j,f} \right) \quad (2.82)$$

where  $N_b$  is the number of parcels, occupying the cell during the Eulerian time-step  $\Delta t$ , and  $\vec{U}_{b,j,0}$  and  $\vec{U}_{b,j,f}$  are respectively initial-, and final velocity of the  $j$ -th parcel of the mass  $m_{b,j}$  within the cell  $i$ . Solution of PISO algorithm is afterwards continued as usual.



# 3. Turbulence modeling in single- and two-phase flows

---

In this Chapter, some core question considering the theory of turbulence, as well as the modeling approaches relevant for this publication will be addressed. Special attention will be dedicated to the eddy-resolving (eddy-sensitized) class of RANS models, one of which is used continuously throughout this publication. Lastly, some modeling considerations in relation to the bubble induced turbulence (BIT) are presented.

## 3.1. Introduction

Most flows encountered in nature are turbulent. Since no substantially short definition for turbulence exists so far, the author is free to define it by listing some of the most common attributes of turbulent flows instead: *turbulence is associated with stochastic, highly non-linear and dissipative flow systems, which exhibit a random change in flow variables*. Since the general evolution of the flows is believed to be accurately described by the set of Navier-Stokes equations (2.17 and 2.28) derived in the previous Chapter (which are deterministic in nature), source of mentioned chaotic behaviour of its solution remains open. Previous definition therefore requires some clarification.

Suppose a set of boundary conditions, fluid properties and measuring instruments  $\mathcal{E}$  that will be used in some fluid flow experiment is uniquely defined. For such unique  $\mathcal{E}$ , temporal evolution of generic flow variable  $\tilde{\phi}(\vec{x}, t)$  is measured in a single experimental realisation. Afterwards, experiment is repeated under identical  $\mathcal{E}$  (to either the precision of instruments or machine precision). One quickly realises that no matter how many experiments are repeated, identical signal can never be obtained, showing that randomness is an intrinsic property of turbulence.

Source of this randomness is inherently linked with the non-linear nature of turbulence, expressed in the convective term of the momentum equation. Namely, this term includes the multiplication of flow velocity  $\tilde{U}_i(\vec{x})$  with itself, thus creating a positive systemic feedback loop. This means that even a minute differences in  $\mathcal{E}$  will be reintroduced into the system, and (provided that the diffusive mechanisms of the flow are not strong enough) eventually be amplified in time. Therefore, if will

result in flow field changes that cannot be repeated. In reality, it is clear that  $\tilde{\phi}(\vec{x})$  can never be uniquely defined, following the minute variations in flow properties, existence of background noise, imperfections in the measuring equipment, etc.

Role of non-linearity can best be visualized on the example of famous Lorenz attractor, reported in Lorenz (1963), which represents the system of ODEs with the form:

$$\begin{aligned}\frac{dx}{dt} &= \sigma(y - x) \\ \frac{dy}{dt} &= x(\rho - z) - y \\ \frac{dz}{dt} &= xy - \beta z\end{aligned}\quad (3.1)$$

where  $\sigma = 10$ ,  $\rho = 28$  and  $\beta = 8/3$  are the standard sets of parameters. For illustrative purposes, two experiments will be performed. First, system of equations 3.1 is solved for the initial conditions  $x(0) = y(0) = z(0) = 1$ . For the numerical experiment, quadruple machine precision  $\epsilon = 2.220446049250313e - 16$  is used. In Figure 3.1 (left), magnitude of the solution  $\Theta = \sqrt{x^2 + y^2 + z^2}$  is plotted for the first 100s. Second, calculation is repeated for the identical set of initial conditions, whereas the difference between the first and second experiment  $\Theta_1 - \Theta_2$  is plotted.

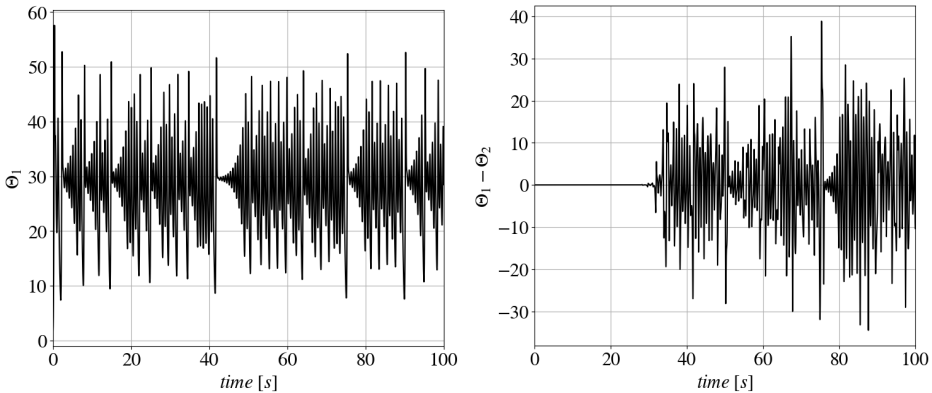


Figure 3.1.: Magnitude of the Lorenz attractor solution (left), and difference between two experiments with identical sets of boundary conditions (right).

As can be seen, for the identical set of initial conditions, two solutions were mostly identical up to the point of  $t \approx 35[s]$ , after which the difference between two curves is comparable with solution magnitude. Even when the highest level of machine precision is used, minute differences in arithmetic are certain to produce differences in the solution, despite the deterministic nature of the non-linear system. By having that in mind, chaotic nature of turbulence is more easily understood.

Turbulence can also be analysed from the point of energy flow. Second law of thermodynamics dictates that the potential energy (chemical-, elastic-, electromagnetic, buoyancy etc.) in any system will spontaneously be transformed first into the mechanical-kinetic energy, in a process that usually occurs at the flow scales comparable with the flow domain. Afterwards, kinetic energy is spontaneously transformed into thermal energy at the smallest scales of turbulence, by the action of diffusion processes (see the dissipation term  $\varepsilon$ , equation 2.38). Batchelor (1982) explains that some intermediary range of scales must therefore exist between the range of largest and smallest scales of turbulence, which is denoted as an *energy cascade*. Practically, large-scale eddies need to undergo the process of breakage into smaller and smaller eddies, until the scale of turbulence reduces enough for the action of diffusion mechanisms. Presence of continuous scale range of coherent structures in a turbulence field is visually represented in the Figure 3.2.

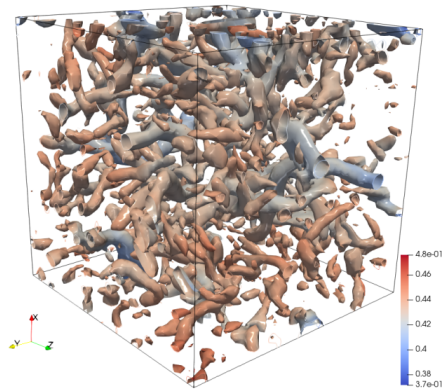


Figure 3.2.: Snapshot of decaying Taylor-Green vortices visualized using the Q-criteria. Reproduction of results by Dr. Nikola Mirkov, using the freeCappuccino code, Mirkov et al. (2018).

If the scale of an arbitrary large eddy<sup>1</sup> is denoted with  $l$ , its wave-number can be denoted with  $\kappa = 2\pi/l$ . Additionally, it is phenomenologically evident that each eddy must contain certain portion of total kinetic energy per wave-number:  $E(\kappa)$ . Total kinetic energy, contained in the turbulent structures, is then obtained by integrating the spectrum like:

$$k = \int_0^{\infty} E(\kappa) d\kappa \quad (3.2)$$

Typical spectral dependence between  $E(\kappa)$  and  $\kappa$  is visually represented in Figure 3.3. Plot is made according to the theoretical model for the spectrum:

<sup>1</sup>The word eddy is vaguely defined, and may be understood as any coherent turbulent structure, whose existence lasts long enough as to be persistently spotted in the field.

$$E(\kappa\eta) = C\varepsilon^{\frac{1}{4}}\nu^{\frac{5}{4}}(\kappa\eta)^{-\frac{5}{3}}f(\kappa\eta)f(\kappa L) \quad (3.3)$$

Here,  $L$  denotes the integral-, and  $\eta$  the Kolmogorov length-scale, which are discussed in the following section. For the more detailed insight into the modeling assumptions behind 3.3, interested reader is referred to Pope (2000).

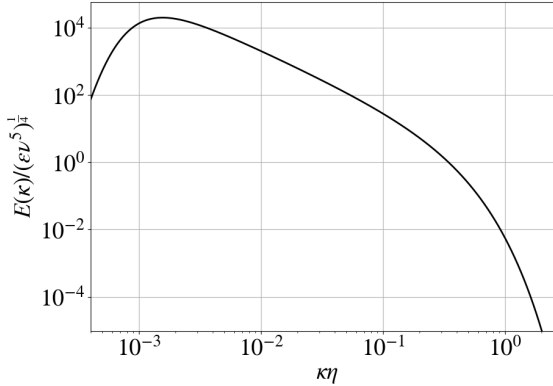


Figure 3.3.: Normalized model spectrum, according to the equation 3.3.

In the range of lowest wave-numbers (largest, top/level scales), slope is positive (approximately quadratic slope), indicating the energy is injected into the spectrum by the action of external forces, as well as due to the deformation of the fluid. Followed by it is an apparently constant-slope range, a so-called *inertial-subrange*, in which no dissipation takes place. Instead, a constant flux of energy from larger to smaller scales occurs due to the breakage and separation of eddies. Citing the derivation presented in Davidson (2015), dimensional analysis reveals that in the inertial subrange, spectral energy is proportional to:

$$E(\kappa) \propto \varepsilon^{2/3}\kappa^{-5/3} \quad (3.4)$$

which represents a condensed form of the equation 3.3. Usually, slope of  $-5/3$  is a very good indicator of the physicality of the solution, as will be presented in the upcoming Chapters. At lowest scales (largest wave-numbers), spectrum gets increasingly concave, indicating a loss of energy, which occurs due to the action of molecular diffusion. By using the dimensional analysis, Kolmogorov (1941) presented the arguments for calculating the smallest scales of turbulence, based solely on the intensity of energy flux (dissipation), as well as the properties of the fluid (viscosity):

$$\eta = \left(\frac{\nu^3}{\varepsilon}\right)^{1/4}, \tau_\eta = \left(\frac{\nu}{\varepsilon}\right)^{1/2}, u_\eta = (\nu\varepsilon)^{1/4} \quad (3.5)$$



where  $\eta$ ,  $\tau_\eta$  and  $u_\eta$  are length-, time- and velocity-scales met at the end of the energy cascade. Equation 3.5 is usually used for setting the lower limit on all the scales calculated by the turbulence model.

## 3.2. Review of the current modeling practices for turbulent flows

As presented in previous Chapters, simulation of turbulent flows encounters at least two important challenges. First, a non-probabilistic evolution of state variables in the turbulent flows which per-se is not the biggest difficulty. As will be seen in short, statistical properties of turbulence (which are of biggest importance for practical engineering) can be deterministically recovered, no matter the method of simulation used. Far bigger concern represents the span of all possible scales (down to the Kolmogorov scale, equations 3.5) which need to be represented by the solution. If  $l_0$  and  $\tau_0$  are the (top-level) length- and time-scale of the flow domain, any relevant turbulence textbook (e.g. Tennekes et al. (1972)) shows that a simple relationship between the smallest- and -largest scales of the flow exist in the form:

$$\frac{l_0}{\eta} \sim Re^{3/4}, \frac{\tau_0}{\tau_\eta} \sim Re^{1/4}, \quad (3.6)$$

where  $Re$  is the Reynolds number based on the top level scale. In the following, several up-to-date strategies for the numerical simulation of turbulent flows are presented. In general, choice of the adequate method is not uniquely defined, but represents a synergy between the available computing power, expertise in the field of numerical method, expertise in the application of the turbulence model, as well as the accuracy required.

Mathematically, obvious choice for turbulence simulation relies on the *Direct Numerical Solution* (DNS) of the Navier-Stokes equations, using well established numerical methods. Usually, either the finite difference method (exemplary in Alfonsi and Primavera (2007)), or some variation of hp-spectral elements (exemplary in Sengupta et al. (2008)) are employed. As noted in Chapter 2, FVM is usually not suitable for tackling the DNS problems, due to its low order of accuracy. One obvious advantage of the DNS approach is the universality of the governing equations and absence of any underlying model of turbulence (which will be demonstrated as problematic in the following sections). However, irrespective of the method used, DNS techniques are ultimately faced with an unavoidable obstacle concerning the capability of the calculation. Namely, as the scaling of spatial points needed to capture the Kolmogorov scales rises with the Reynolds number of the flow ( $N_{cells} \sim Re^{9/4}$ ), computing needs for any industrially relevant flow configuration far supersede the allocatable resources and consequently, gains from such a study. DNS therefore remains a research toll of super-computing academic/industrial entities, and then

again in highly simplified geometries, used mostly for obtainment of validation and calibration cases. Interested reader should find a good overview of DNS applicability and history in Moin and Mahesh (1998). Some recent, exemplary works using the DNS include the flow- and vibration analysis of the axial compressor in Nakhchi et al. (2022), combustion analysis in Gruber et al. (2021), as well as acoustic analysis performed in W. Wang and Miller (2022). To the authors knowledge, largest DNS simulation ever reported up to the publication date of this thesis was presented in Cielo et al. (2021), and employed  $10048^3$  points and 6336 computing nodes, simulating the (magneto-) hydrodynamics of interstellar turbulence.

From the standpoint of the everyday applicability, it is clear that the DNS techniques are far from domesticated within the scientific/engineering community. Next stage in the turbulence simulation is taken by the *Large-Eddy-Simulation* (LES) methods, established in the 1960s. Core idea behind the LES techniques is to apply a low-pass spatial filter to the Navier-Stokes equations, which will *filter-out* the smallest scales of turbulence (which in turn are mostly isotropic and hence easily subjected to modeling), and resolve only the scales larger than the prescribed filter size. Although some sort of modeling paradigm needs to be applied to the unresolved scales, one obvious advantage in comparison with DNS is the reduction in needed computing resources for the obtainment of the solution. Formalism of LES was initially introduced by Smagorinsky (1963) in the field of meteorology. The effect of low-pass filtering is identical to *blurring* procedure in image processing. After applying the filtering operation, initial system of incompressible Navier-Stokes equations takes the form:

$$\begin{aligned} \frac{\partial \overline{U}_i}{\partial x_i} &= 0 \\ \frac{\partial \overline{U}_i}{\partial t} + \frac{\partial \overline{U}_i U_k}{\partial x_k} &= \frac{1}{\rho} \frac{\partial \overline{p}}{\partial x_i} + \overline{\tau}_{ij} + \tau_{ij}^{SGS} \end{aligned} \quad (3.7)$$

where the overbar indicates the filtering operator, and the  $\tau_{ij}^{SGS}$  represents the additional term, stemming from the filtering operation. It resembles the influence of non-resolved (sub-grid) scales. Strategies for modeling of  $\tau_{ij}^{SGS}$  are numerous and beyond the scope of this publication. Very good overview of the mathematical background, as well as up-to date models used can be found in Sagaut (2004), Garnier et al. (2009), as well as a general overview in Zhiyin (2015). A usual approach for modeling of the unclosed term is the usage of sub-grid *turbulence-viscosity* hypothesis:

$$\tau_{ij}^{SGS} = 2\nu_{SGS} \overline{S_{ij}^d} \quad (3.8)$$

As proposed by Smagorinsky,  $\nu_{SGS}$  is usually modeled like:

$$\begin{aligned} \nu_{SGS} &= (C_S \Delta)^2 S \\ S &= \sqrt{2\tilde{S}_{ij}\tilde{S}_{ij}} \end{aligned} \quad (3.9)$$

where  $C_S$  is the modeling constant, and  $\Delta$  is the mesh length scale, having the role of filter. Despite being over half a century old, Smagorinsky model proved to be remarkably reliable in predicting many flow cases from simple to complex. One LES model often cited in this work represents the derivative of the Smagorinsky model called *dynamic Smagorinsky*, presented in Germano et al. (1991). Here, value of  $C_S$  is not constant, but a general function of local flow properties.

Considering its industrial applicability, despite the simplicity in modeling (as will be compared with RANS modeling in short), LES strategies for industrially relevant flow configurations remain mostly outside of the scope for general engineering community, and similarly to DNS, confined within the laboratory-scale experiments. Next to high level of modeling expertise needed, as well as certain numerical challenges (see Piomelli (2014)), highest challenge will for a long time, reside within the high computational cost. This is due to the fact that at industrially relevant Reynolds numbers,  $Re(\geq \mathcal{O}(10^5))$ , over 90% of the total cell count is needed to adequately resolve the boundary layer, which in turn takes less than 10% of the computational volume. Various sources (exemplary Choi and Moin (2012)) estimate that the high- $Re$ , wall-resolved LES cases will not be possible at least until the end of current decade, if the Moore's law were to hold. P. R. Spalart (2000) made a conservative estimate that LES of a full aircraft at flight-related Reynolds numbers will not be possible until 2070.

By far, the most popular approach for modeling of turbulent flows lies within the Reynolds-Averaged-Navier-Stokes (RANS) strategies. Following the inherently random nature of turbulence, an obvious remedy for removal of non-probabilistic instantaneous fluctuations of the flow field is found within the statistical approach, as proposed by Reynolds (see Reynolds (1901)). Namely, instead of trying to predict spatio-temporal evolution of random flow variable, it is reasonable to expect that its statistical moments can be better predicted by using the probabilistic approach, which filters out variations found in  $\mathcal{E}$ , as discussed in Durbin and Reif (2011). If, within an ensemble of  $N$  experiments, the single realisation is indexed with  $i$ , mean (expected) value of  $\tilde{\phi}$  can be calculated as:

$$\Phi(\vec{x}, t) = \bar{\tilde{\phi}} = \lim_{N \rightarrow +\infty} \frac{1}{N} \sum_{i=1}^N \tilde{\phi}(\vec{x}, t) \quad (3.10)$$

where the overbar operator denotes the ensemble averaging. Here, the tilde symbol is used to denote the random, non-probabilistic nature of the evolution in  $\tilde{\phi}$ . It is important to stress that generally, all variables whose evolution equations are derived in Chapter 2 should be written with the tilde symbol. This was however not done due to the simplicity of writing. Therefore, from now on, all capital letters will denote the mean value, while the tilde will be used to denote the instantaneous value of variable. Instantaneous value of fluctuation of  $\tilde{\phi}$  can then be calculated as:

$$\phi' = \tilde{\phi} - \Phi \quad (3.11)$$

Since, per definition,  $\overline{\tilde{\phi}} = \Phi$ , mean value of the fluctuations is equal to zero:  $\overline{\phi'} = 0$ . As already stated and for simplicity reasons, mean values of flow fields are denoted with capital-, and instantaneous value of fluctuations with small letters further on, e.g:

$$\tilde{U}_i = \overline{U}_i + u_i \quad (3.12)$$

$$\tilde{f}_i = \overline{F}_i + f_i \quad (3.13)$$

$$\tilde{p} = P + p \quad (3.14)$$

$$\tilde{T} = T + \theta \quad (3.15)$$

Since averaging is a linear operation, commutation with other linear operators is ensured:

$$\overline{\nabla \tilde{\phi}} = \nabla \overline{\tilde{\phi}} \quad (3.16)$$

However, averaging of the double product of random variables results in an additional double correlation of their fluctuations:

$$\overline{\tilde{\phi}\tilde{\psi}} = \Phi\Psi + \overline{\phi'\psi'} \quad (3.17)$$

This will represent a mayor drawback of the averaging technique. Namely, if the averaging procedure is applied to the system of Navier-Stokes equations 2.16, 2.30, 2.39, one gets in indexed notation:

$$\frac{\partial U_i}{\partial t} + \frac{\partial}{\partial x_k} (U_i U_k + \overline{u_i u_k}) = F_i + \frac{1}{\rho} \frac{\partial P}{\partial x_i} + \frac{\partial}{\partial x_k} \left( \nu \frac{\partial U_i}{\partial x_k} \right) \quad (3.18)$$

$$\frac{\partial U_i}{\partial x_i} = 0 \quad (3.19)$$

$$\frac{\partial T}{\partial t} + \frac{\partial}{\partial x_k} (U_k T + \overline{u_k \theta}) = \frac{\partial}{\partial x_k} \left( \alpha \frac{\partial T}{\partial x_k} \right) \quad (3.20)$$

System of equations 3.18, 3.19 and 3.20, is referred to as Reynolds-Averaged Navier-Stokes Equations (RANS), or just Reynolds Equations for simplicity. Here, all the instantaneous flow variables are exchanged with their mean (expected) values. As stated in Durbin and Reif (2011), Reynolds equations are far less sensitive to the minute differences in the experimental realisations, and therefore, almost perfectly repeatable in contrast to the Navier-Stokes Equations. Note that for statistically steady flow, ensemble averaging may be performed in time as well, whereas in the general case, averaging is performed over a set of experimental realisations. Hence, terms RANS and URANS (*unsteady* RANS) are sometimes be used interchangeably, all denoting the same procedure.

One obvious drawback of using the mean momentum equation 3.18 is the introduction of the unclosed term  $\overline{u_i u_k}$ , commonly referred to as *Reynolds stress tensor*. It is important to state that components of the Reynolds stress tensor don't have

any physical interpretation, but rather represent a mathematical construct, describing the evolution of the statistical properties of the unresolved flow. Analogously, unclosed second moment  $\overline{u_i \theta}$  is also present in the evolution equation for mean temperature 3.18. By applying the averaging procedure, substantial information about the turbulence is lost, and the calculation of  $\overline{u_i u_k}$  requires the presence of additionally developed models, with associated uncertainties. As will be shown, this will affect the reproduction of highly unsteady flows, where the information concerning the temporal evolution of coherent structures may be of special interest to the engineer. Another key deficiency which is native to RANS is the lack of universality (although this is true for every model outside of the DNS domain, it is most pronounced with RANS). Namely, all RANS models rely of the assumption that the behaviour of unresolved scales may in some sense be reconstructed from the behaviour of the resolved scales, using the appropriate calibration and dimensional analysis. This means that the performance of certain RANS model ultimately depends of the exact conditions on which it was calibrated on. The further away the computed case lies from the parameter-space used for calibration, the larger the degradation in results is expected. More about the modeling involved within the RANS framework will be addressed in the following section. Suffice to say that the RANS strategies are, despite some obvious flaws, bound to stay within the engineering community for a perceivable future due to the relatively modest computational resources needed, as stated by Hanjalić (2005).

Finally, in order to overcome the difficulty concerning the high cell count and near-wall resolution with the LES method, numerous eddy-resolving models, based on the hybridisation of LES and RANS methods have been developed over the years. Their principal strategy relies on splitting the solution into the resolved part, which can be directly represented on the computational mesh, and the modeled part, which is treated by an appropriate RANS model. Mathematically, this means that the diffusivity of the underlying RANS equations needs to be reduced down to the point of allowing the larger-than-mesh scales to appear in the solution. This can be done either globally, in which the spectral separation is imposed in every cell of the domain, or zonally, where the certain regions of the domain are treated either with RANS or with an LES model. Among the most popular, hybrid eddy-resolving models are: DES - *Detached-Eddy-Simulation* (P. Spalart and M. Shur (1997), P. R. Spalart (2009), Deck and Renard (2020)), DDES - *Delayed Detached-Eddy-Simulation* (P. R. Spalart et al. (2006a)), IDDES - *Improved Delayed Detached-Eddy-Simulation* (M. L. Shur et al. (2008)), PANS - *Partially-Averaged-Navier-Stokes* - (Girimaji (2006), Basara et al. (2018)) and PITM - *Partially Integrated Turbulence Model* - (Chaouat (2012)). Here, spectral cut-off is either made in dependence on the length scale (resolution capability is triggered by comparing the mesh length scale and the sub-grid turbulence length scale), or by imposing the resolution functions (comparing modeled and resolved portions of the spectrum). Last but not least, methods of SAS - *Scale-Adaptive-Simulations* need to be counted in the global eddy-resolving methods. They will be discussed in substantial details in the following section.

Among the zonal models, WMLES - *Wall-Modeled Large Eddy Simulation* (see Bose and Park (2018)), and ELES - *Embedded Large Eddy Simulation* (see Cokljat et al. (2009)) are mentioned. Here, the domain is split between RANS and LES regions, with special numerical techniques being applied for the treatment of RANS-LES interface. So far, scientific community failed to reach an agreement on ultimate outperforming of any of the noted methods, following the number of inherited modeling problems. They include: explicit dependence on the mesh length-scale, problems of smooth transition between the resolved/unresolved regions, as well as numerical issues (exemplary, commutation error of dynamical ratio of modeled to total kinetic energy in PANS methods with the gradient operator, as demonstrated in Klapwijk et al. (2019)). Concerning the resources required, hybrid methods lie well within the possibilities of the RD sector, although the requirements for the expertise are similar as with the LES. Next to the aforementioned problems, affordable computing resources will ultimately be paid for on the model side, where the quality of the solution also depends on the sub-grid model of turbulence, thus losing the universality.

### 3.2.1. Full closure strategy for Reynolds stress tensor

As outlined in the previous section, existence of the unclosed part of the convective term  $\overline{u_i u_j}$ , denoted as the Reynolds stress tensor, means that the RANS system of equations remains unclosed and requires additional modeling. An obvious (and the most complex) solution represents the derivation of an evolution equation for  $\overline{u_i u_j}$  which is done in details in any relevant turbulence textbook (for example Durbin and Reif (2011), or Hanjalić and B. Launder (2022)) and will not be repeated here. Suffice to say that after subtracting the averaged momentum equation 3.18 from 2.28, multiplying it with the mirror equation (in sense of the index  $j$ ), and averaging the result, one gets:

$$\begin{aligned}
 \frac{D\overline{u_i u_j}}{Dt} &= \underbrace{\frac{\partial \overline{u_i u_j}}{\partial t}}_{L_{ij}} + \underbrace{\frac{\partial U_k \overline{u_i u_j}}{\partial x_k}}_{C_{ij}} = - \underbrace{\left( \frac{\overline{u_i u_k}}{u_i u_k} \frac{\partial U_j}{\partial x_k} + \overline{u_j u_k} \frac{\partial U_i}{\partial x_k} \right)}_{P_{ij}} \\
 &\quad - \underbrace{\frac{p}{\rho} \left( \frac{\partial u_i}{\partial x_j} + \frac{\partial u_j}{\partial x_i} \right)}_{\Phi_{ij}} - \underbrace{\frac{\partial}{\partial x_k} \left( \frac{1}{\rho} p (u_i \delta_{jk} + u_j \delta_{ik}) \right)}_{D_{ij}^p} + \\
 &\quad \underbrace{\frac{\partial}{\partial x_k} \left( \nu \frac{\partial \overline{u_i u_j}}{\partial x_k} \right)}_{D_{ij}^\nu} - \underbrace{\frac{\partial}{\partial x_k} \left( \overline{u_i u_j u_k} \right)}_{D_{ij}^t} - \underbrace{2\nu \frac{\partial u_i}{\partial x_k} \frac{\partial u_j}{\partial x_k}}_{\varepsilon_{ij}}
 \end{aligned} \tag{3.21}$$

which represents a general evolution equation for the Reynolds stress tensor. Reynolds stress tensor is symmetric:  $\overline{u_i u_j} = \overline{u_j u_i}$ , meaning that the evolution equations for six additional variables governing the turbulent flow need to be solved in addition to the equations 3.19 and 3.18. Other approaches, such as eddy-viscosity methods (EVM) are discussed at the end of this section.

On one hand, this will prove most beneficiary since the statistical nature of the averaged-out fluctuations will be captured in a deterministic way in every point of the flow. Additionally, anisotropic nature of these fluctuations is captured. On the other hand, each time the evolution equation for the certain statistical moment is derived, higher moments will appear in the expansion, meaning that the additional closure laws need to be applied. Although this is true for any RANS strategy, it is nowhere as massively present as in the modeling of terms on RHS of the equation 3.21. Here, under-braced terms can be denoted as:  $L_{ij}$ : local change,  $C_{ij}$ : convective transport, and  $D_{ij}^\nu$ : transport through the molecular diffusion, and their physical interpretations are all readily familiar from the previous Chapters. All other terms, including:  $P_{ij}$  - production,  $\Phi_{ij}$  - redistribution,  $D_{ij}^p$  - pressure diffusion,  $D_{ij}^t$  - turbulent diffusion and  $\varepsilon_{ij}$  - dissipation can not be interpreted directly and require some more detailed considerations. By taking half the trace of of the  $\overline{u_i u_j}$ , one gets:

$$k = \frac{1}{2} \overline{u_i u_i} \quad (3.22)$$

which represents the kinetic energy contained in the unresolved, modeled fluctuations, and is shortly denoted as turbulent kinetic energy. Evolution equation for  $k$  should shed some light into the physical significance of other terms. By taking half the trace of equation 3.21, one gets:

$$\frac{Dk}{Dt} = \underbrace{-\overline{u_i u_j} \frac{\partial U_i}{\partial x_j}}_{P_k} - \underbrace{\frac{1}{2} \overline{u_i u_j u_k} \frac{\partial U_k}{\partial x_k}}_{D_k^t} + \underbrace{\frac{\partial}{\partial x_k} \left( \nu \frac{\partial k}{\partial x_k} \right)}_{D_k^\nu} - \underbrace{\nu \frac{\partial u_i}{\partial x_k} \frac{\partial u_i}{\partial x_k}}_{\varepsilon} \quad (3.23)$$

Naming of the individual terms is deliberately kept in accordance with 3.21 to enable straightforward interpretation. Production term may possess a somewhat misleading name. Generally, it only describes that kinetic energy is exchanged between the mean, resolved flow, and the modeled, unresolved flow, through their interaction. As postulated by Durbin and Reif (2011), it can be expected that in most of the usual flow configurations,  $P_k > 0$ , signifying that the unresolved turbulence is directly produced by taking the energy from the resolved flow (Note that the mirror equation for resolved kinetic energy  $\frac{1}{2} U^2$  contains the same term, only with inverted sign), hence the name. This of course doesn't mean that  $P_k < 0$  can not occur, which readily happens in some flow configurations (e.g. impinging jet). In its tensor form,  $P_{ij}$  describes the level of energy exchange of each component of  $\overline{u_i u_j}$  with a mean flow, and can be directly calculated:

$$P_{ij} = - \left( \frac{u_i u_k}{u_i u_k} \frac{\partial U_j}{\partial x_k} + \frac{u_j u_k}{u_j u_k} \frac{\partial U_i}{\partial x_k} \right) \quad (3.24)$$

Past this point, direct calculation of right-hand side terms is impossible and numerous modelling steps need to be undertaken. Based on the individual nature of the modeling assumptions, rich basis of models are available, of which an overview can be found in Hanjalić and B. Launder (2022). Considering the last, dissipation term  $\varepsilon$  in the equation 3.23, one can see that it encompasses the square of the fluctuation gradients, hence  $\varepsilon > 0$ . Combined with the negative sign, it will always represent the sink term (note the identical behaviour in the equation for the instantaneous kinetic energy 2.38<sup>2</sup>), and physically represents a transformation of turbulent kinetic energy into thermal energy, following the irreversible thermodynamic nature of turbulence. Usually,  $\varepsilon$  is referred to as a scale-determining variable since it is used in the definition of turbulence length- and time-scales like:

$$L_t \sim \frac{k^{3/2}}{\varepsilon}, T_t \sim \frac{k}{\varepsilon} \quad (3.25)$$

Closure of  $\varepsilon$  and its tensorisation into  $\varepsilon_{ij}$  puts yet another problem into the buffer of modeling difficulties related to RANS, since the additional evolution equation for  $\varepsilon$  is usually needed. This has been the topic of debate since the exact equation for the evolution of  $\varepsilon$  is usually not used, due to its complexity. Used transport equation is usually derived based on the phenomenological expectation of the mechanisms acting in the turbulent flow (advection+ diffusion+production+destruction).

By combining the modeling assumptions for the equation 3.21 with those for  $\varepsilon$ , one arrives at the full definition of the RANS model used. For this work, a low-Re, differential Reynolds-stress-model (RSM) which was extensively scrutinized in the pioneering work of Jakirlić and Hanjalić (2002) is chosen. This model is usually denoted as JH-RSM (Jakirlić-Hanjalić Reynolds Stress Model), and this abbreviation will be used henceforth. First, an alternative form for the scale-supplying variable through the modification in the dissipation tensor is selected:

$$\varepsilon_{ij} = \varepsilon_{ij}^h + \frac{\partial}{\partial x_k} \left( \frac{1}{2} \nu \frac{\partial \overline{u_i u_j}}{\partial x_k} \right) \quad (3.26)$$

where  $\varepsilon_{ij}^h$  represents a so-called "homogenous" dissipation rate tensor. A choice of  $\varepsilon_{ij}^h$  in place of  $\varepsilon_{ij}$  is justified with a fact that it provides a correct asymptotic behaviour for every component of the dissipation tensor, without introducing additional correctors or limiters in to the model. After inserting 3.26 in to the 3.21, one gets:

---

<sup>2</sup>Note that in 2.38,  $\varepsilon$  denoted the instantaneous dissipation, whereas in 3.23, it represents the statistical quantity.



$$\frac{D\overline{u_i u_j}}{Dt} = \frac{\partial}{\partial x_k} \left[ \frac{1}{2} \nu \frac{\partial \overline{u_i u_j}}{\partial x_k} \right] + P_{ij} + \Phi_{ij} + D_{ij}^t - D_{ij}^p - \varepsilon_{ij}^h \quad (3.27)$$

Furthermore, it is assumed that the anisotropy  $e_{ij}$  of the dissipation tensor proportionally reflects the anisotropy of the large-scale turbulent structures  $a_{ij}$  like:

$$e_{ij} = f_s a_{ij} \quad (3.28)$$

where function  $f_s$  is introduced to relax direct proportionality, and should tend to zero in the isotropic turbulence. Here,  $a_{ij}$  and  $e_{ij}$  are anisotropy tensors of Reynolds stress tensor, and dissipation tensor respectively. They are calculated like:

$$a_{ij} = \frac{\overline{u_i u_j}}{k} - \frac{2}{3} \delta_{ij}, \quad e_{ij} = \frac{\varepsilon_{ij}^h}{\varepsilon^h} - \frac{2}{3} \delta_{ij} \quad (3.29)$$

By combining the invariants of anisotropy tensors for  $\varepsilon_{ij}^h$  and  $\overline{u_i u_j}$ , we obtain:

$$f_s = 1 - E^2 \sqrt{A} \quad (3.30)$$

where  $A$  and  $E$  are Lumley flatness parameters for the  $a_{ij}$  and  $e_{ij}$  respectively. They are calculated like:

$$A = 1 - \frac{9}{8}(A_2 - A_3), \quad A_2 = a_{ij} a_{ji}, \quad A_3 = a_{ij} a_{jk} a_{ki} \quad (3.31)$$

$$E = 1 - \frac{9}{8}(E_2 - E_3), \quad E_2 = e_{ij} e_{ji}, \quad E_3 = e_{ij} e_{jk} e_{ki} \quad (3.32)$$

where  $A_2, A_3$  and  $E_2, E_3$  are second and third invariants of the corresponding tensors. Dissipation tensor is then calculated as:

$$\varepsilon_{ij}^h = f_s \overline{u_i u_j} \frac{\varepsilon^h}{k} + (1 - f_s) \frac{2}{3} \varepsilon^h \delta_{ij} \quad (3.33)$$

Transport equation for  $\varepsilon^h$  will be shown in short. By taking half the trace of 3.23, one notes that the redistribution term disappears, indicating that the interaction between pressure and velocity fluctuations in the incompressible flow does not increase or decrease kinetic energy contained in the fluctuations, but rather redistributes energy between different components of  $\overline{u_i u_j}$ . In general, far from the reflection boundaries (solid walls, free surfaces etc.) it should lead to the isotropisation of turbulence. In JH-RSM, this term is modeled as:

$$\Phi_{ij} = \Phi_{ij,1} + \Phi_{ij,1}^w + \Phi_{ij,2} + \Phi_{ij,2}^w \quad (3.34)$$

$$\Phi_{ij,1} = -C_1 \varepsilon_{ij}^h a_{ij}, \quad \Phi_{ij,2} = -C_2 \left( P_{ij} - \frac{1}{3} P_k \delta_{ij} \right) \quad (3.35)$$

where  $\Phi_{ij,1}$  is a so-called slow, and  $\Phi_{ij,2}$  rapid part of isotropisation. Both terms are additionally modified by the presence of reflection boundaries, which changes them accordingly:

$$\Phi_{ij,1}^w = C_1^w f_w \frac{\varepsilon^h}{k} \left( \overline{u_k u_m} n_k n_m \delta_{ij} - \frac{3}{2} \overline{u_i u_k} n_k n_j - \frac{3}{2} \overline{u_k u_j} n_k n_i \right) \quad (3.36)$$

$$\Phi_{ij,2}^w = C_2^w f_w \left( \Phi_{km,2} n_k n_m \delta_{ij} - \frac{3}{2} \Phi_{ik,2} n_k n_j - \frac{3}{2} \Phi_{kj,2} n_k n_i \right) \quad (3.37)$$

where  $n_i$  represents a normal-to-the wall-pointing unit vector, and various constants modeled as:

$$\begin{aligned} C_1 &= C + \sqrt{AE^2}, \quad C = 2.5AF^{0.25}f, \quad F = \min\{0.6; A_2\} \\ f &= \min\left\{ \left( \frac{Re_t}{150} \right)^{1.5}; 1 \right\}, \quad Re_t = \frac{k^2}{\nu \varepsilon^h}, \quad f_w = \min\left\{ \frac{k^{1.5}}{2.5\varepsilon^h y_n}; 1.4 \right\} \\ C_2 &= 0.8A^{0.5}, \quad C_1^w = \max\{1 - 0.7C, 0.3\}, \quad C_2^w = \min\{A; 0.3\} \end{aligned}$$

Action of pressure-diffusion term  $D_{ij}^p$  can be neglected as small in comparison with other terms, and the turbulent diffusion term  $D_{ij}^t$  be modeled using the simplified gradient hypothesis (SGDH):

$$D_{ij}^t = \frac{\partial}{\partial x_k} \left( \overline{u_i u_j u_k} \right) = \frac{\partial}{\partial x_k} \left( \frac{\nu_t}{\sigma_{\overline{u_i u_j}}} \frac{\partial \overline{u_i u_j}}{\partial x_k} \right), \sigma_{\overline{u_i u_j}} = 1.1 \quad (3.38)$$

Finally, with all the terms modeled, equation 3.21 gets the more clear form:

$$\frac{D\overline{u_i u_j}}{Dt} = \frac{\partial}{\partial x_k} \left[ \left( \frac{1}{2}\nu + \frac{\nu_t}{\sigma_{\overline{u_i u_j}}} \right) \frac{\partial \overline{u_i u_j}}{\partial x_l} \right] + \underbrace{P_{ij}}_{3.24} + \underbrace{\Phi_{ij}}_{3.34} - \underbrace{\varepsilon_{ij}^h}_{3.33} \quad (3.39)$$

which will be used further on. Turbulent viscosity, introduced in the next section, is calculated based on one velocity- and one length-scale, as proposed in Basara and Jakirlić (2003):

$$\nu_t = 0.144A\sqrt{k} \cdot \max \left[ 10 \left( \frac{\nu^3}{\varepsilon^h} \right)^{0.25}, \frac{k^{1.5}}{\varepsilon^h} \right] \quad (3.40)$$

in which the lower limit, based on the Kolmogorov micro-scale (see 3.5) is explicitly set. Concerning the transport equation for  $\varepsilon^h$ , it is given here without the lengthy derivation, which an interested reader can find in the original publication of Jakirlić and Hanjalić (2002):

$$\begin{aligned} \frac{D\varepsilon^h}{Dt} = & \frac{\partial}{\partial x_k} \left[ \left( \frac{1}{2} \nu \delta_{kl} + C_\varepsilon \frac{\varepsilon^h}{k} \overline{u_k u_l} \right) \frac{\partial \varepsilon^h}{\partial x_k} \right] - \left( \varepsilon_{ij}^h \frac{\partial U_i}{\partial x_j} - P_k \frac{\varepsilon^h}{k} \right) \\ & - C_{\varepsilon 2} f_\varepsilon \frac{\varepsilon^h \tilde{\varepsilon}^h}{k} - 2\nu \left( \frac{\partial \overline{u_i u_k}}{\partial x_l} \frac{\partial^2 U_i}{\partial x_k \partial x_l} + C_{\varepsilon 3} \frac{k}{\varepsilon^h} \frac{\partial \overline{u_k u_l}}{\partial x_j} \frac{\partial U_i}{\partial x_k} \frac{\partial^2 U_i}{\partial x_j \partial x_l} \right) \end{aligned} \quad (3.41)$$

with:

$$f_\varepsilon = 1 - \frac{C_{\varepsilon 2} - 1}{C_{\varepsilon 2}} \exp[-(Re_t/6)^2], \quad \tilde{\varepsilon}^h = \varepsilon^h - \nu(\partial k^{1/2}/\partial x_l)^2 \quad (3.42)$$

where various constants are defined as:  $C_\varepsilon = 0.18$ ,  $C_{\varepsilon 1} = 1.44$ ,  $C_{\varepsilon 2} = 1.8$ ,  $C_{\varepsilon 3} = 0.32$ . With some modifications, turbulence model of Jakirlić and Hanjalić will present a baseline for the development of eddy-resolving method (IIS-RSM), which is to be introduced in the following sections.

### 3.2.2. Boussinesq hypothesis - eddy viscosity models

In previous subsection, model of turbulence based on the full closure of Reynolds Stress tensor was introduced as a strategy which will be applied throughout this work. Although the dynamics of the unresolved scales can be modeled very accurately with it, existence of six additional equations, accompanied by the seventh, scale-supplying equation adds to the overall complexity of the system. Outlined equations 3.39 and 3.41 contain multiple source-terms in form of complex, nonlinear functions, which may endanger the convergence, and the robustness of the model. This motivated the development of the family of turbulence models named: eddy-viscosity-models (EVM). Originally stemming from the works of Boussinesq, Reynolds stress tensor is modeled as:

$$-\overline{u_i u_j} = 2\nu_t S_{ij}^d - \frac{2}{3} k \delta_{ij} \quad (3.43)$$

where the  $\nu_t$  is a so-called *turbulent viscosity*, and  $S_{ij}^d$  is the deviatoric part of the strain-rate tensor. By using the EVM approach, transport equation for the resolved velocity 3.18 is transformed into:

$$\frac{\partial U_i}{\partial t} + \frac{\partial}{\partial x_k} (U_i U_k) = F_i + \frac{1}{\rho} \frac{\partial P}{\partial x_i} + \frac{\partial}{\partial x_k} \left[ (\nu + \nu_t) \frac{\partial U_i}{\partial x_k} \right] \quad (3.44)$$

Modeling the influence of unresolved turbulence through the use of artificially introduced turbulent viscosity is also known as a *Boussinesq hypothesis*. It is made on the assumption that the good mixing property of the fully resolved turbulence should be reflected through the increased diffusivity of the equations describing its statistics. Based on it, dynamics of the modeled scales is assumed to resemble

those of the resolved ones. From the mathematical point of view, Reynolds stress tensor is modeled analogously to the shear-stress tensor (hence the name), the only difference being the turbulent viscosity. Term containing the turbulence kinetic energy  $k$  is added to ensure the existence of Reynolds stresses in the isotropic, homogeneous turbulence.

By applying the Boussinesq hypothesis, modeling problem of seven transport equations is reduced to finding the appropriate closure for the turbulent viscosity  $\nu_t$ . Although by doing this, substantial information is lost concerning the behaviour of modeled terms, EVM approach is highly favorable within the engineering community, and the majority of RANS models, available in the commercially used codes, belong to the EVM family. Usually, a good calibration alongside the experience with model usage may cover for some of its downsides. General strategy for calculation of  $\nu_t$  is based on dimensional grounds, involving an appropriately selected velocity- and time scale:  $[m^2s^{-1}] = [ms^{-1}]/[s]$ , velocity- and length-scale:  $[m^2s^{-1}] = [ms^{-1}] \cdot [m]$  or any other combination. A non-exhaustive list with some of the historically most relevant models contains among others:

- $k - \varepsilon$  model by B. E. Launder and Spalding (1983), where  $\nu_t = C_\mu \frac{k^2}{\varepsilon}$
- $k - \omega$  model by Wilcox (1988), where  $\nu_t = \frac{k}{\omega}$ ,  $\omega = \frac{\varepsilon}{C_\mu k}$
- $k - \omega - SST$  model by Menter (1993), made by an appropriate blending of previous two models, where:  $\nu_t = \frac{a_1 k}{\max[a_1 \omega, SF_2]}$

Tackling with the loss of the anisotropy information, an intermediate step between the modeling of full Reynolds stress model and the two equation models presented above is the famous  $k - \varepsilon - \zeta - f$  model by Hanjalić et al. (2004). It represents a numerically robust update of the  $v^2 - f$  model by Durbin (1995),  $v^2$  being the normal-to-streamline component of the Reynolds stress tensor. Here, the value of turbulence viscosity is determined as:

$$\nu_t = \underbrace{C_\mu \zeta k T_t}_{\text{Hanjalić et al. (2004)}} = \underbrace{C_\mu v^2 T_t}_{\text{Durbin (1995)}} \quad (3.45)$$

where  $T$  is the turbulence time scale, and  $\zeta = v^2/k$  is the dimensionless scalar, partially capturing the anisotropy of turbulence. In this way, additional information about the nature of unresolved fluctuations is fed to the model.

### 3.2.3. Near-wall turbulence modeling

All the flow cases investigated in this thesis are the wall-bounded flows. With the exception of the rigid-lid boundaries mentioned in Chapters 8 and 9, all the walls are defined as a solid, no-slip walls, meaning that the velocity on the wall

is equal to zero:  $U_{wall} = 0$ . If the Reynolds number is formed like:  $Re = Uy_n/\nu$ , where  $y_n$  is the wall-normal distance, one quickly realises that with approaching the wall, viscous effects will supersede the inertial ones, resulting in turbulence being substantially modulated in the vicinity of the walls. Next to the viscous effects, pressure reflections from the impermeable walls directly influence the anisotropy of turbulence, by blocking the wall-normal fluctuations (through the pressure-redistribution term, see equations 3.36, and 3.37). A very useful velocity-scale for validation of simulation results may be derived from the wall shear stress  $\tau_w$  like:

$$u_\tau = \sqrt{\frac{\tau_w}{\rho}} \quad (3.46)$$

where  $u_\tau$  is known as friction-velocity. Based on it, dimensionless length- and velocity scales may be defined as:

$$y^+ = \frac{u_\tau y}{\nu}, \quad U^+ = \frac{U}{u_\tau} \quad (3.47)$$

Based on the value of  $y^+$ , several characteristic zones in the typical developed, near-wall turbulence field may be identified: *viscous sublayer* ( $y^+ < 5$ ), where the viscosity effects supersede turbulent effects, *logarithmic layer* ( $y^+ > 30$ ) where the turbulence effects are dominant, and the *buffer layer* ( $5 < y^+ < 30$ ), where both viscous and turbulent effects are of the same order of magnitude. Based on the characteristic velocity profile in the near-wall region, a so called *law of the wall* can be derived (as proposed by Von Kármán (1930)):

$$U^+ = \begin{cases} y^+, & y^+ < 5, \\ \frac{1}{\kappa} \ln(y^+) + B, & y^+ > 30 \end{cases} \quad (3.48)$$

where  $\kappa = 0.41$  is the usual value of Von Karman constant, and  $B$  is the fitting parameter, usually set to 5.2. Note that the system of equations 3.48 provides a very reliable indicator of the near-wall turbulence under the conditions of fully developed flow configurations (channel-flow, pipe-flow, etc.). Correct near wall behaviour is one of the first corner-stones in the validation sequence for all turbulence models, and will be used extensively in Chapter 5. Comparison of the *law of the wall*, equation 3.48, with the DNS data by Abe et al. (2001) for the fully developed channel flow is presented in Figure 3.4.

### 3.3. Towards the spectral resolution - eddy sensitized variants of RANS models

As noted in previous sections, the idea of Reynolds methodology for averaging instantaneous field equations has been introduced in order to eliminate presence of random field fluctuations, and to operate instead with statistical quantities, whose

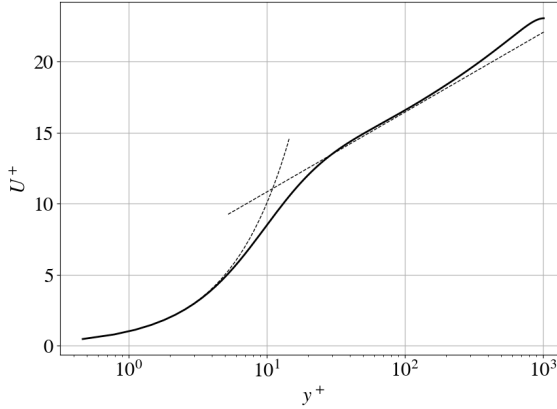


Figure 3.4.: Comparison of the law of the wall (dashed-line), equation 3.48 with the DNS data for the fully developed channel flow - solid line.

evolution is perfectly repeatable (to the level of machine precision) is any numerical experiment. This is possible due to the calibration of the model, which is made to readily quickly dissipate any energy retained at the scale of the resolved flow, and to transfer it to the modeled portion of the spectrum. This process can also be performed in reverse: if the numerically introduced diffusivity of the flow is diminished, modeled terms will be reduced adequately as well. Hence, resolved flow structures will appear in the RANS solution. In this way, original RANS models may be *enhanced* as to reproduce the spectrum, giving a rise to a so-called *eddy-resolving*, (ER) RANS models.

Another formulation of the previous statement is the inability of RANS models to reproduce any length scale that is not comparable with the boundary layer thickness (since the only externally available information on the length scale is fed through the shear rate  $S$ ). This is consequentially reflected through the increased diffusivity of the model. With that in mind, Menter and Egorov (2006) postulated that the URANS methods could be used to produce the spectral content, provided that the turbulence length scale is better defined. This gave birth to a class of models named *scale-adaptive* (SA), which are the foundation stone of the eddy-resolving methodology in this thesis. A pioneering work in finding a more appropriate scale-supplying variable has been performed in Rotta (1968) and Rotta (1972), where a transport equation for the variable  $\Psi = kL$  was derived ( $L$  is the integral length scale of turbulence). By analyzing a developed, two dimensional shear flow, where  $y$  is the wall normal coordinate,  $kL$  can be defined as:

$$kL = \frac{3}{16} \int_{-\infty}^{\infty} R_{ii} dr_y \quad (3.49)$$

where  $R_{ij}$  represents the trace of two point correlation tensor:

$$R_{ij} = \overline{u_i(\vec{x})u_j(\vec{x} + y)} \quad (3.50)$$

Although the derivation of the entire evolution equation for  $\Psi$  will not be repeated here, it is important to stress that it contains an additional sink term with the form:

$$\frac{D\Psi}{Dt} = \dots - \frac{3}{16} \int_{-\infty}^{\infty} \frac{\partial U(\vec{x} + r_y)}{\partial x} R_{12} dr_y \quad (3.51)$$

where  $R_{12}$  represented the auto-correlation obtained in two-dimensional, fully developed flow. With the Taylor expansion, noted sink term may be transformed into:

$$\begin{aligned} \int_{-\infty}^{\infty} \frac{\partial U(\vec{x} + r_y)}{\partial x} R_{12} dr_y &= \frac{\partial U}{\partial y} \int_{-\infty}^{\infty} R_{12} dr_y \\ &+ \frac{\partial^2 U}{\partial y^2} \int_{-\infty}^{\infty} R_{12} r_y dr_y \\ &+ \frac{\partial^3 U}{\partial y^3} \int_{-\infty}^{\infty} R_{12} r_y^2 dr_y + \dots \end{aligned} \quad (3.52)$$

Since  $\nu_t \propto \Psi/\sqrt{k}$ , one can draw an important conclusion from previous derivation: Since the sink term in the evolution equation for  $\Psi$  directly correlates with spatial changes in velocity fields, topology of velocity field ( $\partial^n U_i/\partial y^n$ ) can be used for appropriately decreasing  $\Psi$ , ultimately introducing a shift in the turbulent spectrum through the reduction of modeled terms and allowing the appearance of resolved fields.

Whereas Rotta concluded that the third derivative should be taken as the topology related term, Menter and Egorov (2010) argued that the use of second derivative is a better represent of non-homogenities in turbulence which should trigger the resolution capabilities of the model. Second derivative also offers the correct behaviour of the model in logarithmic layer. Based on the above, they reintroduced the additional sink term in the transport equation for  $\Psi$ , with the form:

$$P_{SAS,kL} \sim -\frac{\partial^2 U}{\partial y^2} \int_{-\infty}^{+\infty} R_{12} r_y dr_y \quad (3.53)$$

where the sub-script SAS denotes the scale-adaptive framework, explained in short. Based on dimensional arguments, noted sink term can be rewritten as:

$$P_{SAS,kL} \approx -const \cdot P_k \frac{\Psi}{k} \left( \frac{L_t}{L_{vk}} \right)^2 \quad (3.54)$$

where  $L_{vk}$  is the Von Karman length scale, and  $L_t$  is the turbulent length scale, defined like:

$$L_{vk} = \kappa \frac{\partial U / \partial y}{\partial^2 U / \partial y^2}, \quad L_t \sim \frac{k^{1/2}}{\omega} \quad (3.55)$$

It is worthwhile noting that the equation 3.54 carries a striking resemblance with the DES like procedures (see P. Spalart and M. Shur (1997)), where the resolution capability of the model is tuned based on the comparison between the turbulent length scale  $L_t$  and the mesh length scale  $\Delta$ . In total, if the turbulent length scale should prove larger than the mesh scale (under-resolved turbulence), the model should push the solution towards the resolved turbulence. Here,  $L_{vk}$  should perform the similar role, serving as an implicit indicator of a local mesh length scale. On one hand, this may pose a reasonable assumption since, the more resolved the mesh is, the more accurate the reconstruction of the derivatives is allowed. This will prove highly advantageous in a case of complexly meshed domains, where highly anisotropic, bad quality meshes substantially complicate the definition of a characteristic grid size. In this way, model is able to capture the mesh resolution fully implicitly. However, this assumption is not straightforward since  $L_{vk}$  does not depend on the local resolution only, but is also dependent on the local flow conditions. In fact, Maduta and Jakirlić (2016) concluded that the Von Karman length scale could not be observed as an isolated grid parameter, but rather as a part of a complex source term, depending on the local flow topology. By introducing the term 3.53 into the transport equation for  $\Psi$ , a novice strategy for the resolution of turbulence spectrum is obtained, using a native RANS framework as a basis. Equation 3.54 can be interpreted straightforwardly: in the case where the turbulence is under-resolved ( $L_t \geq L_{vk}$ ), the whole term 3.54 will increase, hence decreasing the overall diffusivity of the flow down to the point where the new balance is established, i.e. until the length scale of the residual turbulence is comparable with the Von Karman length scale. This ability to readapt the level of residual turbulence to the locally retrievable length scale is native to all SAS procedures. Next to the implicit capture of the mesh length-scale, another advantage of SA-formulation is its natural derivation from the scale-supplying equation, meaning that the theoretical foundation for the ER-RANS models is highly justified. That being said, original scale-supplying equation  $\Psi = kL$  can be transformed into the transport equation for the scale-supplying variable of choice, usually  $\omega$  or  $\varepsilon$ . Exemplary, in the original works of Menter and Egorov (2010),  $\Psi$  is transformed into a new variable  $\Phi = \Psi / \sqrt{k}$ , thus creating a new scale-adaptive model named KSKL (k - square root of k-L), which is directly proportional to turbulent viscosity. Common choice of scale-supplying variable is the specific turbulent dissipation  $\omega$ , which was used for introducing the SAS methodology into the industrially popular  $k - \omega - SST$  model, as discussed in Egorov and Menter (2008). The model reads:



$$\begin{aligned} \left(\frac{D\omega}{Dt}\right)_{SST-SAS} &= \left(\frac{D\omega}{Dt}\right)_{SST} + P_{SAS} \\ P_{SAS} &= \max \left[ 0.026S^2 \left(\frac{L_{SST}}{L_{vk}}\right)^2 - 2T_2, 0 \right] \\ T_2 &= \frac{k}{\sigma_\phi} \max \left[ \frac{(\nabla\omega)^2}{\omega^2}, \frac{(\nabla k)^2}{k^2} \right] \end{aligned} \quad (3.56)$$

where  $L_{SST}$  is the turbulent length scale, calculated by the  $k - \omega - SST$  model. Here,  $P_{SAS}$  is appropriately modified using the transformation:

$$P_{SAS} \sim \frac{\omega^2}{k^{3/2}} P_{SAS,kL}, \quad L_{SST} \sim \frac{k^{1/2}}{\omega} \quad (3.57)$$

As for the second term in the expansion  $T_2$ , its existence is originating from the transformation of scale-supplying variable:

$$\frac{D\omega}{Dt} = \frac{D}{Dt} \left( \frac{k^{1/2}}{\omega} \right) = \frac{3}{2} \frac{\omega}{k} \frac{Dk}{Dt} - \frac{\omega^2}{k^{3/2}} \frac{D(kL)}{Dt} \quad (3.58)$$

Additionally,  $\max$  function in combination with the  $T_2$  term should prohibit the resolution of the spectrum in the vicinity of the wall (logarithmic region), where the RANS solution should be reproduced by the model. The  $k - \omega - SST - SAS$  model hence became the template on which any RANS model can be updated with the SAS methodology.

Maduta (2013) used previously described technique into transforming the JH-RSM model into its resolution-sensitized derivative. First, transport equation for  $\varepsilon^h$ , 3.41 was transformed into the  $\omega^h$ , in order to show consistency with the previously described methodology<sup>3</sup>. After a lengthy derivation, final form of transport equation for  $\omega^h$  reads<sup>4</sup>:

$$\begin{aligned} \frac{D\omega_h}{Dt} &= \frac{\partial}{\partial x_k} \left[ \left( \frac{1}{2}\nu + \frac{\nu_t}{\sigma_\omega} \right) \frac{\partial \omega_h}{\partial x_k} \right] + C_{\omega,1} \frac{\omega_h}{k} P_k - C_{\omega,2} \omega_h^2 + \\ &\frac{2}{k} C_{\omega,3} \nu \nu_t \frac{\partial^2 U_i}{\partial x_j \partial x_l} \frac{\partial^2 U_i}{\partial x_j \partial x_l} + \frac{2}{k} \left( 0.55 \frac{1}{2} \nu + 0.275 \frac{\nu_t}{\sigma_\omega} \right) \frac{\partial \omega_h}{\partial x_k} \frac{\partial k}{\partial x_k} \end{aligned} \quad (3.59)$$

where various constants are defined as:

$$C_{\omega,1} = 0.44, \quad C_{\omega,2} = 0.8, \quad C_{\omega,3} = 1.0, \quad \sigma_\omega = 1.1 \quad (3.60)$$

<sup>3</sup>Transformation of  $P_{SAS}$  directly into the transport equation for  $\varepsilon$  turned excruciatingly complex, resulting in numerous additional source-terms.

<sup>4</sup>Length-scale correction term  $S_l$ , present in the original transport equation for  $\omega^h$  is not written within the equation 3.59, hence it will not be used in ER-mode.

Afterwards, the calibrated  $P_{SAS}$  term was added to the equation:

$$\left(\frac{D\omega_h}{Dt}\right)_{SAS} = \left(\frac{D\omega_h}{Dt}\right)_{eqn:3.59} + P_{SAS,\omega^h} \quad (3.61)$$

where  $P_{SAS,\omega^h}$  was calibrated as:

$$P_{SAS,\omega^h} = 0.004max\left(2.3713\kappa S^2\left(\frac{L_{SST}}{L_{vk}}\right)^{1/2} - 8T_2, 0\right) \quad (3.62)$$

$$T_2 = 3kmax\left[\frac{1}{k^2}(\nabla k)^2, \frac{1}{\omega^2}(\nabla\omega)^2\right]$$

By combining the transport equation for Reynolds-Stress-Tensor 3.39 with the SAS-sensitized transport equation for  $\omega^h$  - equation 3.61, the new model was named Instability-Sensitive Reynolds Stress Model (IS-RSM). It was demonstrated that the newly established model was able to accurately reproduce the top-level instabilities in the massively unsteady, separated flows. At the same time, highest level of modeling practise was achieved since the residual turbulence is captured using 7 different variables, hence the anisotropy can be reconstructed very well. Note that in previous formulation, several changes to the originally introduced SA-models are made. First, the exponent in the length scale-ratation is changed to 1/2. This was done primarily to limit the over-resolution of the model, since with quadratic relation, resolved turbulence will quickly consume the modeled portion, producing a quasi DNS solution. Based on the derivation in similar publications, e.g. Menter and Egorov (2006) or Krumbein (2019), exponent could also be set to 1, without the loss in model consistency. Additionally, model constants were recalibrated. This was due to the fact that the RSM system of equations is generally more dispersive than EVM-based system. Namely, next to the application of non-linear functions in source terms, every instability possesses a six times greater probability of entering into the system of equations, meaning that the resolution property of the model could be triggered more easily. Based on numerous test cases reported (in e.g. Maduta (2013), Jakirlić and Maduta (2015) or Maduta and Jakirlić (2016)), it was shown that the model is able to substantially improve the results obtained with the RANS models in different flow cases, all while demonstrating possibilities for substantial reduction in mesh resolution required by LES.

It is important to stress that in this thesis, original IS-RSM will not be used, but rather its updated version called Improved-Instability-Sensitive Reynolds-Stress-Model (IIS-RSM). First, an important change concerning the inclusion of modeled turbulence within the momentum equation itself is made. Namely, since the flow of energy (from resolved to modeled scales) is neither uni-directional, nor strictly limited by using either JH-RSM or IS-RSM, direct incorporation of Reynolds stress tensor 3.39 into the momentum equation 2.31 will prove too unstable as a formulation. This makes the prevention of the solution blow-out very hard and decreases

the robustness of the model. In order to prevent this, appropriate blending of the Reynolds stress tensor, as originally proposed in Basara and Jakirlić (2003) is performed prior to insertion in the momentum equation in Maduta et al. (2015):

$$\overline{u_i u_j} = (1 - \beta)\overline{u_i u_j} - \beta(2\nu_t S_{ij}^d - \frac{2}{3}k\delta_{ij}) \quad (3.63)$$

where  $\beta$  is the blending function. While some newer publications (Wegst (2021)) used a  $Re_t$ -sensitized blending, original work of Maduta et al. (2015) used a constant factor of  $\beta = 0.8$ . However, in the present publication, value of  $\beta = 0.7$  is used due to the increased stability. Second, a change in the formulation of  $P_{SAS}$  was made. Namely, by revisiting the equation 3.53, one can model the sub-integral quantity more easily as:

$$P_{SAS,kL} \sim -\frac{\partial^2 U}{\partial y^2} \overline{u'v'} L^2 \quad (3.64)$$

By assuming  $\overline{u'v'} \sim k$ , and by applying the procedure from the equation 3.58, one arrives at the final form of  $P_{SAS}$  used in this work, which depends solely on the second derivative of velocity field (as reported in Köhler et al. (2018)):

$$P_{SAS,\omega^h} = P_{\Delta U} \sim \sqrt{k} \frac{\partial^2 U}{\partial y^2} \quad (3.65)$$

After the calibration, it takes the form:

$$\begin{aligned} P_{\Delta U} &= C_1 \max \left[ C_2 \sqrt{k} \nabla^2 U - C_3 T_2, 0 \right] \\ T_2 &= 3k \max \left[ \frac{1}{k^2} (\nabla k)^2, \frac{1}{\omega^2} (\nabla \omega)^2 \right] \end{aligned} \quad (3.66)$$

where the model constants take values:  $C_1 = 0.003$ ,  $C_2 = 29.11$  and  $C_3 = 40$ . Note that since the action of the source terms is not (directly) linked to the Von-Karman length scale, but rather to the second derivative of the velocity field, departure from the original notation takes places ( $P_{SAS} = P_{\Delta U}$ ). The scale-supplying equation takes the form:

$$\left( \frac{D\omega_h}{Dt} \right)_{IIS-RSM} = \underbrace{\left( \frac{D\omega_h}{Dt} \right)}_{3.59} + \underbrace{P_{\Delta U}}_{3.66} \quad (3.67)$$

Hence, the definition of IIS-RSM as a model which will be used in this thesis is completed: As in the first version, it will use the equation 3.39 for the transport of Reynolds stress tensor, equation 3.67 for the definition of the turbulence length scale, and 3.63 for blending. The summary formulation of the model is given in the Appendix A.

Next to the improvements in the stability and robustness of the model, IIS-RSM offers a more theoretically interpretable influence of  $P_{\Delta U}$  as an acting mechanism for the turbulence resolution. The dissipation of modeled terms is increased in

accordance with the second derivative of the velocity field, which here serves as an implicit mesh scale indicator, using the previously stated arguments on the operators reconstruction (note that the ratio of the turbulent-to-Von Karman length scale can be derived easily from this formulation). Basically, the  $P_{\Delta U}$  reacts to the exhibited flow curvature in the velocity field and correspondingly enhances the dissipation. On the other side,  $\sqrt{k}$  serves as a *safeguard* term. In case where the modeled turbulence kinetic energy is reduced towards the residual level, the magnitude of  $P_{\Delta U}$  will be correspondingly reduced and the new balance between the modeled and resolved turbulence will be established.

### 3.4. Modeling of turbulent scalar transport

Flow cases involving heat transfer will be presented in Chapters 6 and 7. Here, the temperature evolution equation will be added to the RANS system of equations. However, due to the specific nature of the problem, material properties will be assumed constant and the temperature will be treated as a passive scalar, transported by the means of the flow convection and diffusion. As shown, Reynolds averaging produces an additional (unclosed) term in the resolved-temperature evolution equation 3.20,  $\overline{u_k \theta}$ , representing the unresolved (sub-grid) temperature fluxes. Following the procedure analogously with the derivation of Reynolds-Stress transport equation, evolution equation for  $\overline{u_k \theta}$  can also be derived, as shown in Hanjalić and B. Launder (2022). However, this is due to the complexity, as well as based on the arguments that will follow in short, too complex of a strategy. Therefore, it will not be used henceforth.

A simplified approach, without using any transport equation is proposed within the works of Daly and Harlow (1970), and is known as *generalized gradient diffusion hypothesis* (GGDH):

$$\overline{u_k \theta} = c_\theta \frac{k}{\varepsilon} \overline{u_k u_j} \frac{\partial T}{\partial x_j} \quad (3.68)$$

where  $c_\theta$  is the modeling constant. Here, similar assumption is used as with the EVM modeling, that the unresolved temperature fluxes should enhance the overall diffusivity of the flow, hence their dependence on the temperature gradient. Calculation of  $\overline{u_i \theta}$  by using the equation 3.68 is most beneficiary due to its implementation simplicity, and the inclusion of the anisotropic influences.

A final, and most simple approach is the strategy known as *simplified gradient diffusion hypothesis* (SGDH), in which the Prandtl analogy is used in conjuncture with the Boussinesq hypothesis. Similarly to the existence of turbulent viscosity, sub-grid fluxes are defined using the turbulent diffusivity as:

$$\overline{u_k \theta} = \alpha_t \frac{\partial T}{\partial x_k}, \quad \alpha_t = \frac{\nu_t}{Pr_t} \quad (3.69)$$

where  $Pr_t$  is the turbulent Prandtl number. By using the SGDH, mean temperature transport equation 3.20 is transformed into:

$$\frac{\partial T}{\partial t} + \frac{\partial}{\partial x_k}(U_k T) = \frac{\partial}{\partial x_k} \left( (\alpha + \alpha_t) \frac{\partial T}{\partial x_k} \right) \quad (3.70)$$

In Chapter 6, both GGDH and SGDH approaches are to be tested in conjuncture with IIS-RSM model.

### 3.5. Bubble-induced turbulence

Passage of bubbles through the flow field often causes the modulation of turbulence. As noted by Elghobashi (1994), the outcome of the relative motion between the dispersed-, and the carrier-phase can be categorized in dependence of the dispersed-phase loading, as well as in dependence of the Stokes number-  $S_t$ , which compares the timescale of the reaction of the moving bubble to the surrounding fluid, and time-scale of the carrier-fluid turbulence. For large  $S_t$ , production of turbulence supersedes the dissipation mechanisms, and vice versa for the small  $S_t$ . As the volume-fraction of the dispersed fluid increases, so does the modulation. This is referred to as the *Bubble-Induced-Turbulence* (BIT).

Since the interaction of bubbles with the surrounding fluid will not be directly captured (due to the fulfillment of Milelli criterion, see the previous Chapter), modulation of turbulence will initially affect the modeled part of the spectrum. Initial proposals by Sato and Sekoguchi (1975) considered the direct modification of the turbulence viscosity by adding an appropriately calibrated BIT-term like:

$$\mu_{eff} = \mu + \mu_t + \mu_{BIT} \quad (3.71)$$

which is applicable within the EVM frameworks. Second approach, used in this thesis, involves the manipulation of transport equations, governing the sub-grid turbulence, in sense of adding the BIT-related source terms to them. Additional production of turbulent kinetic energy is usually associated with the work, exhibited by the drag force, hence taking the form:

$$S_k \propto \vec{F}_d \cdot \vec{U}_r \quad (3.72)$$

where  $\vec{F}_d$  is the drag force, calculated as in the previous Chapter, and  $\vec{U}_r$  the relative velocity:  $\vec{U}_r = \vec{U}_b - \vec{U}$ . It is clear that when dealing with RSM modeling, adequate redistribution of BIT influence among the components of Reynolds-Stress-Tensor is necessary, This is done in the form:

$$S_R = b^* S_k \quad (3.73)$$

where  $b^*$  is the appropriately selected tensor. Based on the additional production, bubble-induced dissipation also needs to be modeled, which is done like:

$$S_{\varepsilon^h} \propto \frac{S_k}{\tau_b} \quad (3.74)$$

where  $\tau_b$  is the appropriately selected time-scale, usually connected with the characteristic time of the bubble:  $\tau = d_b/|U_r$ . However, since in this work,  $\omega^h$  is chosen as the scale-supplying variable, its source term is found from  $S_k$  and  $S_\varepsilon$  following the transformation proposed in Rzehak and Krepper (2013):

$$S_{\omega^h} = \frac{1}{C_\mu k} S_{\varepsilon^h} - \frac{\omega^h}{k} S_k \quad (3.75)$$

Within this work, two respective models for BIT will be subjected to scrutiny within the field of scale-resolving simulations. Naming of each of the respective models is performed based on the redistribution assumptions:

**The Isotropic BIT model** by Troshko and Hassan (2001) assumes an equal, and isotropic redistribution of turbulent kinetic energy among the normal components of Reynolds stress tensor:

$$S_{R,ij} = \frac{2}{3} \delta_{ij} S_k \quad (3.76)$$

where the kinetic energy source term is calculated as:

$$S_k = \vec{F}_d \cdot \vec{U}_r \quad (3.77)$$

Dissipation is based on the previously-mentioned time-scale of the bubble  $\tau = d_b/|U_r|$ , and found after the calibration:

$$S_\varepsilon = 0.45 \frac{3C_d}{2C_{vm}} \frac{S_k}{\tau_b} = 1.35C_d \frac{S_k}{\tau_b} \quad (3.78)$$

where  $C_{vm} = 0.5$  and  $C_d$  are respectively virtual mass-, and drag-coefficient, defined in previous Chapter.

**The Anisotropic BIT model** as reported in Ma et al. (2020), developed as a second-moment closure (SMC) model, using the DNS data of the dispersed bubbly flow in an upward vertical channel, will be tested as well. Source term for turbulent kinetic energy is calculated in dependence of bubble Reynolds number,  $Re_b$ :

$$S_k = \min(0.18Re_b^{0.23}, 1) \vec{F}_d \cdot \vec{U}_r \quad (3.79)$$

whereas the dissipation term is calculated similarly to the 3.78, just with recalibrated constants:

$$S_\varepsilon = 0.3C_d \frac{S_k}{\tau_b} \quad (3.80)$$

Redistribution of  $k$  among the components of the Reynolds stress tensor is performed like:

$$S_R^X = \begin{pmatrix} b_{11}^* & 0 & 0 \\ 0 & \frac{1}{2}(2 - b_{11}^*) & 0 \\ 0 & 0 & \frac{1}{2}(2 - b_{11}^*) \end{pmatrix} S_k \quad (3.81)$$

Here, the assumption is again taken that the injection of energy mainly contributes to the normal components of Reynolds-stress tensor, of which the fluctuations in the direction of relative motion (here taken as a cardinal direction  $x$ ) should be dominant. Fluctuations in the cross-stream directions are assumed to be equal far away from the wall. Previous formulation also guarantees that:  $tr(S_R^X) = 2S_k$ . Again, by fitting the DNS data,  $b_{11}^*$  is calculated as:

$$b_{11}^* = \min(0.67 + 0.67 \exp(370 Re_b^{-1.2}), 2) \quad (3.82)$$

where for low enough  $Re_b$ ,  $b_{11}^* = b_{22}^* = b_{33}^* = 2$ , and model tends to the isotropic redistribution of energy. In the general case, direction of relative motion is of-course not guaranteed to coincide with  $x$  cardinal direction. Hence, rotation of the  $S_R^X$  is performed in order to finally obtain the source-term for the Reynolds-stress-tensor transport equation:

$$S_R = \mathbf{Q}_R \cdot S_R^{SMC} \cdot \mathbf{Q}_R^T \quad (3.83)$$

where  $\mathbf{Q}_R$  is the rotation matrix with the form:

$$\mathbf{Q}_R = \begin{pmatrix} \cos \beta & 0 & \sin \beta \\ \sin \alpha \sin \beta & \cos \alpha \sin \beta & -\sin \alpha \cos \beta \\ -\cos \alpha \sin \beta & \sin \alpha & \cos \alpha \cos \beta \end{pmatrix} \quad (3.84)$$

where the angles  $\alpha$  and  $\beta$  are calculated based on the unit vector of relative velocity  $\vec{u}_r = \vec{U}_r / |\vec{U}_r|$ :

$$\alpha = \arccos\left(\frac{-u_3}{\sqrt{1 - u_1^2}}\right), \beta = \arccos(u_1) \quad (3.85)$$

Since the development of two aforementioned BIT models was latched to the EE (TFM) framework, appropriate mapping strategy between the Eulerian and Lagrangian reference frames is needed for this thesis. Information concerning the relative-velocities, drag coefficients and particle time-scales are available only while looping over the Lagrangian particle list. Therefore, any source term, named in this section can be calculated in the Eulerian frame of reference in the following way:

First, when looping over all the parcels at the beginning of the PISO loop,  $p$ -th parcel will perform  $N_{\delta t_i}$  Lagrangian time steps  $-\delta t_i, j$ , while within the cell  $i$ . Hence, first the BIT source terms (from either the Isotropic-, or Anisotropic model) are calculated for the parcel  $p$  within the cell  $i$  like:

$$S_{p,i}^L = \sum_{j=1}^{N_{\delta t,i}} S_{\delta t_{i,j}} \quad (3.86)$$

where  $S_p^L$  represents any of the source terms, calculated for the single parcel, using the previously outlined equations ( $S \in \{S_R, S_k, S_\varepsilon, S_\omega\}$ ). In this way, value of the corresponding source term is calculated in the Lagrangian reference frame.

In the second step,  $S_{p,i}^L$  needs to be mapped to the Eulerian frame of reference. During the Eulerian time-step  $\Delta t$ ,  $N_{p,i}$  parcels will pass through the cell  $i$ . Summation over all  $N_{p,i}$  parcels that resided in the cell during an Eulerian time step is performed like:

$$S_i^E = \frac{1}{\Delta t V_i} \sum_{p=1}^{N_{p,i}} S_{p,i}^L \quad (3.87)$$

where  $S_i^E$  is obtained as a corresponding source term in the Eulerian frame of reference, hence finishing the mapping procedure.



## 4. Post-processing techniques

---

In this Chapter, advanced post processing techniques that stretch beyond the scope of pure statistical analysis of the turbulent flow field will be presented. First, the concept of Proper-Orthogonal-Decomposition (POD) for discovering of spatially correlated flow structures (that are normally obscured by the turbulence), as well as the characterisation of their dynamics is outlined. Additionally, visualisation of turbulence anisotropy through the usage of componentality contours, based on barycentric coordinates is presented.

### 4.1. Proper-Orthogonal-Decomposition: finding the coherent structures in the turbulent flow field

Turbulent flows can, among other definitions, be defined as systems with random evolution of state variables, possessing infinite number of degrees of freedom. From an engineer's standpoint, interpretation and analysis of such a system is made challenging exactly due to the non-deterministic behaviour of flow variables. Usual solution, as shown in the previous Chapter, involves the usage of statistical tools which provide the average (expected) value of the selected flow variable, as well as any number of its higher statistical moments. In this way, amount of information describing the flow is reduced, and made more understandable for the engineer.

Although statistical tools represent the back-bone of turbulence analysis, their application also tends to filter-out small flow structures, leaving only the *blurred*, summary influence of all the underlying phenomena on the resulting, averaged flow image. A procedure outlined in this section tends to partially bridge the gap being made by the averaging procedure: i.e. to recover the additional data concerning the most relevant features of the flow, all while keeping the amount of gained information relatively small, making it interpretable for a human engineer. This technique is also known as a Reduced-Order-Modeling (ROM), which is a generalized name for a set of procedures in which the behaviour of highly complex systems is simplified by isolating a limited number of dominant features that characterise it. Family of ROM analysis techniques includes sever sub-branches, such as exemplary: dynamic mode decomposition (DMD) and proper-orthogonal-decomposition (POD). Interested reader will find a very detailed discussion of the mentioned techniques in Taira et al. (2017).

As a start for deriving the Proper-Orthogonal-Decomposition procedure, suppose that the state of the system is determined with a flow variable  $U(x, t)$ , which is either measured or numerically calculated. Without the loss in accuracy,  $U(x, t)$  can be represented as a *decomposition* (superposition) of some adequately chosen functions that separate influence of spatial and temporal coordinate like:

$$U(x, t) = \sum_{i=0}^{+\infty} a_i(t)\Phi_i(x) \quad (4.1)$$

Using this change in basis,  $U(x, t)$  can be viewed as a superposition of spatially coherent features  $\Phi_i(x)$ , characterized by their temporal evolution  $a_i(t)$ . The term coherent in spatial sense represents underlying flow structures that show some degree of correlation, with respect to their time dynamics. By using the correlation, random, non-probabilistic features that obscure the flow field can be eliminated from the analysis. As a start, suppose that the measurements from the aforementioned experiment are made available in both space and time. In the certain time-instant, *recording* of  $U$  is made in  $m$  points in the domain. Results can be stacked into a column-vector:

$$S_n = \begin{bmatrix} U_1 \\ U_2 \\ \vdots \\ U_m \end{bmatrix} \quad (4.2)$$

which is to be referred to as a *snapshot* vector. Additionally, let the snapshot  $S_n$  be sampled uniformly, in  $n$  equidistant temporal instances. By concatenating the recording of the snapshot vectors, one gets the  $m \times n$  snapshot matrix in the form:

$$\mathbf{S} = \begin{bmatrix} | & | & \dots & | \\ S_1 & S_2 & \dots & S_n \\ | & | & \dots & | \end{bmatrix} \quad (4.3)$$

If the statistically stationary process is observed, mean value will have no temporal evolution, hence the  $\mathbf{S}$  is mean-padded (in time):

$$\mathbf{S} = \mathbf{S} - \text{mean}(\mathbf{S}) \quad (4.4)$$

where the second term contains the row-wise mean. Correlation involving any pair of spatial data points is contained within the covariance matrix  $\mathbf{C}$ , which is calculated as:

$$\mathbf{C} = \frac{1}{n-1} \mathbf{S}\mathbf{S}^T \quad (4.5)$$

In the next step, eigendecomposition of  $\mathbf{C}$  is performed:

$$\mathbf{C} = \mathbf{\Phi}\mathbf{\Lambda}\mathbf{\Phi}^T \quad (4.6)$$

Eigendecomposition of  $m \times m$  real, positive definite matrix produces an orthogonal matrix  $\mathbf{\Phi}$ , whose columns represent the eigenvectors of  $\mathbf{C}$ , as well as the diagonal matrix  $\mathbf{\Lambda}$ , whose entries contain a real and positive ordered set of its eigenvalues  $\lambda_i$ . Eigendecomposition posses two features that are relevant: first, eigenvectors  $\Phi_i$  represent an orthogonal (spatially-independent) basis for the representation of  $\mathbf{S}$ . Furthermore, captured variance of  $\mathbf{S}$  along each of the calculated vectors  $\Phi_i$  is maximized, and equal to the  $i$ -th eigenvalue:

$$\lambda_i = var(\mathbf{S}^T \Phi_i) \quad (4.7)$$

which gives the modes certain asset: modes associated with the larger captured variance are deemed more important. If  $U$  were the velocity, than the individual eigenvalues will determine how much of the fluctuating kinetic energy is contained in each mode since:

$$k = \frac{1}{2}tr(\mathbf{\Lambda}) \quad (4.8)$$

As will be seen later on, measured data containing large, energetic transients will produce a very distinctive set of eigenvalues, where the largest eigenvalues will contain almost 100% of captured variance. Hence, to summarize the previous discussion: Proper-Orthogonal-Decomposition is a technique based on finding the *orthogonal* basis for the representation of the measured data-set  $\mathbf{S}$ , which is done by calculating the eigenvectors of its covariance matrix. By doing so, spatial points that exhibit some sort of correlation will be isolated, and stacked into an eigenvector  $\Phi$ , which is referred to as *POD-mode*. Due to the orthogonality of the modes, spatially independent coherent structures are isolated. By the word *proper*, intrinsic property of eigendecomposition in maximizing the captured variance per mode is expressed. Now returning to the equation 4.1, spatio-temporal evolution of the discretely sampled observable  $U$  may be expressed as:

$$\mathbf{S} = \mathbf{\Phi}\mathbf{A}_t \quad (4.9)$$

where the rows of  $\mathbf{\Phi}$  contain the orthogonal modes, which are the spatial basis function. Time dynamics of the individual modes is stored within the rows of  $\mathbf{A}_t$ , and is readily found by projecting the modes back to the snapshot-matrix  $\mathbf{S}$ :

$$\mathbf{A}_t = \mathbf{\Phi}^T \mathbf{S} \quad (4.10)$$

Formally, the process of POD analysis is complete: the coherent, spatially orthogonal data structures (*modes*) are found as eigenvectors of the covariance matrix, whereas their temporal dynamics it found from the equation 4.10. However, in the

engineering practice, number of spatial points  $m$  is in the range of several tenths to hundreds of thousands (if the proper spatial resolution is required), which will mean that the eigendecomposition of a very large, dense covariance matrix  $\mathbf{C}$  will need to be performed. This is a time- and memory-consuming task, and often beyond the capability of computing hardware. An alternative concept known as a *snapshot* POD can also be used, by calculating the eigendecomposition of the temporal covariance matrix  $\mathbf{C}^*$ , (which possesses the identical non-zero eigenvalues as  $\mathbf{C}$ ) and then projecting its eigenvectors  $\mathbf{\Psi}$  back to the snapshot matrix:

$$\mathbf{C}^* = \frac{1}{m-1} \mathbf{S}^T \mathbf{S} \quad (4.11)$$

$$\mathbf{C}^* \mathbf{\Psi} = \mathbf{\Psi} \mathbf{\Lambda} \quad (4.12)$$

$$\mathbf{\Phi} = \mathbf{S} \mathbf{\Psi} \quad (4.13)$$

In spite of the accelerated procedure offered by 4.11, (eigendecomposition of  $n \times n$  instead of  $m \times m$  matrix), *snapshot* POD suffers from the same computing difficulties as  $n$  grows. Although some interesting concepts about acceleration of the eigenvalue decomposition through the parallelisation of QR algorithm are proposed in Benson et al. (2013) and Sayadi et al. (2014), eigendecomposition will not be used as a process for obtainment of POD modes. As an alternative, third concept, a singular value decomposition (SVD) can be performed:

$$\mathbf{S} = \mathbf{L} \mathbf{\Sigma} \mathbf{V}^T \quad (4.14)$$

where  $\mathbf{L}_{m \times p}$  is the left singular matrix,  $\mathbf{V}_{n \times p}$  is the right singular matrix, and  $\mathbf{\Sigma}_{p \times p, p = \min(m, n)}$  is the diagonal matrix, whose entries are called singular values. Since both  $\mathbf{L}$  and  $\mathbf{V}$  are orthonormal matrices, it can be shown that the singular-value-, and eigendecomposition can be interchangeably used like:

$$\mathbf{S} \mathbf{S}^T = \mathbf{L} \mathbf{\Sigma} \mathbf{V}^T \mathbf{V} \mathbf{\Sigma} \mathbf{L}^T = \mathbf{L} (\mathbf{\Sigma} \mathbf{\Sigma}^T) \mathbf{L}^T = \mathbf{C} = \mathbf{\Phi} \mathbf{\Lambda} \mathbf{\Phi}^T \quad (4.15)$$

The factor  $n - 1$  is omitted since it will appear in the scaling of time coefficient in any case. Equation 4.15 shows that instead of the costly calculation of  $m \times m$  matrix eigendecomposition, POD-modes can be recovered as a left-singular vectors from the SVD algorithm,  $\mathbf{\Phi} = \mathbf{L}$ , which is computationally much faster. At the same time, eigenvalues of the modes can recovered from the square of the singular values  $\lambda_i = \sigma_i^2$ .

Although the calculation of POD modes using the SVD algorithm proved to be much faster, it is still prone to memory errors and lengthy calculations, especially in the case of eddy-resolving turbulence cases that contain numerous data sampling points for good resolution, as well as due to the lengthy sampling period in order to obtain good statistics convergence. Hence, the final POD algorithm, as used in this work is presented below.

In the first step, **QR** decomposition of the snapshot matrix is performed like:

$$\mathbf{S} = \mathbf{QR} \quad (4.16)$$

which is computationally much faster. In the second step, SVD decomposition of the upper triangular matrix **R** is performed:

$$\mathbf{L}_R \mathbf{\Sigma} \mathbf{V}^T = \mathbf{R} \quad (4.17)$$

It can be proven that the matrices  $\mathbf{\Sigma}$  and  $\mathbf{V}$  are identical for the SVD decomposition of either **S** or **R**. The only thing remaining is to calculate the POD modes as:

$$\mathbf{\Phi} = \mathbf{QL}_R \quad (4.18)$$

With that in mind, the full algorithm for the POD analysis used in this Chapter is presented below:

---

**Algorithm 2** Procedure for calculation of POD.

---

- 1: Assemble all  $n$  snapshots of the system involving  $m$  sampling points into the mean-padded snapshot matrix **S**.
  - 2: Calculate the **QR** decomposition of **S**, using the equation 4.16.
  - 3: Perform the SVD-decomposition of **R** matrix, using the equation 4.17.
  - 4: Obtain the POD modes from the equation 4.18.
  - 5: Calculate the time dynamics from equation 4.10.
  - 6: Store the results.
- 

Implementation of the algorithm was performed in Python programming language by the author, and the code is made publicly available at Joksimović (2022a). Although the concepts presented above stem from the field of linear algebra and statistics, their combination into the POD algorithm is native to the field of turbulence. Introduction of POD can be back-tracked to Lumley (1967), who attempted to represent the stochastic nature of turbulence fluctuations through the set of deterministic functions, who reconstruct dominant portion of turbulence kinetic energy. In the recent years, POD has been established as an analysis tool in numerous studies of turbulence dominated flows with strong transient components (turbulent wakes, separation bubbles, transients in the cavity etc.), examples of which can be found in Murray et al. (2009), Kajishima and Taira (2017), Munday and Taira (2017) and T. Wang et al. (2022), to name a few.

### 4.1.1. Initial examples - strengths and weaknesses

In order to demonstrate the usability of POD for the analyses of turbulence fields, performed in following Chapters, three exemplary numerical experiments will be performed.

**For the first experiment**, the observable  $U$  is going to be composed of two modes, with the form:  $U = a_1\Phi_1 + a_2\Phi_2$ , where both  $\Phi_1$  and  $\Phi_2$  are  $100 \times 40$  matrices, composed as:

$$\begin{aligned}\Phi_{1,ij} &= \begin{cases} 1, & \text{if } 10 \leq i \leq 30, \text{ and } 10 \leq j \leq 30 \\ 0, & \text{otherwise} \end{cases} \\ \Phi_{2,ij} &= \begin{cases} 1, & \text{if } 70 \leq i \leq 90, \text{ and } 10 \leq j \leq 30 \\ 0, & \text{otherwise} \end{cases}\end{aligned}\tag{4.19}$$

Here, it is clear that  $\Phi_1^T \cdot \Phi_2 = 0$ , hence making the set of orthogonal coherent structures. At the same time, to make the system statistically stationary, temporal dynamics of both modes are chosen in the form of sinusoidal functions:

$$\begin{aligned}a_1 &= A_1 \cos(2\pi f_1 t), A_1 = 2, f_1 = 3 \\ a_2 &= A_2 \cos(2\pi f_2 t), A_2 = 1, f_2 = 7\end{aligned}\tag{4.20}$$

Provided that the POD algorithm is properly applied, original spatial modes along with the frequency signatures should be recovered without problem.

**For the second experiment**, temporal dynamics is retained, but the state of observable is superposed with the random noise from the range  $R \in \{-2 \div 2\}$ , which corresponds with the amplitude of the first mode, hence imitating the random turbulent fluctuations:  $U = a_1\Phi_1 + a_2\Phi_2 + R$ . Here, the capability of POD algorithm with reconstructing noisy data will be tested.

**For the third experiment**, noise will be eliminated, but the spatial orthogonality will not be guaranteed, and the modes will be changed as:

$$\begin{aligned}\Phi_{1,ij} &= \begin{cases} 1, & \text{if } 35 \leq i \leq 55, \text{ and } 10 \leq j \leq 30 \\ 0, & \text{otherwise} \end{cases} \\ \Phi_{2,ij} &= \begin{cases} 1, & \text{if } 20 \leq i \leq 40, \text{ and } 45 \leq j \leq 65 \\ 0, & \text{otherwise} \end{cases}\end{aligned}\tag{4.21}$$

which imposes a certain overlap between them, since  $\Phi_1^T \cdot \Phi_2 \neq 0$ . Initial state for all three experiments is shown in Figure 4.1.

Results for the POD analysis for the first experiment are shown in Figure 4.2. As can be seen, rank of the system in the first experiment is correctly identified, with two modes recovered. Distribution between the captured kinetic energy perfectly corresponds to the amplitude ratio  $A_1^2/A_2^2 = 80/20$ , as shown in Figure 4.2 (top-left). Additionally, in the Figure 4.2 (top-right) FFT analysis of the time coefficients  $a_1$  and  $a_2$  is performed, whereas again, dominant peaks are recovered exactly at frequencies  $f_1 = 3 [Hz]$  and  $f_2 = 7 [Hz]$ . Also, both  $\Phi_1$  and  $\Phi_2$  are perfectly reconstructed.

As for the second experiment shown in Figure 4.3, it can be seen that despite the presence of noise which makes the direct observation of  $U$  extremely challenging, the POD algorithm first correctly identifies the rank (although due to the noise,

contained variance is now spread among the other modes). Frequency analysis is once again performed almost flawlessly. Finally, the original modes were (due to their spatial orthogonality) recovered with high accuracy, although the overall quality of the reconstruction is somewhat obscured by the noise.

Finally, for the third experiment, following conclusions can be drawn: first, even in the situation where the spatially-coherent structures are non-orthogonal, POD provides the correct identification of rank of the system, where the original amplitude ratio is preserved. Additionally, temporal signatures of both modes are correctly captured, although the two characteristic frequency peaks appear in both time dynamics signals. However, it is usually possible to isolate the most energetic peak, though the underlying structures are not orthogonal. The point where the POD algorithm fails, is the correct spatial separation of modes. Here, both Mode 1 and Mode 2 share some common properties, but due to their non-orthogonality, correct distinction of the underlying phenomena remains very hard. This feature will prove challenging for exact separation of phenomena who have frequency distinction, but share the same spatial zone in the flow field. Isolation of spatially coherent phenomena with a distinct frequency signature named *spectral* POD (exemplary in Sieber et al. (2016a)) is out of scope for this publication, but remains an interesting opportunity for further research.

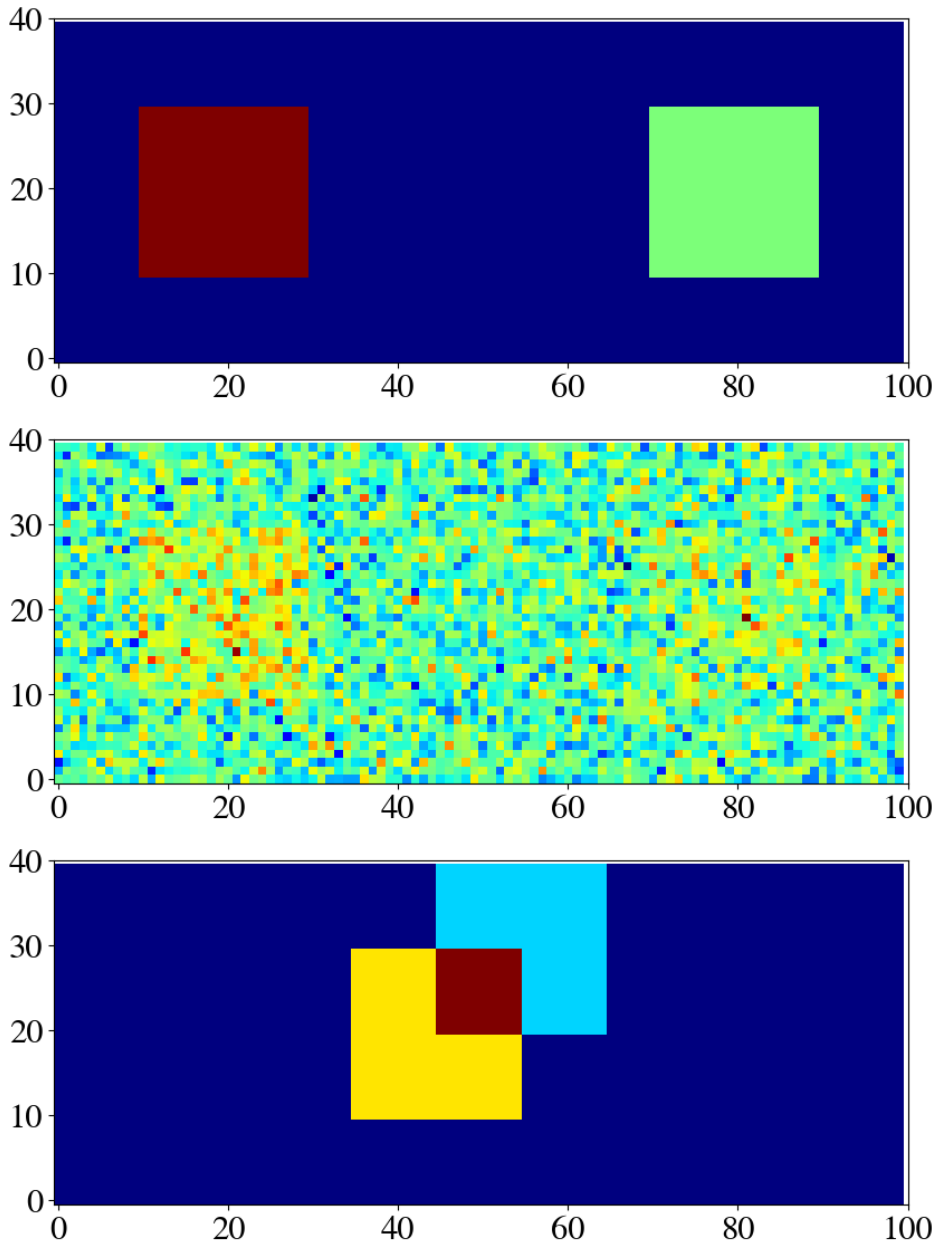


Figure 4.1.: POD analysis: Initial state for all three experiments ( $U(t = 0)$ ). Note the spatial separation for the first experiment (top), obscured nature of data in the second experiment (center), as well as partial overlap of two modes (down).



4.1. Proper-Orthogonal-Decomposition: finding the coherent structures in the turbulent flow field

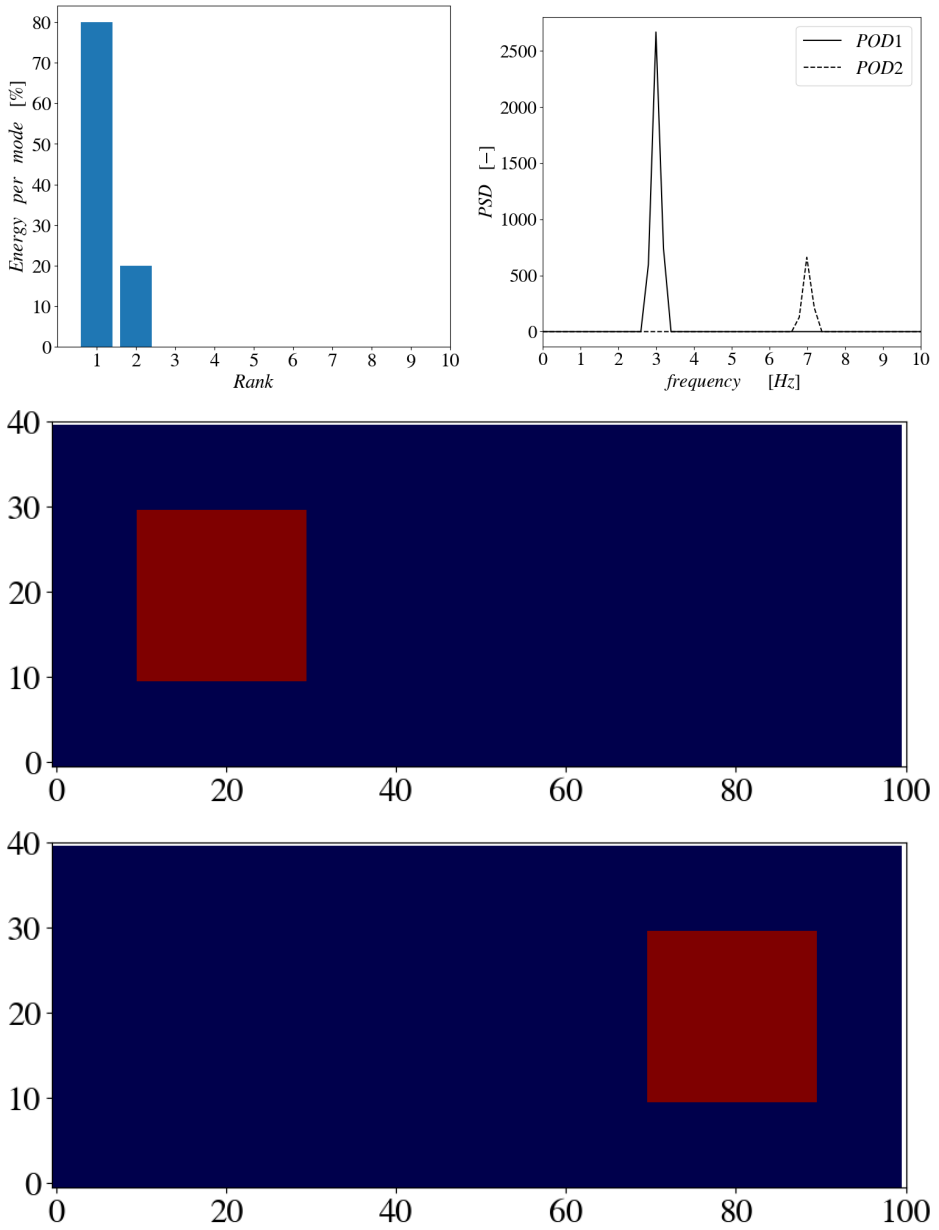


Figure 4.2.: POD analysis for the first experiment: captured variance (top-left), FFT analysis of time coefficients (top-right). Spatial representation of the first mode (center), and the second mode (bottom).

#### 4. Post-processing techniques

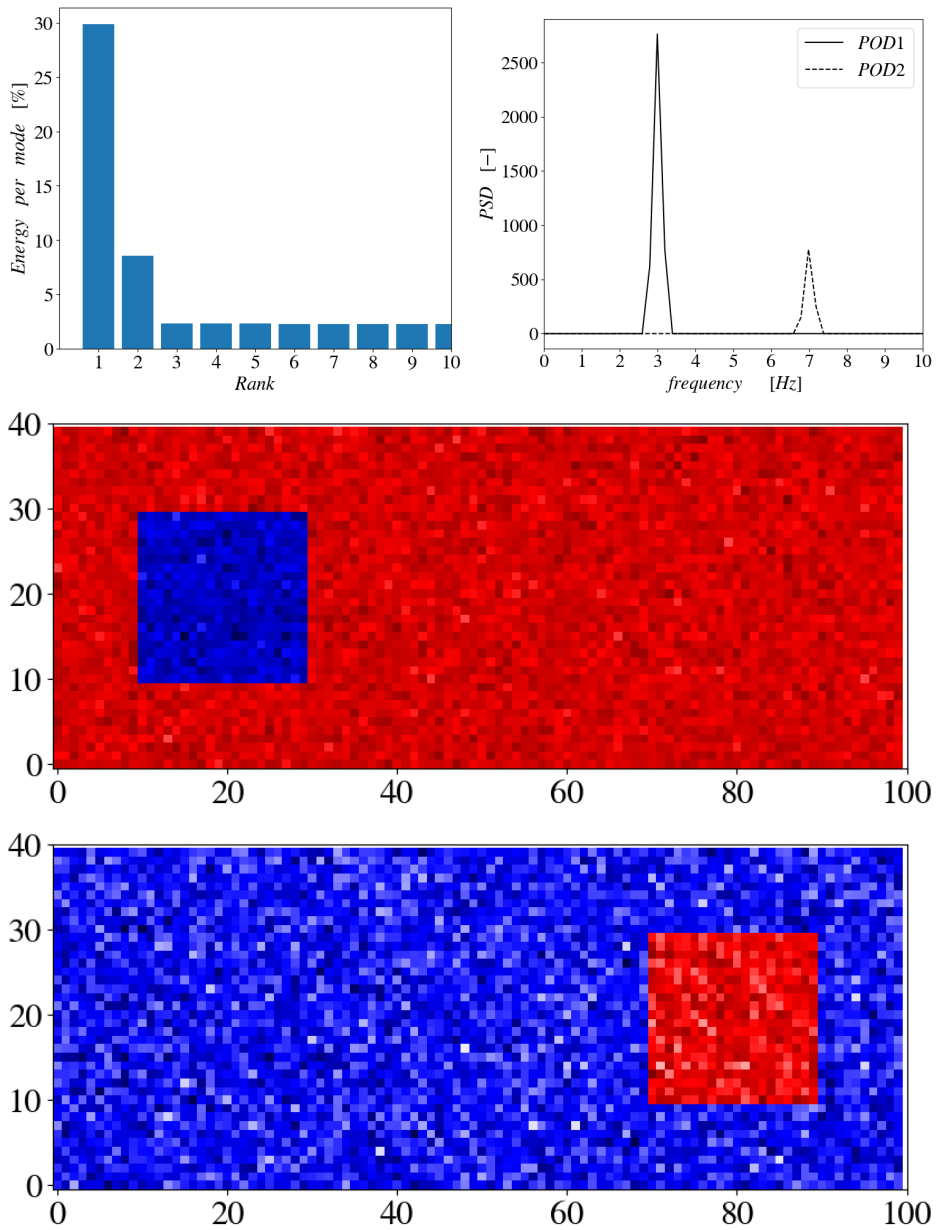


Figure 4.3.: POD analysis for the second experiment: captured variance (top-left), FFT analysis of time coefficients (top-right). Spatial representation of the first mode (center), and the second mode (bottom).

4.1. Proper-Orthogonal-Decomposition: finding the coherent structures in the turbulent flow field

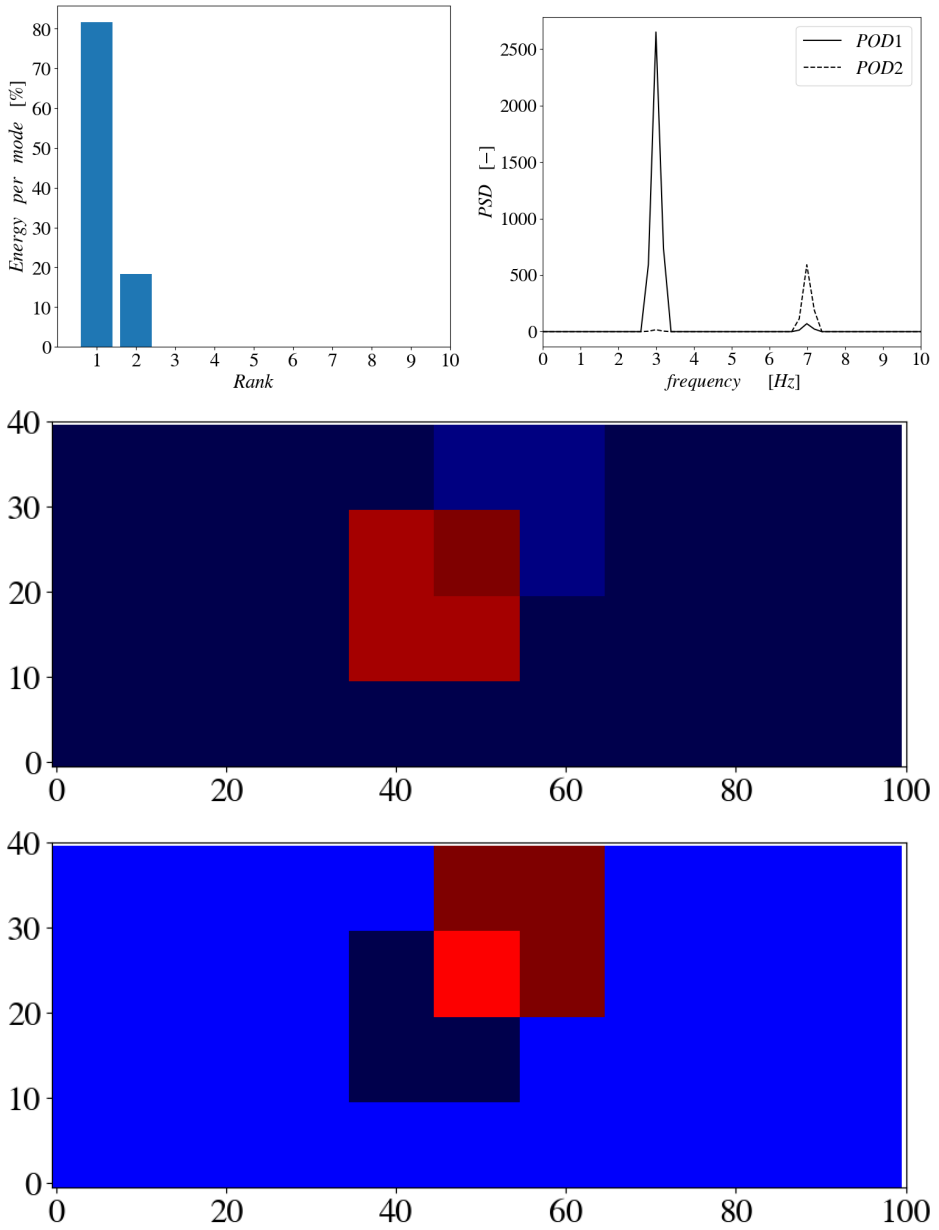


Figure 4.4.: POD analysis for the third experiment: captured variance (top-left), FFT analysis of time coefficients (top-right). Spatial representation of the first mode (center), and the second mode (bottom).

## 4.2. Visualization of Anisotropy - componentality contours based on barycentric coordinates

As indicated in previous Chapters, seemingly chaotic nature of turbulence may be presented in a statistical manner through the second-order symmetric tensor  $\overline{u_i u_j}$ , capturing the covariance of the velocity fluctuations. Since the statistical properties of turbulence are represented with 6 different variables, effortless interpretation of turbulence statistics is possible only in case of simple geometrical domains such as: pipe flow, periodic channel, flat plat boundary layer etc., where the principal direction of the flow is colinear with one of the Cartesian coordinates. In case of the isotropic turbulence, fluctuations are equally distributed in all directions and all the normal components of  $\overline{u_i u_j}$  are equal to  $2k/3$ . In order to assess relative intensity for each of the tensor components in relation to turbulent kinetic energy, a so-called anisotropy tensor was already introduced in the previous Chapter, equation 3.29:

$$a_{ij} = \frac{\overline{u_i u_j}}{k} - \frac{2}{3} \delta_{ij} \quad (4.22)$$

Due to the definition,  $a_{ij}$  represents the traceless tensor, and in case of the isotropic turbulence, it will also represent a zero-tensor. Since  $a_{ij}$  contains six independent variables related to turbulence anisotropy (which are also dependent on the exact orientation of the coordinate system), interpretation of the obtained turbulence states is performed either by taking the principal components  $a_{ii}^*$  of  $a_{ij}$ , or by taking the eigenvalue triplet:

$$[\lambda_1, \lambda_2, \lambda_3] = \text{eig}(a_{ij}), \quad \lambda_1 > \lambda_2 > \lambda_3 \quad (4.23)$$

Domain of realizable turbulence is bounded by three limiting states, which are:

**Isotropic state, three-component turbulence - (3C)**, where the fluctuations in all directions are of equal magnitude, hence:  $a_{ii}^* = 0, \lambda_i = 0$ .

**Axisymmetric, two-component turbulence - (2C)**, where fluctuations of equal magnitude exist along two directions. This state is also referred as *pancake* turbulence. Eigenvalues take the form:  $\lambda_1 = 1/6, \lambda_2 = 1/6, \lambda_3 = -1/3$ .

**One-component turbulence - (1C)** is a flow state where the fluctuations exist only along one direction, and is often denoted as *cigar* turbulence. Eigenvalues take the form:  $\lambda_1 = 2/3, \lambda_2 = -1/3, \lambda_3 = -1/3$ .

Connecting the limiting states are the intermediary turbulence states:

**Axisymmetric expansion** connects the states **3C** and **1C** and is characterized by:  $0 \leq \lambda_1 \leq 1/3, -1/6 \leq \lambda_2 = \lambda_3 \leq 0$ .

**Axisymmetric contraction** connects the states **3C** and **2C**, and is characterized by:  $-1/3 \leq \lambda_1 \leq 0, 0 \leq \lambda_2 = \lambda_3 \leq 1/6$ .

**Two component turbulence** connects the states **2C** and **1C**, and is characterized by:  $\lambda_1 + \lambda_3 = 1/3, \lambda_2 = -1/3$ .

Finally, a most common occurrence is that of plane-strain turbulence, which repre-

sents an intermediary state between the aforementioned ones. It is characterized at least one  $\lambda_i = 0$ . All seven mentioned states can be represented for each point in turbulent flow in a various ways, exemplary by using the Lumley invariant maps, as given in Lumley and Newman (1977). However, this way of representation is not optimal for this work due to the large amount of data points, which will obscure the graph, and complex geometry of the domains.

Technique applied here was presented in Emory and Iaccarino (2014), and relies on adopting the RGB colormap (a usual technique for the spatial representation of scalars), in which every limiting state will be represented by one of the RGB color triplets: Spatial points with the **3C** state of turbulence will be presented by the blue pixels, **2C** by the green pixels, and **1C** by the red colored pixels. Any other realizable state of turbulence will be mapped into a pixel, whose coloration is determined based on assigning different weights to the RGB colormap:

$$\begin{bmatrix} R \\ G \\ B \end{bmatrix} = C_{1c} \begin{bmatrix} 1 \\ 0 \\ 0 \end{bmatrix} + C_{2c} \begin{bmatrix} 0 \\ 1 \\ 0 \end{bmatrix} + C_{3c} \begin{bmatrix} 0 \\ 0 \\ 1 \end{bmatrix} \quad (4.24)$$

where the weights  $C_{1c}, C_{2c}$  and  $C_{3c}$  are directly taken from the barycentric map of turbulence presented in Banerjee et al. (2007), and are calculated as:

$$C_{1c} = \lambda_1 - \lambda_2 \quad (4.25)$$

$$C_{2c} = 2(\lambda_2 - \lambda_3) \quad (4.26)$$

$$C_{3c} = 3\lambda_3 + 1 \quad (4.27)$$

Note that for **1C**:  $C_{2c} = C_{3c} = 0$ , for **2C**:  $C_{1c} = C_{3c} = 0$  and for **3C**:  $C_{1c} = C_{2c} = 0$ . In this way, componentality contours of turbulence anisotropy can be plotted throughout the computational domain. Colormap corresponding to the equation 4.24 is shown in Figure 4.5 (left). In this work however, an alternative colormap is used, since it enables a more clear differentiation of the anisotropy:

$$\begin{bmatrix} R \\ G \\ B \end{bmatrix} = C_{1c}^* \begin{bmatrix} 1 \\ 0 \\ 0 \end{bmatrix} + C_{2c}^* \begin{bmatrix} 0 \\ 1 \\ 0 \end{bmatrix} + C_{3c}^* \begin{bmatrix} 0 \\ 0 \\ 1 \end{bmatrix} \quad (4.28)$$

where  $C_{ic}^* = (C_{ic} + 0.65)^5$ . As will be seen, this technique is going to ease the recognition of the limiting states. In the upcoming Chapters, componentality contours will be extensively used for analysis of turbulence anisotropy, and overall visualisation of flow properties. Colormap presented by the equation 4.28 is shown in Figure 4.5(right).

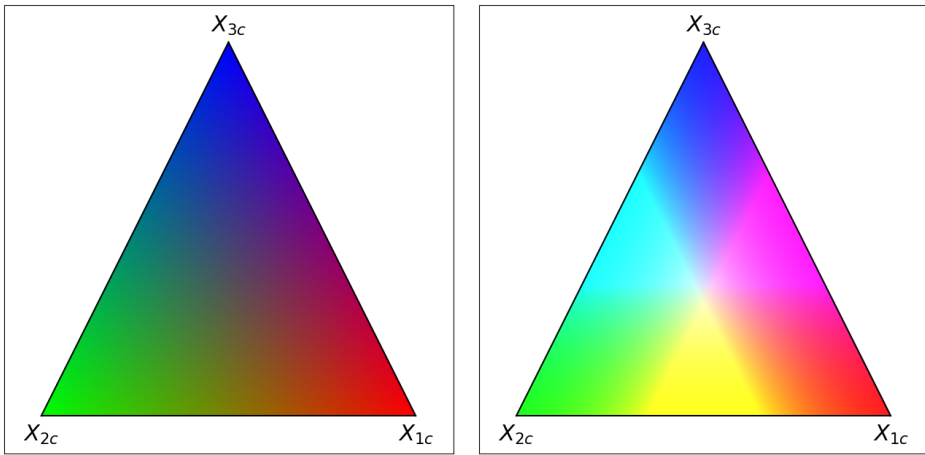


Figure 4.5.: Original colormap (left), obtained by using the equation 4.24, as well as modified colormap (right), according to the equation 4.28.

## 5. Flow configuration I: Generation of inlet turbulence

---

Within this Chapter, a detailed analysis of the IIS-RSM performance in different flow configurations and under various conditions will be introduced. Three important assets will be tested. First, model of turbulence will be systematically tested in reproducing a transient, fully developed turbulence fields in simple geometries of straight, circular pipes. Wide range of industrially relevant Reynolds numbers, including those which surpass the highest  $Re = 166000$  used with IIS-RSM (reported in Maduta et al. (2017)), will be covered, and the performance of the model will be qualitatively and quantitatively assessed. In this way, general applicability of the model will be confirmed. Second, as a result of all the calculations, an extensive database with full statistical analysis will be created, and the obtained data will be used further in Chapters 6 and 7. Namely, all the flow configurations listed in named Chapters require mapping of fully developed and adequately resolved turbulence onto their inflow boundaries, in order to enhance the physicality of the solution. By using the precursor simulations in place of the concurrent algorithms for generation of synthetic turbulence (exemplary *Divergence-Free Synthetic Eddy Method*, Poletto et al. (2013)), highest accuracy with respect to model performance is obtained, as stated by Jarrin et al. (2006). Finally, question of optimal meshing metrics for the upcoming Chapters will be addressed through the grid-convergence study of precursor simulations. Here, a grid size leading to the correct prediction of wall shear stress will be used as an *ad-hoc* indicator, which can point to the optimal meshing resolution used for the cases presented in Chapters 6 and 7. In this way, costly grid-convergence studies involving tenths of millions of cells will be avoided.

Batch of numerical experiments containing 6 different flow cases has been selected. Each flow configuration represents a circular, periodic pipe flow which can be characterised by either its mean velocity-, or friction velocity based Reynolds number, respectively:

$$Re = \frac{U_m D}{\nu}, \quad Re_\tau = \frac{U_\tau D}{\nu} \quad (5.1)$$

Previously, Wegt et al. (2022) performed an in-depth study concerning the optimal geometrical and meshing parameters in case of cyclic, circular domains, with the aim of producing the resolved precursor turbulence fields. Applied meshing strategy is henceforth latched on to the conclusions outlined in this thesis.

Inflow and outflow boundaries are treated with an OpenFOAM® built-in *cyclic* method which eases the quick generation of fully developed turbulence, in which the fields obtained at the outlet section *communicate* directly with the inflow boundary. Axial view of the mesh with typical configuration of the block is presented in Figure 5.1.

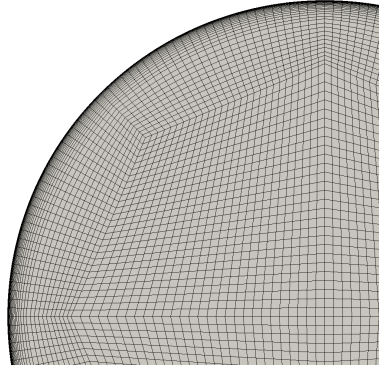


Figure 5.1.: Axial view of the typical multi-block, hexahedral mesh, used in all six precursor cases. Metric corresponding to each case is listed in Table 5.1.

Fully developed, resolved turbulence is obtained in a following way: first, the flow field is initialised with uniform values of all flow variables, except for the velocity field. Here, the random perturbation with the magnitude of 100% of the uniform velocity is initially prescribed in order to quickly trigger the eddy-resolving capability of the turbulence model. PISO algorithm with two pressure correction loops, as described in Chapter 2 is used. Variable time stepping is imposed as to limit the temporal propagation of the solution, and prohibit the blow-up. With use of low diffusion, second order *filteredLinear3* scheme listed in Chapter 2, resolved turbulence is sustained and statistically steady ratio between the modeled and resolved turbulence kinetic energy is established.

Table 5.1 gives a summary list of inflow- and meshing parameters for all the cases. Exact data concerning the inflow conditions (flow rate, viscosity) and geometric dimensions have been left out intentionally, since the results should be interpreted in dimensionless form. Columns 4 to 6 give the optimal values for grid resolution. Mesh employs the use of high-quality, block-structured, hexahedral cells with low non-orthogonality. This type of meshing strategy offers better reconstruction of derivatives at cell faces. Height of the wall-adjacent cells is adjusted, as to allow full resolution of viscous sublayer, hence  $y^+ \leq 1$ . Cells are characterised by their radial -  $\Delta r^+$ , circumferential -  $\Delta \theta^+$  and axial -  $\Delta z^+$  size. All parameters are normalized by the wall-normal distance, corresponding to  $y^+ = 1$ . Results in the last column are explained in short.



Table 5.1.: Inflow conditions and optimal meshing metrics for all six precursor cases.

No.	$Re$	$Re_\tau$	$\Delta r^+$	$\Delta \theta^+$	$\Delta z^+$	$\Delta u_\tau[\%]$
1	12795	384	1÷7	7	21	2.14
2	25853	712	1÷11	11	33	3.03
3	59862	1499	1÷30	30	120	3.82
4	86757	2087	1÷40	40	160	4.75
5	107893	2537	1÷70	70	210	2.51
6	380000	7901	1÷100	100	300	3.2

Usually, finding the optimal mesh resolution in scale-resolving simulations represents a time-exhausting task, where first the initial transient needs to be successfully eliminated, followed by the lengthy averaging period. Finally, whole process is repeated until the mesh convergence is reached, and the physically sound solution is obtained. Based on the author's experience, duration of this process can be substantially reduced. First, during every simulation time-step, instantaneous value of the surface-averaged wall shear stress (WSS)  $\tau_w$  is calculated as:

$$\tau_w(t) = \frac{1}{A_{walls}} \int_{A_{walls}} \bar{\vec{\tau}}(t) \cdot \vec{n} dA \quad (5.2)$$

Based on numerous try-outs, it was found that the cases where the value of  $\tau_w$  (calculated per equation 5.2) corresponds closely with theoretical estimation<sup>1</sup>, prediction of all the statistical properties of the flow will be very accurate. Hence, WSS proved to be a remarkably reliable indicator of the physicality of the solution. In the second step, evolution of WSS is monitored, as shown in Figure 5.2.

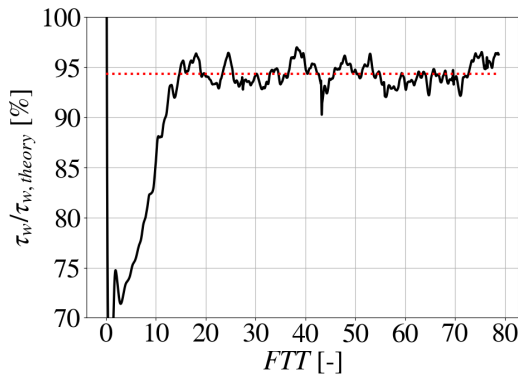


Figure 5.2.: Evolution of Wall Shear Stress, shown as a percentage of theoretical value.

<sup>1</sup>Under the theoretical estimation, usage of Colebrook–White formula for calculating WSS is meant.

In horizontal axis, dimensionless time (so called *flow through time*  $FTT = tU_m/L$ , where  $L$  is the flow length of the domain), is shown. On the vertical axis, instantaneous value of  $\tau_w$  is indicated, as a fraction of theoretical value. One can see that the initial transient is successfully eliminated after 10-20 flows through time, after which the averaging process may begin. Red dotted line represents the quasi steady state value of  $\tau_w$ , after the averaging process is finished. In the third step, averaged value of  $\tau_w$  is compared with the theoretical value. If the ratio doesn't reach 93% or more of the theoretical value <sup>2</sup>, simulation is terminated, refinement of the mesh takes place and the whole simulation is repeated. At the end, optimal cell size (columns 4 to 6 in Table 5.1) is determined. Last column in Table 5.1 lists the smallest deviation of the numerically obtained friction velocity  $u_\tau$ , from the theoretical one, achieved during the mesh optimisation process.

## 5.1. Discussion of results

Figure 5.3 shows the iso-surfaces of the instantaneous vorticity field, which are typically resolved during the simulation. In Figure 5.4 contours of instantaneous streamwise velocity field are plotted for two exemplary cases, with  $Re_\tau = 712$  and  $Re_\tau = 7901$  in order to stress differences in the resolvable structures, which are visible in ever more detail with increase in  $Re$  (and with corresponding mesh refinement). Note the substantially finer scale recovered with  $Re_\tau = 7901$ .

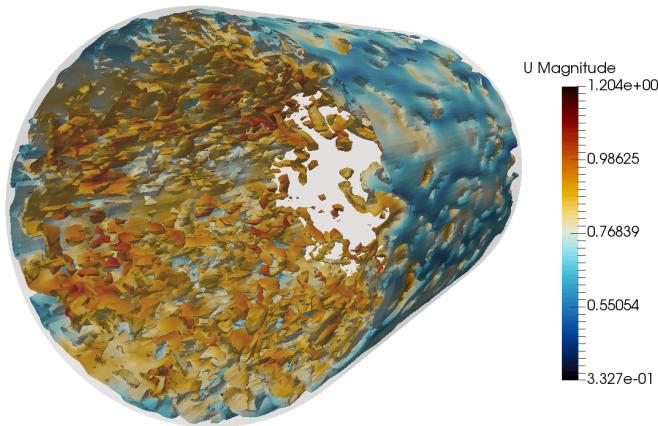


Figure 5.3.: Visualisation of the resolved flow in the typical precursor simulation: iso-surfaces of the vorticity magnitude. Background coloring shows the instantaneous velocity magnitude.

<sup>2</sup>Criteria determined in private discussion with Dr.-Ing. Robert Maduta.

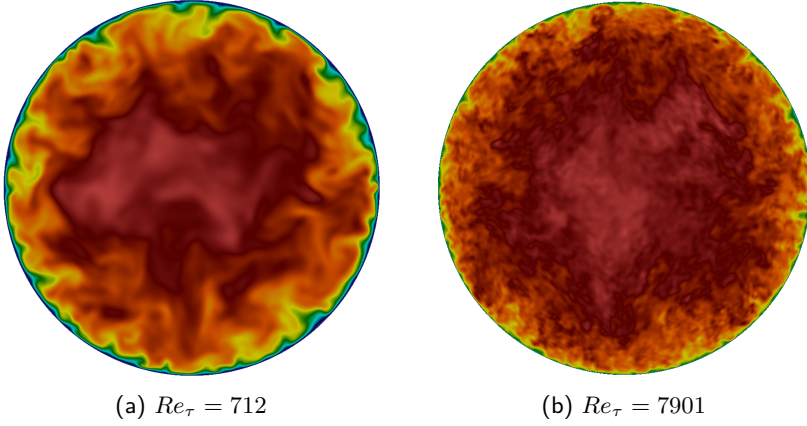


Figure 5.4.: Visualisation of the obtained flow field for two representative precursor cases: contours of the instantaneous streamwise velocity.

In order to quantitatively assess the performance of the IIS-RSM, radial profiles of first- and second order statistics are compared with the DNS data in Figures 5.5 to 5.7. As a DNS reference for comparison of the results, databases published in Hultmark et al. (2012) and Pirozzoli et al. (2021), involving the cases of fully developed flow fields in circular pipes will be used. Every numerical profile is plotted against two "nearest" experimental data sets in sense of  $Re_\tau$ .

In Figure 5.5, dimensionless mean velocity  $U^+$  is plotted against the dimensionless wall normal coordinate  $y^+$  for all six precursor cases. It can be stated that all the profiles show a high level of congruence with experimental data, suggesting that the model reacts well under the various meshing and flow configurations. Small deviations in the logarithmic layer are noticeable in cases  $Re_\tau = 2537$  and  $Re_\tau = 7901$ . Although the origin of these overshoots could not be completely clarified, it can be speculated that it correlates closely with the reduced diffusivity of the flow (which should flatten-out the local peaks in the velocity profiles). This indicates that possible deviations between the physical reality and the calculated spatial distribution of turbulence kinetic energy exist in region  $y^+ \geq 100$ , leading to the diminished mixing properties of the mean flow. This hypothesis will be confirmed in short. However, it can be concluded that independently of the inflow conditions, model reproduces the first-order statistical properties of the flow in all of the discussed cases in a satisfactory manner.

In Figure 5.6, distributions of streamwise-  $u_z^+$ , spanwise-  $u_\theta^+$  and wall-normal  $u_r^+$  component of the velocity fluctuations are shown. It can be seen that generally, very good prediction of turbulence anisotropy has been made, independently of the inflow conditions. Noted deviations from the experimental data will be addressed.

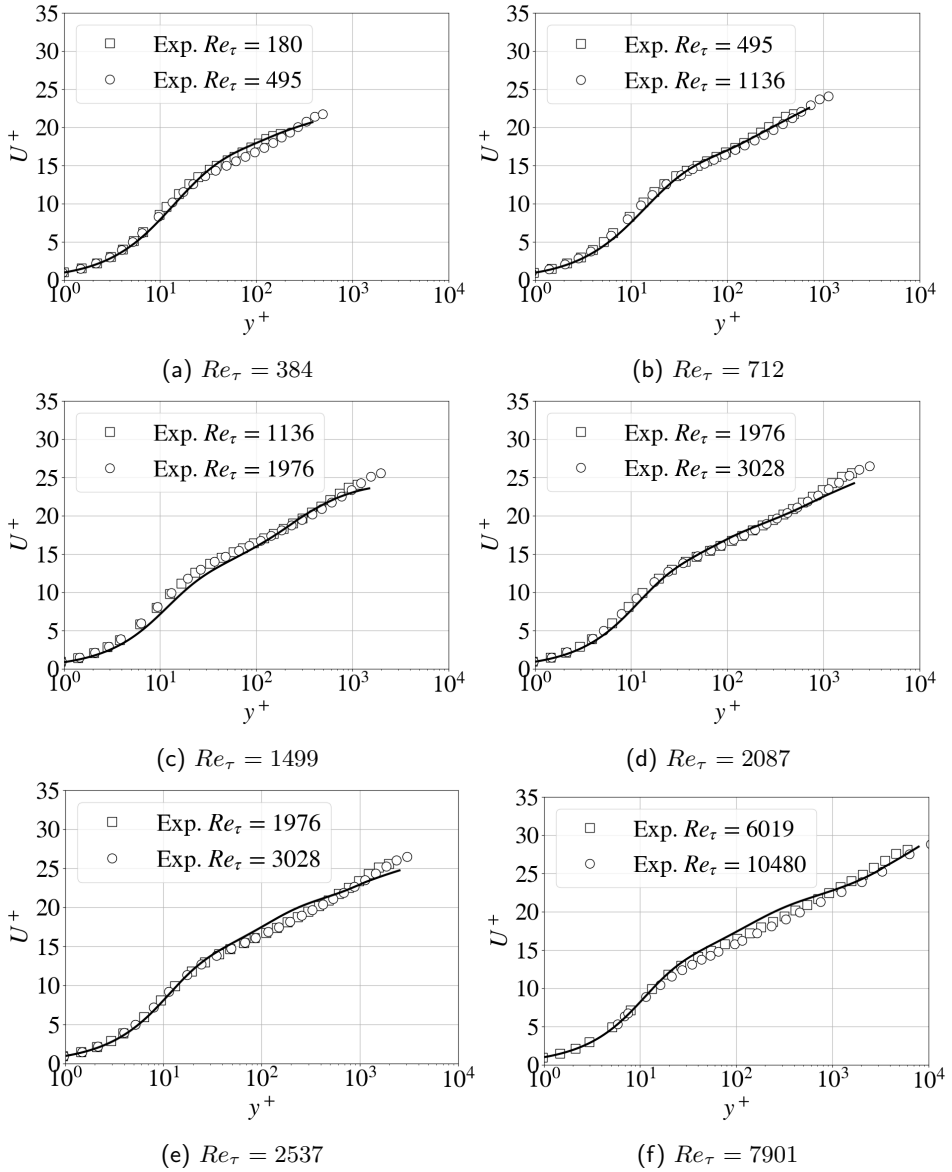


Figure 5.5.: Profiles of mean streamwise velocity for all six precursor cases.

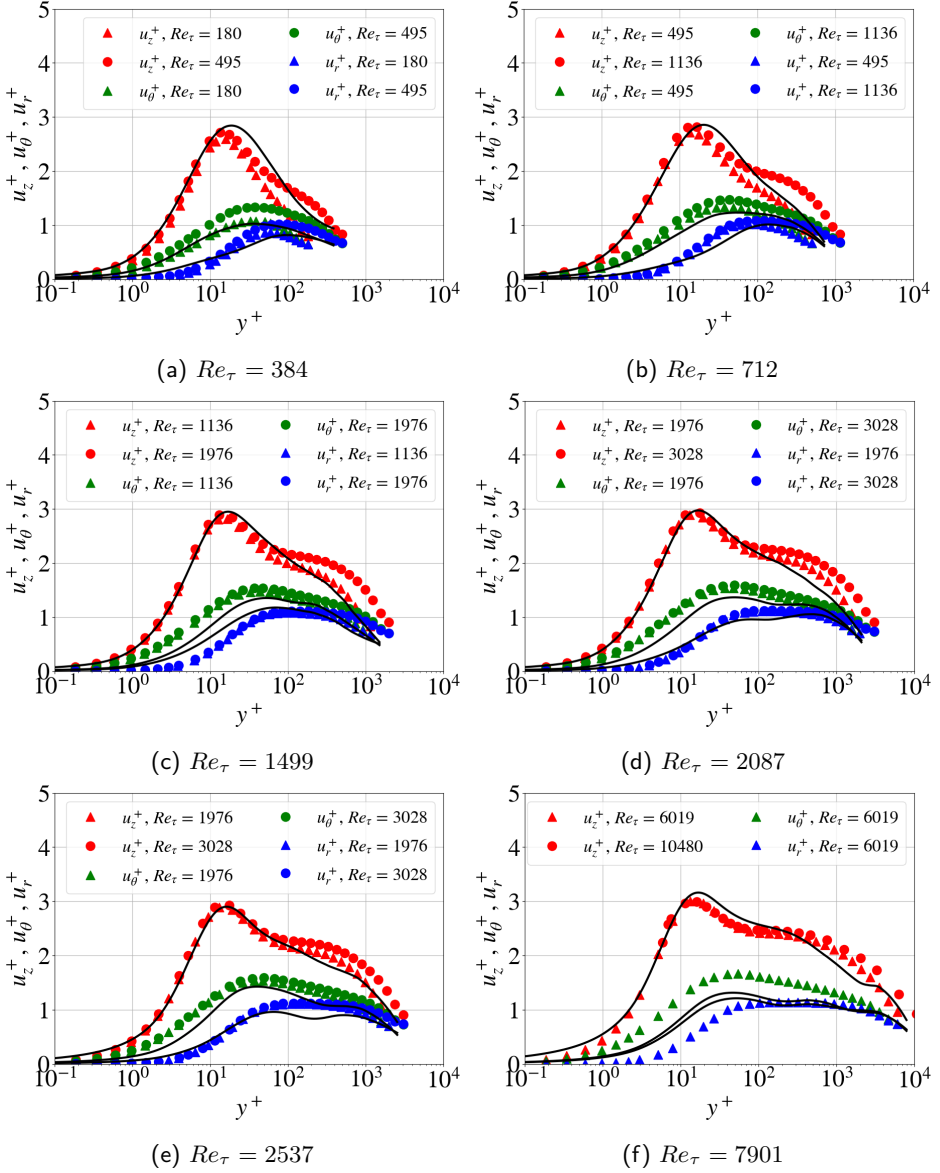


Figure 5.6.: Profiles of normal Reynolds stress tensor components for all six precursor cases.

Prediction of streamwise velocity fluctuation is very consistent with experiments, up to the distance  $y^+ \approx 100$ , which is a scale surprisingly uniform for all the cases. In spite of the strong geometric anisotropy of the cells in the vicinity of the wall, quality of the numerical prediction remains high and all the local extremes in the data are congruently met. However, past this point, deviations in the profiles in relation to the experimental database are noted, and streamwise fluctuations tend to undershoot the expected values for the cases where  $Re_\tau \geq 1499$ . This effect remains more pronounced as the  $Re$  gets higher. Spanwise and wall-normal fluctuation components show a rather interesting behaviour, where the wall normal component slightly overshoots, and spanwise component undershoots the data-set. This behaviour remains persistent with the increased wall distance, albeit tending to the correctly predicted, nearly isotropic state in the centre of the pipe. Note that for the last data-set,  $Re_\tau = 7901$ , two neighbouring sets of DNS were available only for the streamwise fluctuation component.

Profiles of turbulent kinetic energy are shown in Figure 5.7. It can be stated that the overall prediction remains good in all the observed cases, with correctly predicted position, and intensity of near-wall peaks. For the lower range of  $Re_\tau = 384 \div 712$ , predicted profiles fall into the experimental range, whereas for higher  $Re$ , there is a slight undershoot past the wall distance of  $y^+ \approx 100$ . As expected, this behaviour correlates with already mentioned deviations in Reynolds stress tensor components. Dashed lines represent the modeled part of the turbulent kinetic energy, governed by the background SMC model. Near the wall, modeled spectrum accounts from 25% to 55% of total turbulence. However, further away from the wall, residual turbulence vanishes almost completely, which seems to be the main reason for the demonstrated undershoots of the profiles on higher  $Re$ .

In Figure 5.8 (left), ratio between the characteristic mesh scale  $\Delta_{max}$ , and the Kolmogorov micro-scale ( $\eta$ ) is shown for all cases. Here, the maximum distance between the nodal points in streamwise direction is taken as a representative mesh scale, due to the anisotropy of the grid. At low  $Re$ , mesh resolution falls close to the criterion for the LES-required resolution, as proposed in Pope (2000). However, for higher  $Re$ , this ratio increases, being in the range  $25 \div 450$ . For the simulations in the following Chapters, this will mean that the substantial savings in the mesh size and resolution can be achieved by using the IIS-RSM in place of the LES frameworks, which would require a more dense resolution. As will be seen in Chapter 7, mesh size could be reduced by a roughly factor of 10, while keeping the accuracy of prediction. In Figure 5.8 (right), ratios of modeled-to-total turbulence kinetic energy have been plotted for every case. Since the mesh scale doesn't fall close to the Kolmogorov scale, whole spectrum is not sufficiently resolved at higher  $Re$ , although the modeled turbulence gets completely (nonphysically) dissipated through the action of  $P_{\Delta U}$  term. In the range of largest  $Re_\tau$ , modeled terms in the core zone beyond  $(1 - r)/R = 0.3 \div 0.5$  fall well below 1%, whereas all the profiles show a remarkably similar decrease in modeled energy, which seems to be less dependent on the used meshing resolution and  $Re$ .

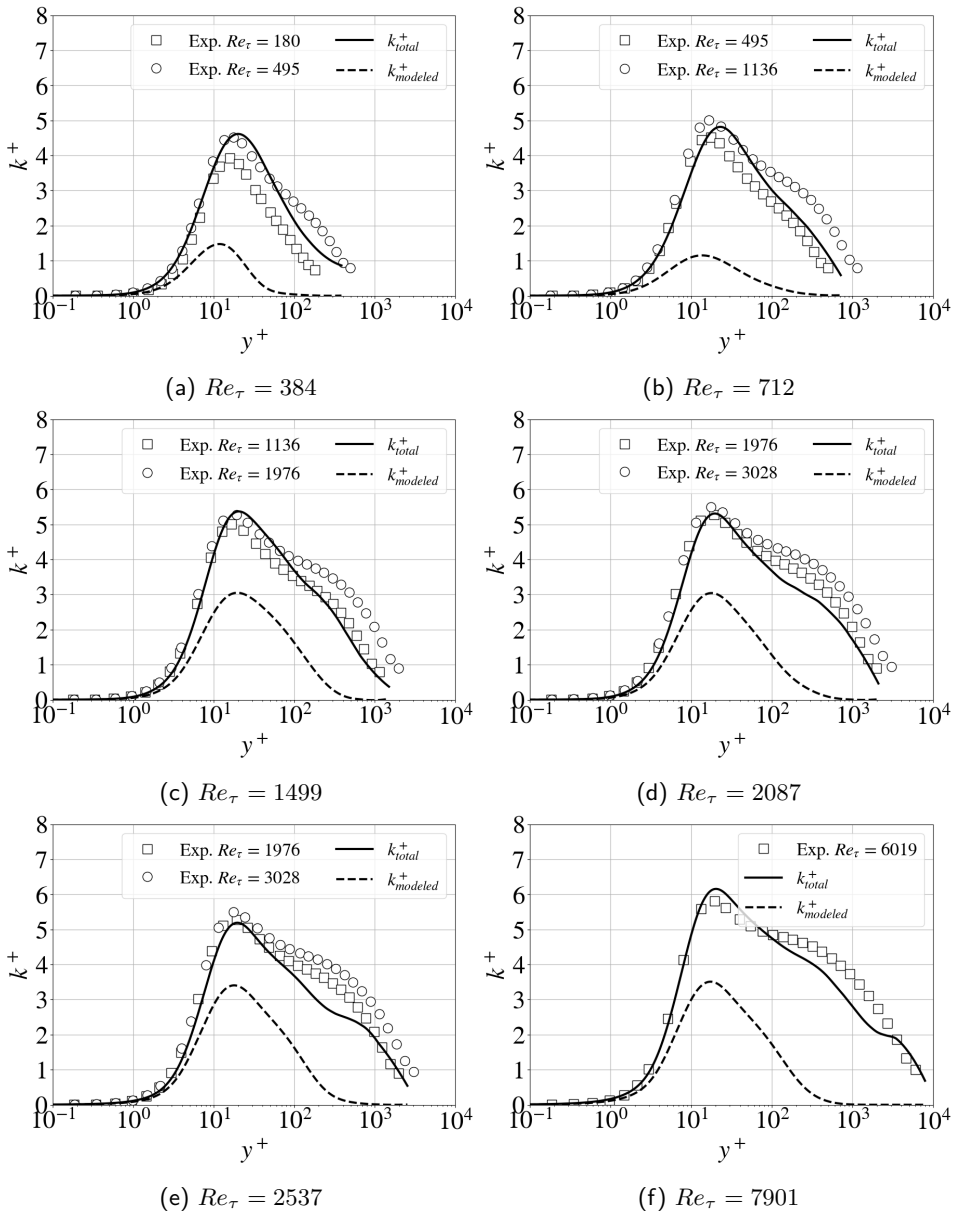


Figure 5.7.: Profiles of turbulent kinetic energy for all six precursor cases. Dashed lines indicate the modeled turbulence kinetic energy.

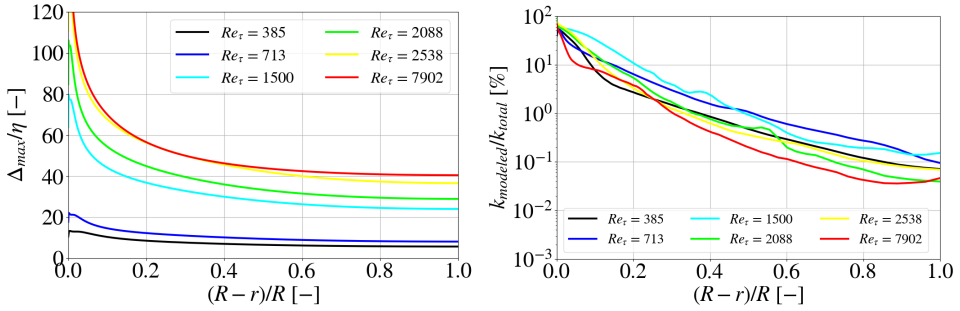


Figure 5.8.: Profiles of maximum cell size, compared with Kolmogorov length scale (left), and profiles of modeled turbulence kinetic energy ratio (right).

Retention of modeled turbulence in the solution is jeopardized by two independent mechanisms. First, by the very formulation of the background turbulence model, there is no guarantee that the divergence of Reynolds stress tensor will be diffusive in nature (as is the case for eddy-viscosity based models), allowing for the back-scattering. This means that the unidirectional flow of energy from resolved to unresolved scales is not ensured. Second, although the proper safeguard in form of  $\sqrt{k}$  from the equation 3.66 should theoretically balance-out the modeled and resolved turbulence, it seems that once the eddy-resolving capability is triggered through the action of  $P_{\Delta U}$ , inherent instability of the model (augmented through the action of six independent turbulence variables) pushes the resolution towards the *coarse* DNS state in the free-stream regions of the flow. Finally, energy equilibrium is established with modeled turbulence being negligible far away from the wall. This behaviour is nonetheless in full congruence with the mathematical definition of the model, since no limit on the dissipation of modeled quantities is explicitly set.

An interesting concept for improving of the SAS model in terms of limiting the over-resolution behaviour according to the implicit mesh limit can be found in the works of Yue et al. (2018), who reformulated a standard DES  $k - \omega - SST$  model by readapting the dissipation term in the evolution equation for  $k$ :

$$\frac{Dk}{Dt} = \dots - F_{DES}k\omega \quad (5.3)$$

where  $F_{DES}$  is a function that explicitly increases the dissipation of the modeled quantities if the mesh is sufficiently resolved:

$$F_{DES} = \max \left\{ \frac{L_t}{C_{DES}\Delta}, 1.0 \right\} \quad (5.4)$$

with  $L_t$  being the turbulence length scale,  $\Delta$  the characteristic mesh length scale, and  $C_{DES}$  the calibration constant. Hence, as long as the turbulent length scale is greater than the mesh length scale, turbulence remains underresolved and



the diffusivity of the model is reduced by artificially increasing the dissipation, which is the approach already discussed in Chapter 3. As an improvement, and to avoid explicit grid dependence, characteristic mesh scale is substituted with the Von Karman length scale  $L_{vk}$ , thus creating a so called Improved-Scale-Adaptive-Simulation paradigm (ISAS):

$$F_{ISAS} = \max \left\{ \frac{L_t}{C_{ISAS} L_{vk}}, 1.0 \right\} \quad (5.5)$$

By applying this procedure, IIS-RSM acquires three distinct advantages. First, it will retain the capability to accurately operate on coarse meshes. Second, it will still allow the implicit capturing of mesh size variability. Lastly,  $\max$  function should automatically prohibit any over-resolution of the mesh. It is to be expected that such a model will be more diffusive on coarse grids than IIS-RSM. Modification of the dissipation term in the transport equation for the Reynolds stress tensor 3.39 follows naturally, like:

$$\frac{DR_{ij}}{Dt} = \dots - F_{ISAS} \varepsilon_{ij}^h \quad (5.6)$$

## 5.2. Conclusions

In this chapter, IIS-RSM was tested in a periodic pipe geometry, using six test-cases spanning the wide range of Reynolds numbers. As a result, precursor database is obtained, which will be used in following Chapters. A mesh-optimization process, based on the prediction of wall shear stress, provided an *ad-hoc* estimate for the required mesh resolution for the upcoming simulations. Based on the results from all six studies, it was concluded that the mean velocity profiles, as well as the profiles of velocity fluctuations showed a good level of congruence with the available experimental data, especially in the near wall zone, proving the applicability of the model. A rather puzzling behaviour is spotted for all tested  $Re$ , where the modeled turbulence vanishes almost completely in the free-stream zone. Although the mathematical formulation of the model should theoretically prohibit such a behavior, levels of modeled turbulence remained very low. This ultimately leads to the reduced intensity of turbulence in the zones further away from the wall, which is specially pronounced at higher  $Re$ . Despite that, near-wall behaviour is predicted very accurately.



## 6. Flow configuration II: Turbulent thermal mixing in a T-Junction

---

In this Chapter, applicability of IIS-RSM will be tested in simulating turbulent thermal mixing of two fluid streams, in an industrially-relevant case involving the T-Junction geometry. T-Junctions represent pipework components in which two fluid streams, usually with different temperatures/solvent concentrations are dynamically mixed in its outlet section. They are used over the wide range of industries, in nuclear- and thermal power plants, processing industries, air-conditioning and many more. In the following, motivation for application of eddy-resolving models in simulating T-Junction cases is discussed.

Namely, in spite of the very simple geometry involved, T-junction related flow topology is characterized with a highly three dimensional nature, with large-scale top-level transients in the flow field, and high anisotropy of turbulence. Concerning the mixing of two streams with different temperatures, random fluctuations of temperature field, combined with the existence of noted large-scale transients lead to the very serious problem from the standpoint of structural integrity of the pipe. Namely, thermal pulsations are diffused (and partially damped) through the viscous sublayer and ultimately transferred to the surrounding wall structure. A periodically changing temperature field establishes in the wall material, leading to the propagation of small cracks. Ultimately, structural failure of the wall may occur due to the thermally-induced high-cycle fatigue. Described process is known as *thermal stripping*, and caused several notable incidents in the nuclear industry, of which a good overview can be found in Jungclaus et al. (1998). One of the especially consequential accidents, related to the phenomena of thermal stripping, represents a leakage in the pipework of residual heat removal system of French PWR Civaux 1 nuclear power plant in 1999, resulting in the loss of coolant (Metzner and Wilke (2005)).

Next to the amplitude of thermally induced stresses, propagation of thermal stripping phenomena is also tightly related to their frequency content. Chapuliot et al. (2005) performed an analysis involving the analytical model of fracture growth under a periodically changing temperature field, and concluded that the low frequency pulsations at  $f < 10 [Hz]$  lead to the highest variation in stresses, hence carrying the greatest risk for the propagation of thermal stripping.

In line with the industrial relevance of thermal stripping in T-Junctions, research community featured numerous experimental and numerical publications, with aim of documenting the most important flow features and validating the numerical models. A non-exhaustive list of dominantly cited experimental test-cases involves:

1. T-Junction experiment, carried out by Vattenfall Research and Development AB in 2006 at the Älvkarleby laboratory, reported by Westin et al. (2006). Both pipes were held at  $Re \approx 195,000$ , with a temperature difference of  $15 [^{\circ}\text{C}]$  between the streams. Measured data included first- and second-order statistics of temperature field on the outer walls.
2. Braillard (2008) reported an experimental case named FATHERINO for studying thermal reaction in the solid wall structure of the T-junction. Maximum temperature difference of  $75 [^{\circ}\text{C}]$  could be imposed between the streams, whereas the Reynolds number based on the maximum flow rate was:  $Re = 270,000$ . Measured data included the statistical properties of temperature fluctuations on the outer walls.
3. Another experimental test-case performed at Vattenfall Research and Development Laboratory at Älvkarleby was published in Smith et al. (2011). Reported temperature difference was  $17 [^{\circ}\text{C}]$ , and the Reynolds numbers in main-, and branch pipe were  $Re = 100,000$  and  $Re = 80,000$ , respectively. Mean- and RMS data for temperature and velocity fields were reported.
4. Zboray et al. (2007), and Walker et al. (2009) reported a series of experimental measurements of turbulent mixing in a T-Junction, involving both isothermal, and thermal conditions at the Laboratory for Nuclear Energy Systems, Institute for Energy Technology, ETHZ, Zürich, Switzerland. Next to the rich database involving spatial measurements of both velocity and temperature fluctuations, spectral properties of the mixing process were also reported. Maximum Reynolds number was  $Re = 43,860$ .
5. Kamide et al. (2009) conducted a thermal mixing experiment named WATLON at Japan Atomic Energy Agency. While holding the branch mass flow constant, main pipe flow was varied in order to establish a database involving several distinct flow configurations. Temperature difference between streams was held at  $15 [^{\circ}\text{C}]$ , and maximum Reynolds number, reached in the main pipe, was  $Re = 380,000$ . Detailed measurements of temperature and velocity field statistics, along the spectral analysis of temperature fluctuations were reported.
6. Zhou et al. (2018) performed series of experiments at the Fluid-Structure-Interaction (FSI) test facility at the University of Stuttgart, with a goal of investigating thermal fatigue in the mixing zone of the horizontal T-junction. Temperature difference of  $260 [^{\circ}\text{C}]$  was imposed between two streams, whereas

---

the maximum Reynolds number in the main pipe reached  $Re = 78,400$ . Measurements included the distribution of mean and RMS temperature for various momentum ratios between streams.

Summarising the conclusions outlined in the noted experimental publications, it can be stated that the dynamics of the mixing process in a T-Junction is mainly governed by the inflow momentum distribution between the streams. Dominance in the main stream momentum leads to the formation of wall-bounded recirculation zones, involving high velocity and temperature gradients, coupled with a spatially limited regions of high-intensity temperature fluctuations. Poor mixing at the edge of recirculation zones produces a thin shear layer with high levels of anisotropy. Instabilities of the shear layer affect the spectral content of the turbulent mixing, introducing a top-level transients into the system, which cannot be attenuated by the wall structure, and who play dominant role in its degradation. Visualisation of typical such an instability is given in Figure 6.1.

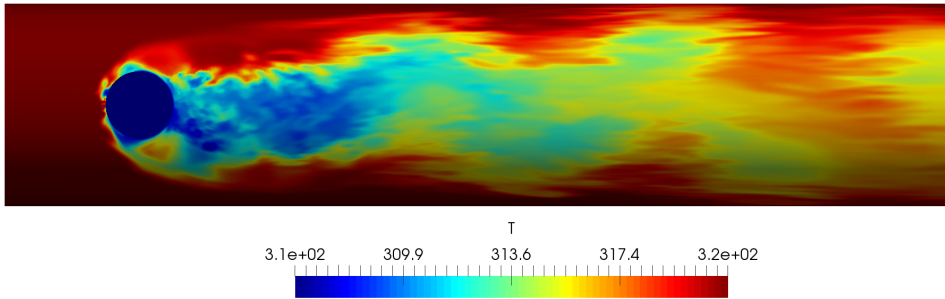


Figure 6.1.: Instantaneous temperature contours on the inner wall surface: Influence of shear-layer, Kelvin–Helmholtz instabilities on the mixing process.

Over the past two decades, multiple numerical studies, dominantly referring to the previously described T-Junction experiments have been published. Concerning the RANS framework, its performance was evaluated to be very poor in predicting even the first order statistics in various T-Junction cases, irrespective of the used experimental reference. A good overview of typical RANS results can be found in Frank et al. (2010), who used  $k - \omega - SST$ , as well as in Walker et al. (2010), who cross-compared the performance of the  $k - \varepsilon$ ,  $k - \omega - SST$  and BSL Reynolds stress model. Next to the problem in convergence and oversized mesh, notable mismatches and over/under predictions were present in the data. Although Kok and Van der Wal (1996) proposed an artificial increase of turbulent mixing through increase in Prandtl/Schmidt number as an effective remedy to increase the accuracy of simulation, this solution remains non-genuine and thus not generally applicable. It is the general opinion within the research community that RANS methods don't represent an applicable strategy for capturing T-Junction mixing phenomena.

So far, greatest popularity in predicting the wide range of T-Junction related experiments resides within the LES methods, with numerous publications, exemplary: Sakowitz et al. (2014), Selvam et al. (2015), R. Tunstall et al. (2016b), Evrim and Laurien (2020) and Zhou et al. (2022). A very detailed performance comparison of several different turbulence models is summarised in Smith et al. (2013), where the results from 29 different research groups (including variations of LES, DDES and SAS-SST methods) were cross-compared against the experimental reference of Vattenfall T-junction test rig, reported in Smith et al. (2011). Most reported meshes fall in the range of 1 to 5 Million cells, with maximum in 70 Million cells. A clear trend can be spotted in the reported study. Namely, LES methods with a highly resolved mesh dominantly outperformed other methods ((D)DES,RANS,SAS-SST) in matching the experimental data. SAS-SST showed some notable deficiencies which will be discussed further on. Several publications e.g. Tanaka et al. (2010) and Kim and Jeong (2012), offered a very coarse mesh estimate in the range up to 1 Million cells, in spite of the high Reynolds number of the flow. Although the mean fields and transient response of the system were reconstructed within the acceptable tolerance even with usage of coarse meshes, RMS values of both velocity and temperature fields were seriously over/underpredicted, especially in the vicinity of the walls. This underperformance was largely attributed to the usage of wall functions. Jayaraju et al. (2010) as well as R. Tunstall et al. (2016a) explored the application of wall-functions in LES studies for thermal fatigue problems. Both studies demonstrated that their usage leads to the inaccuracies in predicting second order statistics. A general conclusion concerning the LES methods is that the excessive computing results are still required, even at modest Reynolds numbers, in order to achieve desired accuracy in results. Question of industrial applicability of LES methods in the cases involving thermal mixing and thermal fatigue problems remains open.

Scale-adaptive methodologies remain among the least used with the T-Junction related problems. A general trend, spotted in the numerical publications, is that the used SAS-SST method is either too inaccurate (Smith et al. (2013)), or that it was very diffusive and prone to destruction of resolved turbulence if the dispersive CD scheme is not used (Gritskevich et al. (2014)). Natural question that arises is why the SAS methodology will be tested a new, since its performance was demonstrated as bad?

To the authors best knowledge, a two equation  $k-\omega-SST-SAS$  by Egorov and Menter (2008) was the only SAS model tested so far. Since it has only two equations, it is less likely that any small perturbation will push the model towards the resolved state as in by IIS-RSM. Also, since the production of turbulent kinetic energy in SAS-SST model can only be positive by definition, no back-scattering may occur and perturbations in the modeled turbulence cannot protrude the resolved part so easily. Ultimately, this leads to the overall greater diffusivity of the model. Additionally, original version of the model, proposed by Egorov and Menter (2008) imposes a further limitation on the turbulent viscosity, dictated by the WALE model.

In this version, mesh length scale  $\Delta$  is explicitly given. In this way, the original *grid-free* formulation vanishes, thus losing the very important asset of the model. Finally, since the steady-state inlets are used in both cases, it is questionable whether the intermediate zone between the resolved and fully modeled flow offers enough spatial separation, as to allow the second derivative to trigger the resolution capability adequately. It is within the scope of this Chapter to test the IIS-RSM on the specific experimental test case and to fill the knowledge gap in relation to the performance of scale-adaptive methods.

For this reason, already mentioned WATLON experimental test-case, reported by Kamide et al. (2009) will be used. Next to the very detailed documentation of mean-, RMS- as well as temporal properties of the flow, high Reynolds number should offer an industrial asset in substantial computational resource savings. In the WATLON experiment, T-Junction configuration with 3:1 diameter ratio was subjected to the varying flow rates in the main pipe, whereas the flow rate in the branch pipe was held constant. Main pipe diameter is set to  $D_m = 150$  [mm], and the branch pipe diameter to  $D_b = 50$  [mm]. Temperature difference between streams is also held constant, at 15 [°C]. In dependence on the momentum differences between the streams, several distinct flow topologies were obtained. They were named based on the most dominant mixing pattern as: Wall jet (W-Ref), Impinging jet (I-Ref) and Deflecting jet (D-ref). Intermediate states between these three configurations are also reported. In this thesis, only two first characteristic configurations will be reproduced numerically. In Figure 6.2, mixing process in cases W-Ref (left), as well as I-Ref (right) is visualized, with dyed branch flow. Distinct mixing patterns can be spotted in the outlet zone in both configurations. Overview of the experimental conditions for both cases is given in Table 6.1.

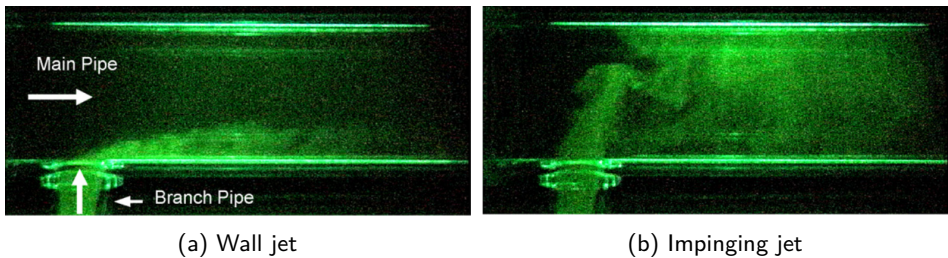


Figure 6.2.: Visualisation of the mixing patterns in two discussed test cases in WATLON experiment.

Schematics of the computational domain with geometrical details is given in Figure 6.3. Lengths of both inlet pipes were set as to position the mixing zone far enough from the inflow boundaries. In order to avoid already mentioned problems with SAS methodology and steady-state inlet treatment, fully developed, three dimensional turbulence was directly mapped from the parallel running precursor

simulations, outlined in Chapter 5 (see cases:  $Re_\tau = 1499$ ,  $Re_\tau = 2087$  and  $Re_\tau = 7901$ ). Contours of the instantaneous velocity in the precursor simulations were shown close to the inflow boundary on which they are mapped, in order to emphasise the resolution obtained at both inlets. Detail showing the mesh quality in the mixing zone is also shown below.

Table 6.1.: Inflow conditions for WATLON experiment.

Case	W-Ref	I-Ref
Main pipe Reynolds number [-]	380,000	59,862
Branch pipe Reynolds number [-]	86,757	86,757
Main pipe average velocity [ $m/s$ ]	1.46	0.23
Branch pipe average velocity [ $m/s$ ]	1.0	1.0
Main pipe temperature [ $^{\circ}C$ ]	48	48
Branch pipe temperature [ $^{\circ}C$ ]	33	33

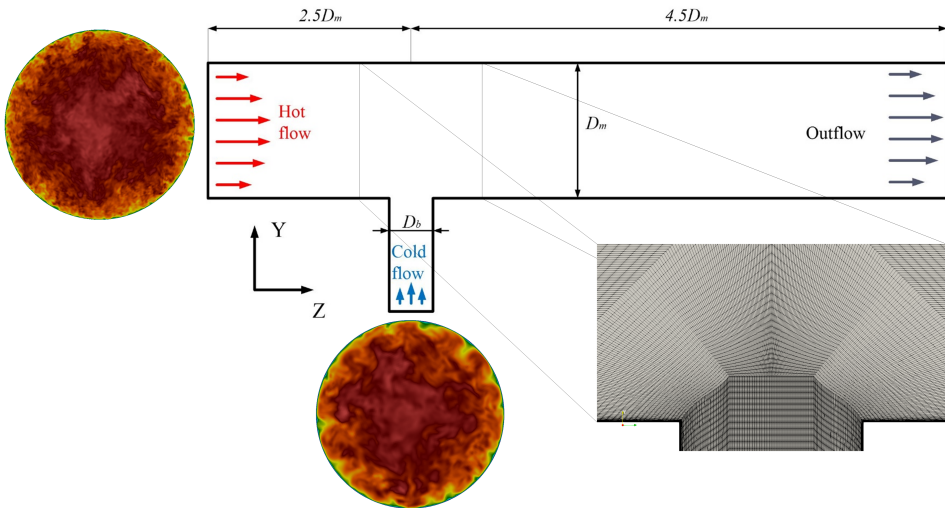


Figure 6.3.: Schematics of the computational domain used for reproducing WATLON experiment. Origin is shown in offset to its real position.

Concerning the meshing strategy, multi-block structured hexahedral strategy was inherited from Chapter 5, due to the geometrical simplicity of the domain and due to the optimal tradeoff between accuracy and mesh size. Same mesh will be applied in both cases. Identical resolution in radial and circumferential direction was applied as in the Chapter 5 for  $Re_\tau = 7901$  ( $\Delta r^+ = 1 \div 100$ ,  $\Delta \theta^+ = 100$ ). Close to the



---

main inflow, axial resolution is also the same ( $\Delta z^+ = 300$ ). By approaching the mixing zone, cells are gradually refined in axial direction and are nearly isotropic close to the origin (located at the intersection of pipe axes). Downstream of the origin, cells are again elongated accordingly. Mesh in the branch pipe is of identical shape, just three times downscaled in cell size. Total number of cells was close to 17 million. Additionally, temperature evolution was reproduced using the equation 3.70. Adiabatic boundary conditions were set at the walls, with constant, prescribed values at inflow boundaries. Simulations were run till the mean and RMS contours of all quantities showed convergence. Sub-grid energy fluxes were calculated using both SGDH and GGDH approach, as outlined in Chapter 3.

## 6.1. Wall jet case

Magnitude of the instantaneous velocity field is visualized in Figure 6.4. Fully developed turbulence, initially mapped at both inflow boundaries, sustains its quality  $\approx 1D_m$  behind the main-, and  $\approx 2D_b$  behind the branch inlet. This indicates that the mixing zone is positioned far enough from the domain boundaries. Due to the presence of highly isotropic cells in the interconnection zone, very detailed flow structures can be resolved. Further away from the mixing region, elongation of cells in the flow direction forces the model to become more dissipative. Hence, the lower resolution near the outflow boundary is obtained. As a result of the steadily advected fine flow structures, originating from the mixing, dissipation mechanisms can not eliminate resolved eddies, and partially resolved structures persist in the flow down to the outlet. Flow rate of the main stream significantly supersedes the flow rate of the branch stream, which is unable to penetrate deeply into the mixing zone. Instead, it exhibits the separation on the trailing edge of the T-junction and creates a recirculating, low velocity wake that is advected in the vicinity of the lower wall. Limited separation zone can also be spotted on the leading edge of the junction. Separation bubble acts as an obstacle towards the main flow, effectively reducing the cross-section, which produces the local acceleration of the flow above it.

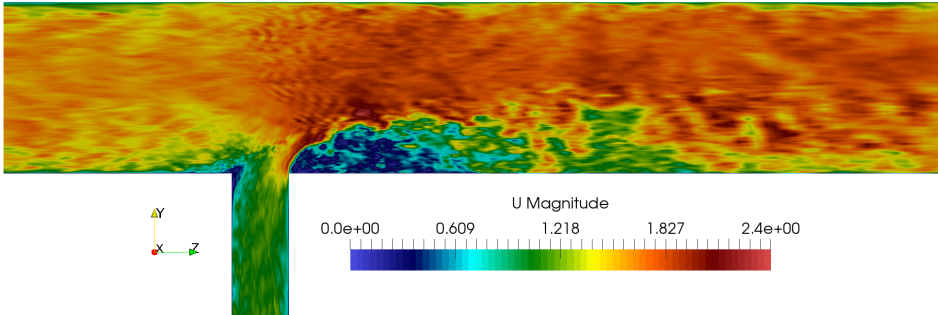


Figure 6.4.: Contours of instantaneous velocity field, W-Ref case.

Contours of instantaneous kinematic pressure ( $p/\rho$ ) are given in Figure 6.5. Due to the incompressible nature of the flow, pressure directly correlates with the velocity field. Reference, zero-pressure plane is positioned on the domain outlet as a boundary condition. Downstream of the trailing edge, several large-scale coherent structures, characterized with low pressure points can be found. These suction zones originate from the energetic, strongly rotating eddies which are produced adjacently to the edge of the separation bubble. They are however readily dissipated by the flow and do not survive past the length of the separation bubble. Aforementioned separation of the leading edge can be attributed to the high pressure zone, indicating the strong deceleration of the flow due to the bending.

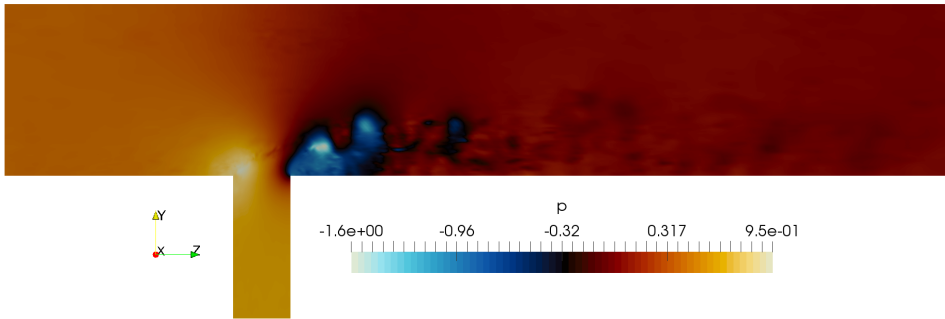


Figure 6.5.: Contours of instantaneous kinematic pressure field, W-Ref case.

An interesting, model-related feature can be spotted by inspecting the mean velocity field in Figure 6.6, where the separation bubble exhibits a so-called back-bending behaviour of the mean dividing stream-line, violating the smooth, spherical contour of the mixing zone. This deviation can be attributed to the pressure-redistribution term  $\Phi_{ij}$ , (equations 3.34 to 3.37), indicating the prevalence of the modeled portion of the spectrum close to the wall.

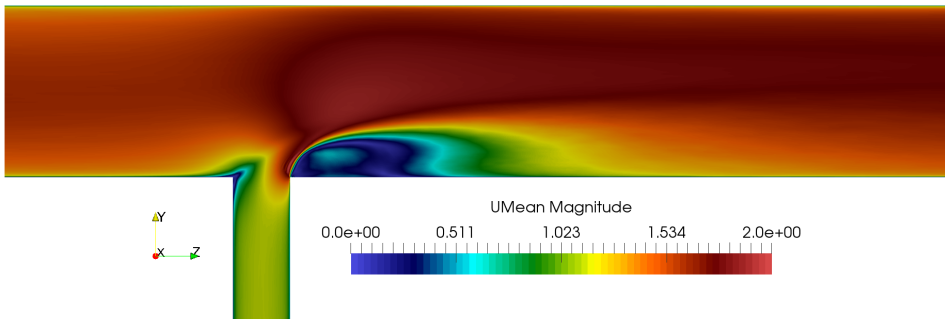


Figure 6.6.: Contours of mean velocity field, W-Ref case.

Further insight into the quality of the mixing process can be found by inspecting the contours of instantaneous- and mean temperature field, in Figures 6.7 and 6.8. Following the sharp bending of the branch stream, most of the velocity fluctuations normal to the dividing streamline are suppressed. Since the main flow is locally accelerated in the upper portion of the junction, it advects the mixing wake adjacently to the lower wall, all the way to the outlet, with very poor mixing outside of the separation bubble.

Next to the inspection of the mean-field statistics, distribution and intensity of temperature field variance needs to be investigated in more detail due to its direct correlation with the progression of thermal stripping phenomena. Contours of the

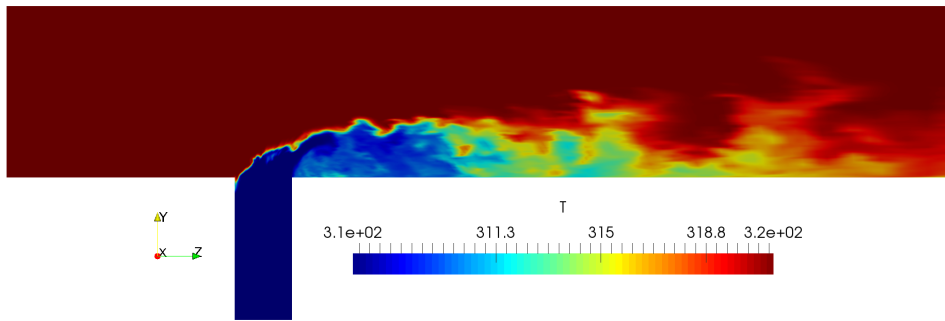


Figure 6.7.: Contours of instantaneous temperature field, W-Ref case.

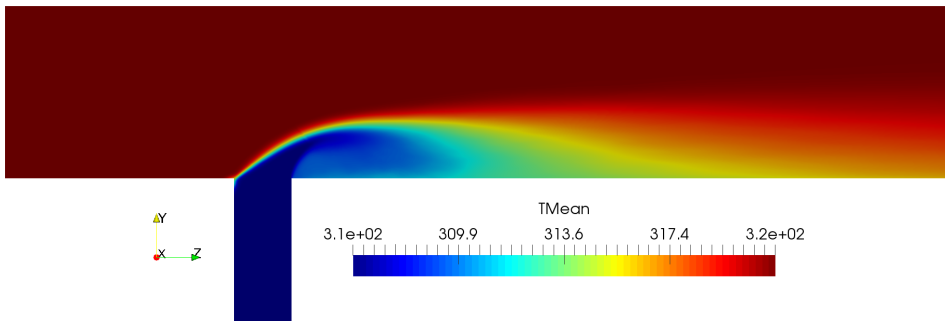


Figure 6.8.: Contours of mean temperature field, W-Ref case.

RMS temperature field are shown in Figure 6.9. It can be seen that the zone of pronounced amplitude of the temperature field coincided perfectly with the edge of the mixing wake between the separation bubble and the main stream. Spatially limited spikes RMS temperature reach approximately 40% of the total temperature difference. Overall maximum in variance is located at the leading edge of the junction. Following the shear layer contour, fluctuation intensity gets more diffused downstream. Since the mixing wake is attained in the vicinity of the solid structure, contours of RMS temperature are also shown at the lower wall in Figure 6.10. From the standpoint of variance maximum, two zones in pronounced danger from thermal stripping are identified. First, the complete leading edge zone experiences the RMS fluctuations in range  $\approx 30\%$  of the total temperature difference. This zone is particularly endangered not only from the high amplitudes of temperature, but also due to the structural degradation in the vicinity of the welded zone.

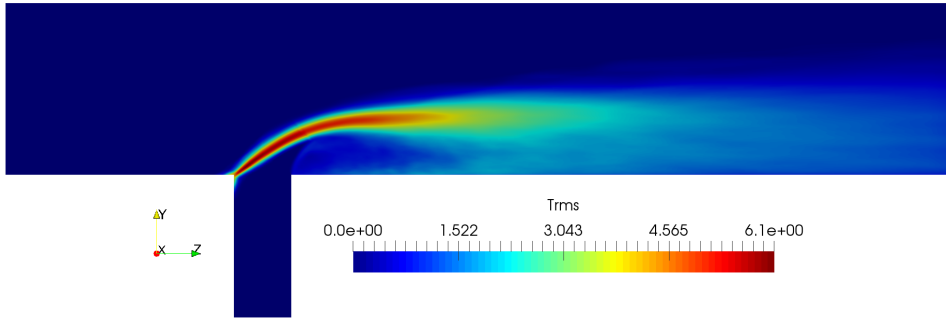


Figure 6.9.: Contours of RMS temperature, W-Ref case.

Namely, in case the T-Junction is fabricated by welding the pipes edges, heat affected zones (HAZ) are especially prone to crack propagation due to the thermocyclic degradation mechanisms, as demonstrated in Sbitti and Taheri (2010). Second, two symmetric, high RMS belts are identified, stretching far beyond the separation bubble length. As will be demonstrated, these characteristic regions are directly correlated with the zone encapsulating the Kelvin-Helholmtz instability, which develops in the shear layer at the edge of separation bubble (see Figure 6.1). Periodic switching of mixing structures produces high amplitudes of temperature field.

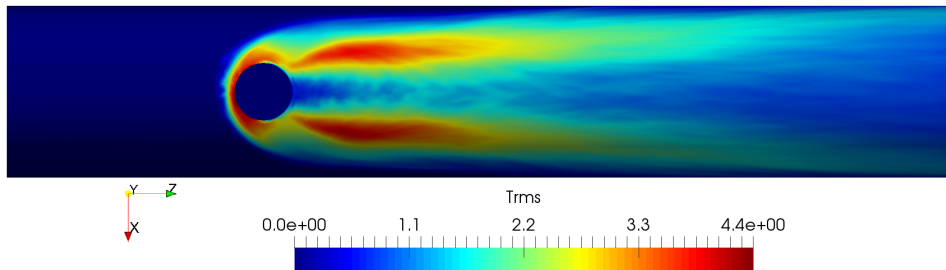


Figure 6.10.: Contours of RMS temperature on the lower wall, W-Ref case.

Comparison of obtained results with the experimental reference is performed on two vertical lines, positioned at  $z = 0.5D_m$  and at  $z = 1D_m$ , downstream of the junction center. In Figure 6.11, image matrix involving the validation of calculated temperature field is given. Top row refers to the position  $z = 0.5D_m$ , and the bottom row to the position  $z = 1D_m$ . Left column refers to the mean values of dimensionless temperature  $T^* = T - T_{min}/(T_{max} - T_{min})$ , whereas the right column refers to the dimensionless RMS temperature  $T_{RMS}^* = T_{RMS}/(T_{max} - T_{min})$ . As can be

seen, almost perfect match is obtained not only for mean values, but also for RMS distribution, which is a significant shift forward concerning the (relatively) coarse resolution for this class of Reynolds numbers. Size and temperature distribution in- and outside of the separation bubble are adequately predicted. Intensity of the fluctuations in the shear layer and at the wall are predicted with a high level of accuracy as well.

Presented results were produced using the SGDH hypothesis, as outlined in Chapter 3. Results obtained with GGDH approach gave almost identical results as SGDH, in terms of the first- and second-order statistical moment of temperature field. This behaviour is most likely caused by the strong, resolved transients in the separation bubble, which seem to account for the most of the variance content. Based on that, differences in performance between GGDH and SGDH could not be precisely determined. In Chapter 7, strong transients are also present. Therefore, SGDH will be used henceforth due to the fact that it guarantees the diffusivity of the thermal energy.

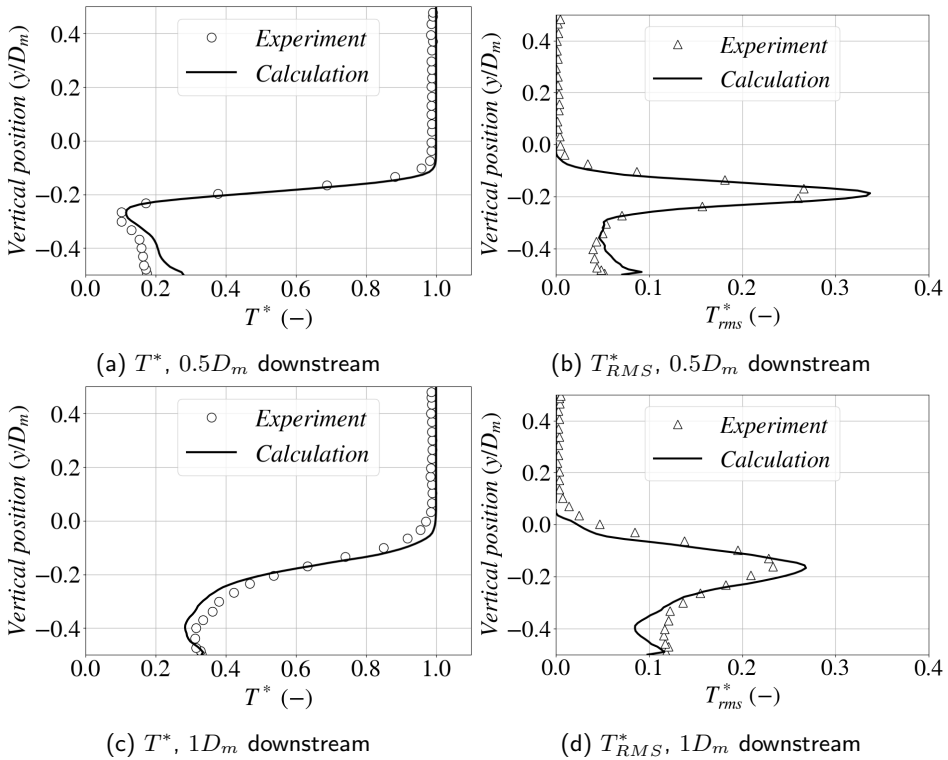


Figure 6.11.: Profiles of the first- and second order statistics for the temperature field.

Previous analysis is repeated for the velocity field as well. Comparison of the results is shown in Figure 6.12. Identical configuration involving spatial position and statistical comparison is retained as in Figure 6.11. Here, quality of prediction is almost identical to the temperature field. Not only do the mean field values coincide almost perfectly with measure data, but the RMS values of the velocity field follow the experimentally obtained values very closely, especially at the edge of the separation bubble. Slight underprediction is made in the free-stream zone, with a repeated match on the upper wall. This is most likely a consequence of the destruction of modeled turbulence in the free stream zone, as discussed in the previous Chapter.

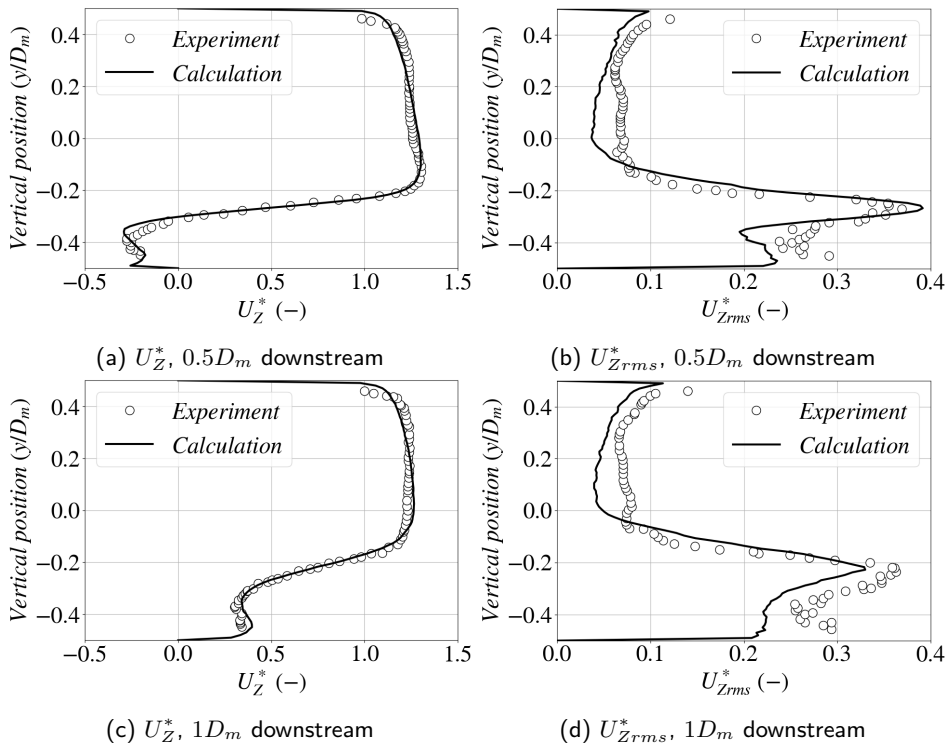


Figure 6.12.: Profiles of the first- and second order statistics for the velocity field.

Qualitative comparison of results is performed in Figure 6.13, where the calculated streamlines of the mean flow are plotted against the experimentally obtained ones. Visually, very good match is obtained, especially from the standpoint of reattachment point, overall dimensions of the separation bubble and the flow topology within.

The only feature which was overlooked by the model was small nested vortex in the vicinity of the separation bubble edge, which is not predicted in the calculation. In spite of this fact, overall prediction can be considered very good.

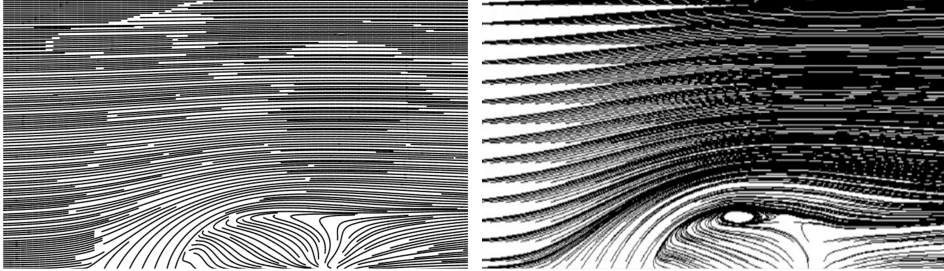


Figure 6.13.: Comparison of mean flow streamlines: calculation (left) and experiment (right).

Anisotropy of the flow, represented through the componentality contours is visualised in Figure 6.14. Most of the turbulence, both in the free stream zone, as well as within the separation bubble can be characterised isotropic and hence highly three dimensional. Zones of increased anisotropy are spotted, as expected adjacently to the walls (predominantly **2C**), as well as in the shear layer zone (**2C**, tending to **1C**), most likely due to the onset of shear layer instabilities which promote strong amplitudes of velocity field in the direction tangentially to the separation bubble surface.

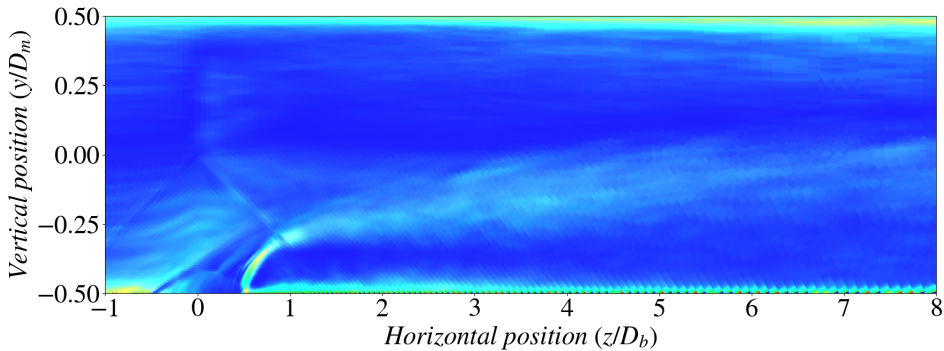


Figure 6.14.: Turbulence anisotropy, visualized using componentality contours.

Phenomena of thermal stripping is not only tightly related to the distribution of temperature field fluctuations, but also to the temporal characteristics of such fluctuations. They can substantially accelerate structural degradation in case of



the highly energetic, low-frequency content. Experimental report by Kamide et al. (2009) shows that in case of the Wall jet configuration, notable attenuation of spectral energy is spotted in the *dangerous* frequency range, below  $10 [Hz]$ , which means that this configuration possesses pronounced risk of component failure due to the thermal stripping. In the experimental reference, frequency characteristics of the mixing structures were obtained using a single point FFT analysis, without correlating the spectral response of the system with the underlying coherent structures. In order to enrich the understanding of interaction between the coherent patterns in the mixing wake and their transient response, POD analysis will be performed.

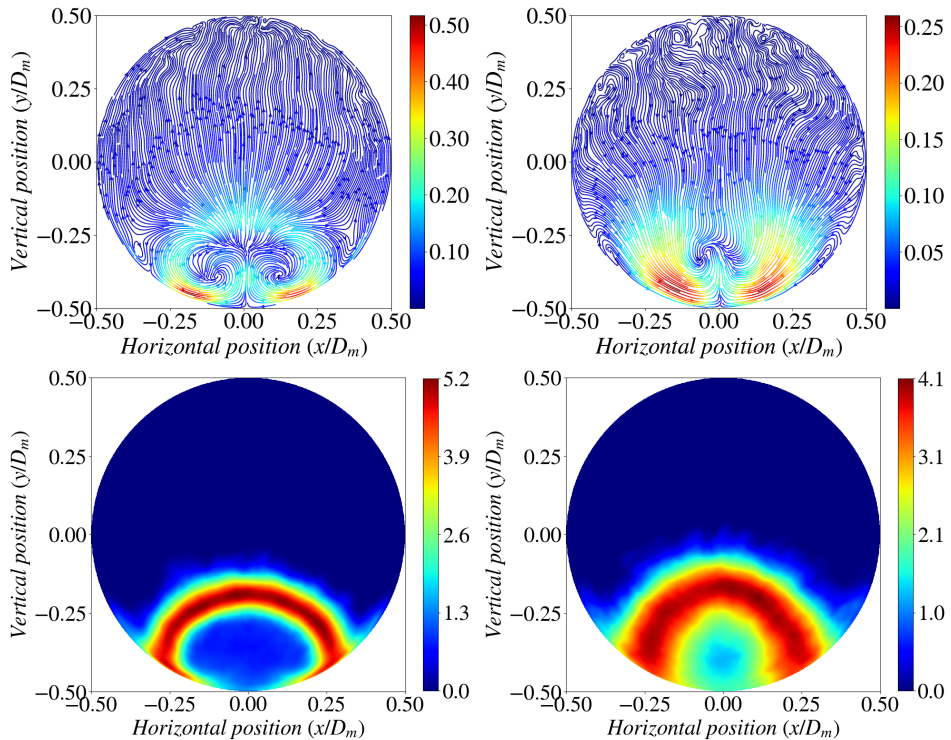


Figure 6.15.: Streamlines of the mean secondary flow (top row) and contours of the  $T_{RMS}$  (bottom row) at locations:  $z = 0.5D_m$  (left column) and  $z = D_m$  (right column).

Downstream location at  $z = 0.5D_m$  was deemed an ideal candidate for the POD analysis, due to the presence of several transient phenomena. In Figure 6.15 flow properties at this point are shown in the cross-section view. Concerning the temperature field, previous statement on the variance distribution is confirmed

and the region of locally high amplitudes of temperature field coincides with the shear layer zone. Second, inside of the separation bubble, distinct pair of so called Dean-eddy vortices is spotted. Origins and dynamics of such secondary flow patterns are discussed in high detail in the next Chapter. At this point, it will be said that the symmetric vortex pair emerges due to the curvature of flow streamlines, inflicted through geometry. It is associated with a so-called switching phenomena, in which the intensity of one vortex supersedes the other. Vortex switching introduces another distinct signal in the spectral signature of the temperature fluctuations, which may affect the thermal stripping. Results of the POD analysis involving the instantaneous velocity field at the downstream position  $z = 0.5D_m$  were given in Figures 6.16 and 6.17.

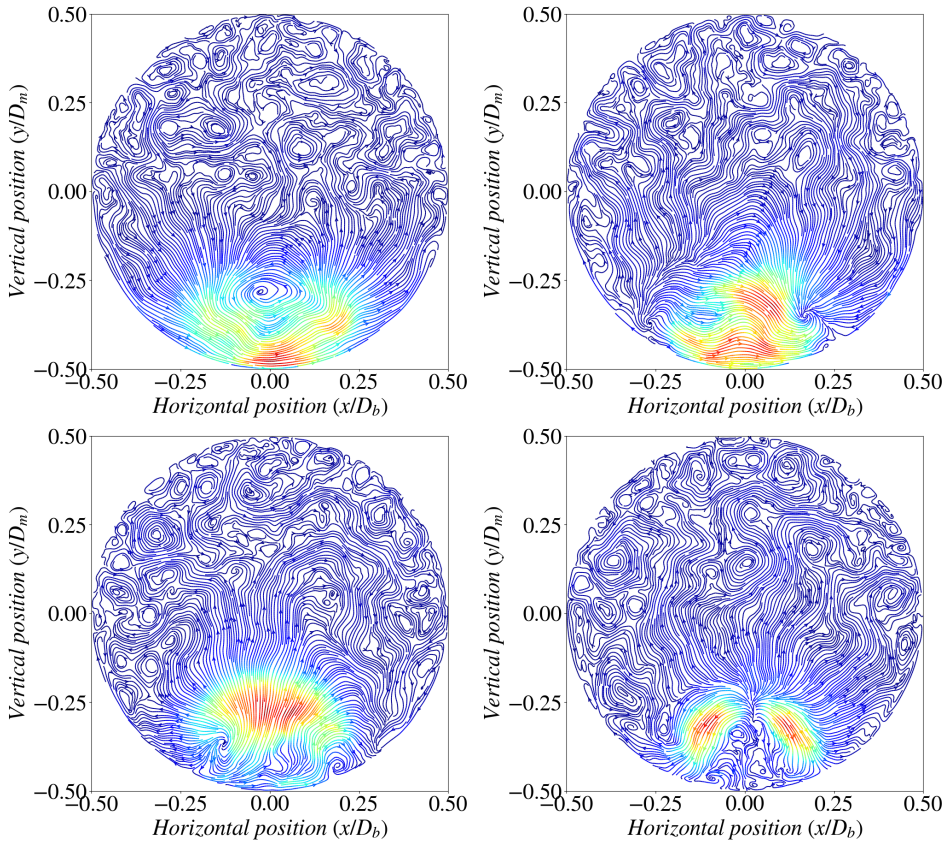


Figure 6.16.: Topology of first 4 POD modes of the velocity field at position  $z = 0.5D_m$ : POD1 (up-left), POD2 (up-right), POD3 (down-left) and POD4 (down-right). No color-bar is shown due to the orthonormal nature of modes.

Cumulative distribution of captured energy per mode, given in 6.17 (left) shows that the first 4 POD Modes contain around 27% of total variance, after which no distinct mode can be identified. Two most energetic modes: (respectively  $\approx 10\%$  and  $\approx 7\%$  of total variance) reveal a strong, horizontally oriented switching motion which is presented in two counter oriented loop patterns. Frequency peaks associated with these two coherent patterns are practically aligned and show strong accumulation of spectral energy at  $St \approx 0.2$ , which is a characteristic frequency of vortex shedding associated with Kelvin-Helmholtz type instabilities, found regularly in the literature (here, the value of Strouhal number is formed based on the mean pipe flow velocity and the branch pipe diameter  $St = fD_b/U_m$ ). Modes 3 and 4 show mostly vertical orientation, aligned with frequency peaks at  $St \approx 0.3$  and  $St \approx 0.5 \div 0.6$ . However, Mode 3 is more widely spread along the edge of separation bubble, whereas the Mode 4 shows two highly symmetrical directions of fluctuation. Mode 3 is therefore most likely associated with another, vertically oriented oscillation harmonic of the shear-layer instability, formed due to the separation of the branch flow at the trailing edge of the junction. Due to the symmetry and spatial limitation of the streamlines which connect two vortex centres, Mode 4 is most likely connected with the already mentioned vortex switching phenomena. Due to the inability of the POD procedure to distinguish between the non-orthogonal phenomena at the same frequency (only the spatially-orthogonal structures can be discriminated, not the spatial-temporally orthogonal structures), both modes share almost identical spectral signature.

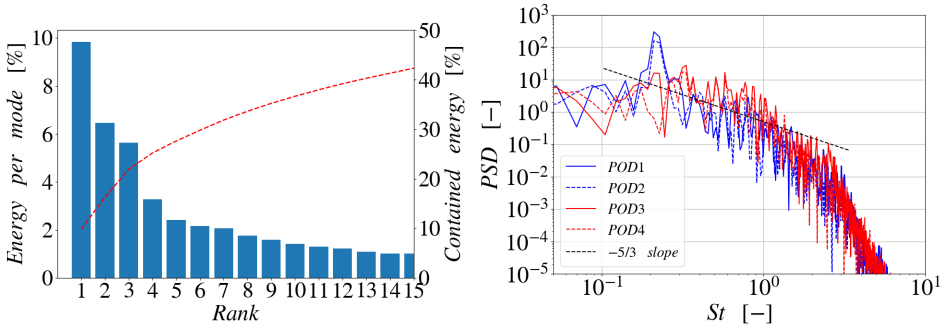


Figure 6.17.: Accumulation of captured variance (left) and FFT analysis of time coefficients (right) for the  $z = 0.5D_m$ .

As will be discussed in the next Chapter, theoretical rationale for determining the characteristic vortex switching frequency, based on the external parameters of the flow (velocity, flow hydraulic diameter etc.) is not yet established. Therefore, based on the spectral distance to the principal switching frequency at  $St \approx 0.2$ , one can deem  $St \approx 0.3$  to be the frequency associated with the vertically oriented pulsation, originating from the flow separation, whereas the frequency  $St \approx 0.5 \div 0.6$  can be associated with the vortex switching. All frequency signatures share a common  $-5/3$  slope in the certain part of the spectrum, indicating that the POD analysis

also confirms the proper spectral resolution of the flow with IIS-RSM. Most of the aforementioned frequencies appear in range  $f < 10$  [Hz], meaning that dominant processes, appearing in the mixing zone, carry pronounced risk for the propagation of thermal stripping. For the final assessment of the wall structure's susceptibility to thermal stripping, POD Analysis is repeated on the instantaneous temperature field, projected on to the lower wall. Mode importance as well as the FFT Analysis of time coefficients are shown at Figure 6.18. Additionally, spatial visualisation of modes is given in Figure 6.19.

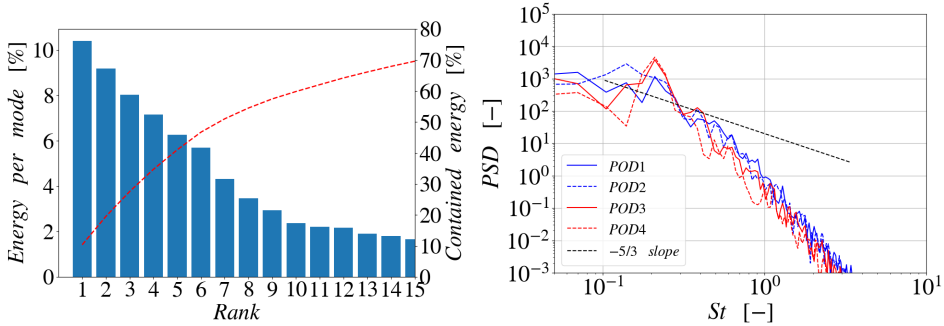


Figure 6.18.: Accumulation of captured variance (left) and FFT analysis of time coefficients (right) for the temperature field POD analysis at the walls.

Accumulation of captured energy per-mode doesn't have a clear interpretation and the diminishing of captured variance progresses with higher mode number. Again, only the first four modes will be presented. Modes 1 and 2 clearly point to the high-intensity fluctuation zone in the vicinity of the leading edge and in the zone around the branch inflow. Modes 3 and 4 dictate the presence of coherent structures more downwards, in the mixing zone. Inspection of time coefficients reveals a more dense accumulation of spectral energy around  $St \approx 0.2$  for all inspected modes, which indicates that the thermal stripping phenomena is mostly governed by the Kelvin-Helmholtz instabilities. Additional phenomena like separation induced pulsations in the vertical direction, as well as vortex switching, related to the separation bubble, have very little influence on the thermal pulsations in the wall structure.

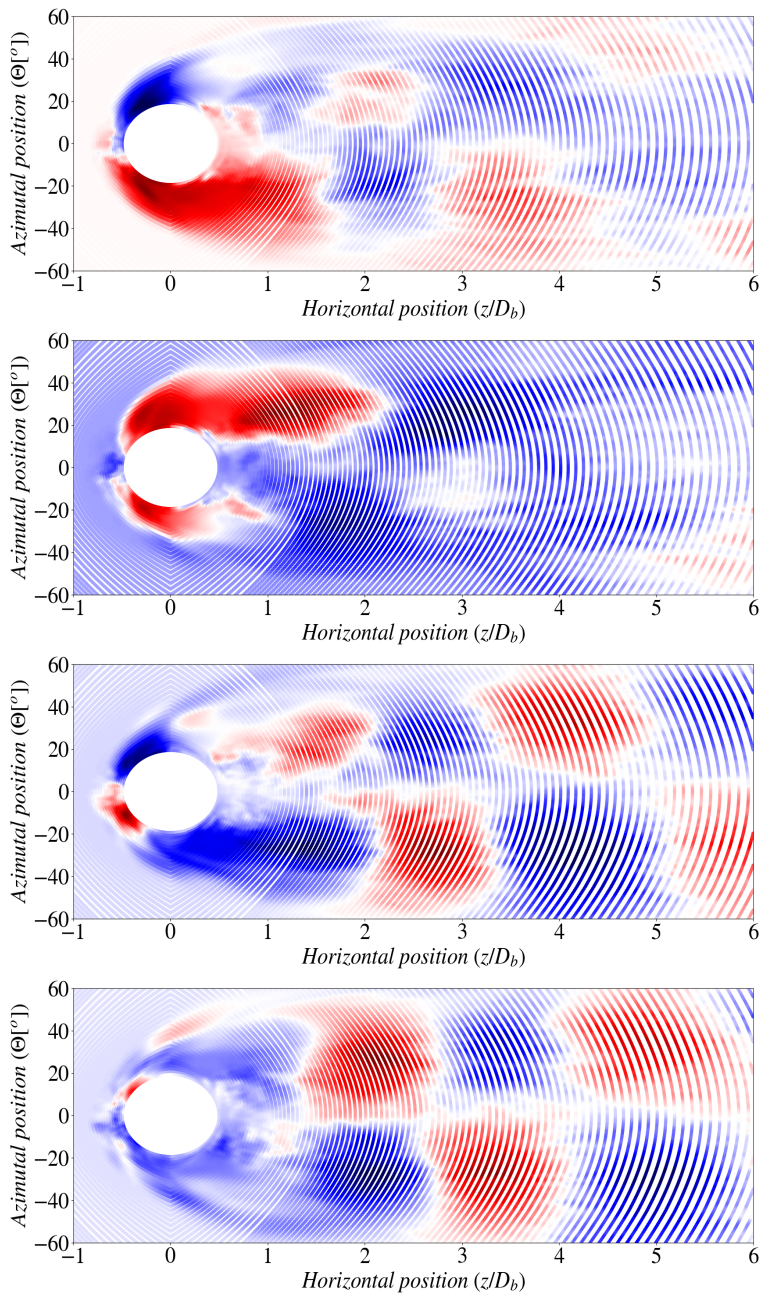


Figure 6.19.: Intensity of first 4 POD modes of the temperature field at the walls: POD1 (up), POD2 (center up), POD3 (center down) and POD4 (down).

## 6.2. Impinging jet case

Concerning the Impinging jet case, all the usual techniques used for analysis in the Wall jet case were used here as well. In Figure 6.20, contours of the instantaneous velocity magnitude are shown. Flow topology is practically reversed, and due to the distribution in momentum, branch flow penetrates the main flow completely, exposing the upper wall structure to the temporally changing cold stream, which stretches and mixes with the hot flow along the upper wall. Additionally, central region downstream of the branch jet exhibits elevated levels of turbulence, which is directly visualized through the presence of top level, resolved scales that are more clearly defined in comparison with an upstream region.

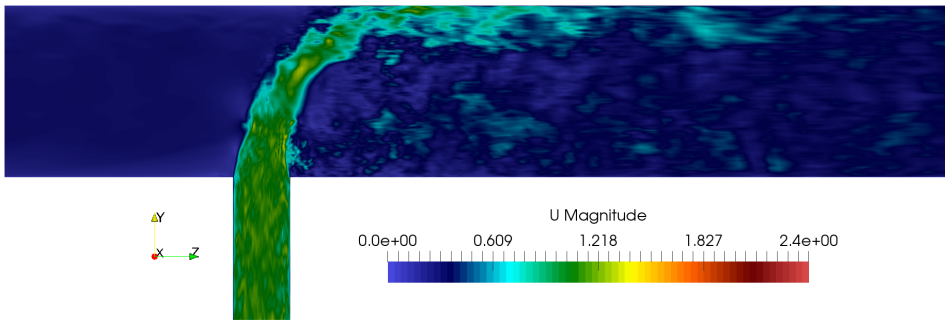


Figure 6.20.: Contours of instantaneous velocity field, I-Ref.

Contours of instantaneous pressure, shown in Figure 6.21 reveal several coherent vortices stemming from the separation at the leading edge. Additionally, zones of decreased pressure are found in the whole mixing region, downstream of the branch jet.

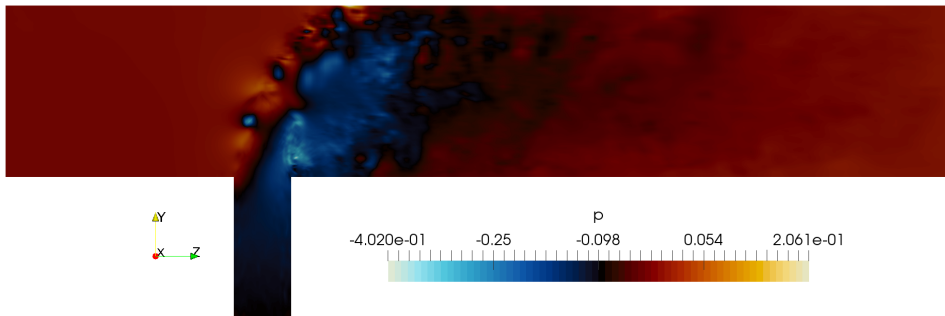


Figure 6.21.: Contours of instantaneous pressure field, I-Ref.

Contours of the instantaneous temperature field in Figure 6.23 reveal that Impinging jet configuration exhibits identical poor mixing in the vicinity of the junction, but due to the gradual breakage of leading- and trailing-edge separation vortices, mixing process enhances along the branch-jet path. Zone downstream of the junction reveals a highly resolved region with pronounced mixing.

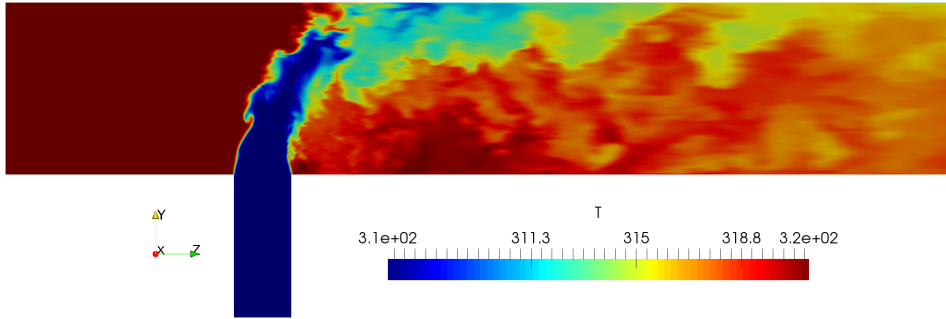


Figure 6.22.: Contours of instantaneous temperature field, I-Ref.

Mean temperature contours reveal a more uniformly mixed zone in the outlet of the junction, as compared to the Wall jet case. Upper wall is still predominantly influenced by the temperature field stemming from the branch jet.

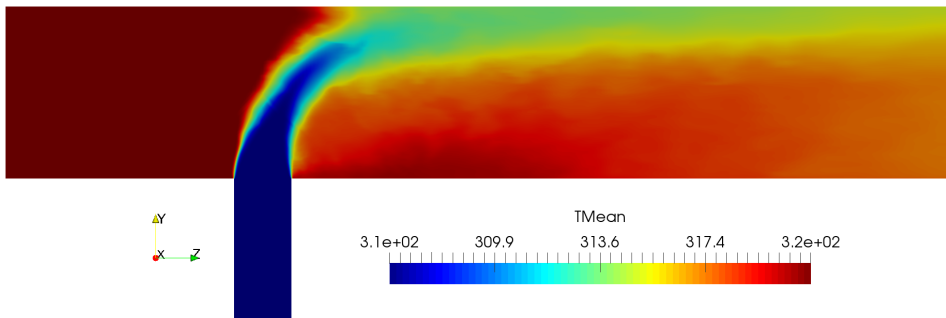


Figure 6.23.: Contours of mean temperature field, I-Ref.

Although the momentum distribution is fundamentally different in relation to the Wall jet case, second-order statistics of the temperature field reveals some similarities between two cases, which will in the end affect the thermal stripping phenomena. Here, zones of maximal amplitudes, coinciding with the shear layer forming between the branch jet and main flow exhibit very similar level of  $T_{RMS}$  intensity. This is specially notable at the leading edge zone, where the identical

maximum in  $T_{RMS}$  is reached. This points to the conclusion that large-scale, top-level structures stemming from the separation at the leading edge also govern the mixing process in the zone close to the junction. However, due to the different flow topology, most of large-scale mixing disappears until the branch stream reaches the top wall, containing the process in the interior of the domain. Hence, fluctuation intensity in the vicinity of the upper wall does not exceed 2.2 [°C], which is around 50 % of the fluctuation intensity exhibited by the Wall jet configuration.

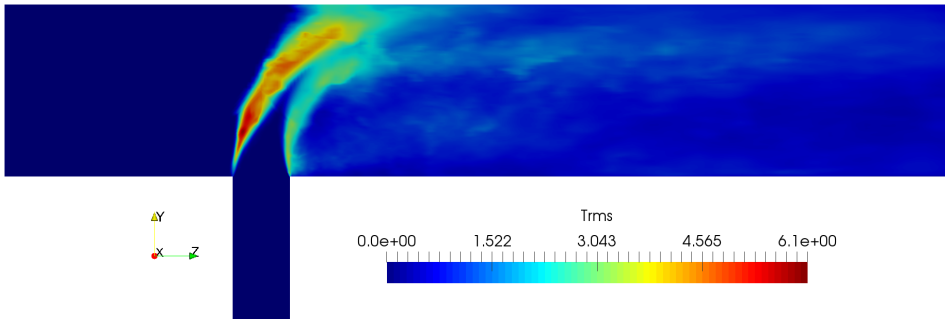


Figure 6.24.: Contours of RMS temperature, I-Ref.

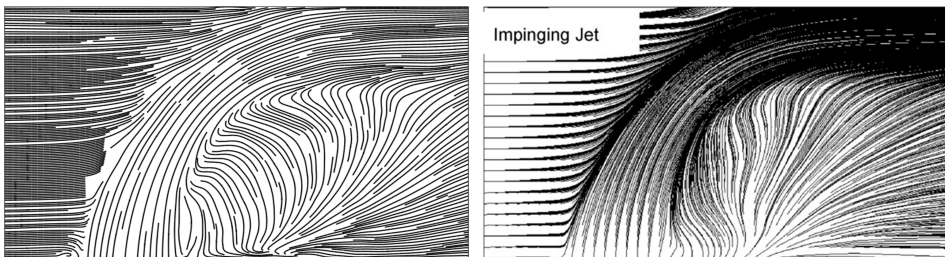


Figure 6.25.: Comparison of mean flow streamlines: calculation (left) and experiment (right).

Concerning the validation of obtained data, no detailed experimental, in-stream measurements of velocity and temperature statistics are reported in the Impinging jet case by Kamide et al. (2009). As for the second-order statistics for the temperature field, its convergence was substantially slower than in the Wall jet case, due to the lower fluctuation intensity. In the end, no smooth contours of RMS values for temperature were obtained. Therefore, assessment of the flow will be done only qualitatively, thus making this section shorter. In Figure 6.25, streamlines of the mean flow, calculated in the central plane are compared with the experi-



mentally obtained ones. Once again, visually adequate prediction is made, both from the standpoint of the branch flow propagation, as well as in the distribution of streamlines in the downstream zone, past the branch stream.

Contrary to the previous section where the POD analysis offered some valuable insights into the flow field, here, POD analysis of neither temperature nor velocity field offered any interpretable results, and no distinguished coherent structures could be identified. This is most likely the consequence of wrongly positioned sampling planes, which were set at the identical position as in the Wall jet case ( $z = 0.5D_m$ ), which is probably too far from the zone of energetic transients. Consequently, they will not be reported further on. Although this finding is disappointing, it is nonetheless congruent with the results of Kamide et al. (2009), who reported no isolated peaks in their point-wise FFT analysis of the temperature field.

### 6.3. Conclusions

In this Chapter, IIS-RSM was tested in the case of complex turbulent mixing of two streams in straight T-Junction configuration, as reported in the experimental campaign by Kamide et al. (2009). Two flow topologies named Wall jet and Impinging jet were tested. Statistical properties of the flow were predicted very accurately, especially from the standpoint of thermal fluctuations which carry the crucial role in the thermal-stripping phenomena, and whose propagation was the primary motivator for the experimental campaign. This has proven that the IIS-RSM can be successfully applied at the higher end of the  $Re$  spectrum, which is a range usually prohibitive for the usage of LES. At the same time, notable savings in mesh size were achieved, concerning the relatively high Reynolds number used in this study. POD technique was used in order to isolate coherent structures in the flow. It was found that the Wall jet configuration is in prominent danger from thermal fatigue, due to the large-scale, high energy oscillations in the wake, produced by the Kelvin-Helmholtz instabilities.



## 7. Flow Configuration III: Temporal dynamics of secondary flows in a T-Junction with an upstream elbow

---

Based on the results discussed in the previous Chapter, it was concluded that IIS-RSM represents a reliable tool for predicting complex flow patterns over a wide range of Reynolds numbers. It was shown that large-scale transients in the mixing zone can be predicted very accurately, especially from the standpoint of the low-frequency fatigue propagation in the walls. Here, the frequency signatures stemming from the underlying mixing structures were produced at the spot, without any external, large-scale transient phenomena. However, industrial pipeworks often include geometrical features such as upstream bends, which can introduce additional transient behaviour into the flow, thus modifying the spectral properties of the mixing process. Neglecting such geometrical details may lead to the loss in accuracy of the underlying CFD study.

Through the presence of an upstream flow bend, additional unsteadiness is generated by the action of secondary vortices, which are created as a result of the streamline curvature. Existence of these secondary flows is already visualized in Chapter 6, Figure 6.15. On the account of centripetal acceleration, pressure gradient in the plane perpendicular to the main flow will form, pointing from the centre of curvature and creating the region of high pressure on the outer-, and low pressure on the inner side of the bend. In the vicinity of the wall, low inertia fluid will be forced to move towards the zone of low pressure on the inner side of the bend. On the account of the continuity, streamlines in the plane normal to the main flow will form, where the fluid exhibits a secondary motion in the form of characteristic counter-rotating vortex pair. Existence of such a flow feature was initially described by Eustice (1910) and analytically analysed by Dean (1928), from whom they are named Dean vortex pairs. Emergence of secondary flow structures due to the streamline curvature is common under both laminar and turbulent flow conditions. Intensity and topology of the secondary flows are dependent on the diameter-based Reynolds number  $Re$ , as well as on the curvature characteristics of the bend  $\delta = R/R_c$ , where  $R$  and  $R_c$  is the pipe- and curvature radius, respectively.

In the turbulent flows through the sharp bends, Dean vortices exhibit a large-scale instability, where the pair erratically oscillates between the two bi-stable states, in which the intensity of one vortex core surpasses the other. Such a transient response of the secondary flows was first mentioned in M. Tunstall and Harvey (1968), who investigated flows through both the mitred, as well as sharp bends. The phenomena was named: *swirl switching*. By the means of spectral analysis, several characteristic frequency peaks can usually be found in correspondence with the swirl switching phenomena. Exact correlation between the switching frequency and the integral parameters of the flow such as  $Re$  or  $\delta$  is not yet well understood. Over the recent years, several experimental and numerical studies have been published (e.g. Kalpakli Vester et al. (2015) and Hufnagel et al. (2018)), aiming at establishing a database for the vortex switching phenomena. In general, it was found that the switching frequency is very sensitive to boundary- and modeling conditions such as, treatment of inlet turbulence, large-scale phenomena in the straight pipe section upstream of the bend, as well as instabilities of the shear layer in the bend. Despite using the wide range of  $Re$  and  $\delta$ , no definitive conclusion could be made about their impact. Apart from the experimental study of vortex-switching by Sakakibara et al. (2010), Reynolds number corresponding to each of these cases is substantially lower in comparison with the case studied in this thesis.

Consistently with the results from previous Chapter, T-junction related mixing phenomena will now be superimposed with the effect of Dean vortex switching, through the numerical reproduction of the configuration with a  $90^\circ$  upstream bend. As a validation reference, dynamic Smagorinsky LES study by R. Tunstall et al. (2016b) is chosen. Schematics of the flow domain is given in Figure 7.1. Main, hot flow enters through the vertically oriented pipe with the diameter  $D_m$  and the length of  $10D_m$ , and passes through the  $90^\circ$  bend, with the curvature radius of  $R_c = 1.4D_m$ . Bend related coordinate  $\Theta = [0 \div 90]$  is used for characterising the flow position in the bend. Downstream of the elbow section, flow is mixed with a branch stream, positioned  $2D_m$  behind the bend exit. Mixing zone features a so-called reattached jet configuration. An overview of all the flow conditions is provided in Table 7.1. Note that the temperature is regarded as a passive scalar, and hence treated in dimensionless form. Total cell number reported in the LES study was close to 80 Million.

Considering the set-up of the IIS-RSM case, already conducted precursor study for  $Re = 107, 893$  from the Chapter 5 was run in parallel with main case, mapping the established fields on to the main inlet boundary. Exemplary, this method is in congruence with similar studies by Rütten et al. (2005), but differs from the generation of inlet turbulence in the reference LES case, where the Divergence-Free-Synthetic-Eddy-Method (DFSEM) by Poletto et al. (2013) was used. Reason for using the mapped method in place of DFSEM simply stems from the fact that the application of the DFSEM remained untested in conjunction with the IIS-RSM model. Details related to the development length, accuracy and modeled-to resolved-ratio of turbulent kinetic energy remained unclear. Advantages and disadvantages of this

approach will be discussed along with the interpretation of results. As for the branch inlet, low Reynolds number prohibited the obtention of any resolved turbulence in branch precursor, hence the steady state, prescribed values for each field are provided at the branch inlet. Next to the inlet fields, all parameters involving the mesh metrics were taken from the precursor simulation, see Table 5.1 and will not be repeated here. With precursor pipe included, this results in a mesh size of approx. 7.8 Million cells, including precursors. This is close to the factor 10 reduction in computational burden, as compared with dyn. Smagorinsky LES study.

Table 7.1.: Geometrical- and inflow conditions. Temperature given in dimensionless form.

Parameter	Main pipe	Branch pipe
Diameter [mm]	108	21
Bulk velocity [m/s]	0.89	0.23
Reynolds number [-]	107,893	5422
Inlet temperature [-]	1	0

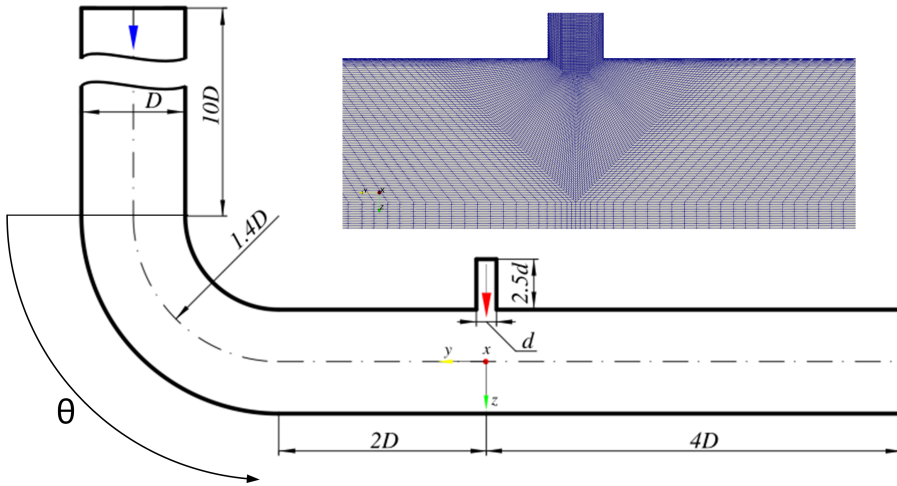


Figure 7.1.: Schematics of the flow domain with details of the mesh in the mixing zone.

## 7.1. Results

Calculations were performed until the clearly defined contours of secondary flows were observed, and turbulence statistics reached convergence. In Figure 7.2, contours depicting the instantaneous velocity magnitude are provided for the reference LES case (top), as well as for the IIS-RSM simulation (bottom). As expected, LES provides more structural resolution of the flow. In spite of that, IIS-RSM seems to offer qualitatively congruent flow results. On the outer wall of the bend, curvature of the flow enforces a local deceleration zone due to the presence of adverse pressure gradient. Low velocity zones are of similar size and intensity in both studies. Due to the continuity, region of increased velocity is spotted close to the inner wall. Approximately  $55^\circ$  behind the bend entrance, primary separation zone establishes, characterised by the region of low velocity, which is separated from the main flow by the clearly defined shear-layer. Overall size of the primary separation zone is slightly larger in the case of IIS-RSM simulation. Topology of the flow field in the elbow is dominantly dictated by the presence of Dean-eddy vortices and secondary flows, formed in the separation bubble. A detailed discussion of these phenomena will follow up shortly. Flow field in the whole straight section downstream of the junction is governed by the structures establishing in the wake of the primary separation zone.

As for the mixing region close to the junction, instabilities from the main pipe are propagating all the way to the branch inlet, creating a transient flow response in the branch pipe. Due to the steady-state treatment of the branch inlet, length of the branch pipe is shortened in the IIS-RSM study, in comparison with LES reference. Since the momentum carried by the branch pipe is substantially lower than that in the main pipe, branch flow is unable to penetrate the main flow significantly and the locally confined separation bubble forms in the vicinity of the upper wall.

In Figure 7.3, streamlines of the averaged velocity field are shown for two cases. Coloring represents the intensity of the local streamwise component of the flow. Here, some more pronounced differences between cases are visible. First, a presence of a larger primary separation zone is detected in the IIS-RSM case. This possibly indicates a higher intensity of secondary flows within the elbow. Although the position of the separation point is nearly identical for both cases, it seems that the flow field from the IIS-RSM case features an additional, third separation bubble immediately downstream of the bend. Reasons for this behaviour are not clear, but are likely linked to the intrinsic behaviour of the model. Distortion of streamlines is also likely responsible for the retention of separation wake in the vicinity of the upper wall. Note that the separating shear layer in the LES study never reaches an apparent horizontal alignment, contrary to the IIS-RSM. None the less, magnitudes of both data sets are qualitatively mostly congruent with no drastic discrepancies.

As seen in Figure 7.10, ratio of modeled turbulence is elevated in separation bubble, as well as in the zone adjacent to the upper wall, meaning that the local flow behaviour is also dictated by the model of turbulence.

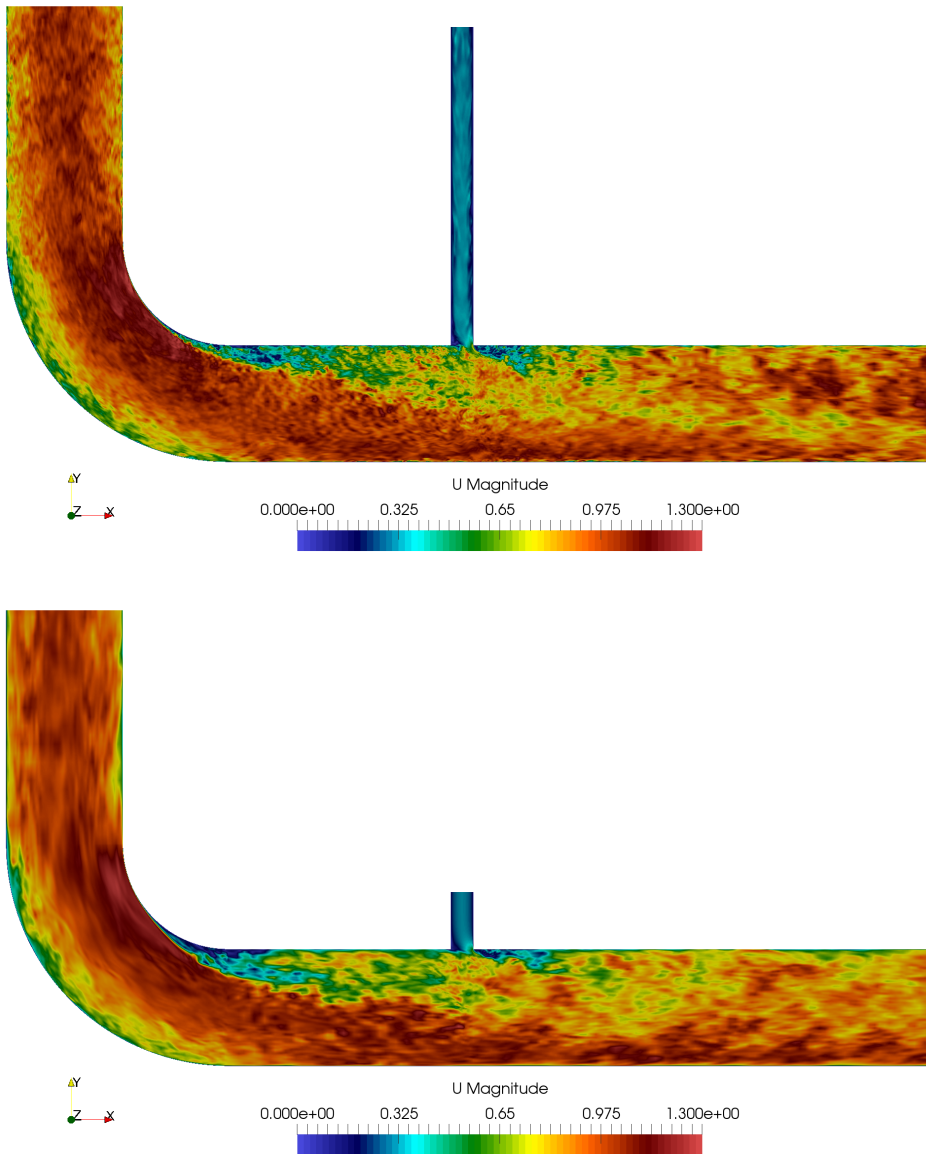


Figure 7.2.: Contours of the instantaneous velocity field magnitude. LES study by R. Tunstall et al. (2016b) (top) and IIS-RSM case (bottom).

## 7. Flow Configuration III: Temporal dynamics of secondary flows in a T-Junction with an upstream elbow

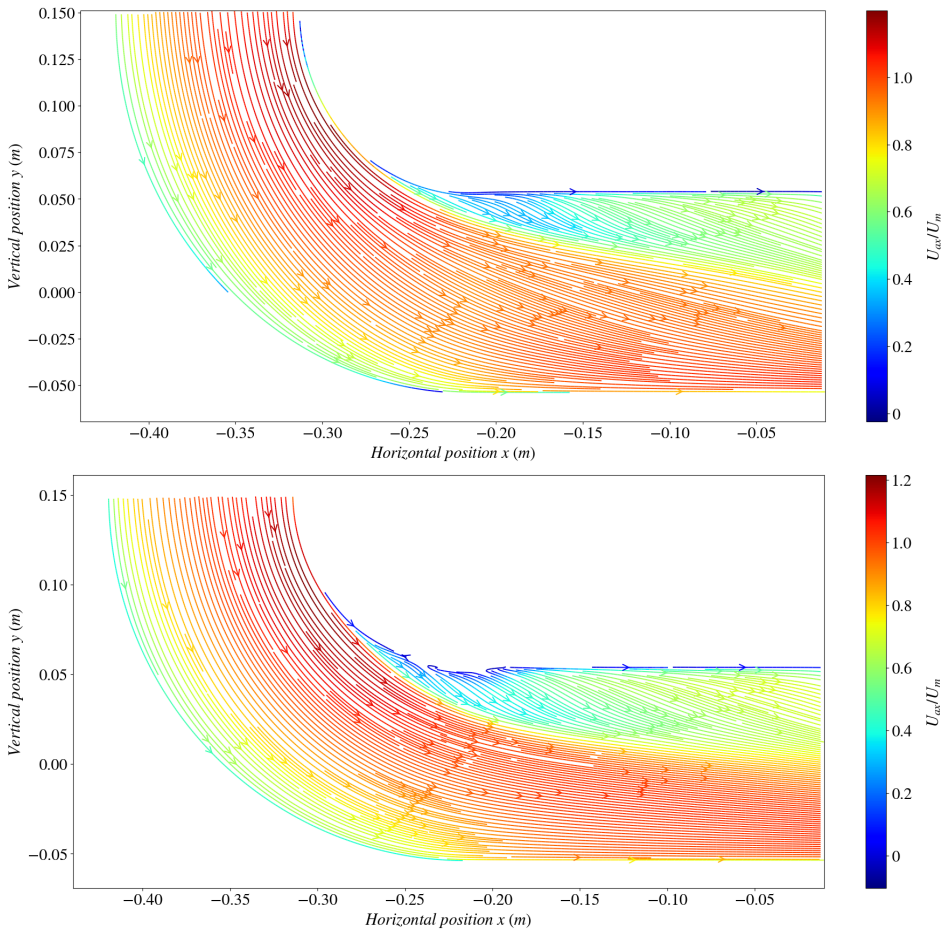


Figure 7.3.: Streamlines of the mean flow, LES study (top) and the IIS-RSM (bottom). Coloring represents a local streamwise component of the flow.

In Figure 7.4, contours of instantaneous temperature field are given. Following to the qualitative similarity with the reference LES case, only the IIS-RSM temperature has been plotted. Due to the relatively small mass flux of the branch flow, mixing process ends in the vicinity of the separation bubble, where the large-scale coherent structures indicate (as demonstrated in previous Chapter) poor mixing of streams at the edge of the separation wake.

In Figure 7.5, streamlines in the plane normal to the elbow centerline are depicted for six angular positions in the bend. Background coloring represents the streamwise velocity, normalized by the mean flow velocity  $U_m$ . A clearly developed pair of



vortices can be spotted at each of the cross-sectional planes. As the flow progresses through the elbow, both vortices migrate towards the upper wall. Past the angle of  $60^\circ \div 65^\circ$ , shear effects change the eddy shape from the originally ellipsoidal, up to the kidney-like. Secondary currents in the vicinity of the upper wall transport the low inertia fluid towards the centre, thus influencing the size of the primary separation zone, defined through the area of small axial velocity. At elbow exit, influence of centrifugal force vanishes and the vortex pair now migrates towards the axis of symmetry, as seen in Figure 7.6. Elongation of the streamlines leads to the breakage of vortex cells into the quadruplet of vortices as seen in Figure 7.6 (b), whereas the uppermost pair continues to dominate the flow. This topology is retained down to the mixing zone, where the separation bubble related to the branch jet is formed. However, due to the strong main flow, branch jet is quickly reattached and vanishes at the distance of  $2D_b$  downstream of the junction. Comparison of the obtained secondary flows with the LES reference is performed on 3 positions within the straight section, as seen in Figure 7.7. Regrettably, data related to the secondary flows in the elbow were not available.

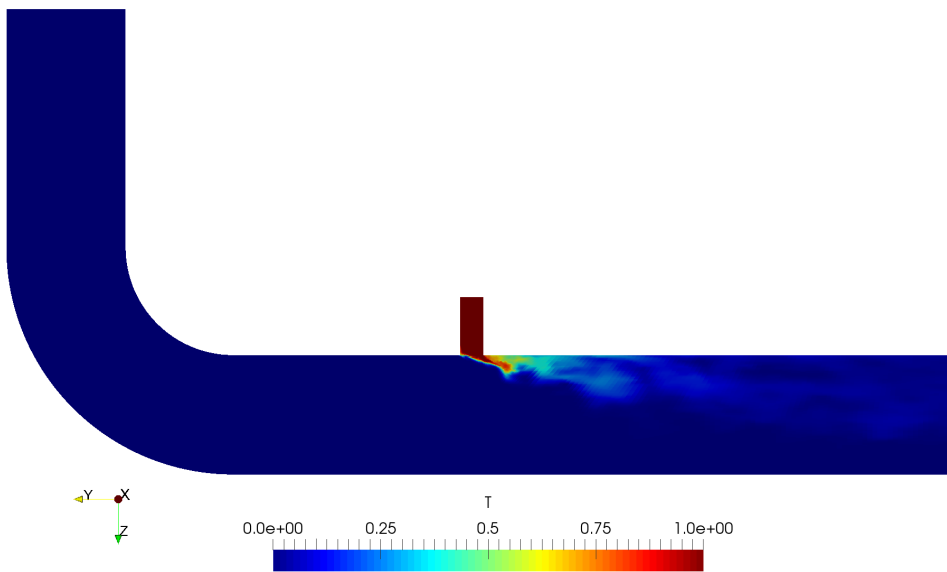


Figure 7.4.: Contours of the dimensionless instantaneous temperature field.

## 7. Flow Configuration III: Temporal dynamics of secondary flows in a T-Junction with an upstream elbow

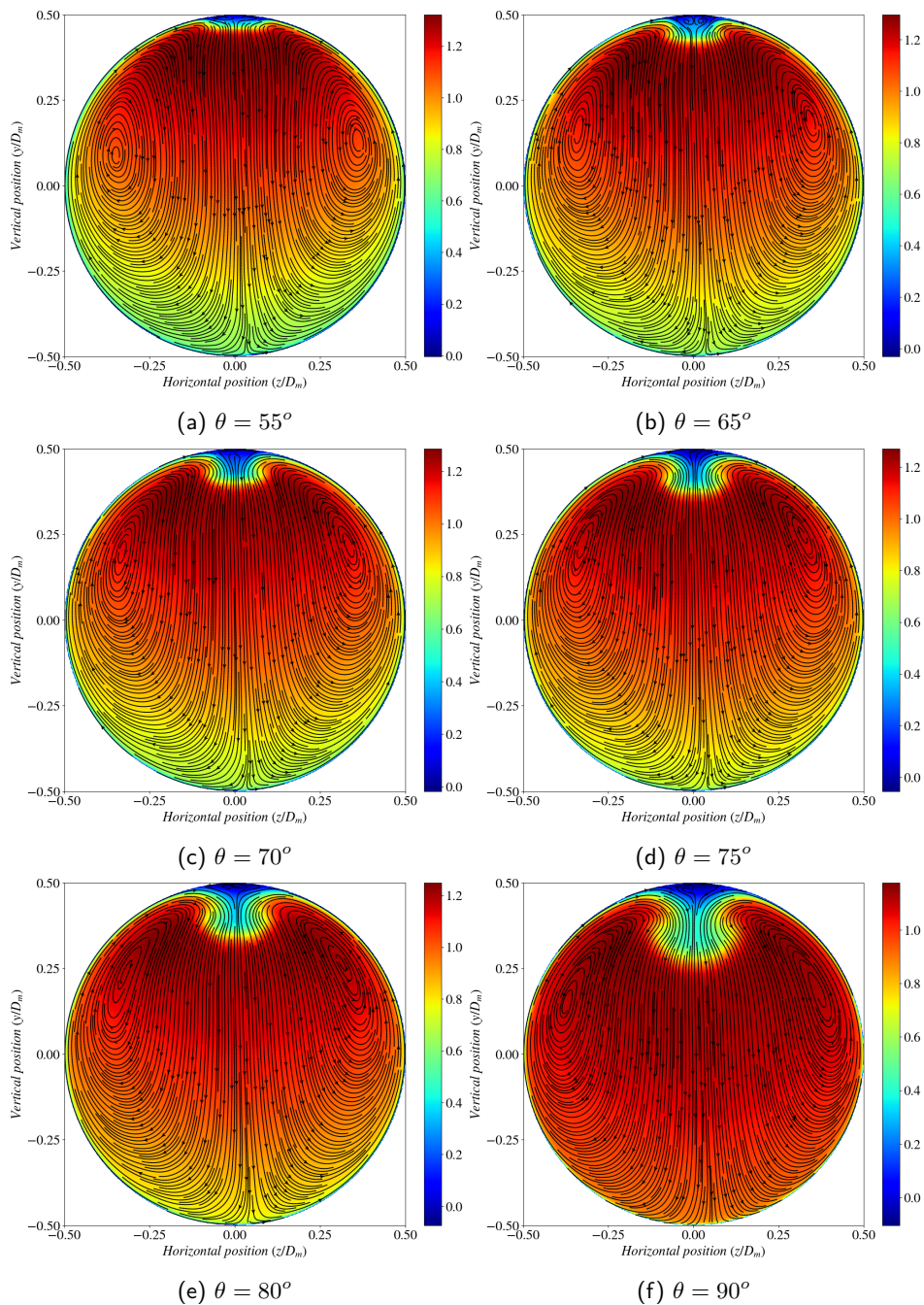


Figure 7.5.: Progression of secondary flows in the elbow. Background coloring denotes the normalized streamwise velocity magnitude.

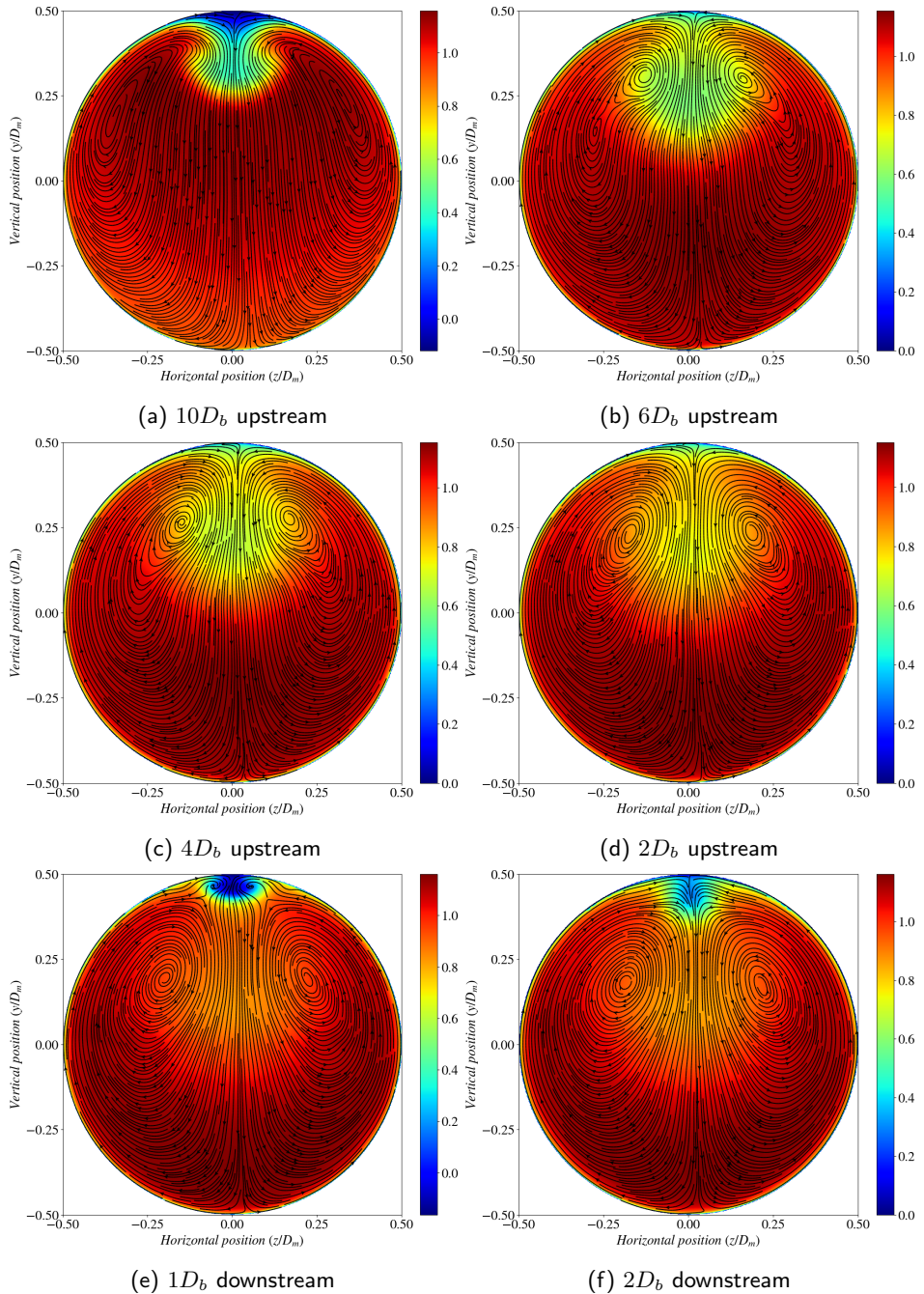


Figure 7.6.: Progression of secondary flows in the straight section. Background coloring denotes the normalized streamwise velocity magnitude.

## 7. Flow Configuration III: Temporal dynamics of secondary flows in a T-Junction with an upstream elbow

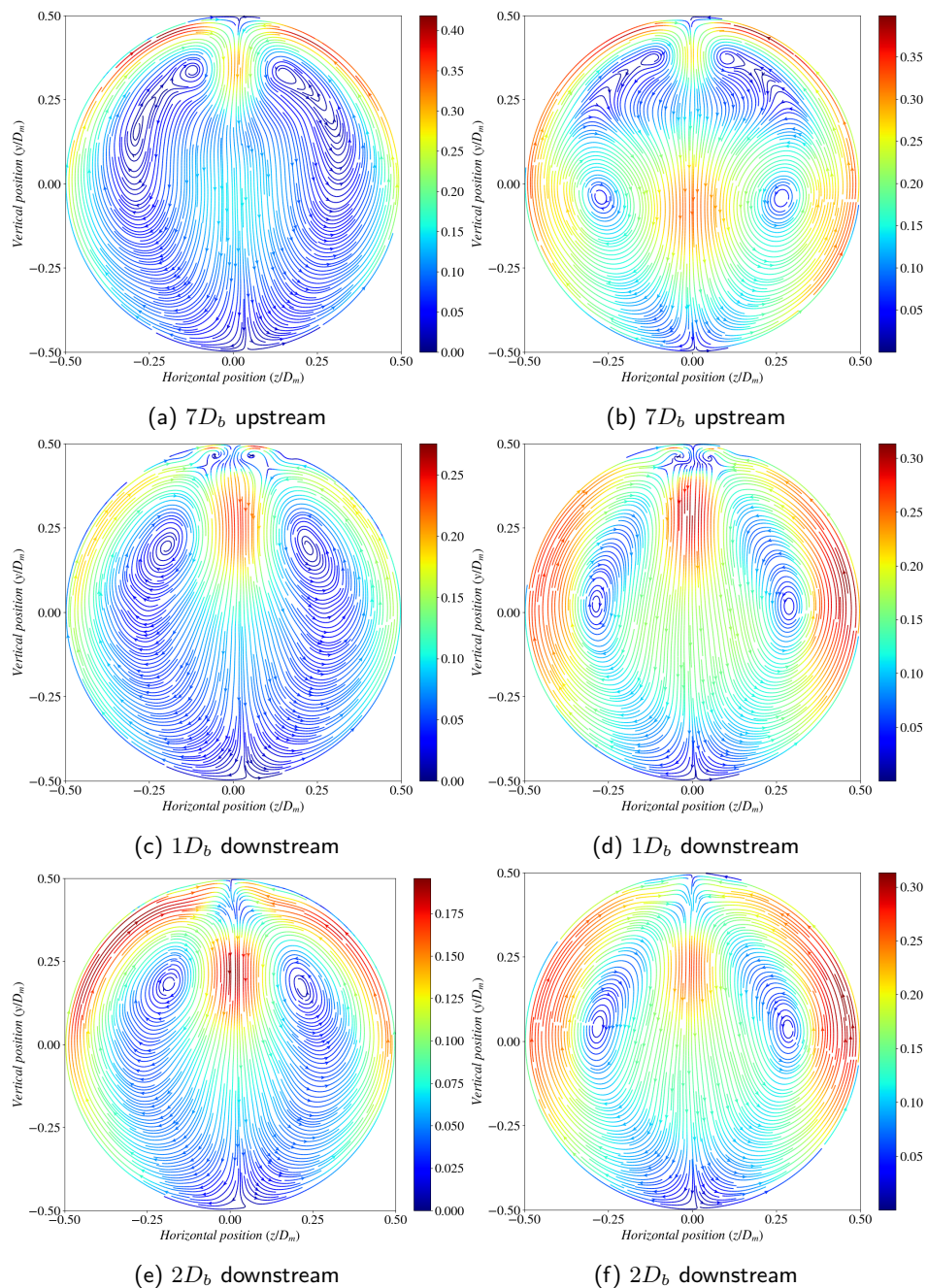


Figure 7.7.: Comparison between calculated IIS-RSM solution (left) and the LES reference (right). Streamlines colored by the secondary flow magnitude.

Upstream of the junction centre, intensity of the secondary flows near the upper wall, as well as the position of the upper vortex pair have been correctly predicted. However, kidney-like vortex shape generated by the IIS-RSM model leads to the complete destruction of the bottom vortex pair. As for the positions downstream of the junction centre, flow intensity in the vicinity of the upper wall, as well as the position of the vortices associated with the secondary separation bubble, is predicted correctly as well. However, in both cases, there are certain deviations from the reference data in the position of the dominant vortex pair, which migrates more slowly towards the lower wall, as compared with the LES study.

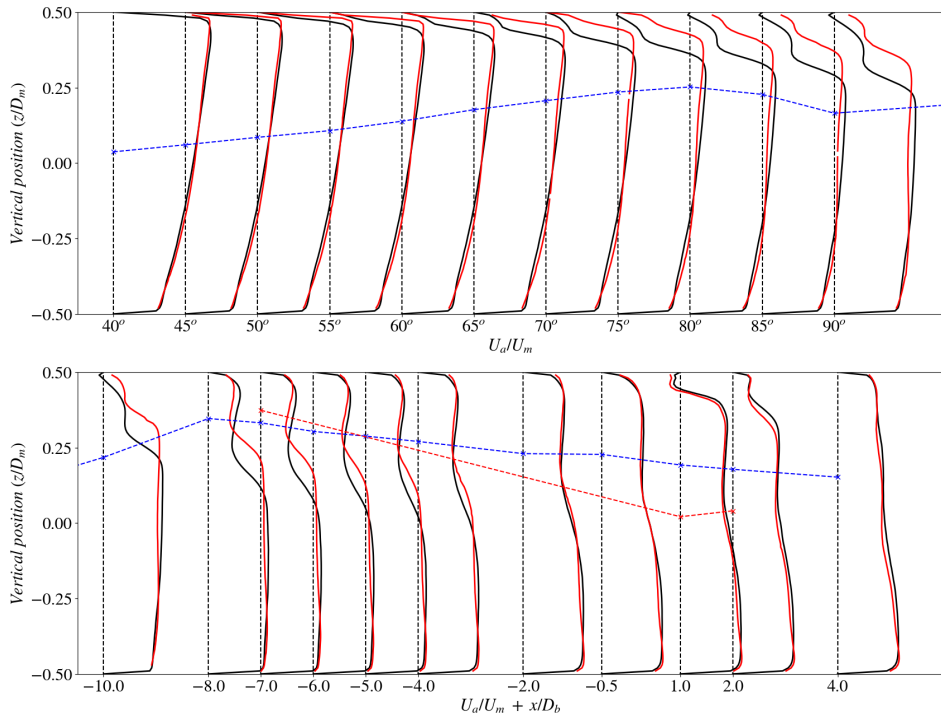


Figure 7.8.: Profiles of the streamwise velocity in the elbow (top), as well as in the straight section, downstream of the elbow (bottom). Black lines indicate the IIS-RSM, and the red ones the LES solution. Position of the vortex centres in the IIS-RSM case is depicted with the dashed blue line. Position of the vortex centres in the LES solution are depicted with red dashed line, at available measurement points.

Profiles of streamwise velocity for both the LES, and the IIS-RSM solution in the elbow are plotted in the Figure 7.8 (top). As can be seen, although the position of the separation onset is correctly predicted, separation zone is clearly bigger in the

IIS-RSM case, which can be attributed towards the higher intensity of the secondary flows in the vicinity of the wall. As for the position of the vortex pair, it is shown that it progresses steadily towards the inner wall up to the angle of  $\Theta \approx 80^\circ$ , after which it is reflected back to the center. Same analysis is repeated for the profiles in the straight section, downstream of the elbow in Figure 7.8 (bottom). Here, LES and IIS-RSM solution gradually approach, and downstream of the  $-4D_b$  position, no significant differences in the velocity profiles are visible. This can be explained by the gradual weakening of the secondary flows along with the streamwise coordinate. By comparing the progression of vortex centres for both solutions, a clearly visible downtrend exists, somewhat stronger with the LES solution. Onset position for the creation of the vortex quadruplet is clearly matched in both cases, at the position  $\approx -8D_b$ , upstream of the junction. Although the flow topology related to the primary separation has been predicted with some discrepancies, secondary separation and subsequent reattachment of the branch jet have been predicted with almost perfect match, showing that branch jet reattaches at the upper wall at the distance  $\approx 2D_b$  past the junction.

Finally, in Figure 7.9, contours of the normalized RMS Temperature are shown on the lower wall. Although the position and shape of the variance dominated zone is correctly predicted, comparison with experimental data indicates that maximum in  $T_{RMS}$  is about  $20 \div 30\%$  underpredicted. As it will be shown in short, dynamics of the structures around the separation bubble is now dictated more strongly by the incoming flow, and not by the natural response of the main stream towards the presence of the separation bubble. This means that the structures generated in the elbow zone dictate the mixing process. As shown in Figure 7.7 and 7.8, dominant vortex pair is positioned closer to the upper-wall, in comparison with experimental reference. This suggests that the vortex switching phenomena is more constricted in space, which naturally explains the under-predicted variance.

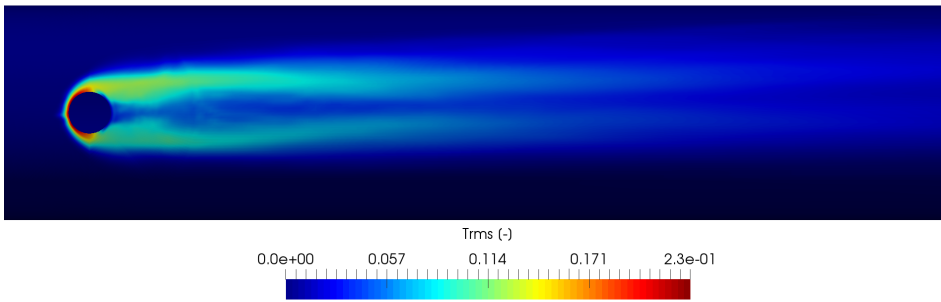


Figure 7.9.: Contours of dimensionless  $T_{rms}$  on the junction walls.

In Figure 7.10, contours depicting the ratio between modeled and total turbulent kinetic energy are given. Due to the direct mapping of the inlet turbulence, resolved turbulence dominates the region close to the centerline, as well as the zone upstream

of the elbow and the mixing zone. Again, regions far away from the wall show almost negligible intensity of modeled turbulence, which falls below 1 %. This behaviour prevails throughout the domain. Near-wall zone is dominated by the residual flow, where on average, about 20 % of the total turbulence is modeled. Ratio of modeled to total kinetic energy shows abrupt increase close to the separation point in the elbow. This zone of increased modeled turbulence is consequently advected downstream and largely retained in the vicinity of the upper wall.

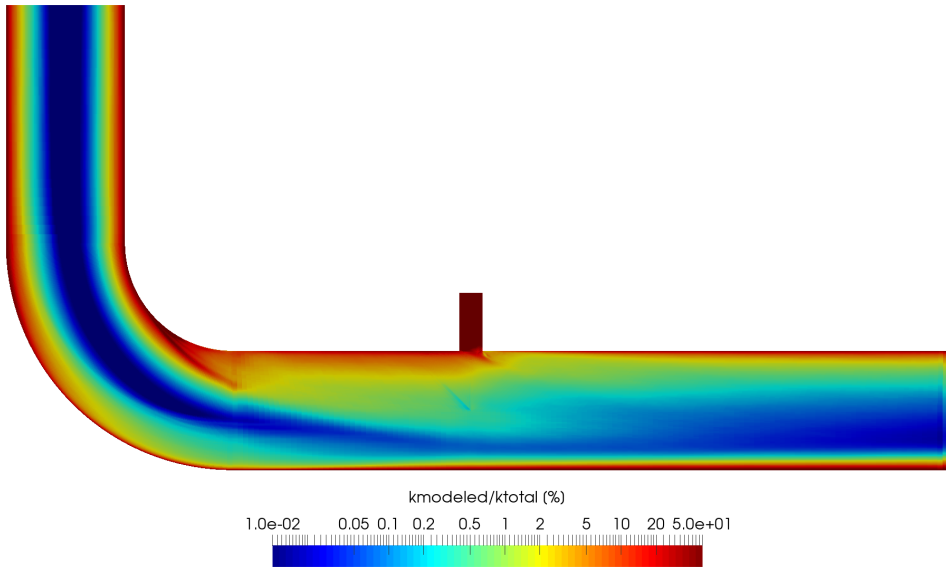


Figure 7.10.: Ratio of modeled-to-total turbulent kinetic energy in the IIS-RSM case.

Next to the reproduction of statistical properties of the flow, accurate recovery of the system's dynamic response constitutes the applicability of the model. Based on the results from previous Chapter, it is evident that the cross-flow configuration between the branch jet and the main stream will introduce certain transient characteristics into the system, thus enabling the propagation of low-rank temperature pulsations. In order to assess how the secondary flows influence these pulsations, POD analysis is performed, with aim of capturing dominant directions of vortex switching and associating them with certain frequency content.

In Figure 7.11, POD analysis of the secondary flow velocity,  $7D_b$  upstream of the junction, is shown. It can be seen that the most energetic flow pattern (around 6% of total captured variance) represents the nearly horizontal switching of the upper vortex pair, created through the elongation of the originally ellipsoidal elbow vortex structures.

7. Flow Configuration III: Temporal dynamics of secondary flows in a T-Junction with an upstream elbow

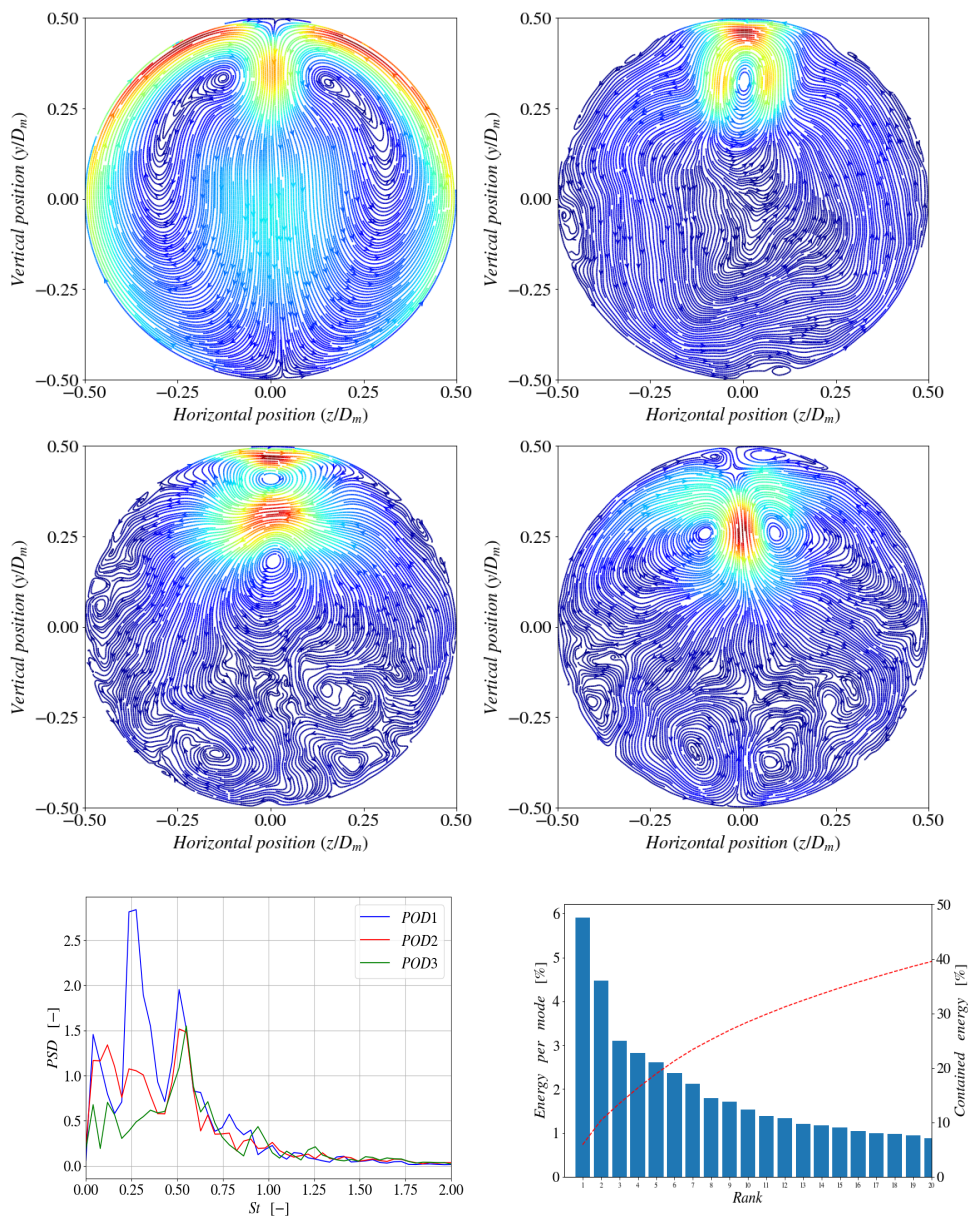


Figure 7.11.: POD Analysis of the velocity field,  $7D_b$  upstream of the junction. Respectively, mean flow (top-left), mode 1 (top-right), mode 2 (center-left) and mode 3 (center-right). In the bottom row, FFT Analysis of three time coefficients (left), as well as the accumulation of captured variance (right) are shown.



There are at least three characteristic frequencies corresponding to this motion. First, the most energetic peak at  $St \approx 0.21 \div 0.27$ . Spectral position of this peak is in accordance with the LES data, suggesting that the vortex switching phenomena was reliably predicted. Second, there is a very low frequency region at  $St \approx 0.05$  and thirdly, another dominant peak, present at  $St = 0.5$ . Their physical significance can be best understood with interpretation of POD modes 2 and 3. Somewhat weaker, but strictly horizontal switching can be spotted in mode 2, where the regions of high variance correspond first with the third separation zone on the upper wall, and secondly with the vortex switching path. Whereas the vortex switching path resonates somewhat more weakly in the signal (note the isolated peak at  $St \approx 0.25$ ), low frequency motion  $St < 0.1$  is most likely associated with the shear layer effects. The weakest, third mode (3% of captured variance) reflects the vertical movement of the vortex pair. This mode is associated with the single peak at  $St = 0.5$ . Noted vertical movement possibly points to the increase in the variance of secondary flows, caused by the precursor. An unusual behaviour of all three modes is captured at  $St = 0.5$ , suggesting a globally present mechanism. Explanation is found to be unrelated to the vortex switching phenomena, but in fact stemming from the precursor simulation. Namely, since the length of the precursor pipe is  $2D_m$ , artificial pulsations are introduced into the system at the frequency which corresponds to  $St = 0.5$ . In the incompressible fluid, these oscillations are propagated through the inlet pipe and elbow, hence the additional frequency peaks on all modes. With respect to the treatment of the inlet turbulence, eliminating these oscillations would only be possible with usage of the synthetic turbulence, which is an approach already evaluated as unfit for this Thesis in Chapter 5. Overall, POD Analysis shows that the vortex switching exhibits spatially complex migration patterns, with horizontally oriented vortex switching occurring at the theoretically predicted, dominant frequency of  $St \approx 0.25$ .

POD analysis of the velocity field is also performed at the downstream position,  $1D_b$  behind the junction. Here, the horizontally directed switching expressed through the mode 1 dominates over all other modes (more than 10% of the total variance accumulated). Contrary to the expectations (high energy of the mode may suggest a clearly isolated spatio-temporal phenomenon), this mode exhibits a complex frequency response, with several isolated peaks in the range  $St = 0.1$ , up to  $St = 0.8$ . Here, switching phenomena is more dominantly related with the two wall streams, whose intensity undergoes a transient change. Considering the temporal response, all peaks shown in previous POD analysis are inherited, although the relative strength of the vortex switching phenomena loses prevalence (note that the artificially introduced peak at  $St = 0.5$  dominates the spectrum). Change in vortex intensity is better reflected in the second POD mode, where the horizontal switching direction is clearly captured. Spectral peaks migrate towards the higher frequency region, at  $St \approx 0.7 \div 0.8$ . Note that the vortex switching from the separation bubble is also visible in the upper zone of mode 2. If the analysis from previous Chapter is to be repeated, frequency response correlating with Kelvin-Helmholtz instabilities

around the separation bubble should be visible at  $fD_b/U_m \approx 0.21$ . The expected frequency response should then lie in the range  $St \approx 1.1$ , which is clearly visible in the spectrum of the second mode.

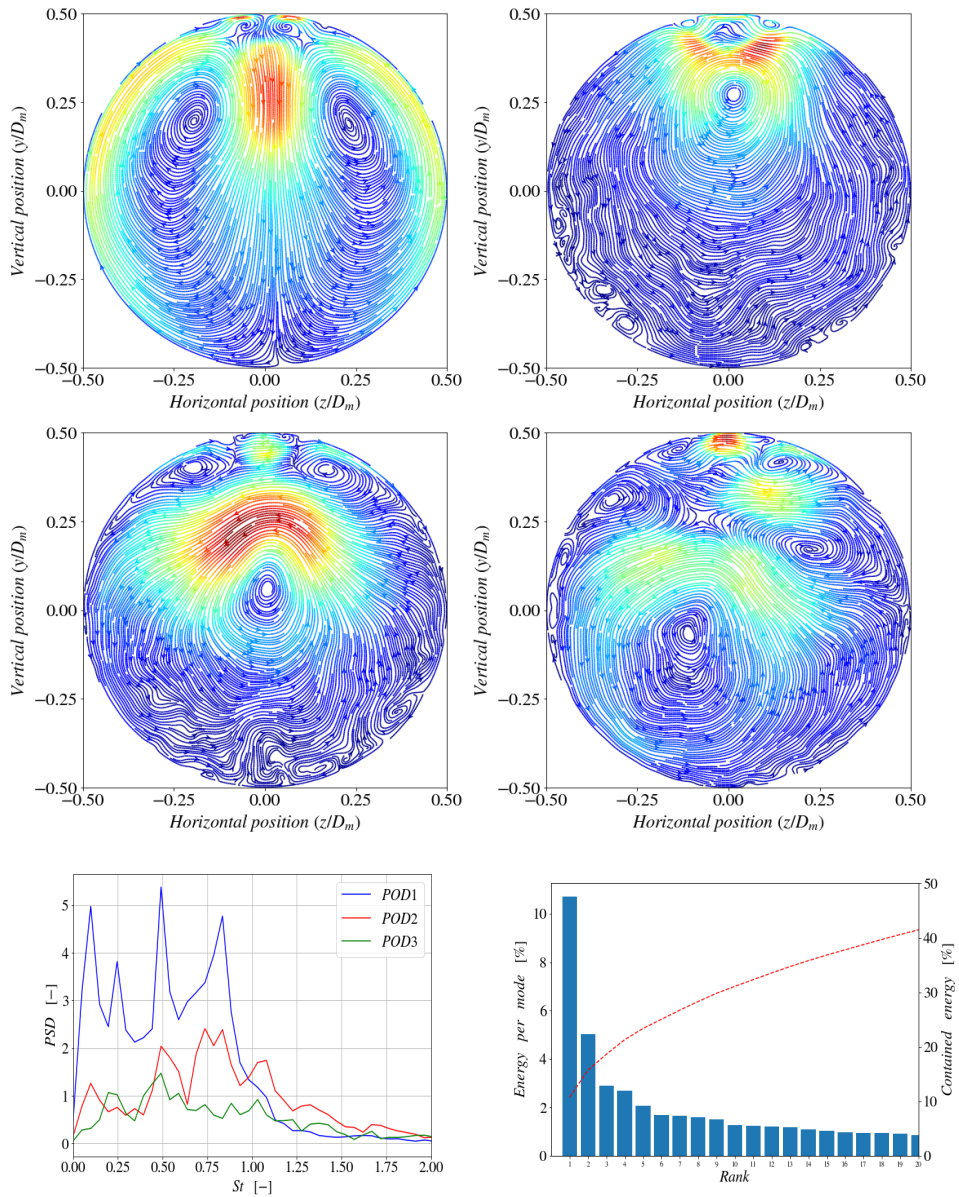


Figure 7.12.: POD Analysis of the velocity field,  $1D_b$  downstream of the junction. Respectively, mean flow (top-left), mode 1 (top-right), mode 2 (center-left) and mode 3 (center-right). In bottom row, FFT Analysis of three time coefficients (left), as well as accumulation of captured variance (right) are shown.

7. Flow Configuration III: Temporal dynamics of secondary flows in a T-Junction with an upstream elbow

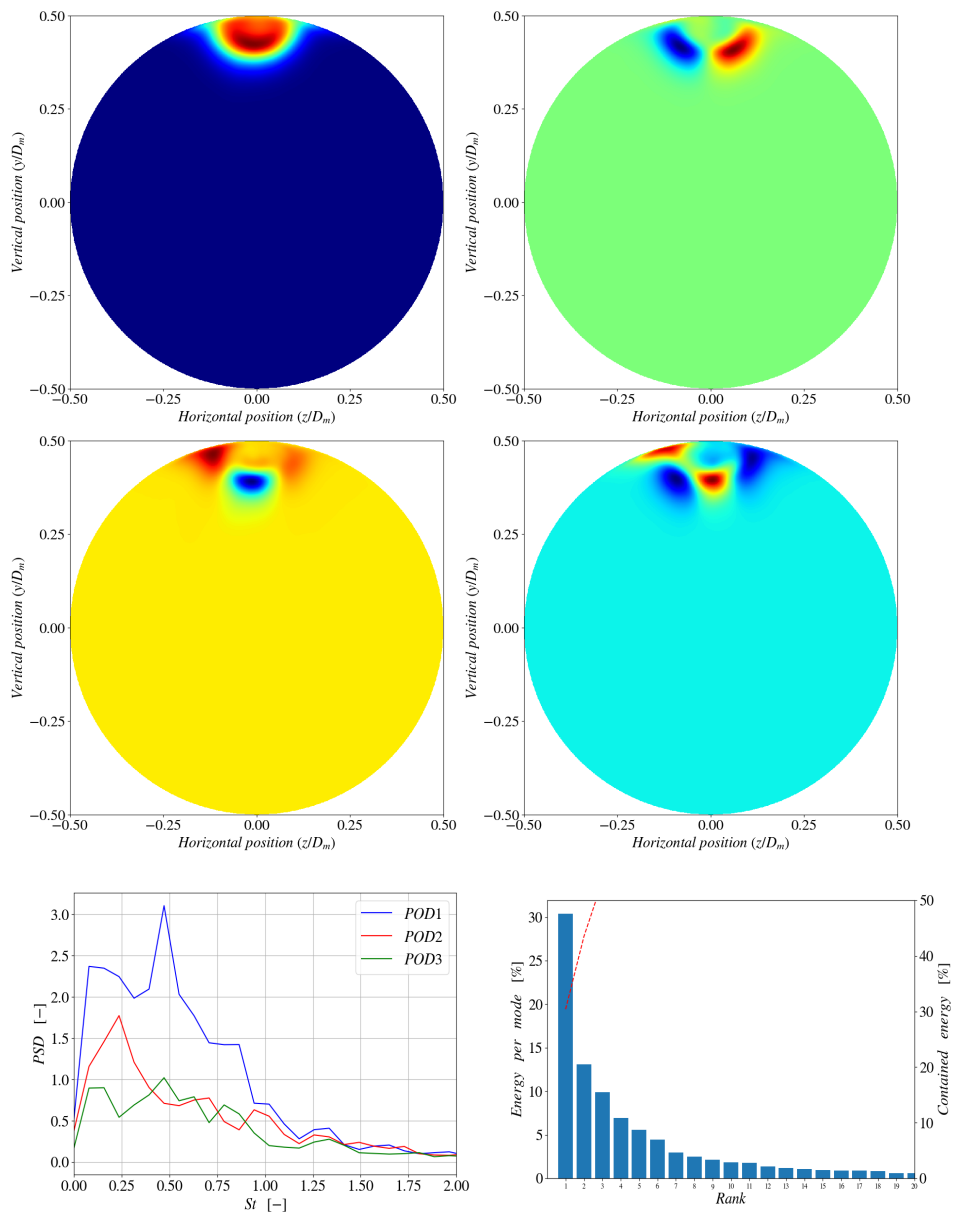


Figure 7.13.: POD Analysis of the temperature field,  $1D_b$  downstream of the junction. Respectively, mean flow (top-left), mode 1 (top-right), mode 2 (center-left) and mode 3 (center -right). In bottom row, FFT Analysis of three time coefficients (left), as well as accumulation of captured variance (right) are shown.

Temperature field is also subjected to the POD analysis, at the identical position,  $1D_b$  downstream of the junction. Results are visualized in Figure 7.13. Similarly to the findings presented in the previous Chapter, zones of pronounced fluctuation intensity are found at the edge of the separation bubble, where the existence of the low-frequency, high energy mixing structures statistically promotes high variance of the temperature field. First mode accounts for around 30% of the total accumulated variance, and can be the primary indicator of the nature of the temperature-field switching. Topology of the mode suggests the existence of strong horizontally oriented switching between two states of local temperature extremums exist. In the previous Chapter, this motion has been correlated with the natural response of the system to the anisotropy of the flow, and formation of the Kelvin-Helmholtz instabilities. Here, inspection of the spectral properties of the mode reveals a different source. First, natural switching frequency of the separation bubble  $St \approx 1.1$  shows no distinct peaks, indicating that the mixing process is governed mainly by the secondary flow, generated and advected downstream of the elbow. Prominent peaks are found first in the region  $St = 0.05 \div 0.28$  and secondly, at  $St \approx 0.5$ , indicating that the boundary condition related unsteadiness dominantly influences the flow. This points to two important aspects in predicting the mixing processes in T-Junction geometries: first, that the artificial unsteadiness, created through the precursor, exhibits an additional influence on the mixing dynamics. Only by using the synthetically generated turbulence at the inflow boundaries can this problem be mitigated. Second point relates directly to the usage of synthetic eddy method. Namely, all unsteadiness in the LES simulation stems exclusively from the natural response of the system towards the separation. If the mixing processes are clearly influenced by any upstream transient (which are a common occurrence in pipelines like: pumps, valves etc), accuracy in predicting realistic T-Junction conduits can not be obtained if such a transient is neglected and in that case, synthetic eddy method will clearly fail to predict the correct mixing dynamics.

## 7.2. Conclusions

Results presented in this Chapter demonstrated that complex flow conditions, involving the secondary flows generated in the upstream elbow, and turbulent, thermal mixing in the T-Junction may be predicted with a substantial cut in the computational cost in comparison with the LES methods. Both the statistical properties of the flow, as well as the dynamical response of the turbulent flow structures were predicted with the reasonable level of accuracy, since all of the underlying signals from the LES study were recovered in the FFT Analysis of IIS-RSM results. Additionally, formation of secondary vortex pair and its dynamics showed a good level of accuracy, since the peak frequency of  $St \approx 0.21 - 0.28$  corresponds very well with the reference data. Also, topology prediction of secondary flows and formation of vortex quadruplet all clearly point to the achieved accuracy of the model.

However, presented simulation setup demonstrated two deficiencies, which decisively affected the accuracy of computation results. First, usage of precursor simulation introduced artificial unsteadiness, which propagated throughout the simulation domain and created the synthetic peaks in all frequency signatures. POD analysis was not able to spatially discriminate this peak from the other modes of the vortex switching process. Second deficiency may be attributed to the model itself. It seems that the primary and tertiary separation zones shifted the distribution of secondary flow patterns and retained the trajectories of the Dean-eddy vortex pair in the upper zone of the junction. This changed the dynamics of the mixing structures past the branch inlet, damping the amplitude of temperature fluctuations in the mixing zone. Since the behaviour of the model was deemed very accurate in predicting most of the statistical properties in Chapters 5 and 6, noted deviations from the experimental reference are less likely correlated with the deficiencies of the model, and more likely caused by its interaction with the boundary conditions. Future research should therefore be directed into using the synthetically generated turbulence at all inlet boundaries and concentrate efforts into adequately predicting the zone downstream of the separation point in the elbow.

## 8. Flow configuration IV: Two phase flows in buoyancy driven bubble columns

---

Results presented in previous Chapters demonstrated that the performance assets of scale-adaptive, second-moment turbulence closure can be successfully used in the realm of industrially relevant thermotechnical flow cases, involving high Reynolds numbers and complex flow conditions. In this Chapter, IIS-RSM performance will be extended into the area of two-phase, bubbly-laden flows. Turbulent, buoyancy driven, dispersed gas-liquid flows in the bubble columns will be computed. To the best of authors knowledge, the only case study involving the scale-adaptive simulation of gas-liquid flow in the bubble column, not limited to the original  $k - \omega - SST - SAS$  model, was published in Ullrich et al. (2014) as well as in Ullrich (2017), who applied the IIS-RSM in conjuncture with Euler-Euler modeling paradigm. In quest for validating IIS-RSM with EL framework, a non-exhaustive list of modeling constrains is presented, making the choice of the validation case very challenging:

- First, the gas flow rate must be high enough as to ensure reasonably high Reynolds number. This will make the method competitive with simpler but computationally more demanding scale-resolving methods like LES. As demonstrated in previous Chapters, IIS-RSM proves its industrial competitiveness through the overall savings in the mesh, which justifies its numerical complexity. On the other hand, gas flow rate must not be too high, since only the fully dispersed, bubbly flow regimes can be adequately captured with EL method. Other flow regimes typically present in the pipe-like conduits, such as churn-, cap-, slug- and annular regimes (for details, see Whalley (1996)) will require cross-hybridisation of EE, EL and VoF models with current methodology, which is beyond the scope of this work.
- Flow case should be well documented, especially from the point of first- and second-order statistics, transient response of the flow, as well as gas void fraction in order to enable proper validation of model.
- Flow conditions, domain geometry as well as bubble size should be optimally combined as to allow the cell size small enough to resolve the most dominant flow features, while at the same time, keep the bubble diameter small enough,

as not to violate the Milelli criterion. ( $1.2 < \Delta/d_b$ ). Violation of this lower mesh limit may lead to the inaccurate solution due to the partial resolution of the bubble wake. This criterion proved to be substantially problematic from the standpoint of wall bounded bubbly flows, where the integration through the viscous sublayer is needed. Due to the violation of Milelli criterion in the vicinity of the wall (high  $Re$  directly corresponding with very thin near wall cells), interpolation stencil will not be able to correctly capture the interfacial forces, thus falsely predicting the flow. Although this may be circumvented by the usage of wall functions, introductory section of Chapter 6 posed the argument that wall functions produce inaccuracies in the solution, under the conditions of non-homogeneity, especially in predicting second-order statistics. An illustrative example represents the upwardly directed bubbly flow through the sudden expansion, as reported in the experimental study by Fdhila et al. (1991). Although the correspondingly high Reynolds number, as well as detailed spatial distributions of measured quantities were provided, flow configuration posed several simulation problems:

First, based on the authors experience, the fully developed nature of two phase flow at the inlet proved very challenging to obtain. Although this problem may be alleviated by the prescription of boundary values for all Eulerian fields, Lagrangian parcels do not possess such a feature, which deems the initialization of the correct inflow field extremely challenging. On the other hand, EE method proved to be unstable in combination with IIS-RSM and false predicting when combined with meso-scale mesh. Hence, no viable solution for the treatment of inlet with scale-resolving simulations could be found. Second, it is overall questionable how the integration through the viscous sublayer, as well as the overall interpolation between the phases should be treated. Namely, since the single bubble encompassed around 4% of the small pipe diameter (as given in Ullrich (2017)), it is assured that the interpolation stencil will produce some errors in assigning the interfacial forces. A very interesting remedy for this problem is given in the works of Caliskan and Miskovic (2021), who proposed a chimera-like approach, involving the usage of two separate meshes for a single EL case: one fine for the Eulerian fields, and the other coarse, for the Lagrangian particles, which are fulfilling the Milelli criterion. In this work though, this approach was not used due to the programming complexity and time limitation. For the future works with Euler-Lagrange flows with the usage of scale adaptive simulation paradigm, this approach should be of highest importance to the researcher.

All the mentioned items represent a very narrow-band filter for the test cases which may be used for validation of IIS-RSM, as well as for other scale-resolving strategies. This was reflected onto the scientific community, where the number of various geometries and flow configurations remains very small. Henceforth, two distinct experimental configurations, widely dominating in the published literature



will be tested. First: a wall bounded bubble column experiment, and the second: turbulent bubbly jet in the wide domain, where the influence of nearby walls possesses a minute effect on the bubbly plume.

## 8.1. Gas-liquid flows in wall bounded domains: bubble column case

Concerning the validation of wall bounded bubbly flows by the scale resolving methods, various researches use the famous bubble column experiment, reported in N. G. Deen et al. (2000a), N. G. Deen et al. (2000b) or N. Deen (2001) almost by the rule. Here, the flow geometry represents the rectangular domain with the square base of the width  $W$ , filled with stagnant water to the height  $H$ . At the bottom, square sparger of the dimension  $S$  serves to inject dispersed air bubbles throughout the domain. Schematics of the domain, including the coordinate axes and up to scale visualisation of bubbles is presented in Figure 8.1. Bubbles are colored based on their instantaneous velocity, which will be the object of discussion later on. Reported results include detailed first- and second-order statistics for liquid and gas phase, which makes this flow case extremely valuable for the researches. This is reflected in numerous publications who investigated the application of different modeling strategies for turbulence, as well as for the inter-phase closure. In the following, exemplary publications relevant to the field of scale-resolving simulations, dealing with the flow geometry reported in Deen's case will be mentioned. Practically from the beginning, LES models such as Smagorinsky and dynamic Smagorinsky proved advantageous and generally offered better results in comparison with RANS models. Dhotre et al. (2013) published a very detailed study, discussing the application of LES for dispersed bubbly flows, including multiple guidelines for the scale-resolving simulations as well as recommendations for the future research. Interestingly enough, they recommended the value of Smagorinsky constant  $C_S$  to be parameter subjected to optimisation, rather than to have the notion of modeling constant. This highlighted the complex nature of turbulence modeling in multiphase flows, even for numerically simple models belonging to Smagorinsky family.

Stephens et al. (2015) tested Euler-Lagrange method in conjuncture with 4 different closure combinations for lift and drag, as well as 4 different values for the Smagorinsky constant  $C_S$ . Overall agreement with the data was reasonably good, although no definitive conclusion could be drawn in relation to the optimal choice of closure laws. It was found that the vertical fluctuation intensity depends more strongly on the value of  $C_S$  than the horizontal one, and lower values for  $C_S$  gave more accurate predictions, pointing to the advantageous nature of suppressed numerical diffusion for such flows.

Masood et al. (2015) used Euler-Euler method in combination with three different turbulence models:  $k - \varepsilon$ ,  $k - \omega - SST - SAS$  and  $k - \omega - SST - SAS$  coupled with Sato model (Sato and Sekoguchi (1975)) for the bubble induced turbulence.  $k - \varepsilon$

model showed least accurate performance of all, leading to the large asymmetry in the velocity profile. This was attributed to the existence of large-scale, meta-stable vortices in the flow, whose switching was evidently suppressed through the higher diffusivity of the  $k - \varepsilon$  model. In general, similar prediction will always be achieved with globally unstable flows. Scale-adaptive strategy in combination with BIT produced reasonable agreement in terms in first order statistics. Levels of turbulent kinetic energy were also predicted reasonably well, although some notable under-predictions were present at certain points. When compared with previous works by Dhotre et al. (2013), no significant difference in performance was found.

Ma et al. (2015) reported an Euler-Euler simulation of the Deen's case, with usage of Smagorinsky LES, as well as  $k - \omega - SST - SAS$  model. Performance of both models with and without the Sato BIT modeling was investigated. Both LES and SAS gave very similar results in terms of mean velocity, turbulence as well as spectral resolution. It was also found that the introduction of BIT increases the effective viscosity to the point where the fluctuations are more dominantly dumped, distorting the obtained profiles. Hence, better agreement with the results was found without the introduction of BIT.

Asad et al. (2017) reported a very detailed Euler-Lagrange study, investigating multitude of modeling parameters, including the three different modeling closures for the drag force, as well as the effect of different injection strategies (three different injection configurations and three different gas inflow velocities). As a sub-grid model, DDES Spalart-Almaras (P. R. Spalart et al., 2006b) was used. Interestingly, none of the previously tried combinations of parameters lead to the ultimately superior performance in producing experimental results. Generally, all models under-predicted the level of turbulent fluctuations, although the prediction of mean velocity magnitude may be deemed satisfactory. Importantly, this work demonstrated that the final outcome showed very little dependence on the initial velocity of the injected bubbles, which will be used when setting the initial conditions in this work.

Masterov et al. (2018) performed the EL simulation of Deen's case using 2 different LES models (Vreman - Vreman (2004) and Smagorinsky), as well as 3 different DES methods, with  $k - \varepsilon$ ,  $k - \omega - SST$  and Spalart-Almaras models for residual turbulence. Although the results for liquid velocity showed reasonable accuracy for all the turbulence models used (except for DES Spalart-Almaras, which showed substantial deviations), results for turbulent kinetic energy showed some notable deviations from the experimental results, independently of the DES model used.

Liu and Li (2018) used Euler-Euler strategy in combination with with dynamic Smagorinsky model, and compared their results with  $k - \varepsilon$  model. Again, LES proved superior and the overall results were satisfactory both from the standpoint of first and second-order statistics. Additionally, grid to bubble size spacing ratio was tested, and it was found that the cells comparable with the bubble scale  $\Delta/d_b = 1.25 \div 1.5$  showed superior solution in comparison with either coarser or finer cells. No substantial difference in result was made by using the Sato BIT modeling. Through

the frequency analysis of velocity signal, they found an additional spectral slope of  $-25/3$  to be valid in the high frequency region, deviating from the  $-5/3$  law. Origins of such a deviation however remained unclear, and need to be subjected to further research efforts.

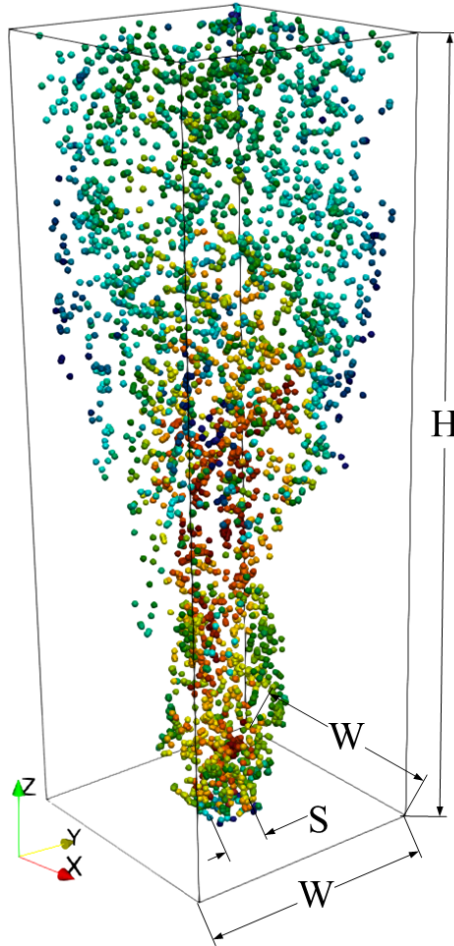


Figure 8.1.: Schematics of the computational domain in DEEN's bubble column case, with indication of dimensions, as well as visualisation of bubbles. Coloration of bubbles indicates their instantaneous velocity, with color-bar intentionally being left-out.

As already said, considering the application of IIS-RSM within the bubble column case, a very detailed study involving the Euler-Euler framework was published in Ullrich (2017), with accurately captured both first- and second-order statistics for

the gas and liquid phase. Here, no utilisation of additional BIT models was necessary. In general, previous publications showed that all scale-resolving simulation strategies offered mostly similar results, with highest accuracy achieved when the characteristic mesh size was in the range of bubble diameter. This could point to the conclusion that LES methods represent an optimal choice due to the numerical simplicity of the model. However, this may pose an advantage only when the bubbly flow occupies the complete or most of the domain volume. In case where the bubbly plume doesn't represent the only significant occurrence in the domain (as demonstrated in the following Chapter), usage of LES like methods may prove to be too costly for industrial use. Therefore, testing of scale-resolving models has a distinct requirement.

Concerning the simulation setup and boundary conditions, dimensions of the domain are set according to the reference:  $W = 0.15 [m]$ ,  $H = 0.45 [m]$ . Sparger width is set to  $S = 0.037 [m]$ . Total of 49 air-injection points are uniformly distributed across the sparger surface, corresponding in full with experimental reference. Superficial gas velocity  $J_G = 0.0049 [m/s]$ , calculated over the entire cross-sectional area, is provided from the experimental reference as well. Uniform bubble size of  $d_b = 4 [mm]$  is prescribed to each computational parcel, and during each second of the simulation time, 3358 bubbles with zero initial velocity are injected at the sparger surface. Considering the bubble forces, models for drag-, lift-, virtual mass, far-field, gravity- and buoyancy force are taken from Chapter 2 without modification. As provided in Chapter 3, two models for Bubble Induced Turbulence (BIT) will additionally be tested: an anisotropic model derived by Ma et al. (2020), as well as isotropic model by Troshko and Hassan (2001), thus making three simulation test cases in respect to the BIT treatment. As for the Eulerian phase, no-slip boundary conditions were used for velocity on each of the wall boundaries, except on the sparger and on the free surface. Although this case represents a wall bounded flow, regions of dominant interest are located centrally in the plume, which means that the under-resolution of the wall boundary layer doesn't carry the decisive role in the reproduction of experimental data. In order to simplify the model, free surface boundary is approximated with the free-slip wall. Extensive discussion of validity of this so called *rigid-lid* approximation will follow in the next Chapter, where also the appropriate modifications of turbulence boundary conditions on the free surface will be derived. Uniform cell size of  $\Delta x = \Delta y = \Delta z = 5 [mm]$  was used, thus ensuring that  $\Delta/d_b = 1.25$ . Physical properties for both phases are listed in Table 8.1.

Table 8.1.: Physical properties of liquid- and gas phase.

$\rho_l [kg/m^3]$	$\rho_g [kg/m^3]$	$\nu_l [m^2/s]$	$\sigma [N/m]$
999.19	1.225	$1.14 \cdot 10^{-6}$	$72.8 \cdot 10^{-3}$

For each of the simulations, initial state is set with zero-velocity and zero turbulent kinetic energy for the liquid phase, without any bubbles in the domain. Injection of gas phase is coincident with the start of the calculation. After the injection start,

certain time is needed for the transfer of kinetic energy, first between the bubbly-phase and the continuous phase, as well as between resolved and modeled flow, and finally directly between bubbles and modeled flow (if any BIT models are used). Due to this time delay, onset of the averaging needs to be determined based on the energy transfer dynamics, and not solely upon reaching the quasi steady number of particles in the domain.

Three integral parameters were therefore followed in order to correctly determine the start of the averaging period:

- 1) Total volume occupied by the bubbles:

$$V_{bubbles} = N_{bubbles} \frac{d_B^3 \pi}{6} \quad (8.1)$$

- 2) Total kinetic energy contained in the resolved scales:

$$K_{resolved} = \sum_{i=1}^{N_{cells}} \frac{1}{2} \rho_i \vec{U}_i \cdot \vec{U}_i V_i \quad (8.2)$$

- 3) Total kinetic energy contained in the modeled scales:

$$K_{modeled} = \sum_{i=1}^{N_{cells}} \frac{1}{2} \rho_i tr(R_{ij}) V_i \quad (8.3)$$

Once that all three parameters reach an apparent steady-state behaviour (either constant value, or constant mean and variance), it can be concluded that the delay in energy transfer is terminated and that the averaging process may begin. On average, 3400 parcels are present in the domain in each instant. Instantaneous view of the column outline, with the visualisation of bubbles is shown in Figure 8.2 for 6 consecutive time instances. Here, case without BIT treatment is used for demonstration. After the injection, bubble plume exhibits a toroidal evolution pattern, with maximum in bubble velocity located in the plume center.

After reaching the free surface, computational parcels, representing the bubbles, are eliminated from the domain, whereas those captured by the recirculation vortices are reintroduced into the plume. In Figure 8.3, protrusion of generated instabilities into the domain is visualised on the iso-surfaces, depicting the magnitude of instantaneous vorticity. Identical time instances as in Figure 8.2 are shown. As seen, initial resolved structures are located in the plume wake due to the vertically oriented advection. In Figure 8.4, streamlines of the mean flow are presented for all three cases. Large-scale vortex pairs serve as a transport medium for the resolved turbulence, which gradually fills the whole domain. In the background, intensity of the vertical velocity component is shown. Due to the continuity, flow transported upwardly in the center is forced to recirculate to the bottom, creating a characteristic pair of vortices. No substantial differences in velocity magnitude, as well as in the topology of the velocity field are observable. Regions of the velocity maximum are

## 8. Flow configuration IV: Two phase flows in buoyancy driven bubble columns

coincide with the plume center, whereas the elliptical zones of equal velocity are spreading concentrically around it. Centers of largest vortex pairs are located in the vicinity of the column walls, with another pair of vortices located near the bottom.

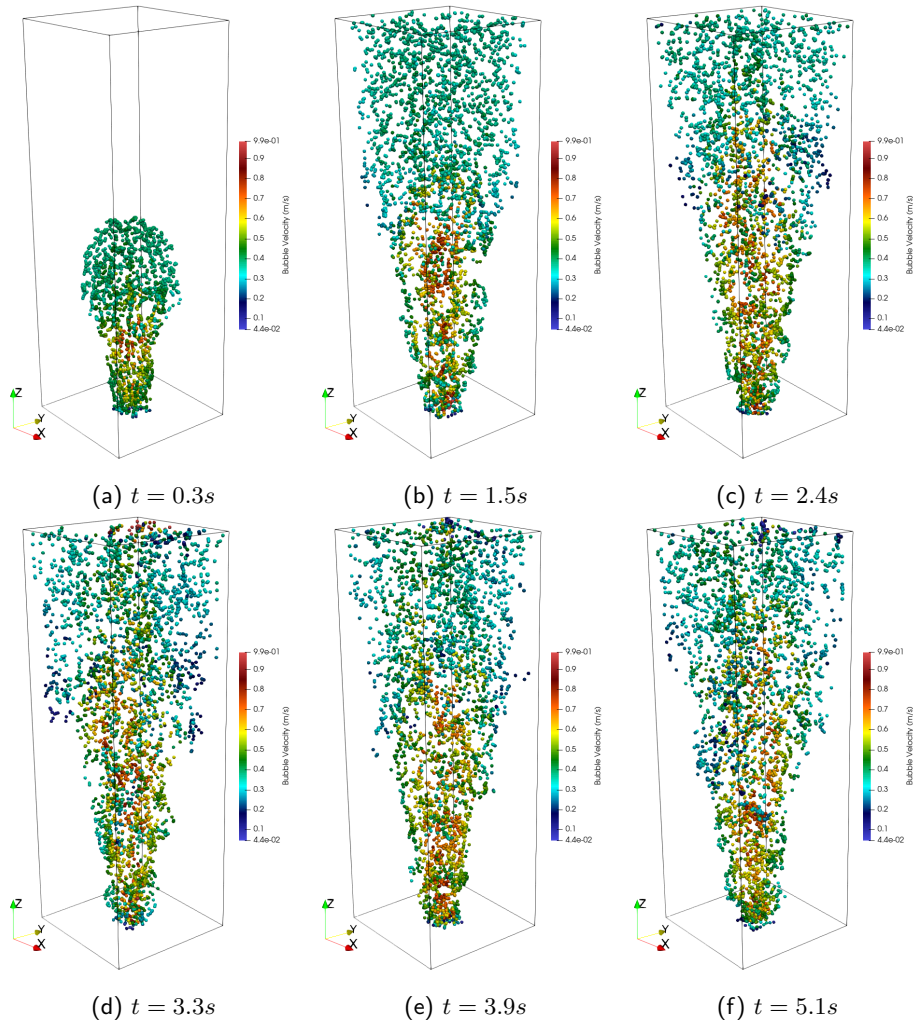


Figure 8.2.: Visualisation of instantaneous bubble positions, with coloring indicating the instantaneous velocity magnitude of individual bubbles.

## 8.1. Gas-liquid flows in wall bounded domains: bubble column case

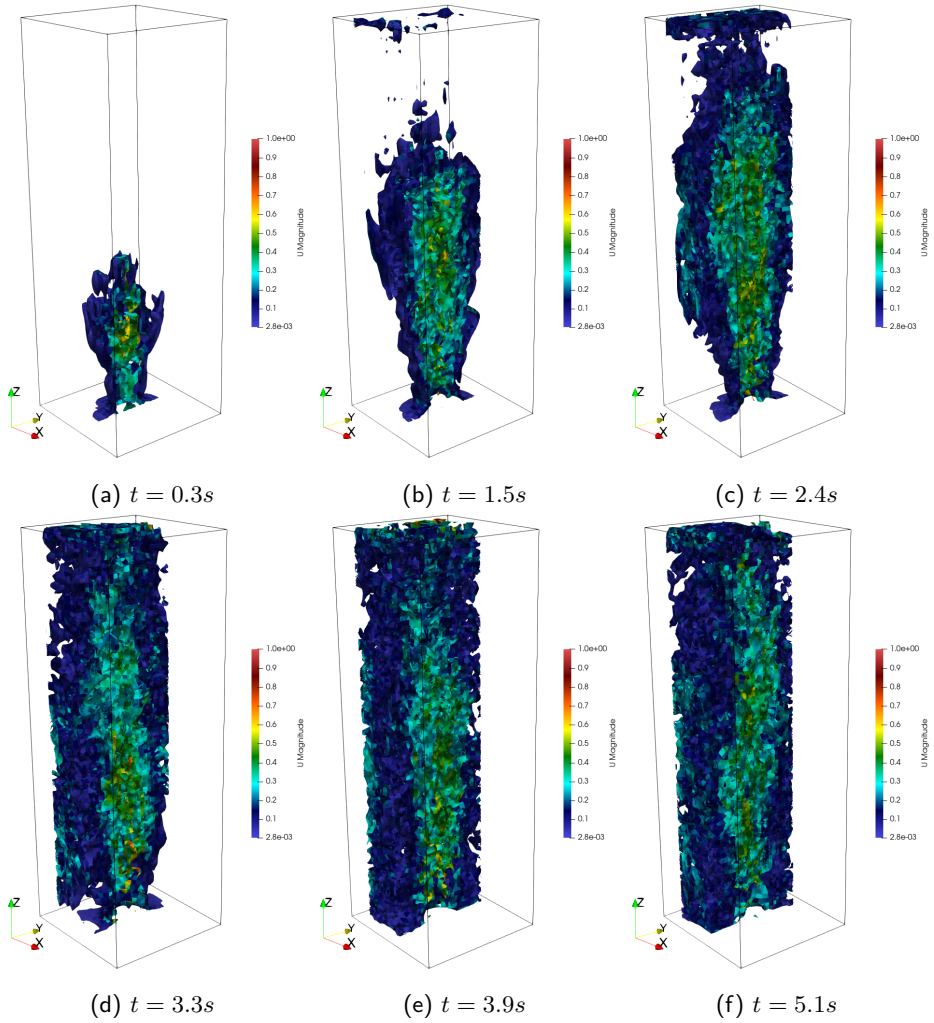


Figure 8.3.: Visualisation of resolved turbulence protrusion into the domain: iso-surfaces, depicting the instantaneous vorticity levels are shown. Background coloring depicts the instantaneous velocity magnitude.

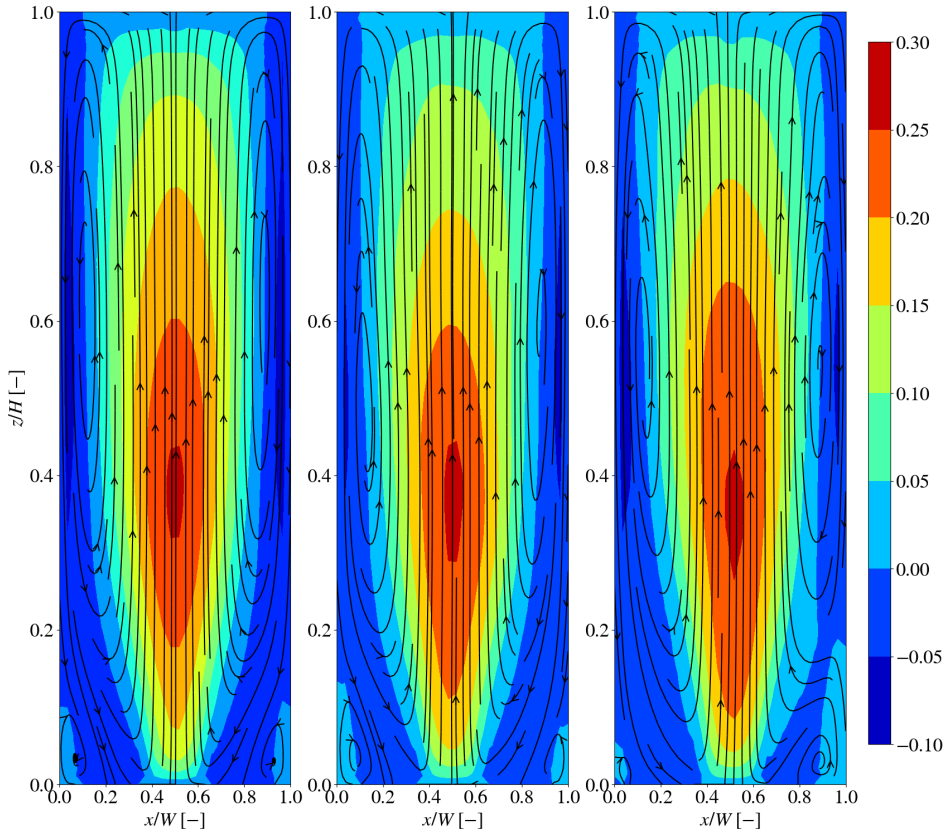


Figure 8.4.: Streamlines of the mean velocity field. Background coloring denotes the vertical velocity magnitude for cases without BIT (left), with anisotropic BIT (center), and with isotropic BIT (right).

Contours of modeled kinetic energy ratio have been plotted in Figure 8.5. All plots have been normalized by the maximum ratio of modeled turbulence kinetic energy, which corresponds to 4%, 48% and 36% for cases without BIT, with anisotropic BIT, and isotropic BIT respectively. For the case with no BIT, flow is least resolved directly on the free surface, where the modeled portion of spectrum reaches around 4%. This zone resembles to a certain extent an impinging jet case. Spectral resolution changes substantially with the introduction of BIT terms. As can be seen in Figure 8.5 center and Figure 8.5 right, transfer of energy created in the bubble wake occurs immediately after the plume injection, although at different levels. With the anisotropic BIT treatment, modeled kinetic energy ratio reaches almost 50% close



to the injection point. In the isotropic BIT case,  $16 \div 20\%$  is modeled. Also, zone of the increasingly modeled spectrum is stretched further upward, whereas in the isotropic BIT case, is limited to the injection zone.

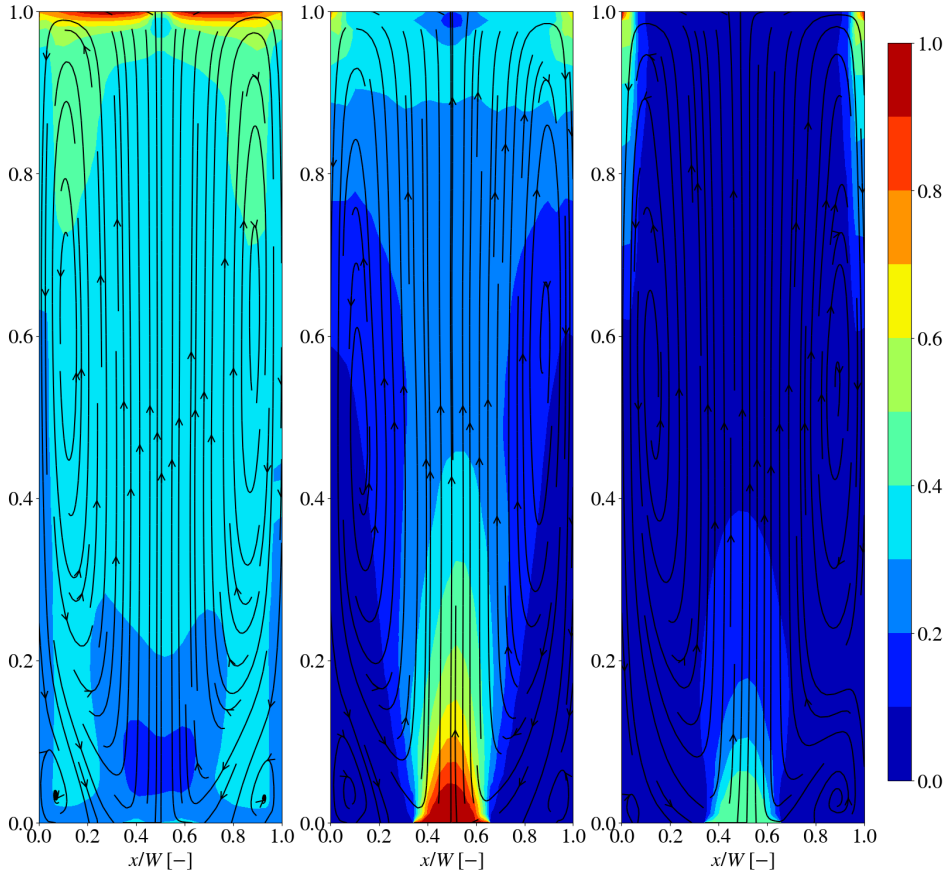


Figure 8.5.: Contours of normalized turbulent kinetic energy ratio for the case without BIT (left), with anisotropic BIT (center), and with isotropic BIT (right). Contours normalized by the maximum in modeled turbulence kinetic energy, respectively: 4% (left), 48% (center) and 36% (right).

Anisotropy of turbulence, reflected in the contours of Lumley's flatness parameter  $A$ , is shown for all three cases in Figure 8.6. It can be seen that for all three cases, central region of the plume remains highly isotropic, with  $A$  having the value very close to 1. Further away from the plume center, and coincidentally with the recirculation vortices, turbulence tends to the more anisotropic state, indicated by the lower value of  $A$ . This is likely a consequence of the suppression of horizontal

component of turbulence fluctuations further away from the plume zone. A non-intuitive artifact occurs in the isotropic BIT case as seen in Figure 8.6 (right), where in the upper zone of the plume, large-scale asymmetry in the flow can be spotted. This can be attributed to the possibly insufficiently long averaging time.

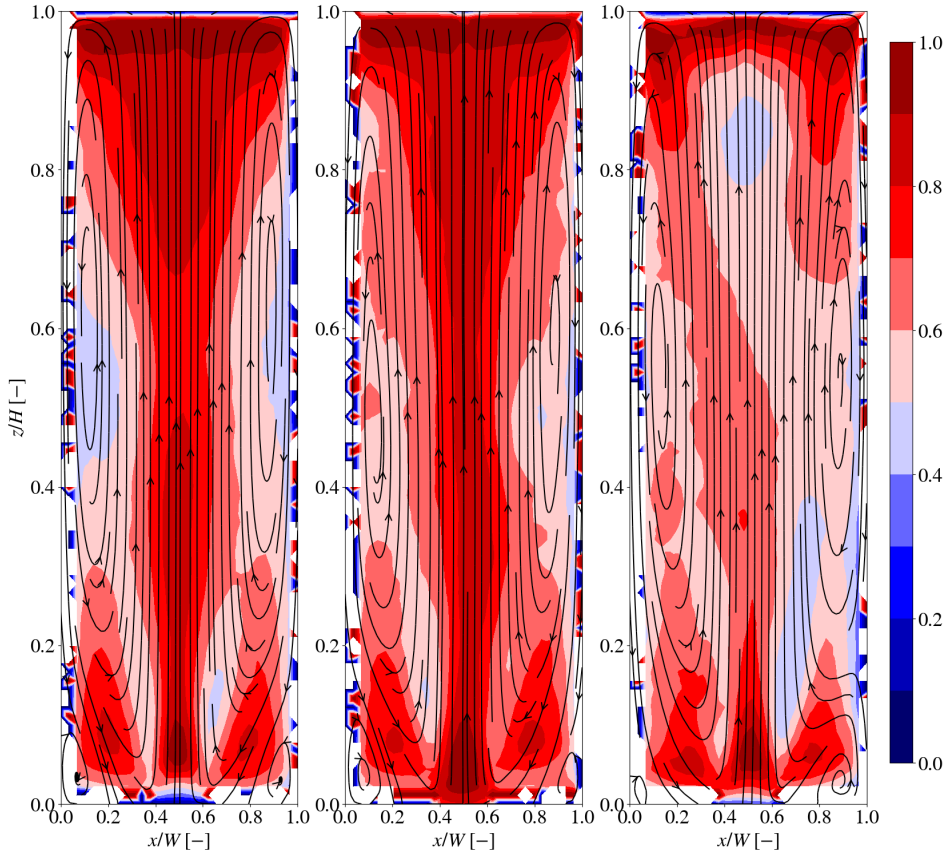


Figure 8.6.: Visualisation of turbulence anisotropy through the contours depicting the value of Lumley's flatness parameter  $A$  for cases: without BIT (left), with anisotropic BIT (center), and with isotropic BIT (right).

For the validation of results, first- and second-order statistics is plotted, using the experimental samples on two horizontal lines, located at  $z/H = 0.63$  in Figure 8.7 and at  $z/H = 0.72$ , as shown in Figure 8.8. Concerning the vertical component of the velocity field, all three models give accurate predictions which stand in almost full congruence with the data, with minute differences between them. Meticulous inspection of the profiles may deem the isotropic BIT case to be least accurate,

although only by the small magnitude. Concerning the prediction of vertical velocity fluctuations, the best results are produced by the anisotropic treatment of BIT, where the prediction follows the experimental data at closest. Double peaks in the experimental data are successfully met both by the case without BIT, as well as the anisotropic BIT, though slightly underpredicted by the former. Isotropic treatment of BIT performed by far the worst, resulting in underpredictions of vertical fluctuations, as well as missing the profile shape, having only one characteristic peak in the centre.

In the case of horizontal fluctuations, case with no BIT treatment performed the best, matching the data in the middle with high accuracy, whereas the isotropic BIT gives comparable results. Here, anisotropic BIT model gives some slight over-prediction. When comparing the calculated levels of turbulence kinetic energy, it can be stated that case without BIT, as well as with anisotropic BIT treatment give overall very similar results for  $k$ , not only in magnitude, but also in shape of the profile, matching the double peaks. Isotropic BIT model failed to predict this behaviour, although correctly matching the level in the column center. Predicted intensity of turbulence fluctuations is not significantly increased by the usage of BIT models for this class of flow conditions, which served as an additional redistribution mechanism, rebalancing the resolved and modeled portions of the spectrum. This is further confirmed by inspecting the ratio of modeled-to-total turbulence kinetic energy. Spectral cut-off is as expected at its lowest with no usage of BIT models (around 1%), and nearly doubled with the usage of isotropic BIT model. At its extreme, by using the anisotropic BIT model, level of modeled turbulence has increased more than 10 times in comparison with the case without BIT. However, since no notable changes can be spotted at the overall levels of turbulence kinetic energy, previous argument concerning the redistribution of energy remains valid. Lastly, value of the Lumley's flatness parameter  $A$  was plotted in order to evaluate the influence of the model to the anisotropy. Again, no significant change has been spotted between the cases with no BIT, and anisotropic BIT, suggesting the high quality of the predicted turbulence is for this class of bubbly flows. Isotropic BIT model leads to the largest anisotropy in the predictions, most likely due to the suppressed horizontal fluctuations.

Finally, frequency response of the velocity field, sampled at two different positions is shown in Figure 8.9. In spite of some minute differences between the obtained signals, all three BIT treatment methods produce almost identical spectral signatures. Several low frequency peaks in the range  $f = 0.5 \div 2$  [Hz], probed closer to the sparger are visible in the signal, indicating a possible low-rank switching of the plume. By going further upwards, signal gets more smooth, indicating the vanishing influence of the plume switching. Both spectral signatures show a physically sound  $-5/3$  slope in the low frequency region, immediately followed by the  $-25/3$  slope, which is in accordance with other studies of such case, for example LES by Liu and Li (2018).

8. Flow configuration IV: Two phase flows in buoyancy driven bubble columns

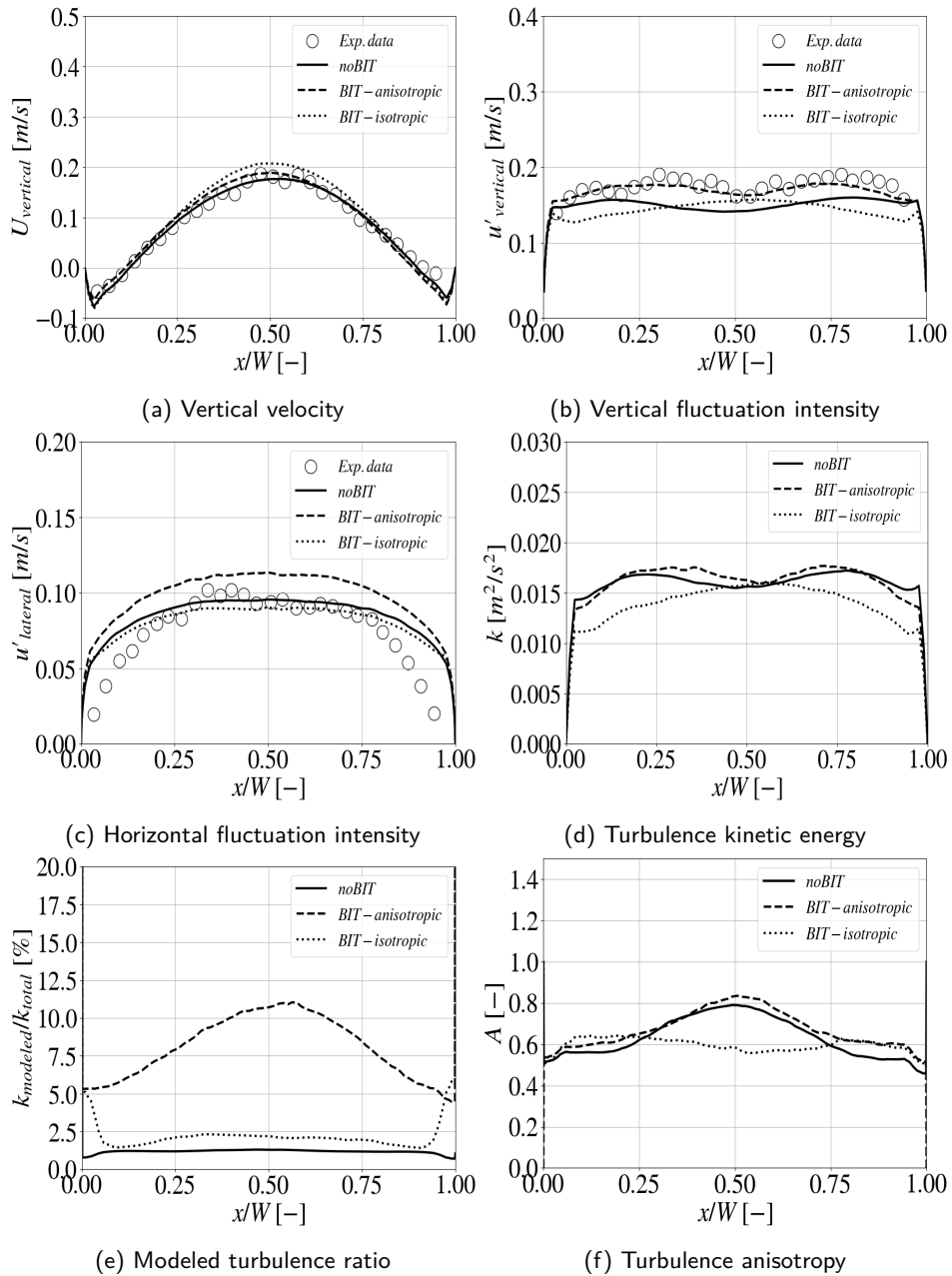
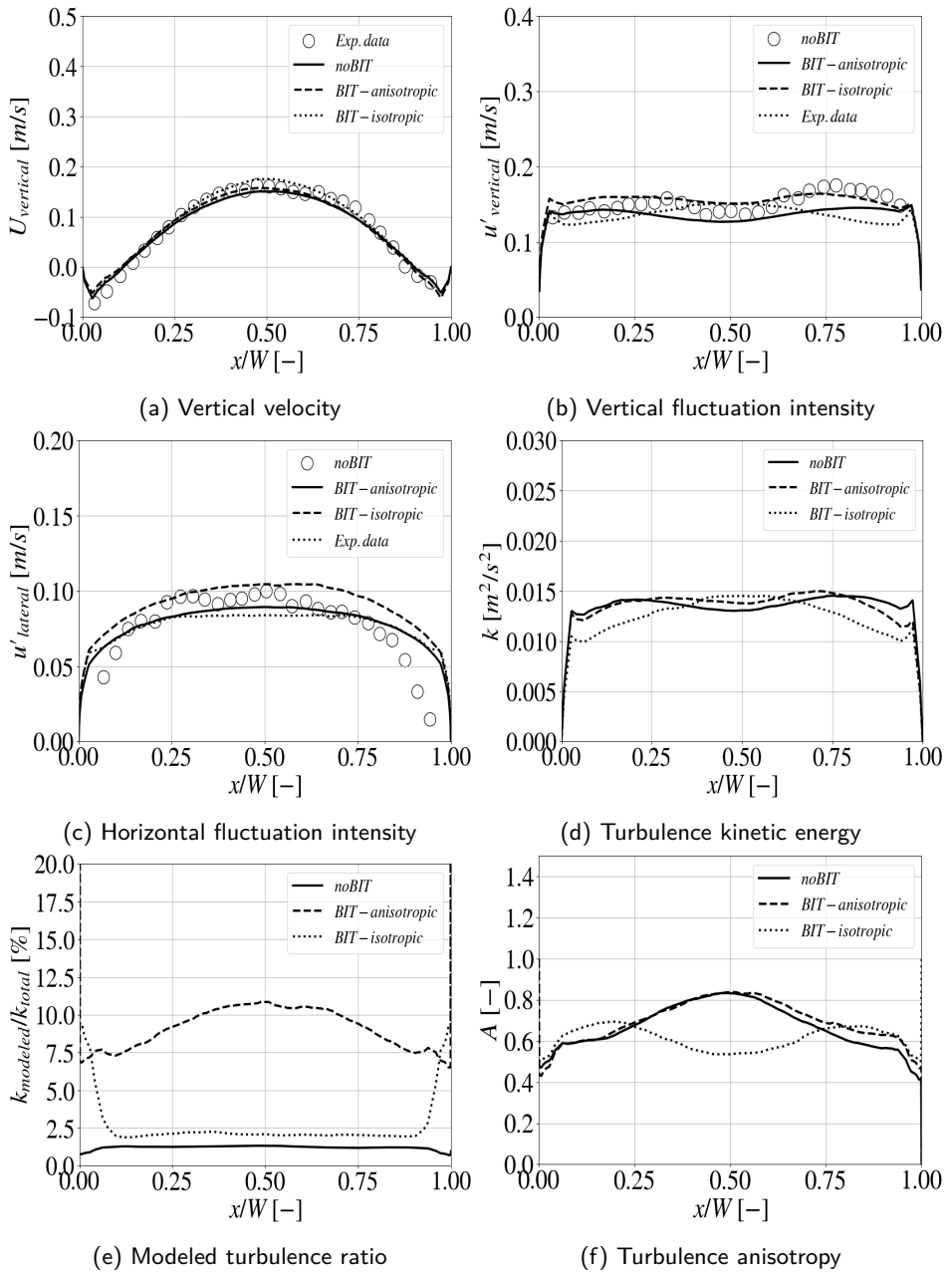


Figure 8.7.: Comparison of calculated and experimental results for  $z/H = 0.63$ .


 Figure 8.8.: Comparison of calculated and experimental results for  $z/H = 0.72$ .

## 8. Flow configuration IV: Two phase flows in buoyancy driven bubble columns

---

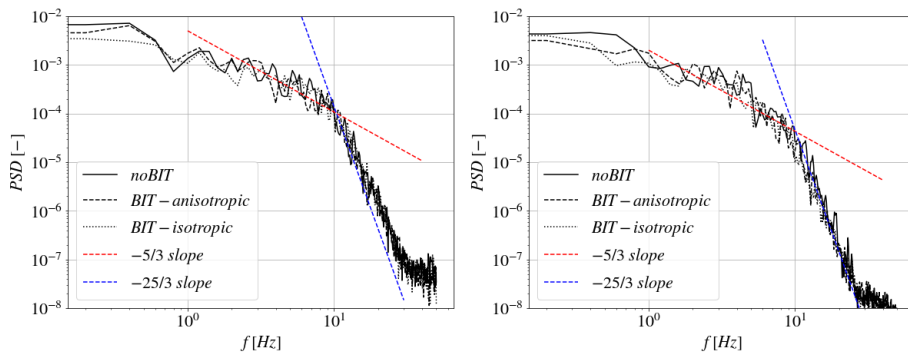


Figure 8.9.: FFT Analysis of the velocity magnitude signal, sampled in the column center at  $z/H = 0.152$  (left), and  $z/H = 0.352$  (right). All three cases of BIT treatment are cross-compared.

## 8.2. Bubble plume in quiescent water

After the fruitful analysis of the bubble column geometry, it was decided to apply the IIS-RSM onto yet another important industrial case, involving the bubble plume in the large domain filled with quiescent, non-stratified liquid. Impact of the recirculation zones and wall presence can be almost completely neglected. As will be stressed in the next Chapter, such a flow configurations are regularly met in the areas of geophysical and atmospheric flows, where the application of LES-like methods is still largely prohibitive from the standpoint of needed resources. It is expected that the usage of hybrid methods like IIS-RSM should enable the prediction of flow characteristics with comparable quality as with LES, while at the same time achieve the substantial savings in the mesh. Also, selected cases are (in spite of the dispersed flow regime) characterised by elevated void fractions in the range which should lead to a more significant contribution of BIT. Injection of energy into the modeled scales will therefore carry more influence with increasing void fraction of bubbles. This should help better understand the advantages and disadvantages of BIT models used.

In total, two experimental cases were chosen for simulation: bubble plume in the gas stirred, conical ladle by Johansen and Boysan (1988) and the bubble plume in the cubic domain, by Fraga et al. (2016). In both cases, aquarium stone is placed at the bottom of the symmetrical domain, filled with initially quiescent water. After the beginning of the injection, nearly mono-disperse plume develops in the domain. Instantaneous view of both cases is shown in Figure 8.10, where the bubble parcels are shown up to scale. Overview of the applied geometric and flow conditions is given in Table 8.2.

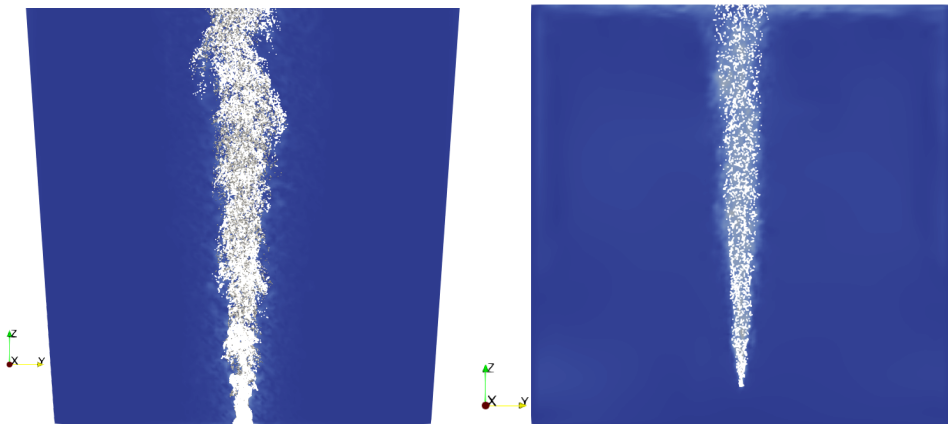


Figure 8.10.: Visualisation of the bubble plume in the cone ladle by Johansen and Boysan (1988) (left), and in the squared domain by Fraga et al. (2016) (right).

Table 8.2.: Geometrical and flow conditions for both bubble plume experiments.

	Case No. 1	Case No. 2
Domain	Cone ladle	Cubic
Base dimensions [m]	0.93x1.1	1x1
Height	1.237	1
Gas flow rate [mm <sup>3</sup> /s]	470,000	8,333
Mean bubble diameter [mm]	3	2

For both cases, identical initial and boundary conditions, as well as fluid properties were set as in the case with bubble column. As for the meshing strategy, multi-block hex meshing was employed. Additionally, in the plume zone, cells were split successively along all three principal axes, as to satisfy the Milelli criterion. In Figure 8.11, top view of the mesh for both cases is shown.

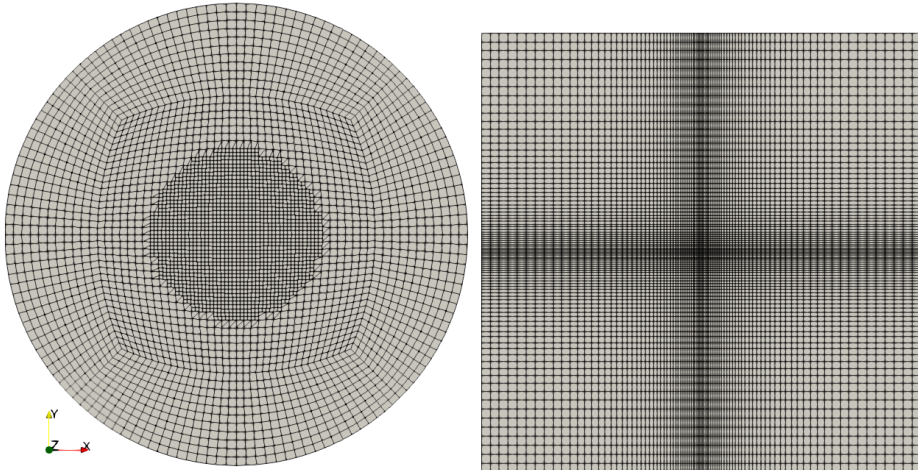


Figure 8.11.: Meshing view for the case of Johansen and Boysan (1988) (left) and Fraga et al. (2016) (right). Note the central refinement needed for the fulfillment of Milelli criterion.

However, final results have proven most disappointing from the standpoint of resolved turbulence. Namely, both cases ultimately return to a RANS solution, with no, or very little resolved turbulence. In order to initially explain this result, visualisation of the resolved turbulence progression is given for the first case, which is characterised with higher gas flow rate. Six different time instants are given. Additionally, results are compared with LES-WALE model in order to investigate the reason for the steady state progression.



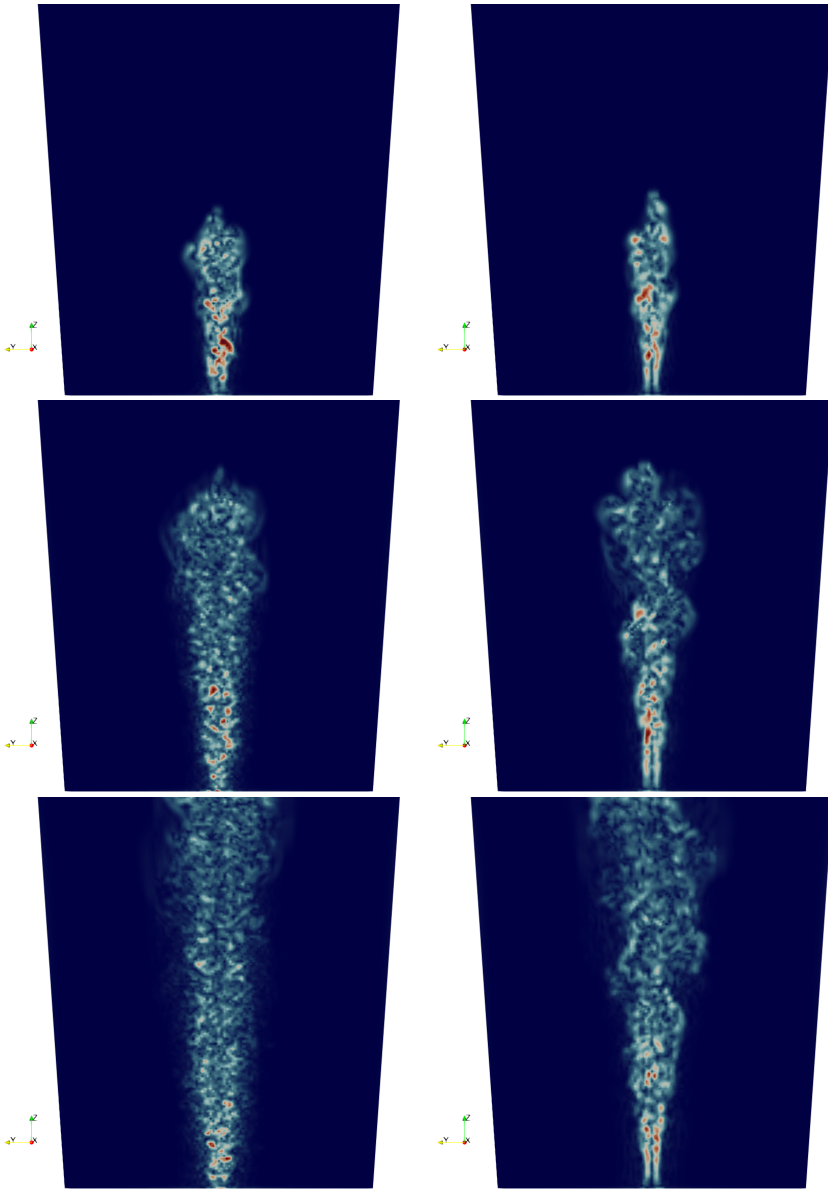


Figure 8.12.: Comparison of IIS-RSM (left column) and LES-WALE (right column) performance in the first case, for time instants:  $t = 1[s]$  (up),  $t = 2[s]$  (center) and  $t = 3[s]$  (bottom). Coloring indicates the intensity of instantaneous vorticity magnitude.

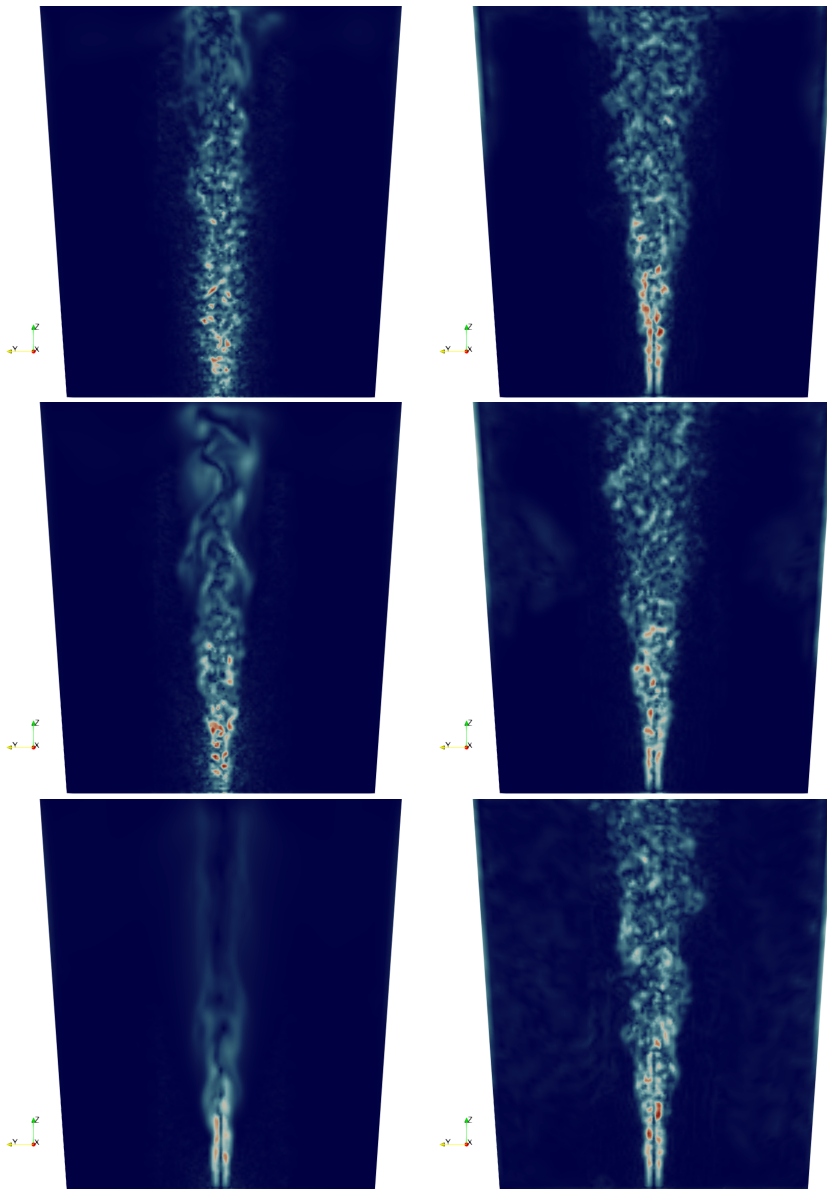


Figure 8.13.: Comparison of IIS-RSM (left column) and LES-WALE (right column) performance in the first case, for time instants:  $t = 6[s]$  (up),  $t = 9[s]$  (center) and  $t = 20[s]$  (bottom). Coloring indicates the intensity of instantaneous vorticity magnitude.

As can be seen, at the beginning of the simulation, followed by the initial few flows through time, IIS-RSM cases show a behaviour very similar to the LES results. However, in the later stages of the plume development, it seems that the IIS-RSM gets progressively diffusive, starting from the top of the ladle and progressing towards the injection point. Identical behaviour is also observed in the reproduction of the case by Fraga et al. (2016) and hence, visualisation concerning their experiment will not be repeated here. Contrary to that, LES-WALE case is characterized by the retention of resolved turbulence. Explanation for such a model behaviour is found by observing the levels of integrated resolved kinetic energy (see equation 8.2) for both IIS-RSM and WALE models, shown in Figure 8.14. Since both cases behaved nearly the same, comparison is performed only in the case of Johansen and Boysan (1988), due to the higher gas flow rate.

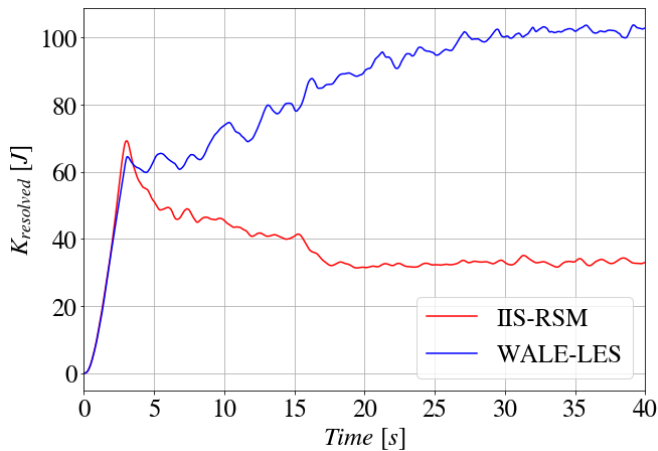


Figure 8.14.: Temporal progression of the integrated resolved, kinetic energy, see equation 8.2, with usage of IIS-RSM and LES-WALE turbulence model.

Up to the certain time instant, levels of resolved turbulence in both WALE and IIS-RSM cases remain nearly the same, which gives almost identical resolution. This is primarily caused by the initialisation of the case: namely, at the beginning of the simulation, both cases have the zero-initialised modeled turbulent kinetic energy. For the IIS-RSM curve, this growth period represents a development time, in which the energy flows from the resolved, towards the modeled turbulence. From the time instant  $t \approx 3$  [s], IIS-RSM curve experiences a sudden change in slope, indicating that the modeled part of the spectrum exhibits increased influence on the resolved part. IIS-RSM fails to recover from this state, resulting in the dropping levels of resolved kinetic energy.

Various numerical remedies were tried out in order to obtain a resolved turbulence solution: from the very aggressive schemes for the convective term, such as pure CD scheme (or in more extreme cases, limited-cubic-scheme), and CN scheme for the time discretisation. It was expected that the numerical perturbations, caused by the highly dispersive nature of the schemes, will ultimately trigger the eddy-resolution capability of the model. Despite of that, IIS-RSM model was always returning towards the unresolved state, provided that the simulation did not blow out due to the aggressive schemes.

Finally, and after a lengthy investigation, attention was drawn to the behaviour of  $P_{\Delta U}$  since it should directly limit the overall growth of modeled turbulence. Surprisingly enough, the value of  $P_{\Delta U}$  was exactly zero in almost entire zone, occupied by the bubble plume! This occurrence is thus worthwhile investigating. By recalling the exact formulation for  $P_{\Delta U}$ , given in 3.66, it is evident that such a distinct value can be achieved only in case when either the second derivative of the velocity field is zero (which is clearly not the case, since the initially generated instabilities are highly resolved), or that the second term  $C_3 T_2$  outweighs the inhomogeneity detection term  $C_2 \sqrt{k} \Delta U$ . Since the role of  $C_3 T_2$  is to provide a full RANS closure to the IIS-RSM in the vicinity of the wall, it can be speculated that the distribution of turbulent quantities in the plume clearly mimics the wall presence, thus eliminating the action of  $P_{\Delta U}$  completely. Although the obvious remedy will be to either recalibrate the model or eliminate the  $T_2$  term, this will render the model useless for the cases of wall bounded flows with free stream bubbly plume, which will be the subject of the next Chapter. Since the obtainment of the resolved turbulence was not possible under the circumstances of this case, testing of BIT models would also not follow.

### 8.3. Conclusions

In this Chapter, performance of IIS-RSM was tested using the Euler-Lagrange framework in the case of buoyancy driven, gas-liquid dispersed bubbly flow. In addition, performance of two models for bubble induced turbulence (BIT) was compared with the case without BIT modeling. Based on the wall-bounded bubble column case, it was concluded that all three models predict the mean flow velocity with high accuracy, whereas the prediction of turbulence was substantially better with usage of either no BIT model, or with anisotropic model. Concerning the impact of the spectral cut-off, it was concluded that the usage of BIT acts as an additional redistribution mechanism, moving the cut-off further up the spectrum. It doesn't notably change the intensity of turbulence in this case.

Afterwards, the model was tested in two different cases of turbulent bubble plumes in the wide quiescent domain, in which the influence of the walls can be mostly neglected. Due to the elevated void fraction of the bubbles, BIT models were expected to have a more significant influence on the solution. Regrettably, it was found that the model was unable to retain the resolved turbulence and very quickly, nearly all resolved scales disappear from the solution domain. It was outlined that the formulation of the  $P_{\Delta U}$  term itself was to blame for such an occurrence. Since the second term in its formulation falsely interprets the plume topology to represent the near wall zone, it renders the  $P_{\Delta U}$  term inactive. Very soon, modeled turbulence starts prevailing in the domain.

At this point, it is important to stress a few additional facts concerning the industrial applicability of the BIT models in conjunction with IIS-RSM. Based on the single phase cases, experience dictates that the small numerical diffusion of the model gives rise to many potential blowout points, meaning that all the used cases need to be properly initialised, and boundary conditions well posed. By adding the additional source terms to the evolution equations for  $R_{ij}$  and  $\omega^h$ , already unstable system is additionally destabilized by adding the explicit correction terms to the right side of the conservation equations 3.39 and 3.67. Although some future improvements can be added through the numerical remedies like implicit correction, cases with additional usage of BIT were not always unconditionally stable in the solution process (in comparison with single phase and no BIT cases). Sometimes, restarting of the simulation coupled with increased number of outer correctors and under-relaxation was needed. Overall, since no substantial improvement in results was obtained by using the BIT models (but what's more, the solution process was destabilized), it was decided that no BIT model will be used in the Chapter 9. Further work on the use of BIT in conjunction with scale-adaptive models is hence strongly encouraged, and additional experimental works dealing with dispersed bubbly flows are therefore urgently needed.



## 9. Flow Configuration V: Bubble plume in open-channel cross-flow

---

Whereas the object of research outlined in Chapter 8 were exclusively cases in which the dispersed gaseous phase was introduced to the quiescent water, modeling of two-phase flows can be substantially more complex if the carrier phase exhibits additional movement, unrelated with the effects of buoyancy force. Turbulence characteristics of such a flows are not only dictated by the parameters of bubbly plume (such as diameter and injection rate), but also through the externally imposed flow conditions. In case of strong secondary currents, as will be demonstrated, rotational symmetry of the bubbly plume is lost, and the two-phase system possesses an externally imposed transient response.

Modeling complexity can be increased if the carrier phase possesses the free surface, where the additional features such as secondary flows are created. Their influence is then superimposed with those of the bubbles. These types of flow patterns are specially relevant in the range of geophysical and atmospheric modeling, as well as in oil-industry, pollutant tracking and many more. Modeling practices for the treatment of free surfaces are in principle dictated by boundary conditions, where in case of the weakly advective flows, inertial forces will be overcome by the effect of gravity and the transient deformations of the free surface could be neglected in comparison with the external dimension of the flow. This effect can be quantified with the *Froude* number:

$$Fr = \frac{U}{\sqrt{gH}} \quad (9.1)$$

where  $U$  represents the free-stream velocity of the flow, and  $H$  the characteristic length scale, usually the depth. In case of  $Fr \ll 1$ , transient deformations of the free surface may be neglected, and a so-called rigid-lid approximation is used, where the free-surface boundary is approximated with the free-slip frictionless wall. Ramos et al. (2019) demonstrated that, in case of low  $Fr$  number, sensitive flow characteristics such as secondary flows and local turbulence intensities can be captured with the high level of accuracy by using the rigid-lid approximation, even if the free surface possesses large-scale stationary deformations, exemplary in open-channel confluences. When all the noted effects are combined within the single case, a non-exhaustive list of challenges is presented to the modeler. Among the most important phenomena that need to be accurately simulated are:

1. Prediction of local and integral characteristics of bubble plume.
2. Prediction of secondary flows and turbulence anisotropy, generated by the complex boundaries and by the bubble motion.
3. Tackling with high  $Re$  flows in terms of the proper turbulence model, operating at reasonable computational cost.
4. Operating at low diffusivity in order to allow large-scale transients to appear in the solution.

Publications related to the numerical modeling of the aforementioned phenomena are not numerous. Exemplary, Mitrou et al. (2018) performed an EL-LES simulation of the bubble plume inside of the narrow open channel at  $Re = 52,363$  without the co-current injecting of air and water. Presented results for the mean velocity were compliant with the experimental data, with around 22 Million cells used. Xiao et al. (2021) performed an EE-LES simulation of the bubble-driven plume in the stratified cross-flow and presented the results for the first-order statistics as a reference. Cell count was reported similar as in the case by Xiao et al. (2021). Le Moullec et al. (2008) performed an EE simulation of the cross-flow gas-liquid wastewater treatment reactor, whereas the performance characteristics of  $k - \varepsilon$  and the Reynolds-Stress-Model (RSM) were compared, and the overall results for RSM showed better congruence with experimental data, although the values of axial velocity were poorly predicted.

Overall, it can be stated that the LES based models predicted the reported velocity fields with a high level of accuracy, whereas the computational burden was mostly prohibitive for the wider industrial application. As expected, results for the RANS simulation study are more dominantly dependent on the model. As an advantage, RANS models required substantially reduced computational burden. None of the previously reported studies provided an in depth analysis of turbulence in respect to its intensity and anisotropy, as well as the possible large-scale transients, whose presence will harden the obtainment of statistically steady results. Since all the used models used exclusively either LES or RANS methodology, problematic concerning the integration of the hybrid, eddy-sensitized RANS model with the free-surface, bubble-laden flows remains open. It is within the scope of this Chapter to partially close this knowledge gap.

An experimental test by Zhang and Zhu (2013) will serve as a data-referencing case. Main part of the experimental facility represents an open-channel with dimensions  $0.65 [m]$  in depth, by  $1.2 [m]$  in width, thus creating an aspect ratio  $A_r \approx 2$ . A steady stream of water is pumped through the channel with the free-stream velocity  $U = 0.2 [m/s]$ , thus creating a moderately high, hydraulic diameter based Reynolds number of  $Re \approx 249,000$ . At the origin, a cylindrical injection column with the diameter  $d_C = 22 [mm]$  is placed. Mixture of air and water is pumped through the nozzle with the diameter of  $d = 6 [mm]$ , placed at the top of the column at the



height of  $h = 120 [mm]$  from the bottom of the channel. All physical properties correspond to Table 8.1, from the previous Chapter. After entering the domain, air-water jet deflects and bends in the direction of the flow, whereas the injected water breaks from the bubbly plume and gets mixed with the oncoming cross-flow. Air plume is discharged from the domain at the free surface. Air and water flow rates can be independently varied, which created a set of 12 different experimental configurations. For this work, an experimental configuration named '3-5' will be reproduced. Visualization of the experimental flow field is given in Figure 9.1. Following the experimental reference, mean bubble diameter remains nearly constant along the trajectory of the plume, and the flow will be considered mono-disperse. An overview of the boundary conditions is given in table 9.1.

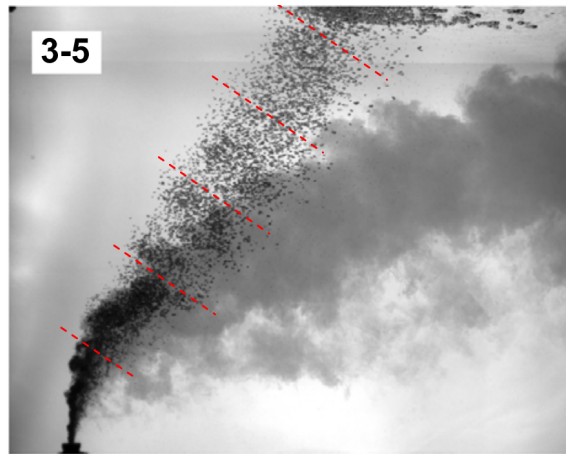


Figure 9.1.: Visualisation of the experimental flow case '3-5', with a dyed nozzle flow. Provided from Zhang and Zhu, 2013.

Table 9.1.: Inflow conditions and geometric parameters.

Width $W [m]$	1.2
Depth $H [m]$	0.65
Aspect ratio $Ar [-]$	1.85
Free stream velocity $U_0 [m/s]$	0.2
Froude number $F_r [-]$	0.03
Hydraulic diameter $D_H [m]$	1.248
Hydraulic diameter based Reynolds number $Re [-]$	249,000
Friction velocity Reynolds number $Re_\tau [-]$	5602
Injected air volumetric flow rate $Q_a [l/min]$	3
Injected water volumetric flow rate $Q_w [l/min]$	5
Mean bubble diameter $d_b [mm]$	2.11
Injection rate [ <i>bubbles/s</i> ]	10,166

Before applying the model in the full scale simulation, its performance needs to be tested in a more simple geometry, in order to assess its prediction capability in open channel flows. Due to the geometrical simplicity, this will normally be done like in previous Chapters, by generating the precursor simulation and adapting the mesh resolution, until satisfactory accuracy has been achieved. Unfortunately, to the authors knowledge, experimental or numerical data for open-channel flow cases at comparable Reynolds numbers are not reported. Therefore, performance of the model will be tested in the case with similar geometry, but with lower Reynolds number. Later on, numerical analysis will then be extrapolated to the main case. Prior to the simulation set-up, some more detailed discussion, pointing towards modifying the boundary conditions on the free surface needs to follow.

## 9.1. Free-surface modeling considerations

As already noted in previous section, due to the relatively low value of  $F_r$ , free surface may be approximated with a free-slip wall, which is better known as a *rigid-lid* approximation. Spectrum is partially governed by the resolved, and partially by the modeled turbulence, thus promoting the need for accurate assigning of boundary conditions for both of the underlying sets of flow variables. If the surface normal coordinate is assigned as  $z$ , then for the free-slip, impenetrable wall one obtains at  $z = 0$ :

$$\frac{\partial U}{\partial z} = \frac{\partial V}{\partial z} = 0, \quad W = 0 \quad (9.2)$$

As for the residual turbulence, a variety of modeling approaches may be used. Whereas the asymptotic value may be assigned to the sub-scale quantities like  $\overline{u_i u_j}$  or  $k$ , treatment of scale determining variable remains open to discussion. Some older date publications, exemplary Gibson and Rodi (1989) suggested a wall-function approach, where the assumption of a linear growth of a turbulent length scale away from the surface is imposed. However, Craft et al. (2000) concluded that the evidence basis for such an assumption lacks, since the results of their free-surface test case provided to be non conclusive. By using the zero-gradient hypothesis, they managed to obtain a qualitatively convincing results in the case of the submerged water jet. Additionally, it is not clear if and how such an approach will affect the resolution capability of the model. Note that the eddy-resolving formulation is based on the integration through the viscous sublayer, whereas the wall-function approach will offer questionable results. With that in mind, an asymptotic boundary conditions need to be derived for six components of  $\overline{u_i u_j}$ , as well as for scale-supplying variable  $\omega^h$ .

Here, a procedure outlined in Swean et al. (1991) will be used. If one assumes the complete destruction of wall-normal fluctuation components on the free surface, and applies the free-slip boundary conditions ( $\partial u/\partial z = \partial v/\partial z = w = \partial^2 w/\partial z^2 = 0$ ), Taylor-like expansion around  $z$  will offer for each fluctuating component:

$$\begin{aligned} u &= a_1 + c_1 z^2 + \dots \\ v &= a_2 + c_2 z^2 + \dots \\ w &= b_3 z + d_3 z^3 + \dots \end{aligned} \quad (9.3)$$

where  $a_i, b_i, c_i, \dots$  are the unknown coefficients, independent of  $z$  (but dependent of the streamwise-  $x$ , spanwise-  $y$ , and temporal-  $t$  coordinate). After cross-multiplication and averaging, one gets:

$$\begin{aligned} \overline{uu} &= \overline{a_1 a_1} + \overline{2a_1 c_1} z^2 + \dots \\ \overline{vv} &= \overline{a_2 a_2} + \overline{2a_2 c_2} z^2 + \dots \\ \overline{ww} &= \overline{b_3 b_3} z^2 + \overline{2b_3 d_3} z^4 + \dots \\ \overline{uv} &= \overline{a_1 a_2} + (\overline{a_1 c_2} + \overline{a_2 c_1}) z^2 + \dots \\ \overline{uw} &= \overline{a_1 b_3} z + (\overline{a_1 d_3} + \overline{b_3 c_1}) z^3 + \dots \\ \overline{vw} &= \overline{a_2 b_3} z + (\overline{a_2 d_3} + \overline{b_3 c_2}) z^3 + \dots \end{aligned} \quad (9.4)$$

Evidently, all wall-normal components of  $\overline{u_i u_j}$  may be assigned with zero-value, Dirichlet-type boundary conditions. Since all the other components of  $\overline{u_i u_j}$  possess a finite value on the free-surface, a simple workaround will be to assign the zero-gradient, Neumann-type boundary conditions to them (note the quadratic dependency of higher order terms). Separate treatment of boundary conditions for different components of  $\overline{u_i u_j}$  may pose certain implementation difficulties. However, inherent instabilities of the model promote an almost complete destruction of modeled turbulence near the surface, as will be demonstrated shortly. This means that zero-gradient boundary condition may be assigned to all of the tensor components, without the notable loss in accuracy, since the major part of the spectrum is governed by the resolved fields, whose boundary conditions are correctly provided.

Additionally, asymptotic boundary conditions for  $\varepsilon_{ij} = 2\nu \overline{\frac{\partial u_i}{\partial x_k} \frac{\partial u_j}{\partial x_k}}$  may be derived. Here, only the normal components of  $\varepsilon_{ij}$  will be investigated. After a lengthy derivation, compression of terms, averaging and neglecting of higher order terms, one obtains:

$$\begin{aligned} \varepsilon_{11} &= E_0^{11} + E_2^{11} z^2 + E_4^{11} z^4 + \dots \\ \varepsilon_{22} &= E_0^{22} + E_2^{22} z^2 + E_4^{22} z^4 + \dots \\ \varepsilon_{33} &= E_0^{33} + E_2^{33} z^2 + E_4^{33} z^4 + \dots \end{aligned} \quad (9.5)$$

where  $E_m^{ii}$  are the coefficients absorbing the derivation, cross-multiplication and averaging of  $a_i, b_i, c_i, \dots$ . As for the dissipation rate  $\varepsilon$ , derivation is straightforward after taking one half of the trace:

$$\varepsilon = E_0 + E_2 z^2 + E_4 z^4 + \dots \quad (9.6)$$

Some obvious differences in relation to the no-slip wall boundary condition are notable: Although the value for  $\varepsilon$  is certainly definite at the free-slip surface, a clear quadratic behaviour around  $z \approx 0$  can be derived for the free-slip wall, as compared to the linear dependence on the no-slip wall. Hence, a zero-gradient boundary condition may be used. By using the same procedure, asymptotic behaviour for  $k = \frac{1}{2} \overline{u_k u_k}$  can be obtained like:

$$k = K_0 + K_2 z^2 + K_4 z^4 + \dots \quad (9.7)$$

Since the free-surface value for  $k$  is definite (due to the presence of streamwise and spanwise fluctuations), zero-gradient boundary condition can be used again. Analogously, the value for the homogeneous dissipation rate  $\varepsilon_h = \varepsilon - \frac{1}{2} \nu \frac{\partial^2 k}{\partial x_i^2}$  is:

$$\varepsilon_h = E_0^h + E_2^h z^2 + E_4^h z^4 + \dots \quad (9.8)$$

Finally, for the specific homogeneous dissipation rate, one gets:

$$\omega^h = \frac{E_0^h}{K_0 + K_2 z^2 + \dots} + \frac{E_2^h z^2}{K_0 + K_2 z^2 + \dots} + \frac{E_3^h z^3}{K_0 + K_2 z^2 + \dots} + \dots \quad (9.9)$$

Since the value for  $\omega^h$  on the wall is finite, validity of zero-gradient boundary condition will be investigated by deriving the previous equation. Only the first term in the expansion will be shown. It is obtained as:

$$\left( \frac{\partial \omega^h}{\partial z} \right)_{z=0} = \frac{2E_0^h K_2 z + \dots}{(K_0 + K_2 z^2 + \dots)^2} + \dots = 0 \quad (9.10)$$

Summarising this section, it has been shown that due to the quadratic behaviour near the free surface, as well as due to the assumption for the over-resolution of the model far away from the (no-slip) boundaries, zero-gradient boundary condition may be enforced for the modeled turbulence variables:

$$\frac{\partial \overline{u_i u_j}}{\partial z} = \frac{\partial k}{\partial z} = \frac{\partial \omega^h}{\partial z} = 0 \quad (9.11)$$

## 9.2. Open-channel developed turbulence

Before proceeding towards the simulation of the complete experimental test case, some additional steps need to be undertaken. If one aims into repeating the simulation procedure from previous Chapters, the precursor simulation will initially be used to test the turbulence model in the conditions of similar geometry, to validate results based on the available experimental data, and to supplement an optimal meshing parameters which will be used in the main case. Turbulence fields generated in the precursor phase will then be mapped to the main case inflow.

However, two difficulties are met, related to the present experimental case. First, despite supplying the detailed measurements for the bubble plume, no data has been reported on the distribution and dynamics of the velocity field. Second, precursor phase is substantially more difficult to validate since, to the authors knowledge, no open-channel DNS/LES simulations cases were reported at Reynolds number corresponding to the main case. Therefore, the numerical workflow will be modified. First, the well documented, lower  $Re$  experimental case will be reproduced, and the obtained results will be analysed. After proving the ability of the model to successfully simulate the free surface flows, the analysis will be extrapolated towards the higher  $Re$  precursor simulation. Tominaga. et al. (1989) reported an experimental open-channel flow case at  $Re \approx 73,100$  with an aspect ratio  $A_r = 2$ . Additionally, Shi et al. (1999) used the identical geometry of the channel, but with somewhat higher Reynolds number ( $Re \approx 91,400$ ) in their LES study. Supplied results include mean streamwise velocity and secondary flows, along with the distribution of turbulence intensity. Within this stage, the LES test case with higher Reynolds number will be reproduced. Due to the geometrical simplicity, block-structured hexahedral meshing strategy was used. Near wall resolution was fine-tuned so as to fully resolve viscous sublayer. Mesh dependency analysis was performed identically as in previous Chapters, and will not be repeated here. After reaching the satisfactory resolution and proper prediction of wall shear stress, mesh size was set to approximately 866,000 cells. An overview of the optimal mesh metrics is given in Table 9.2.

Table 9.2.: Mesh metrics for the first open-channel flow case.

$A_r$	$U_0$	$Re_{D_h}$	$Re_\tau$	$Fr$	$\Delta x^+$	$\Delta y^+$	$\Delta z^+$
2	1.507	90,400	2157	0.54	90	$1 \div 30$	$1 \div 30$

After superimposing the initial perturbation, equations are integrated in time and space. In Figure 9.2, isosurfaces of the instantaneous vorticity are used to visualize the flow. As can be seen, a very resolved flow structures are obtained. Averaging was performed until the secondary flow contours, along with Reynolds

stress components reached convergence. Due to the low intensity of the secondary currents (as will be demonstrated shortly), exceptionally long averaging time is needed for the convergence (around 1300 flows through time).

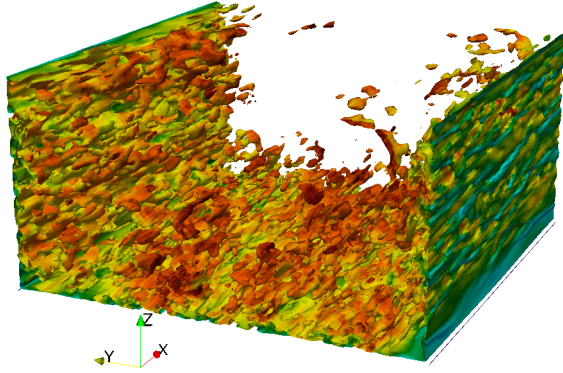


Figure 9.2.: Iso-surfaces of the instantaneous vorticity. Background coloring represents the instantaneous velocity. Identical orientation of coordinates will be used in main case.

In Figure 9.3, cross-sectional view of the channel half-width is shown. Contours of the dimensionless streamwise velocity are compared with an LES reference. A correspondingly good congruence between two data-sets is obtained.

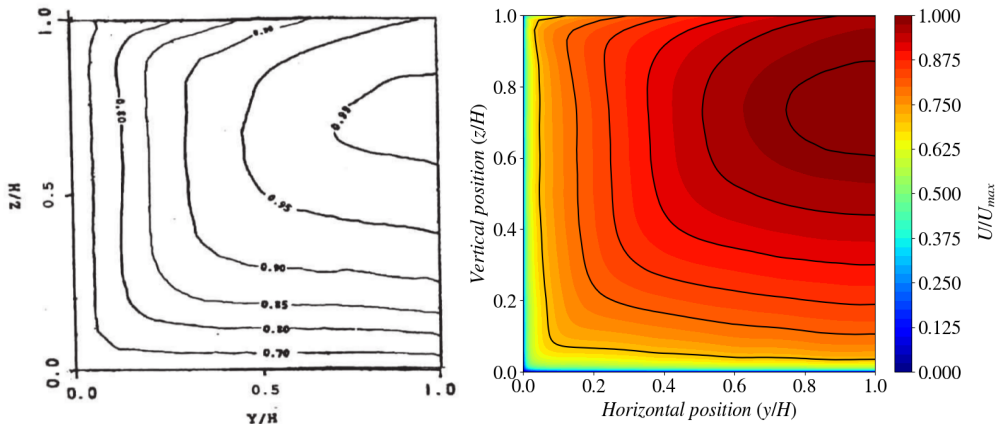


Figure 9.3.: Contours of the streamwise velocity: LES reference (left), and the simulation results (right). Isolines (shown in black) correspond to the same levels in both figures.

One especially notable feature represents the position of the velocity maximum (so called velocity-dip phenomena), which is not located at the free surface, but is rather sub-merged, at the position  $z/H \approx 0.7$ . This phenomena is a standard characteristic of turbulent flows in narrow open channels and can be explained by the presence of strong secondary currents that directly affect distribution of momentum within the flow domain. A more detailed explanation of the velocity-dip phenomena will follow up shortly.

Quantitative comparison is performed in the channel centerline, where the profiles of mean velocity field are plotted against the experimental reference by Tominaga. et al. (1989), as shown in Figure 9.4 (left). Position of the velocity dip has been captured accurately. Minor differences between the data-sets can be attributed towards the higher Reynolds number of the numerical case. Considering the distribution of turbulent fluctuations, results for the normal Reynolds stress tensor components are plotted against the LES reference in Figure 9.4 (right). Good fit has been obtained for all of the components. Note the complete vanishing of the surface-normal fluctuation components at the free surface.

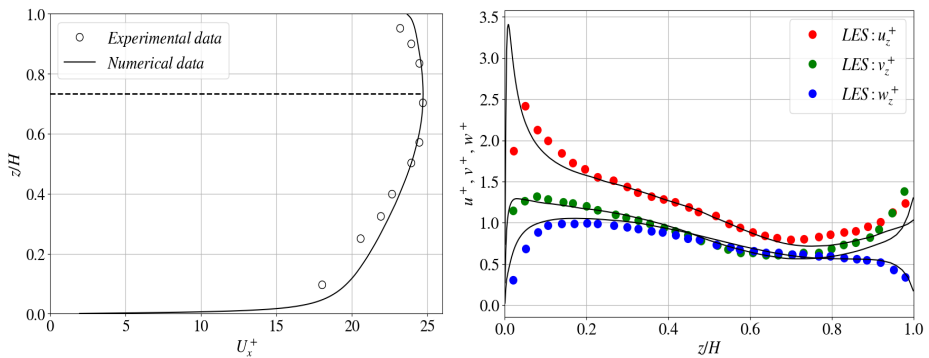


Figure 9.4.: Profile of dimensionless streamwise velocity (left), with experimental data from Tominaga. et al. (1989). Normal Reynolds stresses (right) are plotted against the LES reference by Shi et al. (1999).

In the vicinity of the wall, a small mismatch between the data exists. This is however of no concern since the Shi et al. (1999) explicitly noted that the poor wall resolution and no wall treatment were used in their LES study. Since the value of wall shear stress is predicted accurately, a mismatch may be attributed to the incomplete LES data. Since no clustering of the grid cells is used near the free surface, and the results match the reference nonetheless, it has been concluded that the mesh layering will be used only near the no-slip walls to resolve the viscous sublayer. Free-surface mesh will have the 'free-stream' resolution.

A potent indicator for assessing the capability of the model is the accuracy in predicting secondary flows. In Figure 9.5, streamlines belonging to a plane perpendicular to the main flow have been plotted against the LES reference. Three characteristic vortex zones are identified: 1) the bottom-corner vortex, associated with the inclination between the bottom and side walls, 2) the free stream, large-scale vortex in the vicinity of the free surface, and 3) the surface-corner vortex, associated with the free surface corner.

Concerning the accuracy of the simulation, it can be seen that the position and span of the bottom-corner vortex have been predicted accurately, and that the center of the free-stream vortex is moved slightly towards the centerline of the flow, although the depth of vortex centre matches the LES data. Origin of this small deviation is straightforwardly explained by the presence of the surface-corner vortex, which promotes the compression of streamlines belonging to the free-surface vortex. Although this surface-corner vortex is not recovered in the LES study, its presence is nonetheless physical according to the experimental measurements of Tominaga. et al. (1989). Its absence in the LES study may be explained by the poor wall resolution, whereas in the present study, full integration through the viscous sublayer is performed.

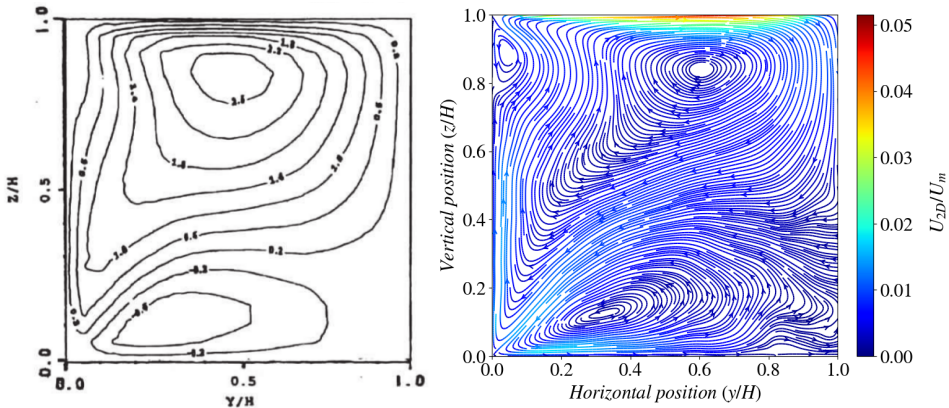


Figure 9.5.: Secondary flow streamlines: LES reference (left) and IIS-RSM results (right).

By inspecting the magnitude of secondary flows, it can be seen that their maximum is reached on the free surface. Although the overall momentum intensity contained within the secondary flows can be considered small in comparison with the streamwise flow (less than 6% of  $U_0$  at the free surface, and around 1% of  $U_0$  in the interior of the domain), distribution of the mean velocity and turbulence anisotropy is decisively affected by it.



When considering flow cases with distinctively mono-directional character (pipes, channels, conduits etc.), emergence of coherent flow patterns in the plane perpendicular to the direction of the mean flow, is a common occurrence. Generally speaking, Prandtl classified two kinds of such flows. Secondary flows of first kind are intrinsically connected with the curvature of the mean flow, which may be a result of geometric constraint such as bends and elbows. They were already investigated in Chapter 7.

Secondary flows of the second type typically accompany turbulent flow configurations that don't possess rotational symmetry, as in this case (channels, non-circular pipes etc.). Here, secondary motion is generated without any external curvature. Prandtl presented arguments that the origin of the second kind of secondary flows is tightly connected with the anisotropy of the turbulence field. A detailed analysis involving anisotropy-related generation of secondary flows is given in Nikitin et al. (2021) and the complete outlined mathematical derivation will not be repeated here. Rather, a descriptive approach will be used. In the case of a fully developed flow field, turbulence in the plane normal to the streamwise flow is governed by the fluctuations both normal- and tangential to the wall. In the presence of non-penetrable boundaries (solid walls, free surfaces), normal-to-boundary fluctuations will be suppressed, leaving the tangential fluctuating component dominant, as presented in Figure 9.6. Close to the corners of the channel, isosurfaces of the tangential fluctuations magnitude  $v^+ + w^+$  will form a curved surface.

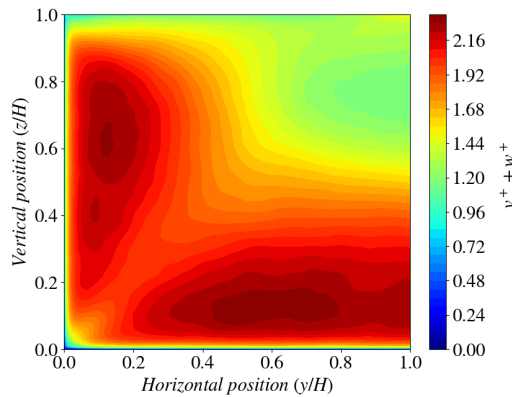


Figure 9.6.: Contours of the spanwise velocity fluctuations.

Any pulsation oriented along the tangent to the surface will create a centrifugal force, oriented opposite from the center of curvature, forcing the flow towards the corner. Due to the continuity, stagnation points will form in each of the corners, ejecting the fluid outwardly along the walls. This creates a characteristic vortex triplet. In case of the free surface vortex, pressure gradient overcomes the Reynolds

stresses on the surface, and the low momentum fluid is transported towards the stagnation point in the centre, and then downwards. This creates the free surface vortex, responsible for the presence of the velocity dip.

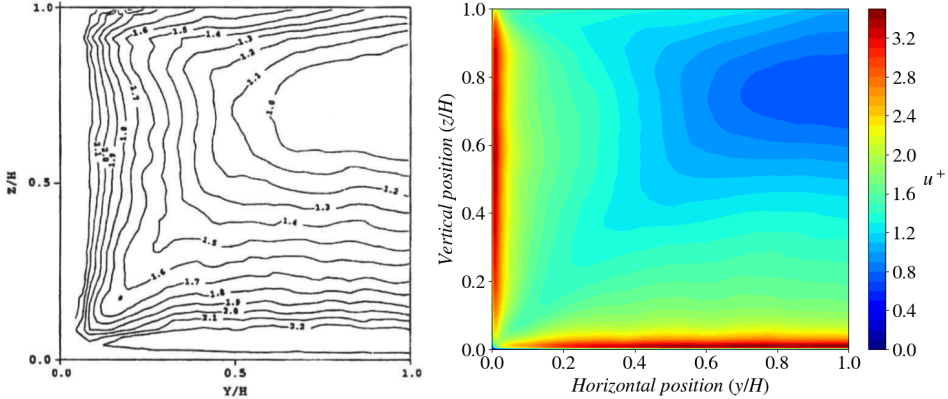


Figure 9.7.: Contours of the streamwise turbulent fluctuations, reference data (left) and simulation results (right).

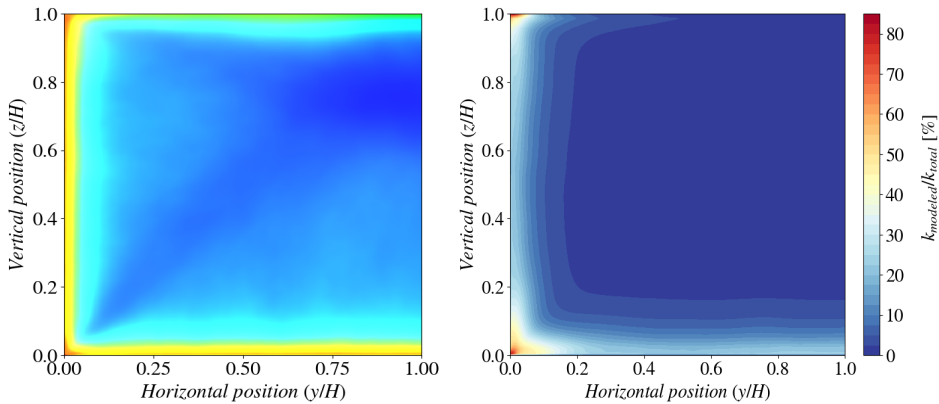


Figure 9.8.: Componentiality contours of turbulence anisotropy (left), and contours depicting the ratio of modeled turbulence kinetic energy (right).

In Figure 9.7, contours of the streamwise turbulent fluctuations are compared with the LES reference. Spatial congruence with the experimental data remained very good. Due to the action of secondary flows, low intensity turbulence is transported in the form of two symmetric spikes towards the bottom corners of the channel,

thus breaking the high fluctuation intensity regions formed in the vicinity of the walls. Near the free surface, bending of isocontours depicting the turbulence kinetic energy is again associated with the strong impact of free surface vortex.

Secondary flows also affect the distribution of the anisotropy, as can be seen in Figure 9.8 (left). Corner-directed flows transport the dominantly isotropic fluid towards the stagnation points, where the turbulence undergoes a change from towards the **3C** state. Next to the free surface, turbulence is mostly two-componental (**2C**), since the third component is suppressed through the boundary condition. In Figure 9.7 (right), ratio of the modeled to total turbulent kinetic energy is plotted. In the vicinity of the wall, the cut-off enables the modeling ratio to lie in range  $20 \div 30\%$ . Further away from the wall, modeled turbulence is almost completely destroyed, which is also the case at the free surface, thus confirming the proposition of using the same boundary condition for all of the components of the Reynolds stress tensor.

### 9.3. Main case

After successfully finishing the simulation for the open-channel flow case in which the ability of the model to predict complex patterns, affected by the corners and by the free surface is confirmed, analysis is moved towards the simulation of the main case. Analogously to the previous Chapters, the precursor simulation will be performed initially. Meshing has been done correspondingly to the previous section, only the mesh size and resolution have been changed. Parameters corresponding with the optimal prediction of wall shear stress are listed in Table 9.3.

Table 9.3.: Inflow conditions and mesh metrics for the main case precursor.

$A_r$	$U_0$	$Re_{D_h}$	$Re_\tau$	$Fr$	$\Delta x^+$	$\Delta y^+$	$\Delta z^+$
1.85	0.2	249,000	5602	0.03	250	$1 \div 70$	$1 \div 70$

Detailed analysis of results will not be repeated here since all of the flow features are connected with the same underlying phenomena. In Figure 9.9, cross-sectional view of the precursor simulation is shown. It can be seen that the velocity dip was obtained again, only this time at the height of  $z/H \approx 0.8$ . From the standpoint of secondary flows, a vortex quadruplet is recovered in the present study. Next to the bottom-corner-, free-stream- and free-surface corner-vortex, a fourth characteristic vortex structure develops due to the extensive curvature of streamlines between the two corners.

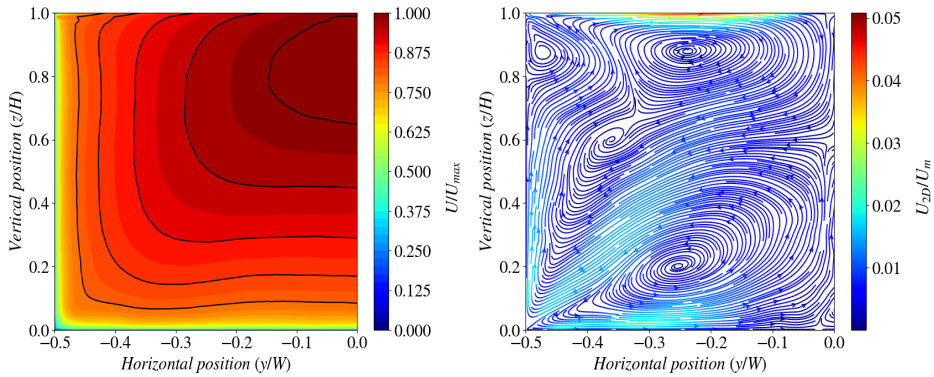


Figure 9.9.: Streamwise velocity contours (left), and the streamlines of the secondary flow (right), with background coloring indicating the magnitude of secondary flows.

Considering the distribution of turbulence anisotropy visualized in Figure 9.10, near-corner regions remain less affected by the more isotropic core flow, which is transported from the channel center by the secondary flows. Core region is mostly dominated by the **2C-3C** zone, with free surface again being mostly in the range **1C-2C** due to the boundary condition induced suppression of the surface-normal

fluctuations. Magnitude of the modeled fluctuations remain again very low far away from the walls, and the ratio of the residual to total turbulence kinetic energy is close to  $1 \div 5\%$ .

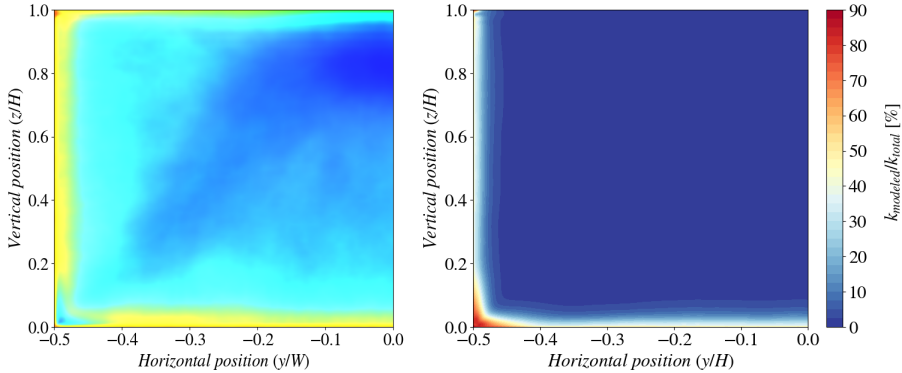


Figure 9.10.: Barycentric visualisation of the flow (left), and modeled-to-total kinetic energy ratio (right).

Concerning the main case, meshing resolution has been set identical as in the precursor, except in the central zone of the bubbly jet. Meshing details corresponding to this zone are given in Figure 9.11 (top). Next to the near-wall regions, compression of the mesh has been applied in the area close to the origin, so that the aspect ratio of the cells lies close to 1. Additionally, in the zone dominated by the plume, refinement box is introduced, as to enable the fine resolution of the bubble related structures. Here,  $\Delta/d_b = 3$ , thus fulfilling the Milielli criterion. Total number of cells is close to 5,914,000. Injection nozzle is placed at the origin. Water injection is imposed at the nozzle tip, with the prescribed volume rate. Bubbles are injected as the parcels, with their initial velocity calculated based on the diameter of the nozzle and the imposed volumetric flow rate of both air and water. Injection rate is 10,166 parcels per second, and the total number of bubbles after reaching the quasi-steady state oscillates around 18,000. Again, all models for bubble forces from the Chapter 2 are used without modification. BIT modeling was not used since it made computations unstable, as already noted in the previous Chapter. In Figure 9.11 (bottom), instantaneous velocity field in the X-Z plane is shown. Upper limit to the velocity magnitude is set at  $0.3 [m/s]$  in order to ease the visualisation. Additionally, injection column is shown, with the each of the bubbles in the domain, represented to the scale.

In Figure 9.12, down, isometric view of the solution domain with some relevant flow features is shown. Bubble dimensions were again visualized to the scale, with their coloring representing the instantaneous velocity. Nozzle-injected water is forced to deflect downstream, and the curvature of streamlines creates a characteristic pair of vortex tubes which are visualized as well. These vortex tubes are advected

downstream, and the large-scale secondary currents dominate the central region of the channel, as shown by the cross-sectional streamlines. Close to the injection point, bubbly swarm separates from the nozzle-injected fluid, and progresses towards the free surface, at an apparently constant angle. Afterwards, it is discharged from the domain.

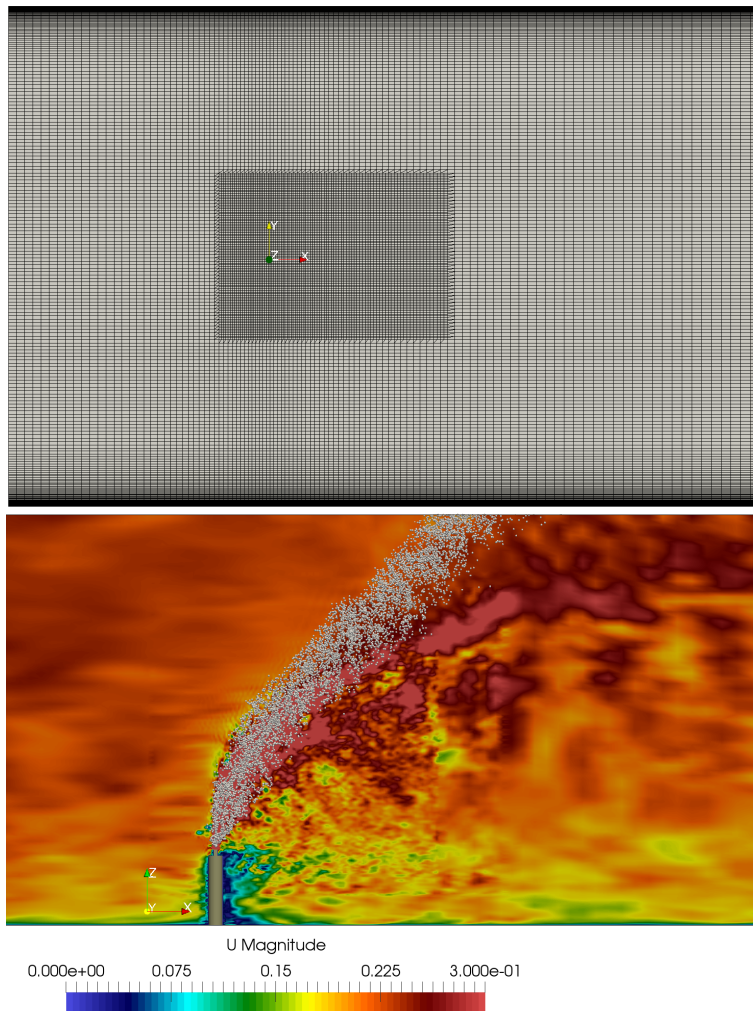


Figure 9.11.: Mesh cross-section in the X-Y plane (top). Instantaneous view of the velocity field in the X-Z plane, with the dispersed bubbles shown to scale (bottom).

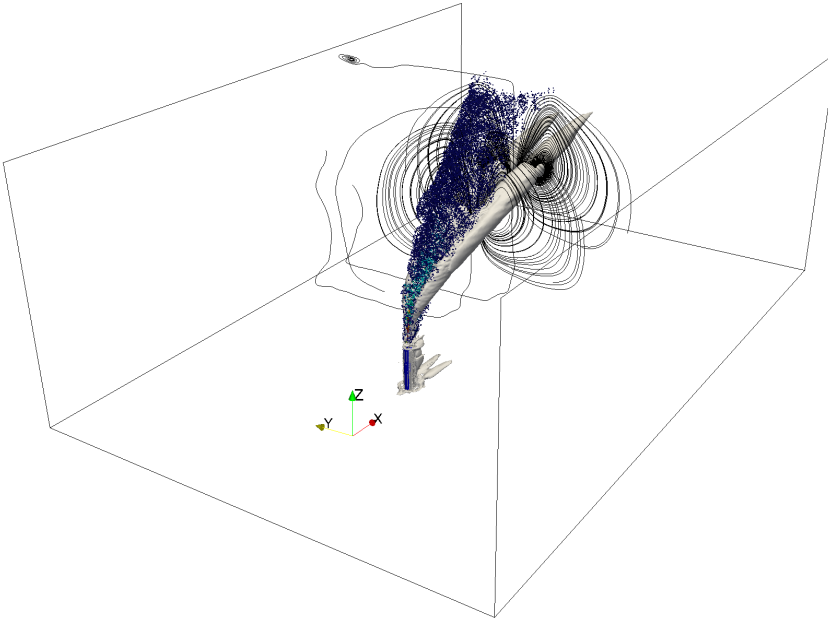


Figure 9.12.: Isometric view of the solution domain, with down-to-scale visualisation of bubbles. Isocontours of mean vorticity are used for visualisation of vortex tubes. Secondary flows are represented through the streamlines in the plane normal to the main flow.

In Figure 9.13, the cross-section in the X-Z plane with contours of first- and second order statistics has been shown. In the top row-left, instantaneous positions of bubble centres were shown along with the streamlines of the mean flow. Bubbles seem to withhold the initially given vertical velocity up to the height  $z \approx 0.22 [m]$ , after which the branch flow deflects downstream at an apparently constant angle, carrying away the bubbly swarm. Continuous red line indicates the position of the bubble-plume center, found from the condition  $|\nabla\alpha| = 0$ . A line-associated coordinate  $\xi$  can be drawn from the center of the nozzle, and following the line, up to the free surface. This coordinate will be used to characterize the local features of the plume in the next section. Since the offset between the real plume center, and the apparent symmetry of the plume exists, it points to the conclusion that the bubbly plume is non-ellipsoidal in nature, which will be investigated shortly. Red crosses indicate the positions of the 4x3 probe set, used for FFT Analysis of the flow dynamics. Their positions are listed in Table 9.4, where for each of the 4 heights, 3 probes were installed: one upstream of the plume, one centrally positioned in the plume, and one downstream of the plume. Naturally, all probes were installed in the X-Z plane, hence  $y = 0$ .

## 9. Flow Configuration V: Bubble plume in open-channel cross-flow

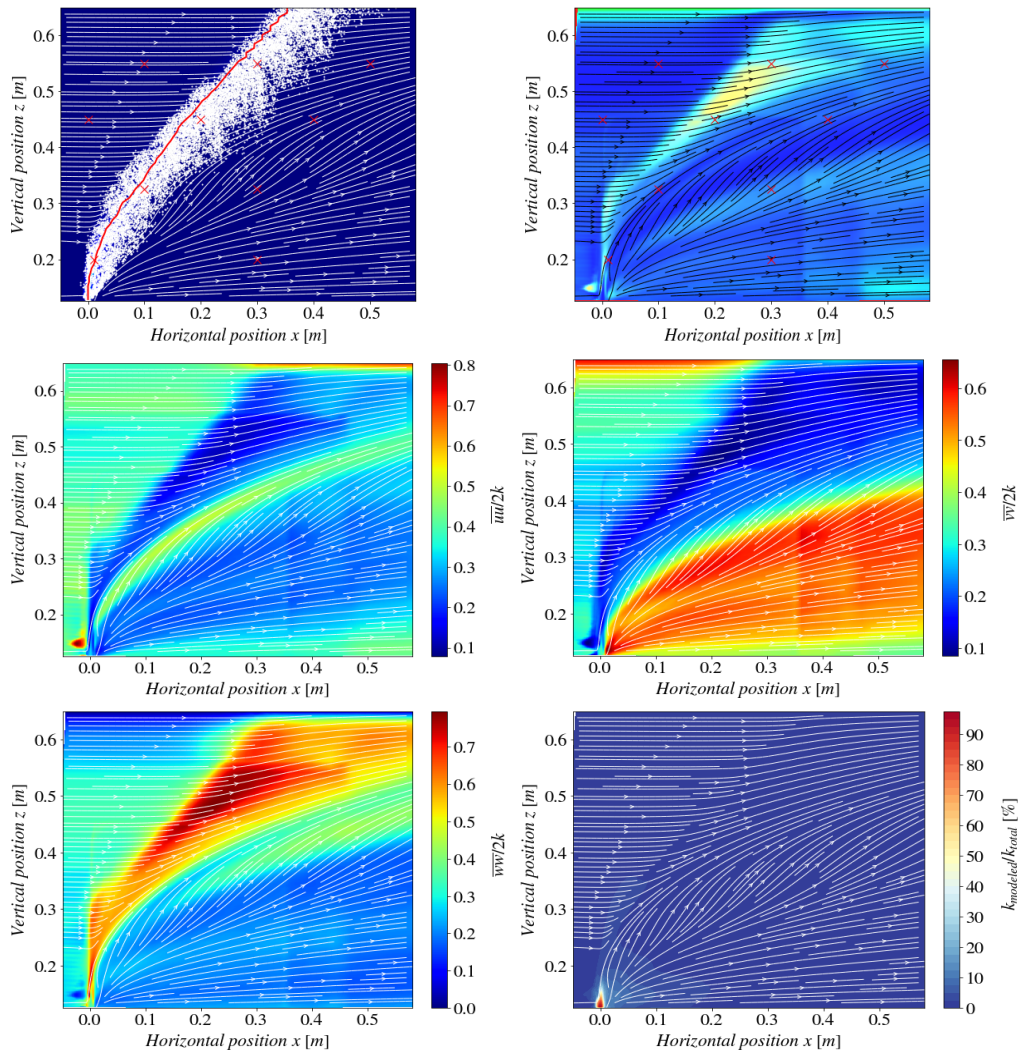


Figure 9.13.: Streamlines of the mean flow, visualized with the bubble centerline (top left), as well as with the componentality contours of anisotropy (top right). In the center, normalized streamwise  $\overline{uu}$  (center left) and spanwise  $\overline{vv}$  (center right) components of Reynolds stress tensor are shown. In the bottom row, normalized vertical  $\overline{ww}$  component (bottom left), as well as ratio of modeled to total turbulence kinetic energy (bottom right) are shown.



In order to obtain an insight into the complex flow topology, mean-flow streamlines are superimposed with the anisotropy contours in the Figure 9.13, top-right. Normalized normal Reynolds stresses are additionally plotted in center- and bottom rows. Although the analysis of componentality contours makes sense only in the beneficially chosen, locally principal coordinate system, we will nonetheless perform it using the projections of Reynolds stress tensor in the established  $x - y - z$  coordinate system, since the directions of dominant flow patterns are mostly coaligned with  $\overline{uu}$ ,  $\overline{vv}$  and  $\overline{ww}$ . Upstream of the injection point, incoming flow can be considered mostly isotropic, where all three components account for roughly one third of total turbulence kinetic energy. Encounter with the bubbly plume is reflected in the main flow similarly to the impingement process, in which the streamwise component is strongly suppressed due to the breakage and deflection of the flow. This points to the poor mixing of the streams in the vicinity of the injection point. Concerning the anisotropy of turbulence in the plume, overall state seems to be the intermediate between **2C** and **3C**. This mechanism is maintained up to the position  $z \approx 0.33 [m]$ , after which the sudden change in the contour continuity occurs. As will be demonstrated, this represents the onset point for the formation of the vortex tubes due to the curvature of the injected water streamlines. Closer to the surface, anisotropy of the flow is mainly governed by the pressure-driven effects that favor distribution of energy in streamwise and spanwise directions, and lead towards the suppression of the surface-normal fluctuations. Upstream of the plume, surface fluctuations are dominated by the spanwise component. However, in the plume zone, sudden redistribution in favor of streamwise fluctuations appears. Concerning the plume spreading zone, it is dominated by the vertical fluctuating component, which is especially pronounced in the zone between  $z \approx 0.4 [m]$  and  $z \approx 0.55 [m]$ , where turbulence tends to **1C-2C** state. Initial speculation that correlated this anisotropy zone with the horizontal vortex switching (described later on) proved to be unfounded, since the orientation of the anisotropy related phenomena is vertical (vertically oriented fluctuations account for more than 70% of the local turbulence kinetic energy). Exact source of this phenomena will be further investigated in the spectral analysis section. Considering the overall modeled-to-total kinetic energy ratio, given in the bottom right row, model is again performing in the over-resolution mode and modeled turbulence doesn't account for more than 2% of total turbulence, except in the vicinity of the injection point, where the resolved flow is explicitly suppressed through the boundary condition. As the injected flow is convected further away, modeled turbulent kinetic energy reduces in magnitude correspondingly.

Since the local characteristics of the bubbly plume have been the key asset of the experimental reference, they will be validated first. In Figure 9.14 changes in local bubble characteristics have been plotted against the plume-associated coordinate  $\xi$  (distance expressed as a number of nozzle diameters -  $d$ ). Plots of the absolute bubble velocity magnitude (top left), as well as relative velocity magnitude (top right) indicate that the terminal stage of the bubbly phase evolution is reached in the range  $50d \div 60d$  behind the injection point, in which both drag and buoyancy

effects reach local equilibrium. Initially, bubbly phase exhibits a strong deceleration, caused by the sudden introduction of the drag force. Although the first experimental point is matched surprisingly well, bubble velocity in the zone  $20d \div 40d$  is slightly underpredicted. Sudden downtrend in the relative velocity indicates the deceleration of the bubbles on the account of the drag force. Since the magnitude of the drag force is proportional to square of the relative velocity and tends to diminish it completely, subsequent uptrend signifies the more dominant influence of the buoyancy force up to the distance  $60d$ .

Bottom row shows the distribution of the bubble probability (void fraction), plotted against the plume centerline  $\xi$  (bottom left), as well as its lateral distribution (bottom right). Here, general trend is again matched well, although some more notable overprediction is present close to the injection point. Reasons for this overprediction can be better understood after the inspection of the general bubble probability relation:

$$\alpha_i = \frac{1}{\Delta t V_i} \sum_{j=1}^{N_b} V_{b,j} \delta t_j \quad (9.12)$$

Increase in bubble probability can either be realised through the increase in residence time of the bubble within the cell,  $\delta t$ , or through increasing the overall number of bubbles  $N_b$  that passed through the cell  $i$  during the Eulerian time step  $\Delta t$ . Overprediction in residence time may be attributed with the underpredicted absolute velocity of the bubbles, signifying that possibly, drag force is not adequately modeled in the regions where  $\alpha$  is higher. However, this assumption doesn't correspond with the available experimental observations. First, mismatch in the  $\alpha$  profile is not proportional to the underprediction in absolute velocity, which tends to be more congruent with the data. Second, by inspecting the spreading rate of the bubble plume (bottom right), quantitatively surprisingly good match is obtained, although the maximum values of  $\alpha$  are overpredicted. This indicates that both the lift force intensity and direction, and the relative velocity as well, have all been predicted with acceptable accuracy. Third, match of the first measurement point for the bubble velocity is in complete contrast to the largest overestimation of  $\alpha$  at the same position.

The only valid explanation seems to be lack of modeling certainty concerning the boundary conditions. Namely, local flow patterns in the nozzle duct are not known a-priori and can only be estimated based on the integral flow quantities like volume flow rate for both bubbles and water phase. Since the numerical modeling of the bubble injection involves placing the 10, 166 bubbles of the prescribed diameter at the injection boundary, and assigning them with initial velocity at each second, all two-phase processes in the injection duct are omitted and the initial state of the injected bubbles possibly doesn't correspond with the realistic swarming effects, reflected through  $N_b$ .

Surprisingly enough, initial mismatch in the data doesn't reflect the terminal state of the plume, which is shown to correspond well with experiment. This may be attributed to the neglecting of bubble-bubble interactions (breakage/coalescence), where the spatio-temporal evolution of the individual bubbles is governed only by the interaction with the carrier phase, and not by the falsely predicted accumulation of bubbles in the injection zone. Furthermore, although the dynamics of carrier phase may be additionally modulated in the vicinity of the nozzle (vortex switching, shown in short), strong streamwise convection prohibits the propagation of this disturbance further upwards, where the bubbles are met with the free-stream fluid, unaffected by the injection zone.

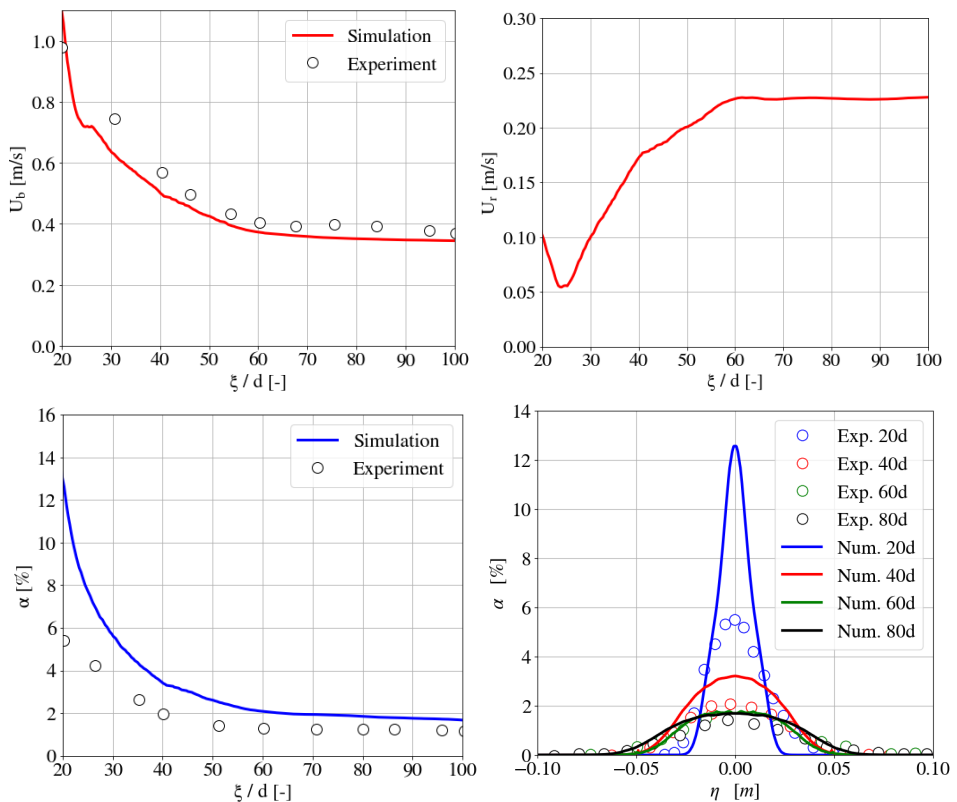


Figure 9.14.: Distribution of local plume characteristics along the plume centerline  $\xi$ : absolute velocity (upper left) and relative velocity (upper right), void-fraction (lower left), and lateral distribution of void fraction (right) in four consecutive positions of  $\xi$ .

Evolution of plume shape in three consecutive positions downstream of the injection point is shown in Figure 9.15. In contrast to the injection of a mono-phase jet in the cross-flow, presence of the secondary streams modifies the shape of the plume. Starting from the expected ellipsoidal shape close to the nozzle, counter rotating vortex pair, originating from the bent water-jet reshapes the plume in the kidney-like form, which is also documented in the experimental reference. Initially disturbed by the secondary flow, elongation of the plume contour progresses further downstream.

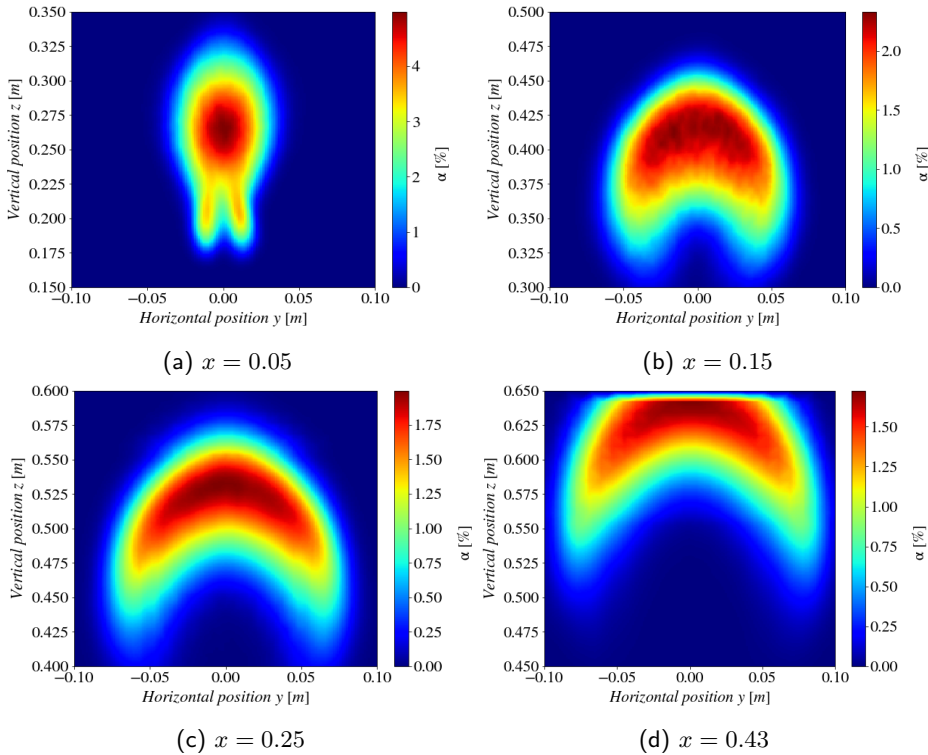


Figure 9.15.: Distortion of initially ellipsoidal plume shape at four downstream positions.

Fluid injected along with the bubbly phase is forced to bend, whereas the streamline curvature increases after the separation from the bubbly plume. This strong curvature is responsible for the generation of secondary flows of the Prandtl's first kind in form of the counter-rotating vortex pair. Spatial evolution of the flow is presented in Figure 9.16 for three consecutive downstream positions. Streamlines depicting secondary flow are imposed at each Figure. In the left column, contours of the normalized streamwise velocity are shown, whereas in the right column, componentiality contours of turbulence anisotropy are shown.

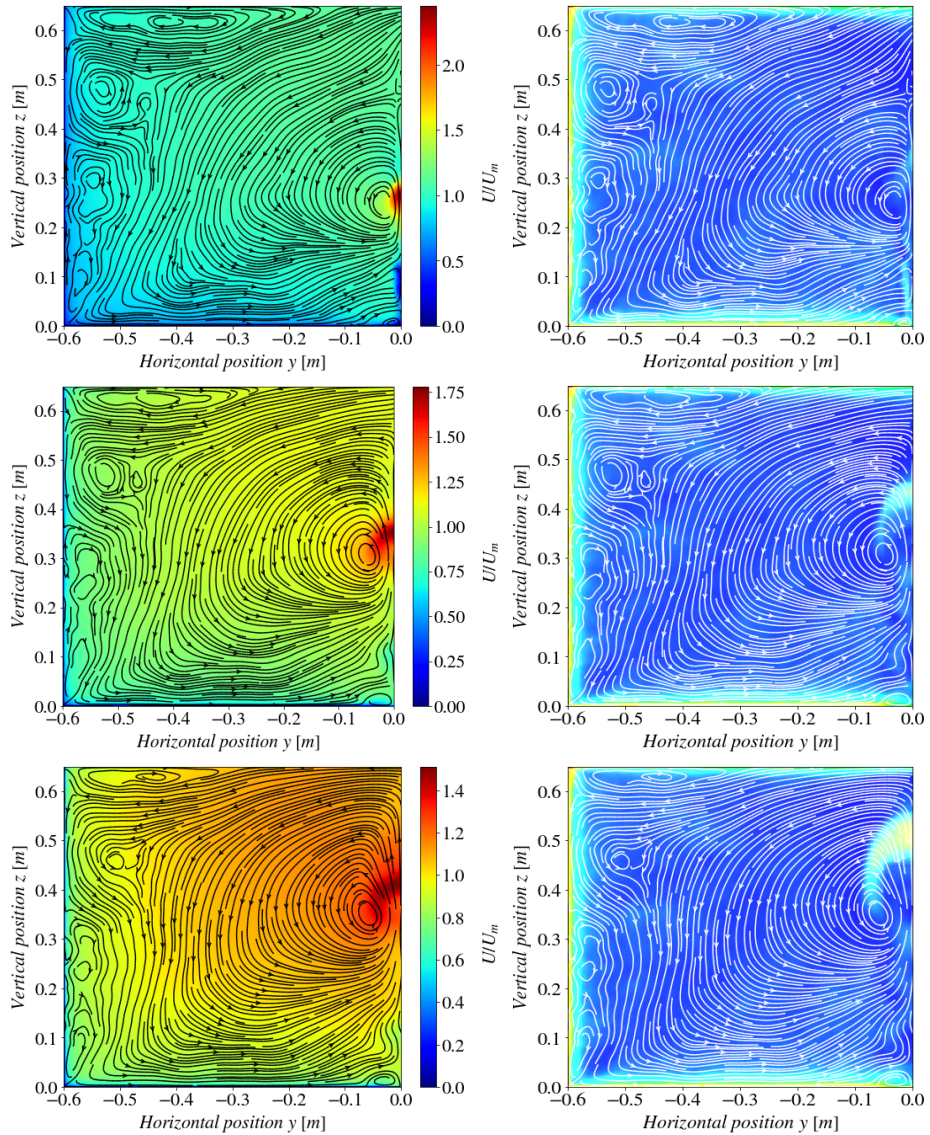


Figure 9.16.: Development of flow properties at three consecutive positions downstream:  $x = 0.05$  (top),  $x = 0.15$  (center), and  $x = 0.25$  (bottom).

Since the branch flow represents a large-scale obstacle towards the main flow, it is expected that the secondary flows will possess some sort of temporal switching dynamics, which makes the averaging, visualisation and analysis of the Prandtl's

second kind of secondary flows challenging. Surface level vortex pairs that were dominating the central region of the precursor are now shifted towards the wall, and the velocity dip phenomena could not be spotted due to the high inertia fluid which is now transported towards the free surface. As a reminiscence of the bottom-, as well as surface-corner vortex pairs, several vortex cells are formed along the side wall and gradually advected towards the bottom, as the fluid progresses further downstream. Since the secondary flow patterns are confined within the relatively narrow domain, they possess a certain diffusive role and the high inertia fluid, originating from the nozzle gets more spread within the cross-section. Overall flow rate in the channel gets additionally accelerated. Position of the bubbly jet can be identified in the regions of maximal velocity and with the characteristic kidney/horseshoe shape. From the standpoint of anisotropy, turbulence in the vicinity of the walls remains relatively unchanged, and spatial distribution in both spanwise coordinates remains almost identical near the wall. As the plume progresses along the streamwise coordinate, anisotropic behaviour tends to change from the **2C -3C**, to **1C -2C** turbulence, seen as the dominantly increasing yellow zone, immediately upwards of the vortex pair. Interestingly enough, this area is also affected by the secondary flow advection, and possesses a kidney like shape. However, since the anisotropy dominated zone is positioned upwardly of the plume center (identified with maximum in velocity magnitude), strong vertical fluctuations spotted in Figure 9.13 do not seem to be directly correlated with the dynamics of the vortex switching itself, but rather represent the artifact related to the zone adjacent and upstream of the plume. In order to investigate the temporal response of the system, twelve different velocity measurement probes were placed in the flow, their positions being listed in Table 9.4.

Velocity magnitude is sampled at each of the probe locations with the time-step of  $\Delta t = 4 \cdot 10^{-3}$  [s]. After a sufficient sampling time, FFT Analysis is performed on each of the signals. Results for each of four heights are given in Figure 9.17. As expected, signals close to the center of the plume are upwardly shifted in terms of attenuated energy. It can be seen that all of the frequency signatures follow a  $-5/3$  slope in the certain region, which indicates that the transient nature of the turbulent spectrum is adequately captured. Additionally, signals in the central position are shifted towards the higher frequencies. These two features can be readily explained by the injection of additional energy into the spectrum by the bubble plume, which first attenuates more energy at all frequencies (hence the upward shift), and then, leads to the increased dissipation in the plume, which shifts the Kolmogorov scales towards the higher wave numbers. Spectral signatures gradually converge as the plume approaches the free surface, which is to be expected since the energy exchange is at its highest rate closer to the injection point. There seems to be a strong attenuation of fluctuating energy at  $f \approx 0.2$  [Hz], whereas the peaks are more pronounced closer to the injection point. As will be seen in the POD analysis, these peaks are correlated with the horizontally oriented switching of the vortex pair, which retains the same dynamic response independently of the height in the plume.

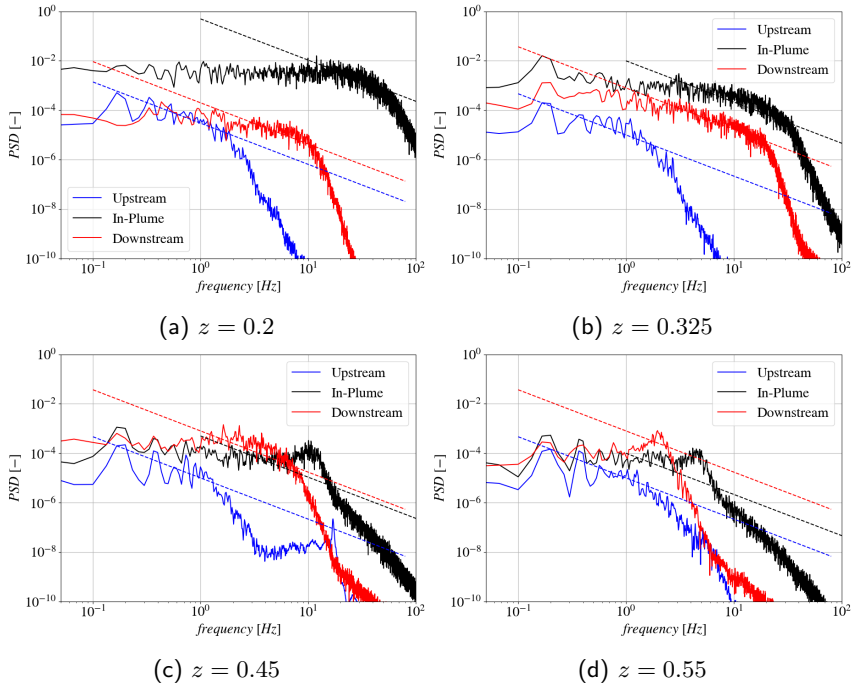


Figure 9.17.: FFT Analysis of the velocity signals at four different heights in the plume. Each measurement height is associated with 3 different positions in the flow.

Table 9.4.: Position of the probe triplets for the FFT Analysis.

Height	Upstream	Plume center	Downstream
$z = 0.2$	$x = -0.1$	$x = 0.01$	$x = 0.3$
$z = 0.325$	$x = -0.1$	$x = 0.1$	$x = 0.3$
$z = 0.4$	$x = 0.0$	$x = 0.2$	$x = 0.4$
$z = 0.55$	$x = 0.1$	$x = 0.3$	$x = 0.5$

An interesting artefact can be spotted at the last two set of probes ( $z = 0.4 [m]$  and  $z = 0.55 [m]$ ), at  $f \approx 4 [Hz]$  within the plume, and at  $f \approx 2 [Hz]$  downstream. Origins of these spectral peaks are open to discussion. On one hand, since the energetic peaks are located more than the order of magnitude higher in the spectrum, it is unlikely that they represent some higher harmonics of the eddy switching process. On the other hand, if the characteristic bubble related frequency is formed at the account of the bubble slip velocity and diameter ( $U_r = 0.05 \div 0.2 [m/s]$ ,  $d_b = 2 [mm]$ ), the resulting frequency lies in range  $f = 25 \div 100 [Hz]$ , which is now an order of magnitude higher in the spectrum in comparison with the artefact. Interestingly enough, both sets of probes are located in the vicinity of the anisotropy dominated zone with strong vertical fluctuations, as seen in Figure 9.13. This clearly dictates that strong vertically oriented pulsations exist in- and upwards of the plume. Since the abrupt change in spectral slope appears immediately after this frequency, it is also possible that this artifact is purely related to the model performance (dynamic shifting of kinetic energy between resolved and modeled flow). Some future analyses may include an additional sampling of data at this point, in order to investigate this phenomenon more deeply.

In order to characterize previously mentioned vortex switching, dominant directions of velocity oscillations are analysed using a POD procedure, involving the snapshots of the velocity in the Y-Z plane at position  $x = 0.25 [m]$ . Results are presented in Figure 9.18. Accumulated energy of first 20 POD modes is shown, capturing around 47 % of the total variance in the flow, as indicated by the red dashed line. The first POD mode accounts for more than 10 % of the fluctuating energy, making it the most dominant feature of the flow. Streamlines correlating with the mean field, as well as the first three POD modes are shown. Additionally, FFT analysis of their temporal dynamics is shown as well.

Clearly defined vortex pair exhibits an energetic oscillation in the horizontal plane, indicating a dominant switching direction. There are three clearly defined peaks related to this oscillation: at  $f \approx 0.15 [Hz]$ ,  $f \approx 0.3 [Hz]$  and  $f \approx 0.45 [Hz]$ , with multiple low-energy harmonics, located further down the spectrum. Failure of POD to separate spatially non-orthogonal structures can clearly be seen on the example of the second most dominant POD mode. Here, two important phenomena are captured in parallel. First, nearly identical temporal dynamics is reflected, although the oscillation direction is not as clear. This points to the rather complex switching pattern of the vortex pair, not only having a horizontal oscillation component, but also a vertical one. Two initial dominant peaks indicate that the underlying source of this vertical-to-horizontal transition is the same as in case of POD mode 1, hence it can be attributed to the vortex switching. Second, zone of high vertical variance is also recovered in the second POD mode, both in the spatial distribution (note the zone  $z \approx 0.4 [m] \div z \approx 0.5 [m]$ ), as well as in the FFT signal (note the very weak, but still dominating peak at  $f \approx 2 [Hz]$  in the log-plot). This shows that the vertically oriented switching phenomena is nearly an order of magnitude weaker in intensity, as compared with vortex switching. As for the third POD mode, its



pattern gets more erratic and harder to interpret, although a certain component of horizontal oscillating patterns is recovered, signifying yet another mode of the vortex switching. Concerning the spectral properties,  $-5/3$  slope is again recovered, indicating a physically sound resolution of the spectrum.

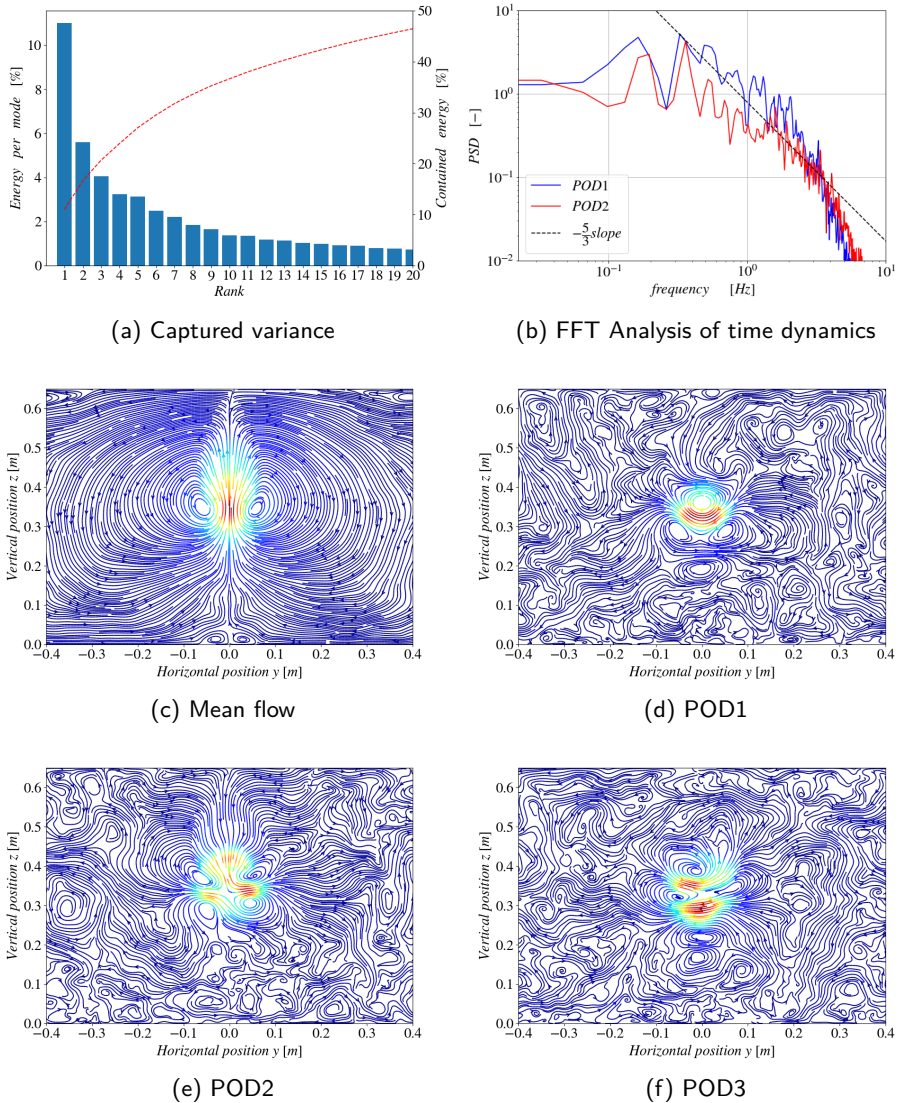


Figure 9.18.: Results of the POD analysis.

## 9.4. Conclusions

In this Chapter, performance of IIS-RSM was tested in flow configuration involving the bubble plume in the open channel cross-flow. Motivation for this study was the knowledge gap in relation to the model behaviour in complex conditions, involving most of the flow phenomena, outlined in previous Chapters. To the authors best knowledge, this was the first publication, aiming at numerical reproduction of the experimental test case by Zhang and Zhu (2013).

Initially, applicability of the model was tested in the straight open channel geometry, with boundary conditions for the treatment of modeled turbulence, at the free surface, applied for the first time in the class of eddy-resolving, second-moment closure. Obtained data were in good congruence with experimental measurements. Secondary flow patterns, stemming from the turbulence anisotropy were also predicted with high level of accuracy. Afterwards, identical workflow was shifted towards the full case, involving the mixture of water and air, injected from the bottom surface. Experimental measurements of the bubbly plume characteristics were compared with numerical data, and good congruence was obtained in the terminal stage of the plume, with some uncertainties in the vicinity of the injection point. This proved the accuracy of the model in the conditions of complex, two-phase flow regime, provided that the boundary conditions were properly applied. Since the validation basis for the first- and second-order statistics of this case was not provided, dominantly qualitative analysis of results was presented. It was discovered that next to the highly three-dimensional flow patterns, at least two characteristic transient phenomena are established within the flow. First, a top-level transient involving the vortex switching around the bubble plume, and second, vertically oriented fluctuation at the edge of the bubble plume. Its origin could not be determined, and may stem from either the periodic vertical acceleration of the flow, or may be model-induced. Some further analyses of the plume dynamics are needed in order to better understand this phenomena.

## 10. Conclusions and outlook

---

In the present thesis, some specifically configured flow configurations relevant to the field of thermotechnical piping systems have been computationally investigated. The flow configurations considered are characterized with high-intensity turbulence, complex topological patterns with high-level energetic transients, heat-transfer, dispersed two-phase flow regimes, and flows influenced by free surface effects. All simulated flow cases represent either a single or a combination of the above-mentioned phenomena. The aim of this work was to validate a computational strategy consisting of an eddy-resolving second-moment closure model (IIS-RSM) in combination with Euler-Lagrange methodology, in search of a simulation tool as universal as possible, capable of capturing all above-mentioned flow phenomena relevant to the field of thermotechnical facilities. On the basis of the computational studies carried out, the following conclusions can be drawn.

- Presently applied model of turbulence allows a significant reduction of the computational costs in all considered flow configurations, where it successfully reproduces the experimentally obtained results. In terms of resources required, over a range of high Reynolds number flows, spatial resolution can be coarsened by approximately factor of ten, in comparison with Smagorinsky-based LES models. Here, the optimal meshing metrics could be determined in a precursor-simulation, where the criterion for *optimal resolution* is based on the accurate determination of wall shear stress. In contrast to other proposed hybrid RANS/LES models, i.e. the eddy-resolving models (as e.g., DES, PANS etc.) that incorporate appropriately modified RANS-based formulations, the IIS-RSM exhibits two distinct advantages: first, the numerical grid-related length scale could be implicitly captured by including higher-order derivatives of the velocity field, which increases the flexibility of the model in dealing with complex grid arrangements where grid-cell quality criteria may be violated. Second, the theoretical rationale of the SAS-methodology allows for a smooth transition between the RANS/LES regions of the flow (or the corresponding parts of the spectrum), without additional blending and correspondingly introduced ad-hoc generated functions, or numerical challenges pertinent to other eddy-resolving methods. This greatly enhances the flexibility of the model. Finally, the treatment of residual turbulence by using the second-moment closure provides the highest quality reproduction of turbulence anisotropy and makes the use of substantially coarsened meshes possible. The experimental

results were successfully reproduced on the basis of two criteria: first, coherent structures at the top energetic level, which are responsible for most of the variance in the flow were directly captured, thus mimicking the resolution capability of LES. On the other hand, treatment of residual turbulence in terms of differential Reynolds stress model provided the maximal insight into the dynamics of residual fluctuations. One of the most notable features of the model was an almost complete damping of the modeled turbulence fraction in the regions far away from the no-slip wall boundaries. So far, this drawback does not reduce the accuracy of the obtained results in the significant portion, since most of the dominant features (flow-separation, heat-transfer etc.) are indeed wall-related and hence, the capture of the residual-turbulence in the free-stream regions was of lesser importance. Here, the resolution of the top-level energetic transients plays a far more important role. Questions governing the limitation of the over-resolution will be addressed further on. The IIS-RSM performed well in predicting strong transients as well as general statistical properties of the flow in case of the high  $Re$  numbers in the T-Junction formed by the straight pipe segments. However, somewhat reduced accuracy was reported in case of the T-Junction with a preceding  $90^\circ$  upstream elbow. Most notable deviations were spotted in the spectral behaviour of the solution, on the account of two acting mechanisms. First, it seems that the parasitic influence of the precursor simulation induced another frequency peak, which affected the mixing process in the T-junction geometry. Although the spectral signatures produced in the reference LES simulation were also present in the IIS-RSM solution, mixing process was ultimately governed neither by the Kelvin-Helmholtz instabilities of the secondary-separation bubble, nor by the switching of the secondary vortex pair, but correlated directly with the characteristic frequency of the precursor simulation. Since the branch flow was of a substantially weaker intensity in comparison with the straight T-Junction case (in relation to the momentum carried), all flow phenomena related to the mixing zone are correspondingly weaker in comparison with transient characteristics related to the precursor. As a result, the precursor simulation gained importance in the study. Second, it seems that the externally imposed transient flow features promoted the change in the average intensity of secondary flows, thus enlarging the primary separation zone in the elbow. Since the turbulence statistics has been predicted accurately upstream of the primary separation, deviations from the reference results are most likely not the result of the model deficiency, but rather linked to the interaction of the model with this additional unsteadiness. Further research efforts should focus on investigating the exact mechanisms leading to this variation. Despite the problems discussed, the model correctly predicted the location of the separation point in the elbow, the size of the branch-related separation bubble, as well as the general position and dynamics of the secondary flow features. In realistic piping systems (especially those with incompressible flows), statistical

---

flow information is therefore not sufficient for the final description of the flow, and often the numerical modeler must be provided with frequency information to validate the calculations.

- In Chapters 8 and 9, application of IIS-RSM was combined with Euler-Lagrange strategy in simulating the turbulent, dispersed bubbly flows. As a first benefit, modeling assumptions behind the continuous (Eulerian) phase remained unchanged since only the bubble-related source terms were added to the momentum equation. This made the computations substantially more stable, and almost indistinguishable in terms of the performance in comparison with a single-phase case. Stabilization of computations within the two-fluid modeling (TFM) strategy remained one of the greatest challenges in second-moment closure due to the large number of coupled equations, as well as the high non-linearity of source terms, increasing the system stiffness. Within the Euler-Lagrange computational framework, no artificial increase in system diffusivity was required to support the iteration process, and the model remained robust, even in the case of a highly dispersed central-differencing scheme, which is much more complex when combined with Euler-Euler method. As a word of caution, it is noted that the implementation of both the turbulence model and the TFM framework was done in OpenFOAM®, while the alternative CFD codes may exhibit different behaviour depending on the numerical implementation. Since the bubble dimension remained in the meso-scale region (comparable with the mesh size), computation was substantially accelerated in comparison with the Euler-Euler-concept-related models. Number of computational parcels was less, or comparable with the number of cells. Second, the time integration of particle evolution equations was done explicitly. In Chapter 8, results related to the bubble column showed the same level of (high) accuracy in reproducing experimental results, achievable with using the LES models. In Chapter 9, flow configuration involving the bubble plume in the cross flow is to the authors knowledge simulated for the first time by using the eddy-resolving modeling approach. Whereas some uncertainties in the boundary conditions promoted slight deviations from the experimental data close to the injection point, development of the bubbly jet gradually approached the experimentally obtained results. This proved the application properties of the EL method in combination with scale-adaptive methodology, with all the benefits from both models combined. One demonstrated drawback of the inherited scale-adaptive formulation of IIS-RSM was also demonstrated in Chapter 8 where in the case of a free bubbly jet, model of turbulence constantly kept returning to the RANS solution. Cause for this behavior was found in the definition of the additional production term  $P_{\Delta U}$ . Based on the above, the possibilities for the application of IIS-RSM in free bubbly jets need further testing. Suggestions for further improvements of the EL-IIS-RSM modeling strategy are presented in the outline.

- Bubble Induced Turbulence (BIT) strategies were used in conjunction with IIS-RSM in order to capture the energy transfer between the residual turbulence and the dispersed bubbles, which is omitted through the modeling of sub-grid turbulence, and the Euler-Lagrange approach. Two model formulations were tested, with main difference being the anisotropic redistribution of BIT fluctuations among the components of Reynolds Stress Tensor. Several conclusions were drawn: first, next to the increase in accuracy of the results, BIT introduced an improvement of spectral properties of IIS-RSM since now, modeled quantities accounted for around 10% of the total turbulence kinetic energy. Since no significant changes can be spotted in the levels of total turbulent kinetic energy, it can be concluded that BIT played a more re-distributive role in this sense. From two tested BIT models, anisotropic model performed substantially better, especially in predicting a double peak of turbulence fluctuations in the case of vertical bubble column. One very notable drawback of the current BIT is the negative effect on the model stability. Due to the explicit correction of transport equations, robustness of the model is jeopardized, and stable computations could not be always guaranteed. Another problem related to the usage of BIT is the relatively low void fraction of the secondary phase, on which the BIT models were tested. Since the computations of the free bubbly jet failed to produce the model unsteadiness, BIT models require additional testing in conjunction with the IIS-RSM, in order to evaluate their performance more accurately. It can be stated that the application of anisotropic BIT model leads to the improvement in scale-resolving computations even at relatively low void fractions, in comparison with isotropic treatment of BIT.
- The eddy-resolving, second-moment closure was tested for the first time ever in conjunction with the free surface flows, in which the so-called *rigid-lid* approximation was used. Asymptotic boundary conditions for the modeled turbulence at the free surface were derived in Chapter 9 in order to provide physically correct treatment of the second-moment closure model at the free surface. The imaging and evolution of anisotropy-related features (in the form of corner vortices) were both accurately captured, again with substantially coarser meshes than in the LES simulations. The free-slip boundary condition for the rigid lid seems to provide reasonable accuracy for flows characterized by low Froude numbers. Once again, it was demonstrated that topologically complex, high  $Re$  number flows can be reproduced with substantially reduced computational resources.
- Proper-Orthogonal-Decomposition (POD) was used for the extraction of most-energetic, spatially correlated flow structures, from the flow affected by the non-probabilistic turbulence pulsations. As demonstrated in Chapters 6, 7 and 9, POD analysis successfully isolated the most dominant flow features, such as Kelvin-Helmholtz instabilities, Dean-vortex switching and flow pulsations, originating from the precursor simulation. Consequentially, a distinction be-

tween the flow-related phenomena and the numerically introduced artifacts was achieved, leading to a better understanding of the flow dynamics and providing insight into the model performance. One of the more serious limitations of POD is the need for spatial orthogonality of POD modes, which is hardly achievable in context of the internal flows. Here, in contrast to the external flow cases, several phenomena with highly different temporal dynamics are usually superimposed. Separation between the modes in sense of their spatial distribution, as well as from the standpoint of temporal dynamics is very challenging. On the other hand, POD is one of the methods where the classification of modes based on their importance is very straightforward (in contrast to the alternative reduced-order-modeling strategies, exemplary dynamic-mode-decomposition - DMD). Although a scattered spectrum of characteristic frequencies (non-isolated peaks) are obtained for each mode, spectral energy was usually densely accumulated around the single mode frequency. The degradation of modes in terms of captured energy progresses quickly, and usually first couple of modes are the only ones that are interpretable.

## 10.1. Outlook

In terms of future work in this direction, several research priorities are proposed. First question that needs to be urgently addressed is the over-resolution property of the model. Until the conclusion, it remained unclear to what extent the highly reduced level of residual turbulence back-propagates to the resolved pulsations. Since the reproduced results showed a very high level of agreement with the experimental results, it would be worthwhile to investigate whether the prediction of modeled quantities is of such quality that the top-level generated unsteadiness can mimic the part of the unresolved spectrum, despite the limitation introduced by the underlying mesh resolution. Further investigations into the relationship between the model-provided spectral cut-off and the mesh-limit need to be performed as well. Applying the so-called Improved-SAS strategy to a second-moment closure, see equation 5.6, could be a worthwhile direction for future model development. In this way, the retention and preservation of the modeled turbulence is explicitly guaranteed.

From the perspective of considering the two-phase model, the demonstrated stability and accuracy of the EL-IIS-RSM combination promotes its further use and development. To cover the widest possible range of scales, hybridization of EL with competing VoF models, such as was done in Evrard et al. (2019), would be very interesting in the domain governed dominantly by LES approaches. Another research direction that could alleviate the meshing limit (especially in the vicinity of the wall) by using a double-grid (chimera) approach was outlined in Caliskan and Miskovic (2021) and represents another worthwhile direction for investigation.

Considering the bubble induced turbulence (BIT), it was concluded that the second-moment, anisotropic closure by Ma et al. (2020) contributes substantially better results in scale-resolving mode. Further testing in the configurations with higher bubble/particulate loading is recommended. In this way, validity of the underlying assumptions may be tested outside of the TFM-RANS framework.

From the standpoint of the coherent structure analysis, upgrade of the outlined POD strategy, named *Spectral-Propor-Orthogonal-Decomposition* (SPOD) which aims at finding the optimal set of spatially correlated structures with a high degree of spectral coherency. Here, the variance maximizing feature of SVD decomposition is used to eliminate (to the high extent) the presence of noise in the signal, similarly to the Welch-like procedure (Schmidt and Colonius (2020)). In this way, each of the underlying flow features can be isolated both in frequency space, as well as in the physical space (Sieber et al. (2016b), Towne et al. (2018)). The implementation of the SPOD procedure, available to the public use, is currently under development and may be tracked at: Joksimović (2022b)



# Bibliography

---

- [1] F. Abbas, B. Wang, M. Cleary, and A. Masri. “Numerical convergence of volume of fluid based large eddy simulations of atomizing sprays”. In: *Physics of Fluids* 33.4 (2021), p. 042119. doi: <https://doi.org/10.1063/5.0045020>.
- [2] H. Abe, H. Kawamura, and Y. Matsuo. “Direct numerical simulation of a fully developed turbulent channel flow with respect to the Reynolds number dependence”. In: *J. Fluids Eng.* 123.2 (2001), pp. 382–393. doi: <https://doi.org/10.1115/1.1366680>.
- [3] G. Alfonsi and L. Primavera. “Direct numerical simulation of turbulent channel flow with mixed spectral-finite difference technique”. In: *Journal of Flow Visualization and Image Processing* 14.2 (2007). doi: <https://doi.org/10.1615/JFlowVisImageProc.v14.i2.60>.
- [4] A. Asad, C. Kratzsch, and R. Schwarze. “Influence of drag closures and inlet conditions on bubble dynamics and flow behavior inside a bubble column”. In: *Engineering Applications of Computational Fluid Mechanics* 11.1 (2017), pp. 127–141. doi: <https://doi.org/10.1080/19942060.2016.1249410>.
- [5] T. Auton. “The lift force on a spherical body in a rotational flow”. In: *Journal of fluid Mechanics* 183 (1987), pp. 199–218. doi: <https://doi.org/10.1017/S002211208700260X>.
- [6] S. Banerjee, R. Krahl, F. Durst, and C. Zenger. “Presentation of anisotropy properties of turbulence, invariants versus eigenvalue approaches”. In: *Journal of Turbulence* 8 (2007), N32. doi: <https://doi.org/10.1080/14685240701506896>.
- [7] B. Basara and S. Jakirlić. “A new hybrid turbulence modelling strategy for industrial CFD”. In: *International journal for numerical methods in fluids* 42.1 (2003), pp. 89–116. doi: <https://doi.org/10.1002/flid.492>.
- [8] B. Basara, Z. Pavlovic, and S. Girimaji. “A new approach for the calculation of the cut-off resolution parameter in bridging methods for turbulent flow simulation”. In: *International Journal of Heat and Fluid Flow* 74 (2018), pp. 76–88. doi: <https://doi.org/10.1016/j.ijheatfluidflow.2018.09.011>.

- [9] G. K. Batchelor. *Cambridge science classics: The theory of homogeneous turbulence*. Cambridge science classics. Cambridge, England: Cambridge University Press, 1982. ISBN: 978-0521041171.
- [10] A. Behzadi, R. Issa, and H. Rusche. “Modelling of dispersed bubble and droplet flow at high phase fractions”. In: *Chemical Engineering Science* 59.4 (2004), pp. 759–770. DOI: <https://doi.org/10.1016/j.ces.2003.11.018>.
- [11] A. R. Benson, D. F. Gleich, and J. Demmel. “Direct QR factorizations for tall-and-skinny matrices in MapReduce architectures”. In: *2013 IEEE international conference on big data*. IEEE, 2013, pp. 264–272. DOI: <https://doi.org/10.1109/BigData.2013.6691583>.
- [12] S. T. Bose and G. I. Park. “Wall-modeled large-eddy simulation for complex turbulent flows”. In: *Annual review of fluid mechanics* 50 (2018), p. 535. DOI: <https://doi.org/10.1146/annurev-fluid-122316-045241>.
- [13] O. Braillard. “FATHERINO experiment for thermal fatigue studies in a mixing tee and nozzle—support of TH and mechanical analysis of thermal load determination”. In: *Ålvkarleby, Sweden* 5 (2008).
- [14] U. Caliskan and S. Miskovic. “A chimera approach for MP-PIC simulations of dense particulate flows using large parcel size relative to the computational cell size”. In: *Chemical Engineering Journal Advances* 5 (2021), p. 100054. DOI: <https://doi.org/10.1016/j.cej.2020.100054>.
- [15] G. Cerne, S. Petelin, and I. Tiselj. “Coupling of the interface tracking and the two-fluid models for the simulation of incompressible two-phase flow”. In: *Journal of computational physics* 171.2 (2001), pp. 776–804. DOI: <https://doi.org/10.1006/jcph.2001.6810>.
- [16] B. Chaouat. “Simulations of turbulent rotating flows using a subfilter scale stress model derived from the partially integrated transport modeling method”. In: *Physics of Fluids* 24.4 (2012), p. 045108. DOI: <https://doi.org/10.1063/1.3701375>.
- [17] S. Chapuliot, C. Gourdin, T. Payen, J. Magnaud, and A. Monavon. “Hydro-thermal-mechanical analysis of thermal fatigue in a mixing tee”. In: *Nuclear Engineering and Design* 235.5 (2005), pp. 575–596. DOI: <https://doi.org/10.1016/j.nucengdes.2004.09.011>.
- [18] H. Choi and P. Moin. “Grid-point requirements for large eddy simulation: Chapman’s estimates revisited”. In: *Physics of fluids* 24.1 (2012), p. 011702. DOI: <https://doi.org/10.1063/1.3676783>.
- [19] S. Cielo, L. Iapichino, J. Günther, C. Federrath, E. Mayer, and M. Wiedemann. “Visualizing the world’s largest turbulence simulation”. In: *Parallel Computing* 102 (2021), p. 102758. DOI: <https://doi.org/10.1016/j.parco.2021.102758>.

- 
- [20] D. Cokljat, D. Caridi, G. Link, R. Lechner, and F. R. Menter. “Embedded LES methodology for general-purpose CFD solvers”. In: *Sixth International Symposium on Turbulence and Shear Flow Phenomena*. Begel House Inc. 2009. DOI: <https://doi.org/10.1615/TSFP6.1900>.
- [21] T. Craft, J. Kidger, and B. Launder. “Second-moment modelling of developing and self-similar 3D turbulent free-surface jets”. In: *International Journal of Heat and Fluid Flow* 21.3 (2000), pp. 338–344. DOI: [https://doi.org/10.1016/S0142-727X\(00\)00018-7](https://doi.org/10.1016/S0142-727X(00)00018-7).
- [22] J. Crank and P. Nicolson. “A practical method for numerical evaluation of solutions of partial differential equations of the heat-conduction type”. In: *Mathematical proceedings of the Cambridge philosophical society*. Vol. 43. 1. Cambridge University Press. 1947, pp. 50–67. DOI: <https://doi.org/10.1017/S0305004100023197>.
- [23] C. Crnojević. *Mehanika fluida*. Beograd: Mašinski fakultet, 2014. ISBN: 978-8670838468.
- [24] B. J. Daly and F. H. Harlow. “Transport equations in turbulence”. In: *The physics of fluids* 13.11 (1970), pp. 2634–2649. DOI: <https://doi.org/10.1063/1.1762039>.
- [25] M. Darwish and F. Moukalled. *The finite volume method in computational fluid dynamics: an advanced introduction with OpenFOAM® and Matlab®*. Springer, 2021. ISBN: 978-3319168739.
- [26] P. A. Davidson. *Turbulence: an introduction for scientists and engineers*. Oxford university press, 2015. ISBN: 978-0198529491.
- [27] W. Dean. “The stream-line motion of fluid in a curved pipe”. In: *The London, Edinburgh, and Dublin Philosophical Magazine and Journal of Science* 5.30 (1928), pp. 673–695. DOI: <https://doi.org/10.1080/14786440408564513>.
- [28] S. Deck and N. Renard. “Towards an enhanced protection of attached boundary layers in hybrid RANS/LES methods”. In: *Journal of Computational Physics* 400 (2020), p. 108970. DOI: <https://doi.org/10.1016/j.jcp.2019.108970>.
- [29] N. Deen. *An experimental and computational study of fluid dynamics in gas-liquid chemical reactors*. Aalborg University Esbjerg, Esbjerg, Denmark, 2001. ISBN: 978-3844009460.
- [30] N. G. Deen, B. H. Hjertager, and T. Solberg. “Comparison of PIV and LDA measurement methods applied to the gas-liquid flow in a bubble column”. In: *10th international symposium on applications of laser techniques to fluid mechanics*. 2000, pp. 1–12.

- [31] N. G. Deen, T. Solberg, and B. H. Hjertager. “Numerical simulation of the gas-liquid flow in a square cross-sectioned bubble column”. In: *Proceedings of 14th Int. Congress of Chemical and Process Engineering: CHISA (Praha, Czech Republic, 2000)*. 2000.
- [32] E. Delnoij, J. Kuipers, and W. P. M. van Swaaij. “Dynamic simulation of gas-liquid two-phase flow: effect of column aspect ratio on the flow structure”. In: *Chemical engineering science* 52.21-22 (1997), pp. 3759–3772. DOI: [https://doi.org/10.1016/S0009-2509\(97\)00222-4](https://doi.org/10.1016/S0009-2509(97)00222-4).
- [33] O. Desjardins, J. McCaslin, M. Owkes, and P. Brady. “Direct numerical and large-eddy simulation of primary atomization in complex geometries”. In: *Atomization and Sprays* 23.11 (2013). DOI: <https://doi.org/10.1615/AtomizSpr.2013007679>.
- [34] M. Dhotre, N. Deen, B. Niceno, Z. Khan, and J. Joshi. “Large eddy simulation for dispersed bubbly flows: a review”. In: *International Journal of Chemical Engineering* 2013 (2013). DOI: <https://doi.org/10.1155/2013/343276>.
- [35] P. A. Durbin. “Separated flow computations with the k-epsilon-v-squared model”. In: *AIAA journal* 33.4 (1995), pp. 659–664. DOI: <https://doi.org/10.2514/3.12628>.
- [36] P. A. Durbin and B. P. Reif. *Statistical theory and modeling for turbulent flows*. John Wiley & Sons, 2011. ISBN: 978-0470689318.
- [37] Y. Egorov and F. Menter. “Development and application of SST-SAS turbulence model in the DESIDER project”. In: *Advances in Hybrid RANS-LES Modelling*. Springer, 2008, pp. 261–270. DOI: [https://doi.org/10.1007/978-3-540-77815-8\\_27](https://doi.org/10.1007/978-3-540-77815-8_27).
- [38] S. Elghobashi. “On predicting particle-laden turbulent flows”. In: *Applied scientific research* 52.4 (1994), pp. 309–329. DOI: <https://doi.org/10.1007/BF00936835>.
- [39] S. Elghobashi and T. Abou-Arab. “A two-equation turbulence model for two-phase flows”. In: *The Physics of Fluids* 26.4 (1983), pp. 931–938. DOI: <https://doi.org/10.1063/1.864243>.
- [40] M. Emory and G. Iaccarino. “Visualizing turbulence anisotropy in the spatial domain with componentality contours”. In: *Center for Turbulence Research Annual Research Briefs* (2014), pp. 123–138.
- [41] J. Eustice. “Flow of water in curved pipes”. In: *Proc. R. Soc. London* 84 (1910), pp. 107–118. DOI: <https://doi.org/10.1098/rspa.1910.0061>.
- [42] F. Evrard, F. Denner, and B. van Wachem. “A hybrid Eulerian-Lagrangian approach for simulating liquid sprays”. In: *ILASS–Europe, Paris, France* (2019), pp. 2–4.

- 
- [43] C. Evrim and E. Laurien. “Large-Eddy Simulation of turbulent thermal flow mixing in a vertical T-Junction configuration”. In: *International Journal of Thermal Sciences* 150 (2020), p. 106231. DOI: <https://doi.org/10.1016/j.ijthermalsci.2019.106231>.
- [44] B. Fdhila et al. “Analyse expérimentale et modélisation d’un écoulement vertical à bulles dans un élargissement brusque”. PhD thesis. Toulouse, INPT, 1991.
- [45] J. H. Ferziger, M. Perić, and R. L. Street. en. 3rd ed. Berlin, Germany: Springer, 2012. ISBN: 978-3642560262.
- [46] B. Fraga, T. Stoesser, C. C. Lai, and S. A. Socolofsky. “A LES-based Eulerian–Lagrangian approach to predict the dynamics of bubble plumes”. In: *Ocean modelling* 97 (2016), pp. 27–36. DOI: <https://doi.org/10.1016/j.ocemod.2015.11.005>.
- [47] T. Frank, C. Lifante, H.-M. Prasser, and F. Menter. “Simulation of turbulent and thermal mixing in T-junctions using URANS and scale-resolving turbulence models in ANSYS CFX”. In: *Nuclear Engineering and Design* 240.9 (2010), pp. 2313–2328. DOI: <https://doi.org/10.1016/j.nucengdes.2009.11.008>.
- [48] E. Garnier, N. Adams, and P. Sagaut. 2009th ed. Scientific Computation. Dordrecht, Netherlands: Springer, 2009. ISBN: 978-9048128198.
- [49] M. Germano, U. Piomelli, P. Moin, and W. H. Cabot. “A dynamic subgrid-scale eddy viscosity model”. In: *Physics of Fluids A: Fluid Dynamics* 3.7 (1991), pp. 1760–1765. DOI: <https://doi.org/10.1063/1.857955>.
- [50] M. Gibson and W. Rodi. “Simulation of free surface effects on turbulence with a Reynolds stress model”. In: *Journal of Hydraulic Research* 27.2 (1989), pp. 233–244. DOI: <https://doi.org/10.1080/00221688909499183>.
- [51] S. S. Girimaji. “Partially-averaged Navier-Stokes model for turbulence: A Reynolds-averaged Navier-Stokes to direct numerical simulation bridging method”. In: (2006). DOI: <https://doi.org/10.1115/1.2151207>.
- [52] M. Gritskevich, A. Garbaruk, T. Frank, and F. Menter. “Investigation of the thermal mixing in a T-junction flow with different SRS approaches”. In: *Nuclear Engineering and Design* 279 (2014), pp. 83–90. DOI: <https://doi.org/10.1016/j.nucengdes.2014.03.010>.
- [53] A. Gruber, M. R. Bothien, A. Ciani, K. Aditya, J. H. Chen, and F. A. Williams. “Direct Numerical Simulation of hydrogen combustion at auto-ignitive conditions: Ignition, stability and turbulent reaction-front velocity”. In: *Combustion and Flame* 229 (2021), p. 111385. DOI: <https://doi.org/10.1016/j.combustflame.2021.02.031>.
- [54] K. Hanjalić. “Will RANS survive LES? A view of perspectives”. In: (2005). DOI: <https://doi.org/10.1115/HT-FED2004-56356>.
-

- [55] K. Hanjalić, M. Popovac, and M. Hadžiabdić. “A robust near-wall elliptic-relaxation eddy-viscosity turbulence model for CFD”. In: *International Journal of Heat and Fluid Flow* 25.6 (2004), pp. 1047–1051. doi: <https://doi.org/10.1016/j.ijheatfluidflow.2004.07.005>.
- [56] K. Hanjalić and B. Launder. 2nd ed. Cambridge, England: Cambridge University Press, 2022. ISBN: 9781108835060.
- [57] F. H. Harlow and J. E. Welch. “Numerical calculation of time-dependent viscous incompressible flow of fluid with free surface”. In: *The physics of fluids* 8.12 (1965), pp. 2182–2189. doi: <https://doi.org/10.1063/1.1761178>.
- [58] M. Heinrich and R. Schwarze. “3D-coupling of Volume-of-Fluid and Lagrangian particle tracking for spray atomization simulation in OpenFOAM”. In: *SoftwareX* 11 (2020), p. 100483. doi: <https://doi.org/10.1016/j.softx.2020.100483>.
- [59] D. P. Hill. “The computer simulation of dispersed two-phase flow”. PhD thesis. Citeseer, 1998.
- [60] C. W. Hirt and B. D. Nichols. “Volume of fluid (VOF) method for the dynamics of free boundaries”. In: *Journal of computational physics* 39.1 (1981), pp. 201–225. doi: [https://doi.org/10.1016/0021-9991\(81\)90145-5](https://doi.org/10.1016/0021-9991(81)90145-5).
- [61] L. Hufnagel, J. Canton, R. Örlü, O. Marin, E. Merzari, and P. Schlatter. “The three-dimensional structure of swirl-switching in bent pipe flow”. In: *Journal of Fluid Mechanics* 835 (2018), pp. 86–101. doi: <https://doi.org/10.1017/jfm.2017.749>.
- [62] M. Hultmark, M. Vallikivi, S. C. C. Bailey, and A. Smits. “Turbulent pipe flow at extreme Reynolds numbers”. In: *Physical review letters* 108.9 (2012), p. 094501. doi: <https://doi.org/10.1103/PhysRevLett.108.094501>.
- [63] M. Ishii and T. Hibiki. 2nd ed. New York, NY: Springer, 2010. ISBN: 978-1441979858.
- [64] R. I. Issa. “Solution of the implicitly discretised fluid flow equations by operator-splitting”. In: *Journal of computational physics* 62.1 (1986), pp. 40–65. doi: [https://doi.org/10.1016/0021-9991\(86\)90099-9](https://doi.org/10.1016/0021-9991(86)90099-9).
- [65] P. Iudiciani. “Lagrangian particle tracking of spheres and cylinders”. In: *Chalmers University of Technology, Gothenburg, Sweden* (2009).
- [66] S. Jakirlić and K. Hanjalić. “A new approach to modelling near-wall turbulence energy and stress dissipation”. In: *Journal of fluid mechanics* 459 (2002), pp. 139–166. doi: <https://doi.org/10.1017/S0022112002007905>.
- [67] S. Jakirlić and R. Maduta. “Extending the bounds of ‘steady’ RANS closures: Toward an instability-sensitive Reynolds stress model”. In: *International Journal of Heat and fluid flow* 51 (2015), pp. 175–194. doi: <https://doi.org/10.1016/j.ijheatfluidflow.2014.09.003>.

- 
- [68] N. Jarrin, S. Benhamadouche, D. Laurence, and R. Prosser. “A synthetic-eddy-method for generating inflow conditions for large-eddy simulations”. In: *International Journal of Heat and Fluid Flow* 27.4 (2006), pp. 585–593. DOI: <https://doi.org/10.1016/j.ijheatfluidflow.2006.02.006>.
- [69] H. Jasak. “Error analysis and estimation for the finite volume method with applications to fluid flows.” In: (1996).
- [70] S. Jayaraju, E. Komen, and E. Baglietto. “Suitability of wall-functions in Large Eddy Simulation for thermal fatigue in a T-junction”. In: *Nuclear Engineering and Design* 240.10 (2010), pp. 2544–2554. DOI: <https://doi.org/10.1016/j.nucengdes.2010.05.026>.
- [71] S. Johansen and F. Boysan. “Fluid dynamics in bubble stirred ladles: Part II. Mathematical modeling”. In: *Metallurgical Transactions B* 19.5 (1988), pp. 755–764. DOI: <https://doi.org/10.1007/BF02650195>.
- [72] I. Joksimović. <https://github.com/IvanJoksimovic/Proper-Orthogonal-Decomposition>. 2022.
- [73] I. Joksimović. <https://github.com/IvanJoksimovic/Spectral-Proper-Orthogonal-Decomposition>. 2022.
- [74] D. Jungclaus, A. Voswinkel, and P. Negri. *Common IPSN/GRS safety assessment of primary coolant un-isolable leak incidents caused by stress cycling*. Tech. rep. 1998.
- [75] T. Kajishima and K. Taira. *Computational fluid dynamics: incompressible turbulent flows*. Cham: Springer International Publishing, 2017, pp. 269–307. ISBN: 978-3319453026.
- [76] A. Kalpakli Vester, R. Örlü, and P.-H. Alfredsson. “POD analysis of the turbulent flow downstream a mild and sharp bend”. In: *Experiments in Fluids* 56 (Mar. 2015). DOI: <https://doi.org/10.1007/s00348-015-1926-6>.
- [77] H. Kamide, M. Igarashi, S. Kawashima, N. Kimura, and K. Hayashi. “Study on mixing behavior in a tee piping and numerical analyses for evaluation of thermal striping”. In: *Nuclear engineering and design* 239.1 (2009), pp. 58–67. DOI: <https://doi.org/10.1016/j.nucengdes.2008.09.005>.
- [78] J. Kim and J. J. Jeong. “Large eddy simulation of turbulent flow in a T-junction”. In: *Numerical Heat Transfer, Part A: Applications* 61.3 (2012), pp. 180–200. DOI: <https://doi.org/10.1080/10407782.2012.644167>.
- [79] M. Klapwijk, T. Lloyd, and G. Vaz. “On the accuracy of partially averaged Navier–Stokes resolution estimates”. In: *International Journal of Heat and Fluid Flow* 80 (2019), p. 108484. DOI: <https://doi.org/10.1016/j.ijheatfluidflow.2019.108484>.

- [80] F. Köhler, R. Maduta, B. Krumbein, and S. Jakirlić. “Scrutinizing Conventional and Eddy-Resolving Unsteady RANS Approaches in Computing the Flow and Aeroacoustics Past a Tandem Cylinder”. In: *Symposium der Deutsche Gesellschaft für Luft-und Raumfahrt*. Springer. 2018, pp. 586–596. DOI: [https://doi.org/10.1007/978-3-030-25253-3\\_56](https://doi.org/10.1007/978-3-030-25253-3_56).
- [81] J. B. Kok and S. Van der Wal. “Mixing in T-junctions”. In: *Applied mathematical modelling* 20.3 (1996), pp. 232–243. DOI: [https://doi.org/10.1016/0307-904X\(95\)00151-9](https://doi.org/10.1016/0307-904X(95)00151-9).
- [82] A. N. Kolmogorov. “The local structure of turbulence in incompressible viscous fluid for very large Reynolds numbers”. In: *Cr Acad. Sci. URSS* 30 (1941), pp. 301–305.
- [83] B. Krumbein. “A modeling framework for scale-resolving computations of turbulent flow over porous and rough walls”. In: (2019).
- [84] B. E. Launder and D. B. Spalding. “The numerical computation of turbulent flows”. In: *Numerical prediction of flow, heat transfer, turbulence and combustion*. Elsevier, 1983, pp. 96–116. DOI: [https://doi.org/10.1016/0045-7825\(74\)90029-2](https://doi.org/10.1016/0045-7825(74)90029-2).
- [85] Y. Le Moullec, O. Potier, C. Gentric, and J.-P. Leclerc. “Flow field and residence time distribution simulation of a cross-flow gas–liquid wastewater treatment reactor using CFD”. In: *Chemical Engineering Science* 63 (May 2008), pp. 2436–2449. DOI: <https://doi.org/10.1016/j.ces.2008.01.029>.
- [86] Z. Liu and B. Li. “Scale-adaptive analysis of Euler-Euler large eddy simulation for laboratory scale dispersed bubbly flows”. In: *Chemical Engineering Journal* 338 (2018), pp. 465–477. DOI: <https://doi.org/10.1016/j.cej.2018.01.051>.
- [87] M. Lopez de Bertodano, S.-J. Lee, R. Lahey Jr, and D. Drew. “The prediction of two-phase turbulence and phase distribution phenomena using a Reynolds stress model”. In: (1990). DOI: <https://doi.org/10.1115/1.2909357>.
- [88] E. N. Lorenz. “Deterministic nonperiodic flow”. In: *Journal of atmospheric sciences* 20.2 (1963), pp. 130–141. DOI: [https://doi.org/10.1175/1520-0469\(1963\)020%3C0130:DNF%3E2.0.CO;2](https://doi.org/10.1175/1520-0469(1963)020%3C0130:DNF%3E2.0.CO;2).
- [89] K. Lu, Y. Jin, Y. Chen, Y. Yang, L. Hou, Z. Zhang, Z. Li, and C. Fu. “Review for order reduction based on proper orthogonal decomposition and outlooks of applications in mechanical systems”. In: *Mechanical Systems and Signal Processing* 123 (2019), pp. 264–297. DOI: <https://doi.org/10.1016/j.ymssp.2019.01.018>.
- [90] J. L. Lumley and G. R. Newman. “The return to isotropy of homogeneous turbulence”. In: *Journal of Fluid Mechanics* 82.1 (1977), pp. 161–178. DOI: <https://doi.org/10.1017/S0022112077000585>.



- 
- [91] J. L. Lumley. “The structure of inhomogeneous turbulent flows”. In: *Atmospheric turbulence and radio wave propagation* (1967), pp. 166–178.
- [92] T. Ma, D. Lucas, T. Ziegenhein, J. Fröhlich, and N. Deen. “Scale-Adaptive Simulation of a square cross-sectional bubble column”. In: *Chemical Engineering Science* 131 (2015), pp. 101–108. DOI: <https://doi.org/10.1016/j.ces.2015.03.047>.
- [93] T. Ma, D. Lucas, S. Jakirlić, and J. Fröhlich. “Progress in the second-moment closure for bubbly flow based on direct numerical simulation data”. In: *Journal of Fluid Mechanics* 883 (2020). DOI: <https://doi.org/10.1017/jfm.2019.851>.
- [94] G. B. Macpherson, N. Nordin, and H. G. Weller. “Particle tracking in unstructured, arbitrary polyhedral meshes for use in CFD and molecular dynamics”. In: *Communications in Numerical Methods in Engineering* 25.3 (2009), pp. 263–273. DOI: <https://doi.org/10.1002/cnm.1128>.
- [95] R. Maduta and S. Jakirlić. “On the von Karman Length Scale as a Triggering Parameter in Eddy-Resolving Simulations of Turbulent Flows”. In: *Symposium on Hybrid RANS-LES Methods*. Springer. 2016, pp. 179–193. DOI: [https://doi.org/10.1007/978-3-319-70031-1\\_15](https://doi.org/10.1007/978-3-319-70031-1_15).
- [96] R. Maduta, S. Jakirlić, and M. Ullrich. “A numerically upgraded instability-sensitized Reynolds stress model for complex turbulent flow applications”. In: *THMT-15. Proceedings of the Eighth International Symposium On Turbulence Heat and Mass Transfer*. Begel House Inc. 2015. DOI: <https://doi.org/10.1615/ICHMT.2015.THMT-15.550>.
- [97] R. Maduta, M. Ullrich, and S. Jakirlić. “Reynolds stress modelling of wake interference of two cylinders in tandem: conventional vs. eddy-resolving closure”. In: *International journal of heat and fluid flow* 67 (2017), pp. 139–148. DOI: <https://doi.org/10.1016/j.ijheatfluidflow.2017.07.012>.
- [98] R. Maduta. “An eddy-resolving Reynolds stress model for unsteady flow computations: development and application”. PhD thesis. Technische Universität Darmstadt, 2013.
- [99] R. Masood, Y. Khalid, and A. Delgado. “Scale adaptive simulation of bubble column flows”. In: *Chemical Engineering Journal* 262 (2015), pp. 1126–1136. DOI: <https://doi.org/10.1016/j.cej.2014.10.076>.
- [100] M. Masterov, M. Baltussen, and J. Kuipers. “Numerical simulation of a square bubble column using Detached Eddy Simulation and Euler–Lagrange approach”. In: *International Journal of Multiphase Flow* 107 (2018), pp. 275–288. DOI: <https://doi.org/10.1016/j.ijmultiphaseflow.2018.06.006>.
-

- [101] F. Menter. “Zonal two equation kw turbulence models for aerodynamic flows”. In: *23rd fluid dynamics, plasmadynamics, and lasers conference*. 1993, p. 2906.
- [102] F. Menter and Y. Egorov. “The scale-adaptive simulation method for unsteady turbulent flow predictions. Part 1: theory and model description”. In: *Flow, turbulence and combustion* 85.1 (2010), pp. 113–138. DOI: <https://doi.org/10.1007/s10494-010-9264-5>.
- [103] F. Menter and Y. Egorov. “Revisiting the turbulent scale equation”. In: *IUTAM Symposium on One Hundred Years of Boundary Layer Research*. Springer, 2006, pp. 279–290. DOI: [https://doi.org/10.1007/978-1-4020-4150-1\\_27](https://doi.org/10.1007/978-1-4020-4150-1_27).
- [104] K.-J. Metzner and U. Wilke. “European THERFAT project—thermal fatigue evaluation of piping system “Tee”-connections”. In: *Nuclear Engineering and Design* 235.2-4 (2005), pp. 473–484.
- [105] M. Milelli, B. Smith, and D. Lakehal. “Large-eddy simulation of turbulent shear flows laden with bubbles”. In: *Direct and Large-Eddy Simulation IV*. Springer, 2001, pp. 461–470. DOI: [https://doi.org/10.1007/978-94-017-1263-7\\_55](https://doi.org/10.1007/978-94-017-1263-7_55).
- [106] N. Mirkov, B. Rašuo, and S. Kenjereš. “On the improved finite volume procedure for simulation of turbulent flows over real complex terrains”. In: *Journal of Computational Physics* 287 (2015), pp. 18–45. DOI: <https://doi.org/10.1016/j.jcp.2015.02.001>.
- [107] N. Mirkov, N. Vidanović, and G. Kastratović. “freeCappuccino—an open source software library for computational continuum mechanics”. In: *Experimental and Numerical Investigations in Materials Science and Engineering*. Springer, 2018, pp. 137–147. DOI: [https://doi.org/10.1007/978-3-319-99620-2\\_11](https://doi.org/10.1007/978-3-319-99620-2_11).
- [108] E. Mitrou, B. Fraga, and T. Stoesser. “An Eulerian- Lagrangian numerical method to predict bubbly flows”. In: *E3S Web of Conferences* 40 (Jan. 2018), p. 05027. DOI: <https://doi.org/10.1051/e3sconf/20184005027>.
- [109] P. Moin and K. Mahesh. “Direct numerical simulation: a tool in turbulence research”. In: *Annual review of fluid mechanics* 30.1 (1998), pp. 539–578. DOI: <https://doi.org/10.1146/annurev.fluid.30.1.539>.
- [110] P. Munday and K. Taira. “Quantifying wall-normal and angular momentum injections in airfoil separation control”. In: *AIAA Journal* (2017).
- [111] N. Murray, E. Sällström, and L. Ukeiley. “Properties of subsonic open cavity flow fields”. In: *Physics of Fluids* 21.9 (2009), p. 095103. DOI: <https://doi.org/10.1063/1.3210772>.

- 
- [112] M. Nakhchi, S. W. Naung, and M. Rahmati. “Influence of blade vibrations on aerodynamic performance of axial compressor in gas turbine: Direct numerical simulation”. In: *Energy* 242 (2022), p. 122988. DOI: <https://doi.org/10.1016/j.energy.2021.122988>.
- [113] N. Nikitin, N. Popelenskaya, and A. Stroh. “Prandtl’s Secondary Flows of the Second Kind. Problems of Description, Prediction, and Simulation”. In: *Fluid Dynamics* 56 (July 2021), pp. 513–538. DOI: <https://doi.org/10.1134/S0015462821040091>.
- [114] W. F. Noh and P. Woodward. “SLIC (simple line interface calculation)”. In: *Proceedings of the fifth international conference on numerical methods in fluid dynamics June 28–July 2, 1976 Twente University, Enschede*. Springer, 1976, pp. 330–340. DOI: [https://doi.org/10.1007/3-540-08004-X\\_336](https://doi.org/10.1007/3-540-08004-X_336).
- [115] Y. Okagaki, T. Yonomoto, M. Ishigaki, and Y. Hirose. “Numerical Study on an Interface Compression Method for the Volume of Fluid Approach”. In: *Fluids* 6.2 (2021), p. 80. DOI: <https://doi.org/10.3390/fluids6020080>.
- [116] *OpenFOAM: User Guide v2112*. <https://www.openfoam.com/documentation/guides/latest/doc/index.html>. Accessed: May 23, 2023. 2022.
- [117] S. Patankar. “Numerical heat transfer and fluid flow”. In: *Chemie Ing. Tech. WILEY-VCH Verlag* 53.3 (1981), p. 225.
- [118] M. Peric. “A finite volume method for the prediction of three-dimensional fluid flow in complex ducts”. PhD thesis. University of London UK, 1985.
- [119] U. Piomelli. “Large eddy simulations in 2030 and beyond”. In: *Philosophical Transactions of the Royal Society A: Mathematical, Physical and Engineering Sciences* 372.2022 (2014), p. 20130320. DOI: <https://doi.org/10.1098/rsta.2013.0320>.
- [120] S. Pirozzoli, J. Romero, M. Fatica, R. Verzicco, and P. Orlandi. “One-point statistics for turbulent pipe flow up to  $Re_{\tau} \approx 6000$ ”. In: *Journal of Fluid Mechanics* 926 (2021). DOI: <https://doi.org/10.1017/jfm.2021.727>.
- [121] R. Poletto, T. Craft, and A. Revell. “A new divergence free synthetic eddy method for the reproduction of inlet flow conditions for LES”. In: *Flow, turbulence and combustion* 91.3 (2013), pp. 519–539. DOI: <https://doi.org/10.1007/s10494-013-9488-2>.
- [122] S. B. Pope. Cambridge, England: Cambridge University Press, 2000. ISBN: 978-0521598866.
- [123] P. X. Ramos, L. Schindfessel, J. P. Pêgo, and T. De Mulder. “Flat vs. curved rigid-lid LES computations of an open-channel confluence”. In: *Journal of Hydroinformatics* 21.2 (2019), pp. 318–334. DOI: <https://doi.org/10.2166/hydro.2019.109>.
-

- [124] O. Reynolds. “On the Dynamical Theory of Incompressible Viscous Fluids and the Determination of the Criterion (Reprinted from Papers on Mechanical and Physical Subjects, Vol 2, Pg 535-577, 1901)”. In: *Proceedings of the Royal Society-Mathematical and Physical Sciences*. Vol. 451. 1941. ROYAL SOC 6-9 CARLTON HOUSE TERRACE, LONDON SW1Y 5AG, ENGLAND. 1901, pp. 5–47.
- [125] L. F. Richardson and P. Lynch. *Cambridge mathematical library: Weather prediction by numerical process*. 2nd ed. Cambridge Mathematical Library. Cambridge University Press, 2007. ISBN: 9780511618291.
- [126] J. Rotta. *Turbulente strömungen*. BG Teubner Stuttgart; 1972. 1972.
- [127] J. Rotta. “Über eine methode zur Berechnung turbulenter Scherströmungen”. In: *Aerodynamische Versuchsanstalt Rep* 69 (1968), A14.
- [128] H. Rusche. “Computational fluid dynamics of dispersed two-phase flows at high phase fractions”. PhD thesis. Imperial College London (University of London), 2003.
- [129] F. Rütten, W. Schröder, and M. Meinke. “Large-eddy simulation of low frequency oscillations of the Dean vortices in turbulent pipe bend flows”. In: *Physics of Fluids* 17.3 (2005), p. 035107. DOI: <https://doi.org/10.1063/1.1852573>.
- [130] R. Rzehak and E. Krepper. “CFD modeling of bubble-induced turbulence”. In: *International Journal of Multiphase Flow* 55 (2013), pp. 138–155. DOI: <https://doi.org/10.1016/j.ijmultiphaseflow.2013.04.007>.
- [131] P. Sagaut. *Large eddy simulation for incompressible flows: an introduction*. 2nd ed. Scientific Computation. Berlin, Germany: Springer Science & Business Media, 2004. ISBN: 978-3662046951.
- [132] J. Sakakibara, R. Sonobe, H. Goto, H. Tezuka, H. Tada, and K. Tezuka. “Stereo-PIV study of turbulent flow downstream of a bend in a round pipe”. In: *14th International Symposium on Flow Visualization, EXCO, Daegu, South Korea, June*. 2010, pp. 21–24.
- [133] A. Sakowitz, M. Mihaescu, and L. Fuchs. “Turbulent flow mechanisms in mixing T-junctions by Large Eddy Simulations”. In: *International journal of heat and fluid flow* 45 (2014), pp. 135–146. DOI: <https://doi.org/10.1016/j.ijheatfluidflow.2013.06.014>.
- [134] Y. Sato and K. Sekoguchi. “Liquid velocity distribution in two-phase bubble flow”. In: *International Journal of Multiphase Flow* 2.1 (1975), pp. 79–95. DOI: <https://doi.org/10.1299/kikai1938.41.3215>.
- [135] T. Sayadi, C. Hamman, and P. Schmid. “Parallel QR algorithm for data-driven decompositions”. In: *Center for Turbulence Research, Proceedings of the Summer Program*. 2014, pp. 335–343.

- 
- [136] A. Sbitti and S. Taheri. “Crack arrest in high cycle thermal fatigue crazing”. In: *Nuclear engineering and design* 240.1 (2010), pp. 30–38. DOI: <https://doi.org/10.1016/j.nucengdes.2009.09.030>.
- [137] L. Schiller. “Über die grundlegenden Berechnungen bei der Schwerkraftaufbereitung”. In: *Z. Vereines Deutscher Ing.* 77 (1933), pp. 318–321.
- [138] O. T. Schmidt and T. Colonius. “Guide to spectral proper orthogonal decomposition”. In: *Aiaa journal* 58.3 (2020), pp. 1023–1033. DOI: <https://doi.org/10.2514/1.J058809>.
- [139] P. K. Selvam, R. Kulenovic, and E. Laurien. “Large eddy simulation on thermal mixing of fluids in a T-junction with conjugate heat transfer”. In: *Nuclear Engineering and Design* 284 (2015), pp. 238–246. DOI: <https://doi.org/10.1016/j.nucengdes.2014.12.025>.
- [140] K. Sengupta, F. Mashayek, and G. Jacobs. “Direct numerical simulation of turbulent flows using spectral method”. In: *46th AIAA Aerospace Sciences Meeting and Exhibit*. 2008, p. 1450. DOI: <https://doi.org/10.2514/6.2008-1450>.
- [141] J. Shi, T. Thomas, and J. Williams. “Large-eddy simulation of flow in a rectangular open channel”. In: *Journal of Hydraulic Research* 37.3 (1999), pp. 345–361. DOI: <https://doi.org/10.1080/00221686.1999.9628252>.
- [142] M. L. Shur, P. R. Spalart, M. K. Strelets, and A. K. Travin. “A hybrid RANS-LES approach with delayed-DES and wall-modelled LES capabilities”. In: *International journal of heat and fluid flow* 29.6 (2008), pp. 1638–1649. DOI: <https://doi.org/10.1016/j.ijheatfluidflow.2008.07.001>.
- [143] M. Sieber, C. O. Paschereit, and K. Oberleithner. “Spectral proper orthogonal decomposition”. In: *Journal of Fluid Mechanics* 792 (2016), pp. 798–828. DOI: <https://doi.org/10.1017/jfm.2016.103>.
- [144] M. Sieber, C. O. Paschereit, and K. Oberleithner. “Spectral proper orthogonal decomposition”. In: *Journal of Fluid Mechanics* 792 (2016), pp. 798–828. DOI: <https://doi.org/10.1017/jfm.2016.103>.
- [145] J. Smagorinsky. “General circulation experiments with the primitive equations: I. The basic experiment”. In: *Monthly weather review* 91.3 (1963), pp. 99–164. DOI: [https://doi.org/10.1175/1520-0493\(1963\)091%3C0099:GCEWTP%3E2.3.CO;2](https://doi.org/10.1175/1520-0493(1963)091%3C0099:GCEWTP%3E2.3.CO;2).
- [146] B. Smith, J. Mahaffy, and K. Angele. “A CFD benchmarking exercise based on flow mixing in a T-junction”. In: *Nuclear Engineering and Design* 264 (2013), pp. 80–88. DOI: <https://doi.org/10.1016/j.nucengdes.2013.02.030>.
- [147] B. Smith, J. Mahaffy, K. Angele, and J. Westin. “Report of the OECD/NEA-Vattenfall T-junction Benchmark exercise”. In: *NEA/CSNI Report* (2011).
-

- [148] M. Sommerfeld. “Numerical methods for dispersed multiphase flows”. In: *Particles in flows*. Springer, 2017, pp. 327–396. DOI: [https://doi.org/10.1007/978-3-319-60282-0\\_6](https://doi.org/10.1007/978-3-319-60282-0_6).
- [149] P. R. Spalart. “Detached-Eddy simulation”. In: *Annual review of fluid mechanics* 41.1 (2009), pp. 181–202. DOI: <https://doi.org/10.1146/annurev.fluid.010908.165130>.
- [150] P. R. Spalart. “Strategies for turbulence modelling and simulations”. In: *International journal of heat and fluid flow* 21.3 (2000), pp. 252–263. DOI: [https://doi.org/10.1016/S0142-727X\(00\)00007-2](https://doi.org/10.1016/S0142-727X(00)00007-2).
- [151] P. R. Spalart, S. Deck, M. L. Shur, K. D. Squires, M. K. Strelets, and A. Travin. “A new version of detached-eddy simulation, resistant to ambiguous grid densities”. In: *Theoretical and computational fluid dynamics* 20.3 (2006), pp. 181–195. DOI: <https://doi.org/10.1007/s00162-006-0015-0>.
- [152] P. R. Spalart, S. Deck, M. L. Shur, K. D. Squires, M. K. Strelets, and A. Travin. “A new version of detached-eddy simulation, resistant to ambiguous grid densities”. In: *Theoretical and computational fluid dynamics* 20.3 (2006), pp. 181–195. DOI: <https://doi.org/10.1007/s00162-006-0015-0>.
- [153] P. Spalart and M. Shur. “On the sensitization of turbulence models to rotation and curvature”. In: *Aerospace Science and Technology* 1.5 (1997), pp. 297–302. DOI: [https://doi.org/10.1016/S1270-9638\(97\)90051-1](https://doi.org/10.1016/S1270-9638(97)90051-1).
- [154] D. W. Stephens, S. Keough, and C. Sideroff. “Euler-Lagrange large eddy simulation of a square cross-sectioned bubble column”. In: *APCChE 2015 Congress incorporating Chemeca*. Vol. 27. 2015, pp. 1–12.
- [155] M. Sussman, P. Smereka, and S. Osher. “A level set approach for computing solutions to incompressible two-phase flow”. In: *Journal of Computational physics* 114.1 (1994), pp. 146–159. DOI: <https://doi.org/10.1006/jcph.1994.1155>.
- [156] T. Swean, R. Leighton, R. Handler, and J. Swearingen. “Turbulence Modeling Near the Free Surface in an Open Channel Flow”. In: *AIAA 91-0613* (Jan. 1991), p. 11. DOI: <https://doi.org/10.2514/6.1991-613>.
- [157] P. K. Sweby. “High resolution schemes using flux limiters for hyperbolic conservation laws”. In: *SIAM journal on numerical analysis* 21.5 (1984), pp. 995–1011. DOI: <https://doi.org/10.1137/0721062>.
- [158] K. Taira, S. L. Brunton, S. T. Dawson, C. W. Rowley, T. Colonius, B. J. McKeon, O. T. Schmidt, S. Gordeyev, V. Theofilis, and L. S. Ukeiley. “Modal analysis of fluid flows: An overview”. In: *Aiaa Journal* 55.12 (2017), pp. 4013–4041. DOI: <https://doi.org/10.2514/1.J056060>.

- 
- [159] M. Tanaka, H. Ohshima, and H. Monji. “Thermal mixing in T-junction piping system related to high-cycle thermal fatigue in structure”. In: *Journal of nuclear science and technology* 47.9 (2010), pp. 790–801. DOI: <https://doi.org/10.1080/18811248.2010.9711655>.
- [160] H. Tennekes, J. L. Lumley, J. L. Lumley, et al. The MIT Press. London, England: MIT Press, 1972. ISBN: 978-0262200196.
- [161] A. Tominaga., I. Nezu, K. Ezaki, and H. Nakagawa. “Three-dimensional turbulent structure in straight open channel flows”. In: *Journal of Hydraulic Research* 27.1 (1989), pp. 149–173. DOI: <https://doi.org/10.1080/00221688909499249>.
- [162] A. Tomiyama, H. Tamai, I. Zun, and S. Hosokawa. “Transverse migration of single bubbles in simple shear flows”. In: *Chemical Engineering Science* 57.11 (2002), pp. 1849–1858. DOI: [https://doi.org/10.1016/S0009-2509\(02\)00085-4](https://doi.org/10.1016/S0009-2509(02)00085-4).
- [163] A. Towne, O. T. Schmidt, and T. Colonius. “Spectral proper orthogonal decomposition and its relationship to dynamic mode decomposition and resolvent analysis”. In: *Journal of Fluid Mechanics* 847 (2018), pp. 821–867. DOI: <https://doi.org/10.1017/jfm.2018.283>.
- [164] A. Troshko and Y. Hassan. “A two-equation turbulence model of turbulent bubbly flows”. In: *International Journal of Multiphase Flow* 27.11 (2001), pp. 1965–2000. DOI: [https://doi.org/10.1016/S0301-9322\(01\)00043-X](https://doi.org/10.1016/S0301-9322(01)00043-X).
- [165] G. Tryggvason, B. Bunner, A. Esmaeeli, D. Juric, N. Al-Rawahi, W. Tauber, J. Han, S. Nas, and Y.-J. Jan. “A front-tracking method for the computations of multiphase flow”. In: *Journal of computational physics* 169.2 (2001), pp. 708–759. DOI: <https://doi.org/10.1006/jcph.2001.6726>.
- [166] M. Tunstall and J. Harvey. “On the effect of a sharp bend in a fully developed turbulent pipe-flow”. In: *Journal of Fluid Mechanics* 34.3 (1968), pp. 595–608. DOI: <https://doi.org/10.1017/S0022112068002107>.
- [167] R. Tunstall, D. Laurence, R. Prosser, and A. Skillen. “Benchmarking LES with wall-functions and RANS for fatigue problems in thermal-hydraulics systems”. In: *Nuclear engineering and design* 308 (2016), pp. 170–181. DOI: <https://doi.org/10.1016/j.nucengdes.2016.08.022>.
- [168] R. Tunstall, D. Laurence, R. Prosser, and A. Skillen. “Large eddy simulation of a T-Junction with upstream elbow: The role of Dean vortices in thermal fatigue”. In: *Applied thermal engineering* 107 (2016), pp. 672–680. DOI: <https://doi.org/10.1016/j.applthermaleng.2016.07.011>.

- [169] M. Ullrich. “Second-moment closure modeling of turbulent bubbly flows within the two-fluid model framework”. PhD thesis. Technische Universität Darmstadt, 2017. URL: <https://tuprints.ulb.tu-darmstadt.de/id/eprint/5942>.
- [170] M. Ullrich, B. Krumbein, R. Maduta, and S. Jakirlić. “An eddy-resolving Reynolds stress model for the turbulent bubbly flow in a square cross-sectioned bubble column”. In: *ASME International Mechanical Engineering Congress and Exposition*. Vol. 46545. American Society of Mechanical Engineers. 2014, V007T09A018. DOI: <https://doi.org/10.1115/IMECE2014-38054>.
- [171] H. K. Versteeg and W. Malalasekera. 2nd ed. Philadelphia, PA: Prentice Hall, 2007. ISBN: 978-0131274983.
- [172] T. Von Kármán. “Mechanische ahnlichkeit und turbulenz”. In: *Math.-Phys. Klasse* (1930).
- [173] A. Vreman. “An eddy-viscosity subgrid-scale model for turbulent shear flow: Algebraic theory and applications”. In: *Physics of fluids* 16.10 (2004), pp. 3670–3681. DOI: <https://doi.org/10.1063/1.1785131>.
- [174] C. Walker, A. Manera, B. Niceno, M. Simiano, and H.-M. Prasser. “Steady-state RANS-simulations of the mixing in a T-junction”. In: *Nuclear Engineering and Design* 240.9 (2010), pp. 2107–2115. DOI: <https://doi.org/10.1016/j.nucengdes.2010.05.056>.
- [175] C. Walker, M. Simiano, R. Zboray, and H.-M. Prasser. “Investigations on mixing phenomena in single-phase flow in a T-junction geometry”. In: *Nuclear Engineering and Design* 239.1 (2009), pp. 116–126. DOI: <https://doi.org/10.1016/j.nucengdes.2008.09.003>.
- [176] T. Wang, Q. Yang, Y. Tang, H. Shi, Q. Zhang, M. Wang, A. Epikhin, and A. Britov. “Spectral Analysis of Flow around Single and Two Crossing Circular Cylinders Arranged at 60 and 90 Degrees”. In: *Journal of Marine Science and Engineering* 10.6 (2022), p. 811. DOI: <https://doi.org/10.3390/jmse10060811>.
- [177] W. Wang and S. A. Miller. “Direct numerical simulation of noise and its source from decaying homogeneous isotropic turbulence with particulates”. In: *Applied Acoustics* 187 (2022), p. 108495. DOI: <https://doi.org/10.1016/j.apacoust.2021.108495>.
- [178] S. Wegt, R. Maduta, J. Kissing, J. Hussong, and S. Jakirlić. “LES-based vortical flow characterization in a 90°-turned pipe bend”. In: *Computers & Fluids* 240 (2022), p. 105418.
- [179] S. Wegt. “Computational characterization of flow and turbulence in IC engine-relevant cooling channels: An LES-and Reynolds-stress-modeling study”. PhD thesis. 2021.



- 
- [180] J. Westin, F. Alavyoon, L. Andersson, and P. Veber. “Experiments and unsteady CFD-calculations of thermal mixing in a T-junction”. In: *OECD/NEA/IAEA Workshop on the Benchmarking of CFD Codes for Application to Nuclear Reactor Safety* (Jan. 2006).
- [181] P. B. Whalley. *Oxford Chemistry Primers*. London, England: Oxford University Press, 1996. ISBN: 978-0198564447.
- [182] D. C. Wilcox. “Reassessment of the scale-determining equation for advanced turbulence models”. In: *AIAA journal* 26.11 (1988), pp. 1299–1310. DOI: <https://doi.org/10.2514/3.10041>.
- [183] S. Xiao, C. Peng, and D. Yang. “Large-eddy simulation of bubble plume in stratified crossflow”. In: *Phys. Rev. Fluids* 6 (4 2021), p. 044613. DOI: <https://doi.org/10.1103/PhysRevFluids.6.044613>.
- [184] L. Yue, a. Xiaorong G., and C. X. “An Improved Scale-Adaptive Simulation Model for Massively Separated Flows”. In: *International Journal of Aerospace Engineering* 2018 (2018).
- [185] R. Zboray, A. Manera, B. Nieeno, and H. Prasser. “Investigations on mixing phenomena in single-phase flows in a T-junction geometry”. In: *12th International Topical Meeting on Nuclear Reactor Thermal Hydraulics, NURETH-12*. 2007.
- [186] W. Zhang and D. Z. Zhu. “Bubble characteristics of air–water bubbly jets in crossflow”. In: *International Journal of Multiphase Flow* 55 (2013), pp. 156–171. ISSN: 0301-9322. DOI: <https://doi.org/10.1016/j.ijmultiphaseflow.2013.05.003>.
- [187] Y. Zhiyin. “Large-eddy simulation: Past, present and the future”. In: *Chinese journal of Aeronautics* 28.1 (2015), pp. 11–24. DOI: <https://doi.org/10.1016/j.cja.2014.12.007>.
- [188] M. Zhou, R. Kulenovic, and E. Laurien. “T-junction experiment with high temperature and high pressure to investigate flow rate influence on mixing characteristics”. In: *International Journal of Heat and Fluid Flow* 71 (2018), pp. 451–459. DOI: <https://doi.org/10.1016/j.ijheatfluidflow.2018.05.004>.
- [189] M. Zhou, F. Wiltschko, R. Kulenovic, and E. Laurien. “Large-eddy simulation on thermal-mixing experiment at horizontal T-junction with varied flow temperature”. In: *Nuclear Engineering and Design* 388 (2022), p. 111644. DOI: <https://doi.org/10.1016/j.nucengdes.2021.111644>.



# List of Figures

---

2.1. Two dimensional representation of the generic, arbitrary shaped FVM mesh, with characteristic geometrical parameters of the cell. . . . .	14
2.2. Reconstruction of face-center values, based on the owner-neighbour stencil. Mesh is non-skewed. . . . .	17
3.1. Magnitude of the Lorentz attractor solution (left), and difference between two experiments with identical sets of boundary conditions (right). . . . .	32
3.2. Snapshot of decaying Taylor-Green vortices visualized using the Q-criteria. Reproduction of results by Dr. Nikola Mirkov, using the freeCappuccino code, Mirkov et al. (2018). . . . .	33
3.3. Normalized model spectrum, according to the equation 3.3. . . . .	34
3.4. Comparison of the law of the wall (dashed-line), equation 3.48 with the DNS data for the fully developed channel flow - solid line. . . . .	48
4.1. POD analysis: Initial state for all three experiments ( $U(t = 0)$ ). Note the spatial separation for the first experiment (top), obscured nature of data in the second experiment (center), as well as partial overlap of two modes (down). . . . .	66
4.2. POD analysis for the first experiment: captured variance (top-left), FFT analysis of time coefficients (top-right). Spatial representation of the first mode (center), and the second mode (bottom). . . . .	67
4.3. POD analysis for the second experiment: captured variance (top-left), FFT analysis of time coefficients (top-right). Spatial representation of the first mode (center), and the second mode (bottom). . . . .	68
4.4. POD analysis for the third experiment: captured variance (top-left), FFT analysis of time coefficients (top-right). Spatial representation of the first mode (center), and the second mode (bottom). . . . .	69
4.5. Original colormap (left), obtained by using the equation 4.24, as well as modified colormap (right), according to the equation 4.28. . . . .	72
5.1. Axial view of the typical multi-block, hexahedral mesh, used in all six precursor cases. Metric corresponding to each case is listed in Table 5.1. . . . .	74

5.2. Evolution of Wall Shear Stress, shown as a percentage of theoretical value. . . . .	75
5.3. Visualisation of the resolved flow in the typical precursor simulation: iso-surfaces of the vorticity magnitude. Background coloring shows the instantaneous velocity magnitude. . . . .	76
5.4. Visualisation of the obtained flow field for two representative precursor cases: contours of the instantaneous streamwise velocity. . .	77
5.5. Profiles of mean streamwise velocity for all six precursor cases. . . .	78
5.6. Profiles of normal Reynolds stress tensor components for all six precursor cases. . . . .	79
5.7. Profiles of turbulent kinetic energy for all six precursor cases. Dashed lines indicate the modeled turbulence kinetic energy. . . . .	81
5.8. Profiles of maximum cell size, compared with Kolmogorov length scale (left), and profiles of modeled turbulence kinetic energy ratio (right). . . . .	82
6.1. Instantaneous temperature contours on the inner wall surface: Influence of shear-layer, Kelvin–Helmholtz instabilities on the mixing process. . . . .	87
6.2. Visualisation of the mixing patterns in two discussed test cases in WATLON experiment. . . . .	89
6.3. Schematics of the computational domain used for reproducing WATLON experiment. Origin is shown in offset to its real position. . . .	90
6.4. Contours of instantaneous velocity field, W-Ref case. . . . .	92
6.5. Contours of instantaneous kinematic pressure field, W-Ref case. . . .	93
6.6. Contours of mean velocity field, W-Ref case. . . . .	93
6.7. Contours of instantaneous temperature field, W-Ref case. . . . .	94
6.8. Contours of mean temperature field, W-Ref case. . . . .	94
6.9. Contours of RMS temperature, W-Ref case. . . . .	95
6.10. Contours of RMS temperature on the lower wall, W-Ref case. . . . .	95
6.11. Profiles of the first- and second order statistics for the temperature field. . . . .	96
6.12. Profiles of the first- and second order statistics for the velocity field. . . . .	97
6.13. Comparison of mean flow streamlines: calculation (left) and experiment (right). . . . .	98
6.14. Turbulence anisotropy, visualized using componentality contours. . .	98
6.15. Streamlines of the mean secondary flow (top row) and contours of the $T_{RMS}$ (bottom row) at locations: $z = 0.5D_m$ (left column) and $z = D_m$ (right column). . . . .	99
6.16. Topology of first 4 POD modes of the velocity field at position $z = 0.5D_m$ : POD1 (up-left), POD2 (up-right), POD3 (down-left) and POD4 (down-right). No color-bar is shown due to the orthonormal nature of modes. . . . .	100

---

6.17. Accumulation of captured variance (left) and FFT analysis of time coefficients (right) for the $z = 0.5D_m$ . . . . .	101
6.18. Accumulation of captured variance (left) and FFT analysis of time coefficients (right) for the temperature field POD analysis at the walls.	102
6.19. Intensity of first 4 POD modes of the temperature field at the walls: POD1 (up), POD2 (center up), POD3 (center down) and POD4 (down). . . . .	103
6.20. Contours of instantaneous velocity field, I-Ref. . . . .	104
6.21. Contours of instantaneous pressure field, I-Ref. . . . .	104
6.22. Contours of instantaneous temperature field, I-Ref. . . . .	105
6.23. Contours of mean temperature field, I-Ref. . . . .	105
6.24. Contours of RMS temperature, I-Ref. . . . .	106
6.25. Comparison of mean flow streamlines: calculation (left) and experiment (right). . . . .	106
7.1. Schematics of the flow domain with details of the mesh in the mixing zone. . . . .	111
7.2. Contours of the instantaneous velocity field magnitude. LES study by R. Tunstall et al. (2016b) (top) and IIS-RSM case (bottom). . .	113
7.3. Streamlines of the mean flow, LES study (top) and the IIS-RSM (bottom). Coloring represents a local streamwise component of the flow. . . . .	114
7.4. Contours of the dimensionless instantaneous temperature field. . .	115
7.5. Progression of secondary flows in the elbow. Background coloring denotes the normalized streamwise velocity magnitude. . . . .	116
7.6. Progression of secondary flows in the straight section. Background coloring denotes the normalized streamwise velocity magnitude. . .	117
7.7. Comparison between calculated IIS-RSM solution (left) and the LES reference (right). Streamlines colored by the secondary flow magnitude.	118
7.8. Profiles of the streamwise velocity in the elbow (top), as well as in the straight section, downstream of the elbow (bottom). Black lines indicate the IIS-RSM, and the red ones the LES solution. Position of the vortex centres in the IIS-RSM case is depicted with the dashed blue line. Position of the vortex centres in the LES solution are depicted with red dashed line, at available measurement points. . .	119
7.9. Contours of dimensionless $T_{rms}$ on the junction walls. . . . .	120
7.10. Ratio of modeled-to-total turbulent kinetic energy in the IIS-RSM case.	121
7.11. POD Analysis of the velocity field, $7D_b$ upstream of the junction. Respectively, mean flow (top-left), mode 1 (top-right), mode 2 (center-left) and mode 3 (center -right). In the bottom row, FFT Analysis of three time coefficients (left), as well as the accumulation of captured variance (right) are shown. . . . .	122

---

7.12. POD Analysis of the velocity field, $1D_b$ downstream of the junction. Respectively, mean flow (top-left), mode 1 (top-right), mode 2 (center-left) and mode 3 (center-right). In bottom row, FFT Analysis of three time coefficients (left), as well as accumulation of captured variance (right) are shown. . . . .	125
7.13. POD Analysis of the temperature field, $1D_b$ downstream of the junction. Respectively, mean flow (top-left), mode 1 (top-right), mode 2 (center-left) and mode 3 (center-right). In bottom row, FFT Analysis of three time coefficients (left), as well as accumulation of captured variance (right) are shown. . . . .	126
8.1. Schematics of the computational domain in DEEN's bubble column case, with indication of dimensions, as well as visualisation of bubbles. Coloration of bubbles indicates their instantaneous velocity, with color-bar intentionally being left-out. . . . .	133
8.2. Visualisation of instantaneous bubble positions, with coloring indicating the instantaneous velocity magnitude of individual bubbles. . . . .	136
8.3. Visualisation of resolved turbulence protrusion into the domain: iso-surfaces, depicting the instantaneous vorticity levels are shown. Background coloring depicts the instantaneous velocity magnitude. . . . .	137
8.4. Streamlines of the mean velocity field. Background coloring denotes the vertical velocity magnitude for cases without BIT (left), with anisotropic BIT (center), and with isotropic BIT (right). . . . .	138
8.5. Contours of normalized turbulent kinetic energy ratio for the case without BIT (left), with anisotropic BIT (center), and with isotropic BIT (right). Contours normalized by the maximum in modeled turbulence kinetic energy, respectively: 4% (left), 48% (center) and 36% (right). . . . .	139
8.6. Visualisation of turbulence anisotropy through the contours depicting the value of Lumley's flatness parameter $A$ for cases: without BIT (left), with anisotropic BIT (center), and with isotropic BIT (right). . . . .	140
8.7. Comparison of calculated and experimental results for $z/H = 0.63$ . . . . .	142
8.8. Comparison of calculated and experimental results for $z/H = 0.72$ . . . . .	143
8.9. FFT Analysis of the velocity magnitude signal, sampled in the column center at $z/H = 0.152$ (left), and $z/H = 0.352$ (right). All three cases of BIT treatment are cross-compared. . . . .	144
8.10. Visualisation of the bubble plume in the cone ladle by Johansen and Boysan (1988) (left), and in the squared domain by Fraga et al. (2016) (right). . . . .	145
8.11. Meshing view for the case of Johansen and Boysan (1988) (left) and Fraga et al. (2016) (right). Note the central refinement needed for the fulfillment of Milelli criterion. . . . .	146

8.12. Comparison of IIS-RSM (left column) and LES-WALE (right column) performance in the first case, for time instants: $t = 1[s]$ (up), $t = 2[s]$ (center) and $t = 3[s]$ (bottom). Coloring indicates the intensity of instantaneous vorticity magnitude. . . . .	147
8.13. Comparison of IIS-RSM (left column) and LES-WALE (right column) performance in the first case, for time instants: $t = 6[s]$ (up), $t = 9[s]$ (center) and $t = 20[s]$ (bottom). Coloring indicates the intensity of instantaneous vorticity magnitude. . . . .	148
8.14. Temporal progression of the integrated resolved, kinetic energy, see equation 8.2, with usage of IIS-RSM and LES-WALE turbulence model.	149
9.1. Visualisation of the experimental flow case '3-5', with a dyed nozzle flow. Provided from Zhang and Zhu, 2013. . . . .	155
9.2. Iso-surfaces of the instantaneous vorticity. Background coloring represents the instantaneous velocity. Identical orientation of coordinates will be used in main case. . . . .	160
9.3. Contours of the streamwise velocity: LES reference (left), and the simulation results (right). Isolines (shown in black) correspond to the same levels in both figures. . . . .	160
9.4. Profile of dimensionless streamwise velocity (left), with experimental data from Tominaga. et al. (1989). Normal Reynolds stresses (right) are plotted against the LES reference by Shi et al. (1999). . . . .	161
9.5. Secondary flow streamlines: LES reference (left) and IIS-RSM results (right). . . . .	162
9.6. Contours of the spanwise velocity fluctuations. . . . .	163
9.7. Contours of the streamwise turbulent fluctuations, reference data (left) and simulation results (right). . . . .	164
9.8. Componentality contours of turbulence anisotropy (left), and contours depicting the ratio of modeled turbulence kinetic energy (right).	164
9.9. Streamwise velocity contours (left), and the streamlines of the secondary flow (right), with background coloring indicating the magnitude of secondary flows. . . . .	166
9.10. Barycentric visualisation of the flow (left), and modeled-to-total kinetic energy ratio (right). . . . .	167
9.11. Mesh cross-section in the X-Y plane (top). Instantaneous view of the velocity field in the X-Z plane, with the dispersed bubbles shown to scale (bottom). . . . .	168
9.12. Isometric view of the solution domain, with down-to-scale visualisation of bubbles. Isocontours of mean vorticity are used for visualisation of vortex tubes. Secondary flows are represented through the streamlines in the plane normal to the main flow. . . . .	169

9.13. Streamlines of the mean flow, visualized with the bubble centerline (top left), as well as with the componentality contours of anisotropy (top right). In the center, normalized streamwise  $\overline{uu}$  (center left) and spanwise  $\overline{vv}$  (center right) components of Reynolds stress tensor are shown. In the bottom row, normalized vertical  $\overline{ww}$  component (bottom left), as well as ratio of modeled to total turbulence kinetic energy (bottom right) are shown. . . . . 170

9.14. Distribution of local plume characteristics along the plume centerline  $\xi$ : absolute velocity (upper left) and relative velocity (upper right), void-fraction (lower left), and lateral distribution of void fraction (right) in four consecutive positions of  $\xi$ . . . . . 173

9.15. Distortion of initially ellipsoidal plume shape at four downstream positions. . . . . 174

9.16. Development of flow properties at three consecutive positions downstream:  $x = 0.05$  (top),  $x = 0.15$  (center), and  $x = 0.25$  (bottom). . . . . 175

9.17. FFT Analysis of the velocity signals at four different heights in the plume. Each measurement height is associated with 3 different positions in the flow. . . . . 177

9.18. Results of the POD analysis. . . . . 179



# List of Tables

---

5.1. Inflow conditions and optimal meshing metrics for all six precursor cases. . . . .	75
6.1. Inflow conditions for WATLON experiment. . . . .	90
7.1. Geometrical- and inflow conditions. Temperature given in dimensionless form. . . . .	111
8.1. Physical properties of liquid- and gas phase. . . . .	134
8.2. Geometrical and flow conditions for both bubble plume experiments.	146
9.1. Inflow conditions and geometric parameters. . . . .	155
9.2. Mesh metrics for the first open-channel flow case. . . . .	159
9.3. Inflow conditions and mesh metrics for the main case precursor. . .	166
9.4. Position of the probe triplets for the FFT Analysis. . . . .	177



# A. Appendix - Improved-Instability-Sensitive Reynolds-Stress-Model

---

Transport equation for the Reynolds stress tensor:

$$\begin{aligned} \frac{D\overline{u_i u_j}}{Dt} = & \frac{\partial}{\partial x_k} \left[ \left( \frac{1}{2}\nu + \frac{\nu_t}{1.1} \right) \frac{\partial \overline{u_i u_j}}{\partial x_k} \right] \\ & + P_{ij} - \varepsilon^h \\ & - \left[ C_1 \varepsilon_{ij}^h a_{ij} + C_2 \left( P_{ij} - \frac{1}{3} P_k \delta_{ij} \right) \right] \\ & + C_1^w f_w \frac{\varepsilon^h}{k} \left( \overline{u_k u_m} n_k n_m \delta_{ij} - \frac{3}{2} \overline{u_i u_k} n_k n_j - \frac{3}{2} \overline{u_k u_j} n_k n_i \right) \\ & - C_2^w f_w \left( \Phi_{mk,2} n_k n_m \delta_{ij} - \frac{3}{2} \Phi_{ik,2} n_k n_j - \frac{3}{2} \Phi_{kj,2} n_k n_i \right) \end{aligned}$$

Various functions and constants in the transport equation for the Reynolds stress tensor:

$$\begin{aligned} P_{ij} = & - \left( \overline{u_i u_k} \frac{\partial U_j}{\partial x_k} + \overline{u_j u_k} \frac{\partial U_i}{\partial x_k} \right), \quad P_k = - \left( \overline{u_i u_j} \frac{\partial U_i}{\partial x_j} \right), \quad C_1 = C + \sqrt{A} E^2, \\ C = & 2.5 A F^{0.25} f, \quad F = \min\{0.6; A_2\}, \quad f = \min \left\{ \left( \frac{Re_t}{150} \right)^{1.5}; 1 \right\}, \\ Re_t = & \frac{k^2}{\nu \varepsilon^h}, \quad k = \frac{1}{2} tr(\overline{u_i u_j}), \quad f_w = \min \left\{ \frac{k^{1.5}}{2.5 \varepsilon^h y_n}; 1.4 \right\}, \\ C_2 = & 0.8 A^{0.5}, \quad C_1^w = \max\{1 - 0.7C, 0.3\}, \quad C_2^w = \min\{A; 0.3\}, \\ a_{ij} = & \frac{\overline{u_i u_j}}{k} - \frac{2}{3} \delta_{ij}, \quad A = 1 - \frac{9}{8} (A_2 - A_3), \quad A_2 = a_{ij} a_{ji}, \quad A_3 = a_{ij} a_{jk} a_{ki}, \\ e_{ij} = & \frac{\varepsilon_{ij}^h}{\varepsilon^h} - \frac{2}{3} \delta_{ij}, \quad E = 1 - \frac{9}{8} (E_2 - E_3), \quad E_2 = e_{ij} e_{ji}, \quad E_3 = e_{ij} e_{jk} e_{ki} \end{aligned}$$

**Blending of the Reynolds stress tensor before introducing in the averaged momentum equation:**

$$\overline{u_i u_j} = 0.7 \overline{u_i u_j} - 0.3 (2\nu_t S_{ij}^d - \frac{2}{3} k \delta_{ij})$$

**Turbulent viscosity:**

$$\nu_t = 0.144 A \sqrt{k} \cdot \max \left[ 10 \left( \frac{\nu^3}{\varepsilon^h} \right)^{0.25}, \frac{k^{1.5}}{\varepsilon^h} \right]$$

**Homogenous stress dissipation rate tensor:**

$$\varepsilon_{ij}^h = f_s \overline{u_i u_j} \frac{\varepsilon^h}{k} + (1 - f_s) \frac{2}{3} \varepsilon^h \delta_{ij}, \quad f_s = 1 - E^2 \sqrt{A}, \quad \varepsilon^h = \omega^h k$$

**Transport equation for specific homogenous dissipation rate:**

$$\begin{aligned} \frac{D\omega_h}{Dt} = \frac{\partial}{\partial x_k} & \left[ \left( \frac{1}{2} \nu + \frac{\nu_t}{1.1} \right) \frac{\partial \omega_h}{\partial x_k} \right] \\ & + C_{\omega,1} \frac{\omega_h}{k} P_k - C_{\omega,2} \omega_h^2 \\ & + \frac{2}{k} C_{\omega,3} \nu \nu_t \frac{\partial^2 U_i}{\partial x_j \partial x_l} \frac{\partial^2 U_i}{\partial x_j \partial x_l} \\ & + \frac{2}{k} \left( 0.55 \frac{1}{2} \nu + 0.275 \frac{\nu_t}{1.1} \right) \frac{\partial \omega_h}{\partial x_k} \frac{\partial k}{\partial x_k} \\ & + P_{\Delta U} \end{aligned}$$

**Eddy-resolving source term:**

$$\begin{aligned} P_{\Delta U} &= C_1 \max(C_2 \sqrt{k} \nabla^2 U - C_3 T_2, 0) \\ T_2 &= 3k \max \left[ \frac{1}{k^2} (\nabla k)^2, \frac{1}{\omega^2} (\nabla \omega)^2 \right] \end{aligned}$$

**Various constants in the scale-supplying equation:**

$$\begin{aligned} C_1 &= 0.003, \quad C_2 = 29.11, \quad C_3 = 40, \\ C_{\omega,1} &= 0.44, \quad C_{\omega,2} = 0.8, \quad C_{\omega,3} = 1.0 \end{aligned}$$

## B. Appendix - Nomenclature

---

### Acronyms

<b>BDF</b>	Backward Differencing Scheme
<b>BIT</b>	Bubble Induced Turbulence
<b>CDS</b>	Central Differencing Scheme
<b>CG</b>	Conjugate-Gradients
<b>CFD</b>	Computational Fluid Dynamics
<b>CNS</b>	Crank-Nicolson Scheme
<b>CV</b>	Control volume
<b>DES</b>	Detached-Eddy Simulation
<b>DDES</b>	Delayed Detached-Eddy Simulation
<b>DFSEM</b>	Divergence-Free Synthetic Eddy Method
<b>DMD</b>	Dynamic Mode Decomposition
<b>DNS</b>	Direct Numerical Simulation
<b>EE</b>	Euler-Euler
<b>EL</b>	Euler-Lagrange
<b>ELES</b>	Embedded Large Eddy Simulation
<b>ER</b>	Eddy-resolving
<b>EVM</b>	Eddy-viscosity method
<b>FDM</b>	Finite Difference Method
<b>FFT</b>	Fast Fourier Transformation
<b>FTT</b>	Flow Through Time

<b>FVM</b>	Finite Volume Method
<b>GAMG</b>	Geometric-Algebraic-Multigrid
<b>GGDH</b>	Generalized Gradient Diffusion Hypothesis
<b>HAZ</b>	Heat-affected zone
<b>HO</b>	High Order
<b>ICA</b>	Independent Component Analysis
<b>IDDES</b>	Improved Delayed Detached-Eddy Simulation
<b>IISRSM</b>	Improved Instability Sensitive Reynolds Stress Model
<b>ISAS</b>	Improved Scale Adaptive Simulation
<b>ISRSM</b>	Instability Sensitive Reynolds Stress Model
<b>JHRSM</b>	Jakirlić-Hanjalić Reynolds Stress Model
<b>KSKL</b>	$k$ - square root of $k$ -L
<b>LES</b>	Large-Eddy Simulation
<b>LHS</b>	Left-Hand Side
<b>LO</b>	Low-Order
<b>LPT</b>	Lagrangian Particle Tracking
<b>NSE</b>	Navier-Stokes Equations
<b>ODE</b>	Ordinary Differential Equation
<b>PANS</b>	Partially Averaged Navier Stokes
<b>PDE</b>	Partial Differential Equation
<b>PISO</b>	Pressure-Implicit with Operator-Splitting
<b>POD</b>	Proper Orthogonal Decomposition
<b>PWR</b>	Pressurized-Water Reactor
<b>RANS</b>	Reynolds-Averaged Navier-Stokes
<b>RD</b>	Research and Development
<b>RHS</b>	Right Hand Side

---

<b>RMS</b>	Root Mean Square
<b>ROM</b>	Reduced Order Modeling
<b>RSM</b>	Reynolds Stress Model
<b>SA</b>	Scale Adaptive
<b>SAS</b>	Scale Adaptive Simulation
<b>SGDH</b>	Simplified Gradient Diffusion Hypothesis
<b>SGS</b>	Sub-grid scale
<b>SMC</b>	Second-Moment Closure
<b>SPOD</b>	Spectral POD
<b>SR</b>	Scale-resolving
<b>SS</b>	Smooth Solver
<b>SST</b>	Shear Stress Transport
<b>SVD</b>	Singular Value Decomposition
<b>TFM</b>	Two-fluid model
<b>UDS</b>	Upwind Differencing Scheme
<b>URANS</b>	Unsteady RANS
<b>VOF</b>	Volume of the Fluid
<b>WALE</b>	Wall Adapting Local Eddy-viscosity
<b>WMLES</b>	Wall-Modeled Large-Eddy Simulation
<b>WSS</b>	Wall shear stress

## Dimensionless numbers

$Co$	Courant number
$Eo$	Eötvös number
$Fr$	Froude number
$Re$	Reynolds number
$Pr$	Prandtl number
$Pr_t$	Turbulent Prandtl number
$S_t$	Strouhal number
$S_t$	Stokes number
$We$	Weber number

## Dimensionless symbols - Latin letters

### **Bold**

<b>A</b>	System matrix
<b>A<sub>t</sub></b>	Matrix containing the row-wise time dynamics of POD modes
<b>b</b>	Free vector
<b>C</b>	Spatial covariance matrix
<b>C*</b>	Temporal covariance matrix
<b>L</b>	Matrix containing left singular vectors
<b>Q</b>	Orthogonal matrix, stemming from QR decomposition
<b>Q<sub>R</sub></b>	Rotation matrix
<b>R</b>	Upper triangular matrix, stemming from QR decomposition
<b>S</b>	Snapshot matrix
<b>V</b>	Matrix containing right singular vectors



---

## Uppercase

$Ar$	Aspect ratio
$A_2$	Second invariant of $a_{ij}$
$A_3$	Third invariant of $a_{ij}$
$A$	Lumley's flatness parameter of $a_{ij}$
$C_d$	Drag coefficient
$C_l$	Lift coefficient
$C_{lim}$	Limiter function
$C_i$	RGB colormap weight
$C_i^*$	Modified RGB colormap weight
$C_\mu$	Modeling constant
$C_{vm}$	Virtual (added) mass coefficient
$C_S$	Smagorinsky constant
$E_2$	Second invariant of $e_{ij}$
$E_3$	Third invariant of $e_{ij}$
$E$	Lumley's flatness parameter of $e_{ij}$
$F_{ISAS}$	Modeling constant in ISAS formulation
$I$	Unit (identity) tensor
$N_{faces}$	Number of faces on the cell
$N_{cells}$	Number of cells in the mesh
$N_{\delta t_i}$	Number of Lagrangian time-steps within the cell $i$
$N_p$	Number of different parcels cell $i$ , during one Eulerian time step
$S$	Source term
$S_n$	$n$ -th snapshot vector
$S_{p,i}^L$	Source term in the Lagrangian frame of reference, for parcel $p$ , residing within the cell $i$
$S_{p,i}^E$	Source term in the Eulerian frame of reference, for the cell $i$

$S_p$	Implicit source term
$S_u$	Explicit source term
$U^+$	Dimensionless velocity

### Lowercase

$a_i(t)$	Time dynamics of $i$ -th POD mode
$a_{ij}$	Reynolds stress anisotropy tensor
$a_{ij}^*$	Principal Reynolds stress anisotropy tensor
$b^*$	Redistribution tensor
$e_{ij}$	Dissipation anisotropy tensor
$f_s$	Relaxation function
$\vec{u}_r$	Unit vector of relative velocity
$\vec{n}_f$	Surface normal unit-vector on face $f$
$y^+$	Dimensionless wall-normal distance

## Dimensioned symbols - Latin letters

### Bold

<b>A</b>	Diagonal matrix in the discretized momentum equation, $kg s^{-1}$
<b>M</b>	System matrix in the discretized momentum equation, $kg s^{-1}$
<b>H</b>	Matrix containing neighbour influence, discretized momentum equation, $N$
<b>p</b>	Vector containing discretized pressure, $Pa$
<b>S</b>	Explicit velocity correction matrix in the discretized momentum equation, $N$

---

## Uppercase

$A$	Surface, $m^2$
$C_{ij}$	Convective term, Reynolds stresses evolution equation, $m^2 s^{-3}$
$D$	Pipe diameter, $m$
$D_b$	Branch-pipe diameter, $m$
$D_m$	Main-pipe diameter, $m$
$D_H$	Hydraulic diameter, $m$
$D_{ij}^t$	Turbulent-diffusion term, Reynolds stresses evolution equation, $m^2 s^{-3}$
$D_k^t$	Turbulent-diffusion term, turbulent kinetic energy evolution equation, $m^2 s^{-3}$
$D_{ij}^\nu$	Molecular-diffusion term, Reynolds stresses evolution equation, $m^2 s^{-3}$
$D_k^\nu$	Molecular-diffusion term, evolution equation for turbulent kinetic energy, $m^2 s^{-3}$
$D_{ij}^p$	Pressure-diffusion term, Reynolds stresses evolution equation, $m^2 s^{-3}$
$E$	Total energy, $J$
$\vec{F}$	Force, $N$
$\vec{F}_A$	Surface force, $N$
$\vec{F}_b$	Buoyancy force, $N$
$\vec{F}_d$	Drag force, $N$
$\vec{F}_f$	Volumetric flux through cell face, $m^3 s^{-1}$
$\vec{F}_g$	Gravity force, $N$
$\vec{F}_V$	Volumetric force, $N$
$\vec{F}_l$	Lift force, $N$
$\vec{F}_{vm}$	Virtual (added) mass force, $N$
$\vec{F}_s$	Surface (far-field) force, $N$
$K$	Kinetic energy, $J$
$K_{modeled}$	Integrated modeled kinetic energy, $J$

$K_{resolved}$	Integrated resolved kinetic energy, $J$
$L$	Integral length scale, $m$
$L_{ij}$	Local term, Reynolds stresses evolution equation, $m^2s^{-3}$
$L_t$	Turbulent length scale, $m$
$L_{SST}$	Turbulent length scale in $k - \omega - SST$ model, $m$
$L_{vk}$	Von-Karman length scale, $m$
$\vec{M}$	Momentum, $kg \cdot ms^{-1}$
$P_{SAS}$	Scale-adaptive source term in transport equation for $\omega^h$ , $s^{-2}$
$P_{\Delta U}$	Eddy-resolving source term in transport equation for $\omega^h$ , $s^{-2}$
$P_{ij}$	Production term, Reynolds stresses evolution equation, $m^2s^{-3}$
$P_k$	Production term, evolution equation for turbulent kinetic energy, $m^2s^{-3}$
$\dot{Q}$	Heat flux, $W$
$\dot{Q}_A$	Surface heat flux, $W$
$\dot{Q}_W$	Volumetric heat flux, $W$
$R$	Radius, $m$
$R_c$	Curvature radius, $m$
$R_{ij}$	Reynolds stress tensor, $m^2s^{-2}$
$S$	Strain-rate, $s^{-1}$
$S_{ij}$	Strain-rate tensor, $s^{-1}$
$S_{ij}^d$	Deviator of the strain-rate tensor, $s^{-1}$
$S_k$	Source term in transport equation for turbulence kinetic energy, $m^2s^{-3}$
$S_R$	Source term in transport equation for Reynolds stress tensor, $m^2s^{-3}$
$S_{\epsilon^h}$	Source term in transport equation for $\epsilon^h$ , $m^2s^{-3}$
$S_{\omega^h}$	Source term in transport equation for $\omega^h$ , $m^2s^{-3}$
$T$	Temperature, $K$
$T_{RMS}$	RMS Temperature, $K$

---

$T_t$	Turbulent time scale, $s$
$\vec{U}$	Velocity, $ms^{-1}$
$\vec{U}_b$	Velocity of the bubble, $ms^{-1}$
$\vec{U}_r$	Relative velocity of the bubble, $ms^{-1}$
$V$	Volume, $m^3$
$V_i$	Volume of the cell $i$ , $m^3$
$\dot{W}$	Work, $W$
$\dot{W}_A$	Work of surface forces, $W$
$\dot{W}_V$	Work of volumetric forces, $W$

### Lowercase

$d_b$	Bubble diameter, $m$
$e$	Specific total energy, $m^2s^{-2}$
$f$	Frequency, $s^{-1}$
$\vec{f}$	Specific volumetric force, $ms^{-2}$
$\vec{g}$	Gravitational acceleration, $ms^{-2}$
$h$	specific enthalpy, $Jkg^{-1}K^{-1}$
$i$	specific internal energy, $Jkg^{-1}K^{-1}$
$k$	Turbulence kinetic energy, $m^2s^{-2}$
$k_t$	Thermal conductivity, $Wm^{-1}K^{-1}$
$l_0$	Top-level length scale, $m$
$m$	Mass, $kg$
$m_b$	Bubble mass, $kg$
$p$	Pressure $Pa$
$\vec{q}$	Specific surface heat flux, $W \cdot m^{-2}$
$t$	Time coordinate, $s$

$\vec{u}$	Velocity fluctuation, $ms^{-1}$
$u_\eta$	Kolmogorov velocity scale, $ms^{-1}$
$u_\tau$	Friction velocity, $ms^{-1}$
$\overline{u_i u_j}$	Reynolds stress tensor, $m^2 s^{-2}$
$\overline{u_i \theta}$	Sub-grid heat flux vector, $mK s^{-1}$
$\vec{x}$	Spatial coordinate, $m$
$\vec{x}_b$	Bubble position, $m$
$\vec{x}_P$	Position of the cell center, $m$
$y_n$	Wall-normal distance, $m$

## Dimensionless symbols - Greek letters

### **Bold**

$\mathcal{E}$	Set of experimental conditions
$\Lambda$	Diagonal matrix containing sorted eigenvalues of either $\mathbf{C}$ or $\mathbf{C}^*$
$\Sigma$	Diagonal matrix containing singular values
$\Phi$	Matrix containing row-wise eigenvectors of $\mathbf{C}$
$\Psi$	Matrix containing row-wise eigenvectors of $\mathbf{C}^*$

### **Uppercase**

$\Gamma$	Diffusivity in the transport equation for generalized variable $\phi$
$\Delta$	Shift (spatial or temporal)
$\Phi_i$	$i$ -th POD mode

---

## Lowercase

$\alpha$	Void fraction of the dispersed phase
$\beta$	Blending function
$\gamma$	Blending function
$\delta$	Curvature characteristics
$\delta_{ij}$	Kronecker symbol, identity tensor
$\zeta$	Anisotropy related variable
$\kappa$	Von Karman constant
$\lambda$	Eigenvalue
$\lambda_f$	Face interpolation factor
$\sigma$	Singular value
$\phi$	Generic flow variable
$\phi'$	Fluctuation intensity
$\chi$	Phase indicator function
$\nabla$	Nabla operator

## Dimensioned symbols - Greek letters

### Uppercase

$\Delta$	Mesh length scale, $m$
$\Phi$	Scale-supplying variable in KSKL model, $m^2 s^{-1}$
$\Phi_{ij}$	Redistribution term, Reynolds stresses evolution equation, $m^2 s^{-3}$
$\Psi$	Scale-supplying variable in Rotta's turbulence model, $m^3 s^{-2}$

### Lowercase

$\alpha$	Temperature diffusivity, $m^2s^{-1}$
$\alpha_t$	Turbulent temperature diffusivity, $m^2s^{-1}$
$\varepsilon$	Dissipation rate, $m^2s^{-3}$
$\varepsilon_{ij}$	Tensor of dissipation rate, $m^2s^{-3}$
$\varepsilon^h$	Homogeneous dissipation rate, $m^2s^{-3}$
$\varepsilon_{ij}^h$	Tensor of homogeneous dissipation rate, $m^2s^{-3}$
$\eta$	Kolmogorov length scale, $m$
$\theta$	Temperature fluctuation, $K$
$\kappa$	Wave number, $m^{-1}$
$\mu$	Dynamic viscosity, $Pa\cdot s$
$\mu_{eff}$	Dynamic effective viscosity, $Pa\cdot s$
$\mu_t$	Dynamic turbulent viscosity, $Pa\cdot s$
$\mu_{BIT}$	Dynamic bubble-induced viscosity, $Pa\cdot s$
$\nu$	Kinematic viscosity, $m^2s^{-1}$
$\nu_{eff}$	Kinematic effective viscosity, $m^2s^{-1}$
$\nu_t$	Turbulent kinematic viscosity, $m^2s^{-1}$
$\nu_{SGS}$	Sub-grid turbulent viscosity, $m^2s^{-1}$
$\rho$	Density $kgm^{-3}$
$\sigma_{ij}$	Tensor of surface forces, $Pa$
$\tau_0$	Top-level time scale, $s$
$\tau_\eta$	Kolmogorov time scale, $s$
$\tau$	Shear stress, $Pa$
$\tau_b$	Bubble time scale, $s$
$\tau_w$	Wall-shear stress, $Pa$
$\tau_{ij}$	Tensor of tangential shear stresses, $Pa$



---

$\tau_{ij}^{SGS}$	Sub-grid stress tensor, $Pa$
$\omega$	Specific dissipation (turbulence frequency) , $s^{-1}$
$\omega^h$	Homogeneous specific dissipation (turbulence frequency) , $s^{-1}$



# C. Curriculum Vitae

---

## Personal information

Name: Ivan Joksimović

## Professional experience

03/2018 - 07/2019 Mechanical Engineer in Vinča Institute of Nuclear Sciences, Belgrade, Serbia

07/2017 - 10/2017 Intern in ANDREAS STIHL AG & Co. KG, Waiblingen, Germany

## Education

10/2019 - 09/2022 Doctoral research in Mechanical Engineering (Dr.-Ing.), Technische Universität Darmstadt, Darmstadt, Germany

09/2015 - 06/2017 Studies in Mechanical Engineering (M.Sc. -Ing), University in Belgrade, Belgrade, Serbia

09/2012 - 07/2015 Studies in Mechanical Engineering (B.Sc. -Ing), University in Belgrade, Belgrade, Serbia